UNIVERSIDAD
DE GRANADA

Universidad de Granada
Departamento de Teoría de la Señal, Telemática y Comunicaciones.

PROGRAMA DE DOCTORADO EN TECNOLOGÍAS DE LA INFORMACIÓN Y LA COMUNICACIÓN

TESIS DOCTORAL:

CONTRIBUTION TO THE DESIGN OF FILTERING AND MULTIPLEXING RF DEVICES AND STRUCTURES FOR WIRELESS AND SATELLITE COMMUNICATION APPLICATIONS

Autor:
Mohamed Taha ELKHORASSANI

Directores:
Dr. Juan Fco. Valenzuela Valdés
Dr. Pablo Padilla de la Torre

Editor: Universidad de Granada. Tesis Doctorales
Autor: Mohamed Taha El Khorassani
ISBN: 978-84-1306-491-8
URI: http://hdl.handle.net/10481/62276

Acknowledgment:

I would like to thank the University of Granada and especially the Escuela Técnica Superior de Ingenierías Informática y de Telecomunicación (ETSIIT-UGR) who supported my work and helped me get results of better quality.

I would like to thank my fellow doctoral students for their feedback, cooperation and of course friendship. In addition, I would like to express my gratitude to my supervisors Prof. Juan Francisco Valenzuela Valdés and Prof. Pablo Padilla de la Torre for their constant supervision, knowledge that was lifting me all along my research, and for their patience and support in overcoming numerous obstacles I have been facing through my research.

I would like to thank my friends for accepting nothing less than excellence from me. Last but not the least, I would like to thank my family: my parents and to my brother for supporting me spiritually throughout writing this thesis and my life in general.

Abstract:

Many investigations on designing electronic devices such as filters, phase shifters and circulators for telecommunication systems are ongoing due to their inevitable role between the transmitter and the receiver in the telecommunication chain. Therefore, studies that investigate the optimization of design of those electronic elements are of great importance.

This Thesis work is devoted to the design of filtering and multiplexing radiofrequency (RF) devices and structures for wireless and satellite communication applications. In this work, a deep state of the art on the filtering and multiplexing technologies has been carried out (chapter 2). It states the background of filters, phase shifters and circulators with the introduction of the technologies of the circuits, their synthesis and design techniques, also introducing optimization procedures, such as the gradient based optimization and the genetic algorithm optimization, that reduce the cost and the time of the design process.

The main work of this Thesis is focused on RF filters (chapter 3), RF phase shifters (chapter 4) and circulators (chapter 5). The design of RF filters (chapter 3) is mainly focused on tunable waveguide band pass filter using rectangular pins covered by graphene material, allowing the tuning of the center frequency and even the bandwidth of the filter. The design of phase shifter (chapter 4) proposes a novel technique for phase shifters with their synthesis and design techniques based on reflective radio frequency circuit, optimized for frequencies up to 18 GHz. The design process is accompanied by a new optimization method based on genetic algorithms to match any input characters needed. The last device under study is the microstrip circulator (chapter 5). Its design is based on stripline/microstrip topology and some circulator design techniques are proposed.

Optimization techniques are also proposed to provide different circulator designs that fulfil demanding requirements in their performance.

This document details the Thesis work, identifying preliminary limits on all those device designs, fulfilling the objectives of the Thesis.

Resumen:

En la actualidad se está llevando a cabo gran cantidad de investigación sobre el diseño de dispositivos electrónicos como filtros, desplazadores de fase y circuladores para sistemas de telecomunicaciones debido a su inevitable papel entre el transmisor y el receptor en la toda la cadena de un sistema de telecomunicaciones. Por lo tanto, los estudios que investigan la optimización del diseño de esos elementos electrónicos son de gran importancia.

Este trabajo de tesis está dedicado al diseño de dispositivos y estructuras de radiofrecuencia (RF) de filtrado y multiplexación para aplicaciones de comunicaciones inalámbricas y satelitales. En este trabajo se ha realizado un profundo estado del arte en las tecnologías de filtrado, multiplexación y guiado (capítulo 2). Se exponen los antecedentes de los filtros, desfasadores y circuladores con la introducción de las tecnologías de los circuitos, su síntesis y las técnicas de diseño, introduciendo también procedimientos de optimización, como la optimización basada en gradientes y la optimización de algoritmos genéticos, que reducen el coste y el tiempo del proceso de diseño.

El trabajo principal de esta tesis se centra en los filtros de RF (capítulo 3), los desfasadores de RF (capítulo 4) y los circuladores de RF (capítulo 5). El diseño de los filtros de RF (capítulo 3) se centra principalmente en el filtro paso-banda de guía de onda sintonizable utilizando pines rectangulares cubiertos por material de grafeno, permitiendo la sintonización de la frecuencia central e incluso el ancho de banda del filtro. El diseño de defasadores (capítulo 4) propone una técnica novedosa para estos dispositivos con corrección de fase con sus técnicas de síntesis y diseño basadas en el circuito reflectante controlable electrónicamente, optimizado para frecuencias de hasta 18 GHz. El proceso de diseño va acompañado de un nuevo método de optimización basado en algoritmos genéticos para hacer coincidir los caracteres de entrada necesarios. El

último dispositivo en estudio es el circulador de microstrip (capítulo 5). Su diseño se basa en la topología de línea stripline/microtrip y se proponen algunas técnicas de diseño de circuladores. También se proponen técnicas de optimización para proporcionar diferentes diseños de circuladores que cumplan con los requisitos exigentes en su rendimiento.

Este documento detalla el trabajo de la Tesis, identificando los límites preliminares de todos aquellos diseños de dispositivos, cumpliendo con los objetivos de la Tesis.

List of Contents:

List of Tables 23

Chapter 1: 25

Motivation and objectives 25

Chapter 2: 29

State of the art 29

2.1 Background and State of the Art 29

2.1.1Bandpass filter synthesis 34

2.1.2Different types of microwave filters 36

2.1.3 Tunable filters 46

2.2 Electronically tunable phase shifters 49

2.2.1 Antenna networks 49

2.2.2 Antenna network based on hybrid couplers **50**

2.3 Built-in microwave phase shifters 52

2.3.1 Phase shifter based on switched lines 53

2.3.2 Phase shifter based on lines loaded with MEMS-RF 54

2.3.3Phase shifter based on hybrid couplers at 90° 55

2.4 Electronic circulator 57

2.4.1 Insulator 58

2.4.1.1.i Operating principle of an insulator 58

2.4.1.1.ii Field displacement isolators 59

2.4.1.1.iii Field displacement isolator in rectangular waveguide 60

2.4.1.1.iv Field displacement isolator made on microstrip line 61

2.4.1.1.v The coplanar resonance isolator 62

2.5 Circulators 63

2.5.1 Principle and different uses 64

Chapter 3: 83

Coupled Resonator Filters 83

3.1 Introduction 83

3.2 Problematic 85

3.3 Introduction to Coupled Resonator Filters methods 86

3.3.1 Coupling matrix representation 86

3.3.2 Example of usage: Synthesis of chebyshev low pass prototype method 90

3.4 Synthesis of pass-band filters using the Polynomial methods 94

3.4.1 Cameron's recursive method 94

3.4.2 Rhodes and Alseyab Alternating method used to determine the denominator polynomial E(s) 98

3.4.3 Examples of usage: Synthesis of passband filters using the Polynomial methods 102

3.5 Rotation method 108

3.5.1 The rational forms of the transfer function $S_{21}(s)$ and the reflection $S_{11}(s)$ function for lossless two-port network. 108

3.5.2 Synthesis of the N+2 transversal Matrix 112

3.5.3 The Reduction of the N+2 transversal Matrix to the folded canonical form 115

3.5.4 Examples of usage: Calculation of the resonators coupling matrix of a folded filter using the method of the rotation 118

3.6Realization the coupling matrix in the microstrip resonators 120

3.6.1 Formulation for Coupling Coefficients 120

3.6.2 Coupling Coefficients as Function of Separation S 123

3.6.3Simulation and Measurement 126

3.7 The gradient based optimization method 128

3.7.1 Gradient calculations 129

3.7.2 Example of usage: trisection bandpass filter with gradient based method 131

3.8 Genetic Algorithm method 132

3.8.1 Fundaments of GA 133

3.9 Graphene-based structures for filters 137

3.10 Conclusion 156

Chapter 4: _____ 159

Electronically reconfigurable phase shifter _____ 159

4.1 Introduction 159

4.2 Experimental approach 161

4.2.1 Example of usage: electronically reconfigurable phase shifter at 12 GHz 161

4.2.1.1 Phase Shifter Design and Performance for 12 GHz 161

4.2.1.1.1 Hybrid coupler (12GHz) 161

4.2.1.1.2 Reflective RF circuit 162

4.2.1.1.3 Complete phase shifter integration (12GHz) 166

4.2.1.2 Double Phase Shifter Design and Performance at 12 GHz 168

4.2.2 The phase Shifter Design and Performance for 18 GHz 171

4.2.2.1 The hybrid coupler (18 GHz) 171

4.2.2.2 Complete phase shifter integration (18-18.5 GHz) 172

4.2.2.3 Complete double phase shifter integration (18 GHz) 175

4.3 Phase Shifter Prototype Performance 177

Chapter 5: _____ 185

Microstrip Wideband Circulator _____ 185

5.1 Introduction 185

5.2 The Wideband Circulator Design in The Literature 185

5.3 The definition of the important parameters of Ferrite Materials 187

5.3.1 Saturation Magnetization ($4\pi M_s$) 187

5.3.2 Resonance Linewidth (ΔH) 188

5.3.3 Compensation Temperature (TN) 188

5.4 he Wideband Circulator Design 189

5.4.1 The Structure of a microstrip Circulator 189

5.4.2 The Theoretical Basis of Wideband Circulator Design 190

5.4.2.1 The Green's Function Approach 190

5.4.2.2 The Design of One Octave Frequency Band Circulator 191

5.5 The Design, and Simulation of one octave Frequency Band microstrip circulator 194

5.5.1 Analytical Design of One Octave Frequency Band Circulator 194
5.5.2 Determination of Ferrite Material 194
5.5.3 The calculation of the coupling angle 196
5.5.4 The calculation of both the Radius and the Thickness characteristics of Ferrite Disk 196
5.5.5 Analytical design of Impedance transformer 198
5.5.6 Simulation results of the circulator designed using the analytically Frequency Band method 200
5.5.7 Simulation results of optimized Y-junction circulator 200

Chapter 6: _____ 205

Conclusion and future work_____ 205

REFERENCES:_____ 215

List of Figures

Fig 2.1 Template for ideal filters 30
Fig 2.2 Low pass prototype of the three types of filters 31
Fig 2.3 Butterworth filter response for different orders 32
Fig 2.4 Chebyshev filter response for different orders 32
Fig 2.5 Template of a bandpass filter 33
Fig 2.6 Equivalent diagram of a low-pass prototype with localized elements 34
Fig 2.7 Equivalent diagram of a bandpass prototype with localized elements 35
Fig 2.8 Equivalent diagram of a bandpass prototype with impedance inverters . 35
Fig 2.9 Quarter-wave stubs filter 37
Fig 2.10 Band-pass filter with coupled lines 37
Fig 2.11 Combline filter in transmission lines 38
Fig 2.12 Interdigital filter 39
Fig 2.13 Waveguide reception filter 40
Fig 2.14 Ridged waveguide bandpass filter 41
Fig 2.15 Dielectric resonator filter [19] 42
Fig 2.16 Dielectric resonator filter coupled by adjusting iris [20] 42
Fig 2.17 Dielectric resonator filter 43
Fig 2.18 Cylindrical metal cavity filter [20] 44
Fig 2.19 Filter with rectangular metal cavities [14] 44
Fig 2.20 SIW filter [24] 45
Fig 2.21 Mechanical tunable waveguide bandpass filter, with its simulation results in K-Band [27] 47
Fig 2.22 Magnetically tunable wideband bandpass filter using ferrite material, with its simulation results in X-Band [27] 48
Fig 2.23 Magnetically tunable bandpass filter, with its simulation results in Ka-Band [27] 48
Fig 2.24 (a) Array Antennas Network Photography (b) Radiation Diagram for the 4 Modes [29] 50

Fig 2.25 (a) Array photograph (b) Principle of the phase shift cell (c)Radiation diagram for different configurations [30] 51
Fig 2.26 (a) Network photography (b) Phase shift cell (c) Radiation diagram for different configurations [31] 52
Fig 2.27 Phase shifter based on switched lines [33], [34] 54
Fig 2. 28 Raytheon's phase shifter, XLIM's phase shifter [35] 54
Fig 2. 29: Equivalent diagram of a hybrid coupler in distributed elements. (a) A hybrid coupler using varactor diodes of the University of Nice (b) in localized elements [36] 56
Fig 2.30 Hybrid coupler phase shifter [37] 56
Fig 2.31 2x2 mm phase shifter chip, 1 way to 4 [38] 57
Fig 2.32 Simplified diagram of operation of a duplexer in a radar circuit 58
Fig 2.33 Schematic diagram of an insulator 59
Fig 2.34 Non-reciprocal propagation and field displacement. (a) propagation according to z> 0. (b) propagation according to z <0 60
Fig 2.35 Field displacement isolator in rectangular waveguide. (a) Direction blocked for propagation in z> 0. (b) forward direction for propagation according to z <0 61
Fig 2.36 Field displacement isolator in microstrip technology. The field lines shown correspond to the vertical electric field. (a) Propagation according to z> 0 for a microstrip line on a polarized ferrite substrate. (b) Propagation according to z <0 for a microstrip line on a polarized ferrite substrate. (c) Insulator in top view. (d) Positioning the Absorbent to Block the Retrograde Propagation 61
Fig 2.37 Coplanar isolator with resonance 62
Fig 2.38 Coplanar lines (transverse view) 63
Fig 2.39 Schematic diagram of a 3-port circulator 64
Fig 2.40 Diagram of operation of a circulator in an antenna circuit 66
Fig 2.41 Diagram of a circulator mounted in isolator 66
Fig 2.42 Diagram of a circulator in a radar circuit 67

Fig 2.43 Some typical uses of circulators: a) demultiplexer, b) phase shifter, c) resistance amplifier (negative) 67
Fig 2.44 Waveguide circulator 69
Fig 2.45 Different configuration of Waveguide Circulator 70
Fig 2.46 Y-circulator using the field displacement phenomenon 70
Fig 2.47 configuration of a Faraday rotation circulator 72
Fig 2.48 Configuration of the Y-plate circulator: (a) sectional view, (b) 3D view 73
Fig 2.49 Geometries used to define the central conductor 74
Fig 2.50 Configuration of Y-junction microstrip circulator 74
Fig 2.51 Microstrip circulator proposed by How 75
Fig 2.52 Configuring a circulator with a sphere 75
Fig 2.53 Configuration of the circulator proposed by Guennou and the performances obtained [50] 76
Fig 2.54 Configuration of the circulator proposed by Yalaoui [51] and the results obtained 77
Fig 2.55 Physical configuration of the different structures proposed by Ogasawara [53]: (a, b, c) sectional views of three different configurations (d) top view of the coplanar structure 78
Fig 2.56 Physical configuration of the various structures proposed by Koshiji [54]: (a, b) sectional views, (c) top view 79
Fig 2.57 Measurement results in terms of insertion loss and insulation for the different versions [54] 79
Fig 2.58 Structure of a coplanar circulator proposed by Oshiro [55]: (a) top view, (b) sectional view 80
Fig 2.59 Oshiro Device Performance: (a) HFSS, (b) measurement [55] 80
Fig 2.60 Circulator configuration proposed by E. Benevento and performances obtained under HFSS [47] 81
Fig 2.61 Circulator with localized elements: (a) equivalent circuit, (b) the heart of the circulator 82

Fig 3.1 Different applications for 5G 84

Fig 3.2 Frequency bands allocated by the ITU 85
Fig 3.3 Equivalent circuit of n-coupled resonators for the formulation of the equations of the meshes for a magnetic type coupling 86
Fig 3.4 Equivalent circuit of n-coupled resonators for electric type coupling 87
Fig 3.5 The magnitude of S_{11} 92
Fig 3.6 The magnitude of S_{21} 92
Fig 3.7 The complete design of 8 th order pass-band filter 93
Fig 3.8 The S-parameters of the 8th order waveguide filter 94
Fig 3.9 The position of the roots of polynomial E(s)E(s)* in the complex plan . 100
Fig 3.10 Obtained singularities of polynomials for eighth degree filter, (N-nfz) even 102
Fig 3.11 Pole-zero diagram of the filtering 104
Fig 3.12 Classical Chebyshev response without transmission zeros 104
Fig 3.13 Pole-zero diagram of the filtering 105
Fig 3.14 Chebyshev response with finite transmission zeros at ±4 rad 106
Fig 3.15 Pole-zero diagram of the filtering 107
Fig 3.16 Fully canonical filtering function 107
Fig 3.17 Two port network 108
Fig 3.18 Steps in the synthesis process for a fourth-order coaxial resonator band pass filter 110
Fig 3.19 N coupled resonators 111
Fig 3.20 the N+2 canoniacal transversal array and its equivalent kth lowpass resonator circuit 112
Fig 3.21 Folded canonical network coupling matrix. (a) Folded coupling matrix. (b) coupling and routing schematic 116
Fig 3.22 The folded quartet configuration of the design filter 119
Fig 3.23 Typical coupling structures of coupled resonators with (a) Magnetic coupling (b) Electric coupling, (c) and (d) Mixed coupling 121
Fig 3.24 Schematic for realizing the couplings 124
Fig 3.25 Coupling coefficient for electric coupling [75] 124
Fig 3.26 Schematic of position of the feed line 125

Fig 3.27 Schematic filter (all dimension in mm) 126
Fig 3.28 Complete filter design 126
Fig 3.29 Reflection parameters of the realized filter Simulation result (solid line) Measurement result(dashed line) 127
Fig 3.30 Transmission parameters of the realized filter Simulation result (solid line) Measurement result(dashed line) 127
Fig 3.31 Layout of the micros-trip trisection filter designed to have a higher selectivity on high side of the pass-band. (b) Simulated performance of the filter 132
Fig 3.32 Flow chart of the algorithm genetics use 134
Fig 3.33 The relation between two software used in the optimization process .. 137
Fig 3.34 different graphic representation of atomic orbitals 139
Fig 3.35 Elementary mesh in the real Bravais sub-network of a honeycomb crystal structure 'graphene' 140
Fig 3.36 Energy band diagram in a crystal structure 141
Fig 3.37 Graphical representation of dispersion E as a function of the $\boldsymbol{kx}$ and $\boldsymbol{ky}$ wave vectors with its relationship in the vicinity of points K and K' [86] 143
Fig 3.38 Ambipolar effect (resistivity and conductivity as a function of a gate voltage Vg) of a graphene monolayer around the Dirac point at 5K, 70K, 300K. For EF = 0 the carrier density is zero (a). For Vg <0 the graphene is of type p-conduction of holes- (b). For Vg> 0 graphene is said to be of type n-conduction dominated by electrons - (c). Here the mobility measured is μ = 5000 cm². (V.s) -1 [97], [98] 145
Fig 3.39 The schematic diagrams of a graphene layer grown on $\boldsymbol{SiO2}$ / $\boldsymbol{Si}$ 149
Fig 3.40 Response in transmission of a structure composed of two resonators 150
Fig 3.41 the Variation of the electrical coupling coefficient as a function of the length of the iris 151
Fig 3.42 Top view of the W-band fourth-order waveguide filter 151
Fig 3.43 The S-parameter results of our proposed W-band waveguide filter. ... 152

Fig 3.44 The input dimension and position of our proposed filter for optimization process 153
Fig 3.45 The first simulation results obtained of the proposed filter 154
Fig 3.46 Optimized dimension and position of rectangular pins of graphene material 155
Fig 3.47 Optimized S-parameters results for both resistances of graphene material 155

Fig 4.1 Diagram of a receiving electronic network antenna 159
Fig 4.2 Coupling 3dB/90: (a) Design, (b) simulated S parameters of the design 162
Fig 4.3 Two cascaded quarter-wave impedance transformers 163
Fig 4.4 Reflective RF circuit design model 164
Fig 4.5 Optimized reflective circuit: (a) $|S_{11}|$, (b) S_{11} phase. 165
Fig 4.6 Complete design of the phase shifter 166
Fig 4.7 Design results of the complete phase shifter: (a) $|S_{11}|$, (b) $|S_{21}|$, (c) phase of S_{21} 168
Fig 4.8 Complete double phase shifter design 169
Fig 4.9 Optimized double phase shifter: (a) $|S_{11}|$, (b) $|S_{21}|$, (c) S_{21} phase 170
Fig 4. 10 Hybrid coupler: (a) Design, (b) S-parameters simulated. 172
Fig 4.11 Optimized phase shifter: (a) Design (b) $|S_{11}|$ c) $|S_{21}|$ (d) S_{21} phase 174
Fig 4.12 Optimized phase shifter: (a) Design, (b) $|S_{11}|$, c) $|S_{21}|$, and (d) S_{21} phase 177
Fig 4.13 Prototype results of the 18 GHz phase shifter: (a) prototype and TRL kit (central image corresponds to a microscope zoom view), (b) arg(S21), (c) Δ(arg(S21)) (related to min arg(S21) value, 0 v), (d) |S21| and (e) |S11| 180
Fig 4.14 Phase shifting performance: (a) comparison between simulation and measurement phase results of the 18 GHz phase shifter, (b) phase/voltage relation (the dashed line is the linear reference and the grey zone is the one that provides at least 360 degrees variation). 181

Fig 5.1 the variation of the magnetization level in terms of the external static magnetic field [133], [134] 187
Fig 5.2 The variation of the losses in the ferrite materials in terms of the internal magnetic field 188
Fig 5.3 The variation of the intensity of magnetization in term of the absolute temperature 189
Fig 5.4 The 3-Dimensions structure of a microstrip circulator 190
Fig 5.5 Top view of the central conductor studied by Bosma and the placement of 3 ports 191
Fig 5.6 Numeric solutions for traffic conditions condition for various coupling angles [141] 192
Fig 5.7 Normalized junction impedance ratio as a function of anisotropic splitting factor calculated from the second circulation condition for various coupling angles [141] 193
Fig 5.8 The second circulation condition for Ψ=0.51 and impedance ratio equation 196
Fig 5.9 The first circulation condition for 0.51 197
Fig 5.10 Ports impedance transformer 199
Fig 5.11 Y-junction circulator with impedance transformers 199
Fig 5.12 Simulation results of first try circulator 200
Fig 5.13 Optimized Circulator circuit. 201
Fig 5.14 The results of the optimization process for 12 GHz Y-circulator 202

List of Tables

Table 1. The g-values coefficients 91
Table 2. The coupling matrix coefficients 92
Table 3. Polynomial coefficients of the fourth order filter without TZs 103
Table 4. Polynomial coefficients of the filter with two TZs 105
Table 5. Polynomial coefficients of the filter with 4 TZs 106
Table 6. The Transfer and Reflection polynomials coefficients 119
Table 7. The N+2 coupling matrix M for the transversal array network of the filter of design 120
Table 8. The folded matrix M of the quartet configuration 120
Table 9. Ferrite materials characteristics 195
Table 10. The properties of the Rogers PCB 195

Chapter 1:

Motivation and objectives

The growth of data exchanged by information and communication networks requires the development of equipment with ever-increasing performance and functionality. With regard to different applications (general public, defence, space, etc.) the integration, reconfiguration, security and cost of the communication devices and equipment are also particular constraints to take into account during the design. In fact, for our modern and next generation wireless applications, the requirements of the radiofrequency (RF) terminals and circuits are becoming one of the most demanding parts of the design of communication systems. In that sense, the RF filters and multiplexers have a key role in radiocommunications and microwave systems. Their biggest needs are the accomplishment of the signal band selection process, the remove of the noise, and the division/combination of signal/channels for further processing. On any commercial or military application, whether in satellite communication or earth stations, they can be always found on multiple technologies, with different topologies, as integrated with other components or as single units. Those electronic devices must meet the constraints of physical nature (weight, bulk, etc.) and electrical (selectivity, group delay, losses, power handling etc.) very strict. In addition, reducing the cost of designing and operating of these devices is a key point in an industrial process.

In this context, the development of appropriate synthesis methodologies is essential in order to design these devices optimally with respect to imposed constraints. These synthesis methods use different models to size the microwave

circuit achieving the desired function by optimizing all the constraints imposed by the application or the circuit environment. This optimization results in a reduction in costs and design time on the one hand, and improved performance and simplification of the system architecture on the other, helping to increase the integration of the equipment. The works presented in this Thesis intend to be a contribution to this line of research. Initially, the goal is to develop an optimal synthesis methodology, to optimize the electrical performance of microwave filters, phase shifters, and wideband microstrip/stripline circulators. In the next step, the goal is to simplify the architecture of tuning waveguide filters and wideband shifters and circulators to improve their compactness.

The first part of this Thesis, in chapter 2, presents the general context of the study, including the role of filters in the payloads of telecommunications satellites. This chapter describes the main technologies of these circuits their synthesis and design techniques, also introducing the gradient based optimization method, with its role in reducing the time and the cost of designing and improving the performance of the system.

With the appropriate modifications in the genetic optimization algorithm method, the adaptation to any electronic device technology and topology can be possible, which is one of the objectives of chapter 3. In that way, it was a success to adapt the optimization method to tunable waveguide band pass filter using rectangular pins covered by graphene material. With the change of voltage applied on the pins comes the change of the resistance of the graphene material. That leads to the tuning of the center frequency and even the bandwidth of the filter.

The second part of this work, in chapter 4, presents a new system of phase shifters with their synthesis and design techniques. All the phase shifters are designed to use a novel reflective RF circuit. The final results are obtained by using a new optimization method based on evolutionary algorithms to find the optimal design of the reflective circuits and, furthermore, any component that forms the system structures.

The last part of this work, in chapter 5, is dedicated to two wideband microstrip/stripline circulators designed based on stripline circulator design techniques. It was necessary to introduce some modifications on the design techniques used, in order to make feasible different circulator technology. As an example, it must be pointed out the introduction of the ferrite magnetic properties, the position and the dimensions of the ferrite disk and the dimension of the impedance line to adapt the access ports of the conductor disk with the 50 ohms ports. The reduction of the calculation time using the optimization process requests a good starting point. Here comes the important role of the results obtained by the electromagnetic simulator of the design achieved using the stripline design techniques.

The main objectives of the Thesis can be summarized as follows:

Objective 1: Design and validation of the design of radiofrequency filters, with special attention to reconfigurable waveguide devices based on the usage of the graphene material as a tuning material, due to the influence of its variation of the resistance on the performance of the bandpass filters caused by the modification of the external voltage applied.

Objective 2: Design and validation of the design of radiofrequency phase shifter, with special attention to reconfigurable microstrip devices based on reflective circuits and electronically controllable varactors.

Objective 3: Design and validation of the design of radiofrequency circulators based on ferrite materials and reflective circuits with electronically controllable varactors.

Objective 4: Implementation of optimization methods for the electromagnetic simulation process, in order to reduce the time and the cost of designing and improving the performance of the devices.

As a summary of this Thesis, we take stock of the various works carried out during this thesis, and we draw up some associated research of the devices that we have developed.

Chapter 2:

State of the art

2.1 Background and State of the Art

In this chapter, a presentation of the filtering and multiplexing devices for microstrip and waveguides will be introduced as well as different examples of use these systems in different bands. Moreover, some optimization methods of the introduced devices will be described.

Filtering and multiplexing systems are among the most important components of wireless and satellite communications systems. Yet, filters do not only serve in the electronic field, filters are widely used in telecommunication, radio, television, radar, image processing, and computer graphics, among others [1], [2].

The role of the filter in the systems is fundamental since it has to get rid of the useless parasitic components from a signal, which can be assimilated to noise. This noise, which can affect severely the telecommunications systems, can appear from various sources. It can be external, introduced by the channel, or internal, introduced by the passive and active components of the system. The signal-to-noise ratio, which defines the ratio of the power of the wanted signal to that of the noise, is an essential parameter in the systems [1]. In addition, the signals emitted and received are parasitic relative to each other, and therefore a good separation of these signals is necessary [3], [4]. Finally, according to the architecture chosen for the system, the appearance of parasitic frequencies,

called images, is also a problem. In both cases, filtering techniques are used [5].

The filtering devices have the property of transmitting selective frequencies. They transmit energy on one or more bandwidths and attenuate the energy in one or several bands.

Filters can be classified, according to the positions of their bandwidths and their attenuated bands, in four categories: low-pass, high-pass, band-pass and band-cut filters [2]. Fig. 2.1 represents the four categories of the filter.

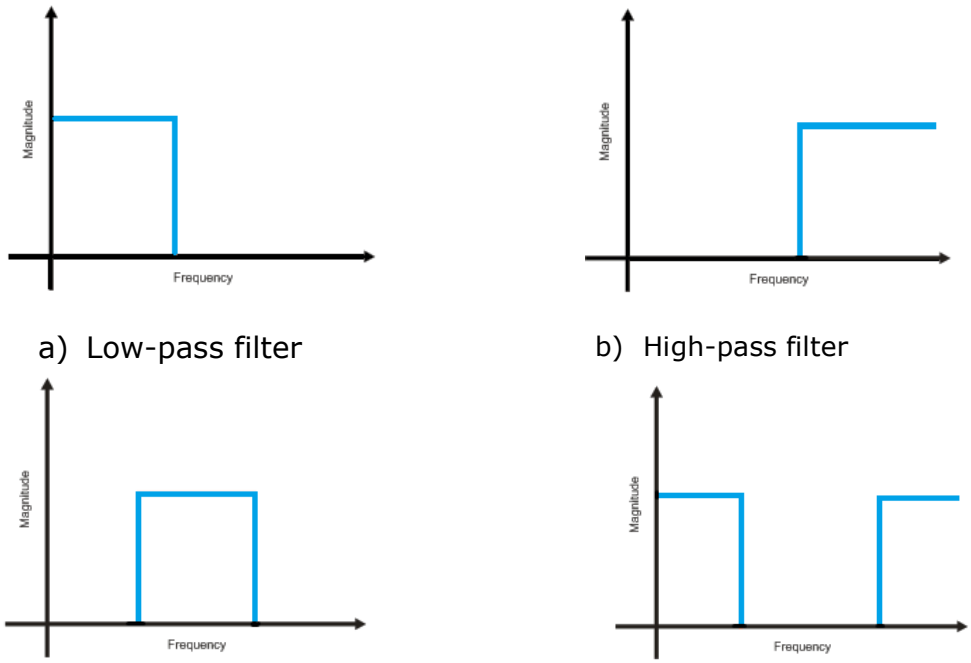

a) Low-pass filter

b) High-pass filter

c) Pass band filter

d) band-cut filter

Fig 2.1 Template for ideal filters

The different filter categories can be deduced from the ideal standard low-pass filter by a frequency transformation. The work done in this Thesis is devoted mainly to the design of bandpass filters [1].

The ideal low-pass filter is impractical because it is characterized by zero attenuation in the bandwidth and a linear phase shift to avoid signal distortion transmitted.

The response of a microwave filter must check the particular electrical stresses fixed by a template [1]. This response can be likened to different approximation functions satisfying the template, such as the functions of the Butterworth type, Chebyshev or Elliptical [6], [7]. Fig. 2.2 presents three common types of approximations, Butterworth, Chebyshev, and Elliptic, for which the rejection levels differ. It appears that the distortion becomes more and more important with the improvement of the rejection.

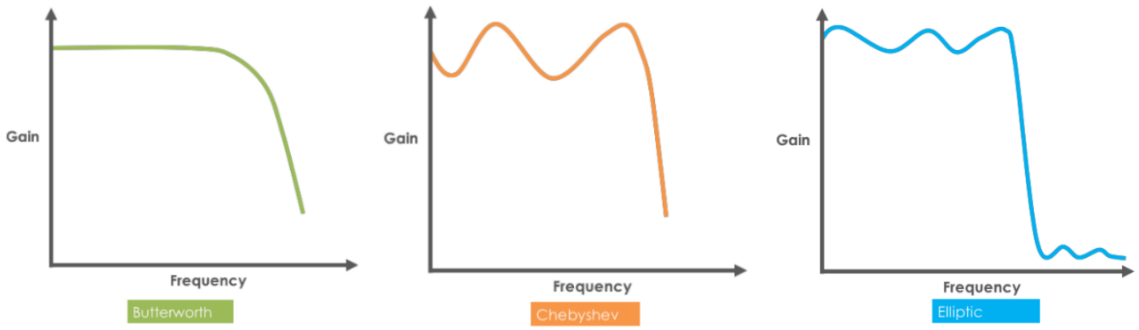

Fig 2.2 Low pass prototype of the three types of filters

The Butterworth approximation is the simplest approximation. This type of filter has no ripple in the bandwidth, but in return, it offers a poor out-of-band rejection. The latter can be improved by increasing the number of poles, but it remains bad than that of other types of filters [1]. It corresponds to a response curve "at maximum flat" and to the function:

$$|S_{12}(j\omega)| = \left(1 + \left(\frac{\omega}{\omega_c}\right)^{2N}\right)^{\frac{1}{2}} \qquad (2.1)$$

where N is the order of the filter and ω_c is the cut-off pulse.

All these curves pass through point $\frac{\omega}{\omega_c} = 1$ and attenuation 3dB. Beyond this point, their slope is even higher as the order of the filter increases. Fig. 2.3 shows a comparison between different orders response of a Butterworth filter.

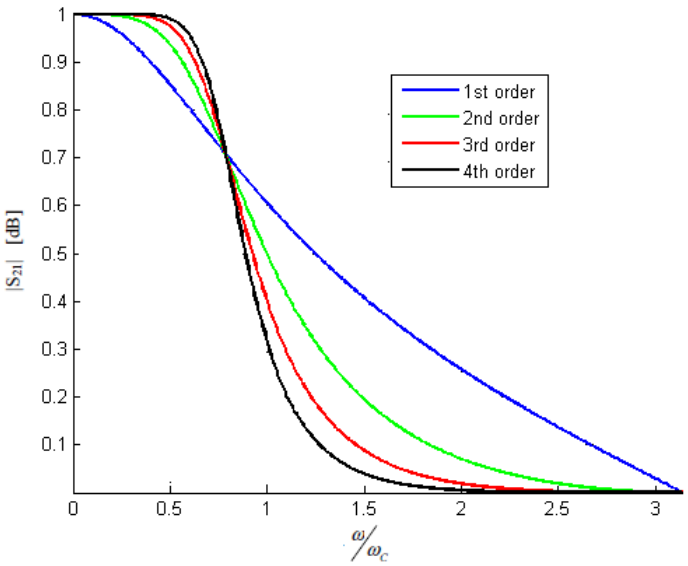

Fig 2.3 Butterworth filter response for different orders

Chebyshev filters tolerate a slight ripple in the band, but have better rejection than the Butterworth filter. The Chebyshev approximation corresponds to the response shown in Fig. 2.4, which represents ripples of amplitude up to $\frac{\omega}{\omega_c} = 1$ and to the function:

$$|S_{12}(j\omega)| = (1 + \left(10^{\frac{Am}{10}} - 1\right)\cos^2(N\cos^{-1}\frac{\omega}{\omega_c}))^{\frac{1}{2}} \quad \text{For } \omega \leq \omega_c \qquad (2.2a)$$

$$|S_{12}(jw)| = \left(1 + 10^{\frac{Am}{10}} - 1\right)\mathrm{ch}^2(N\mathrm{ch}^{-1}\frac{\omega}{\omega_c}))^{\frac{1}{2}} \quad \text{For } \omega \geq \omega_c \qquad (2.2b)$$

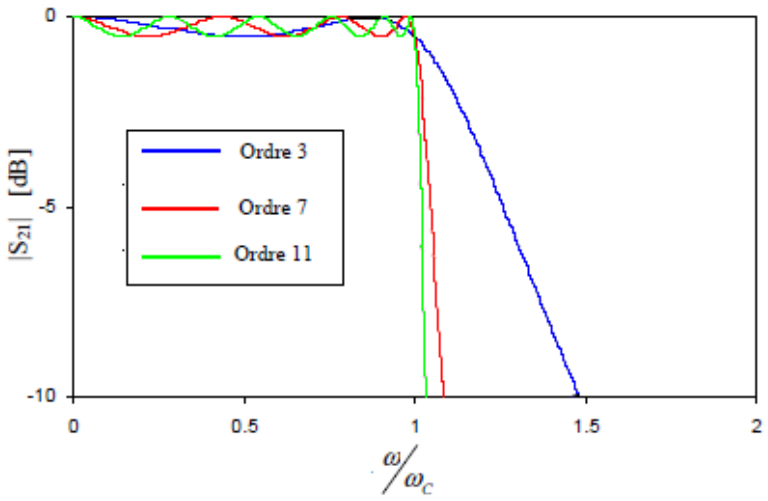

Fig 2.4 Chebyshev filter response for different orders

It is possible to obtain significant levels of rejection in the attenuated band without increasing the order of the filter. Chebyshev filters are characterized by the acceptance of a ripple, or bandwidth or attenuated band. In the first case, it mentions Chebyshev type 1 or direct filters, the second case of Chebyshev type 2 or inverse filters.

Filters that exhibit ripple in both bandwidth and attenuated band are called elliptical filters.

The elliptic approximation has the best rejection at the bandwidth limit because it has transmission zeros out of the band. This function is generally used to design the output multiplexer filters of the repeater of a telecommunication satellite [2], [3]. Although these filters perform well, they are more delicate in terms of design and physical implementation [3]. In [8] a complete presentation describes the theory of elliptic functions.

The definition of the template of each type of response of a bandpass filter is characterized by a certain number of electrical criteria: The central frequency, the width of bandwidth and insertion losses. The Fig. 2.5 represents the general template of bandpass filter.

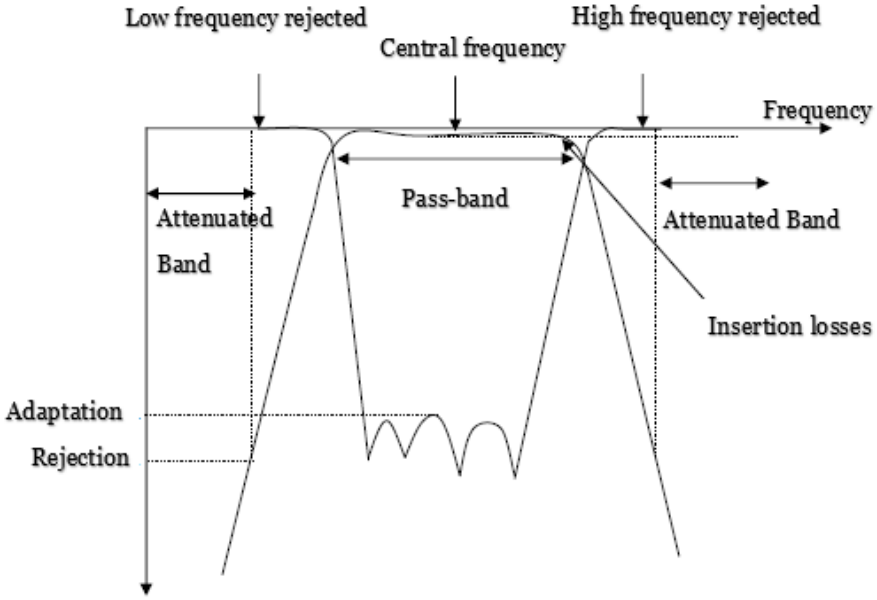

Fig 2.5 Template of a bandpass filter

The calculation of the electromagnetic parameters of this filter is carried out thanks to a low-pass/band-pass transformation. This method of synthesis is explained in the following paragraph.

2.1.1 Bandpass filter synthesis

The synthesis method of a band-pass filter consists initially in the determination of the low-pass prototype equivalent to the filter that it is desired to synthesize. It begins by defining the electrical properties and characteristics of the filter, such as center frequency, bandwidth, insertion losses, by choosing a topology. Then choosing the type of filter response: Chebyshev, Butterworth, Elliptical or pseudo-Elliptic. The Chebyshev filtering function can be synthesized by a localized low-pass prototype network composed of normalised capacitive and inductive elements.

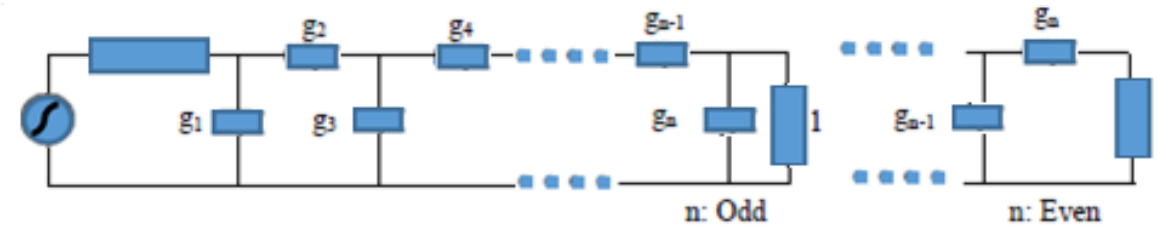

Fig 2.6 Equivalent diagram of a low-pass prototype with localized elements

The values of the low-pass prototype elements g_i are known, they depend on the order of the filter and the ripple in the bandwidth [6]. Knowing the lumped elements of the low-pass prototype network presented in Fig. 2.6, the next step in the synthesis of the filters is to look for the equivalent passband scheme of this network [6]. Using a low-pass/bandpass transformation, each serial element of the low-pass network is transformed into a series resonant circuit, and each parallel element into a parallel resonant circuit, by means of a change of circuit. variable. This method is described in various works [9], [10]. The low-pass prototype with lumped elements of Fig. 2.6 then became:

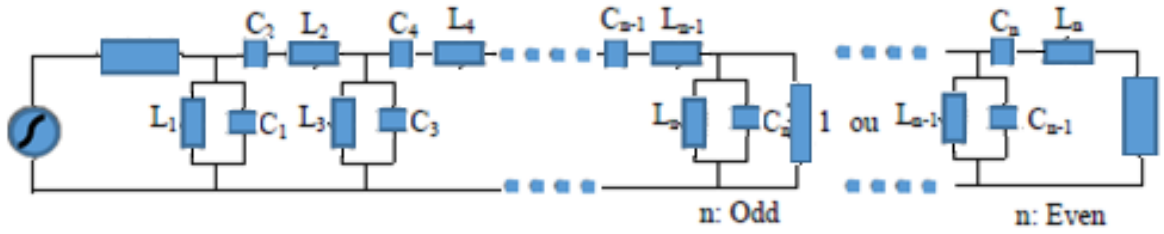

Fig 2.7 Equivalent diagram of a bandpass prototype with localized elements

Resonator-based filter design allows for direct calculation of electrical parameters. However, these localized element filters are mainly used at low frequencies. The challenge of the design of microwave filters is more complex due to the use of distributed parameter elements, as there is no totally general synthesis procedure. In fact, the frequency behaviour of the microwave circuit elements, such as, transmission lines or cavities is complex, which makes it challenging to develop a general and complete synthesis procedure. However, many techniques have been developed to design microwave filters [11]. Many efforts in microwave filter design are directly based on low frequency filter synthesis techniques.

With the case, the microwave filter is made by replacing the coils and capacitors with the appropriate microwave circuit elements, having similar frequency characteristics for the frequency range of work.

For the design of waveguide filters, equivalent circuit models for different waveguide discontinuities are used in combination with prototype arrays and electromagnetic field theory. The bandpass prototype that is shown in Fig. 2.8 is generally used for microwave filter design. The circuit consists of impedance inverters instead of series resonant circuits and parallel resonant circuits.

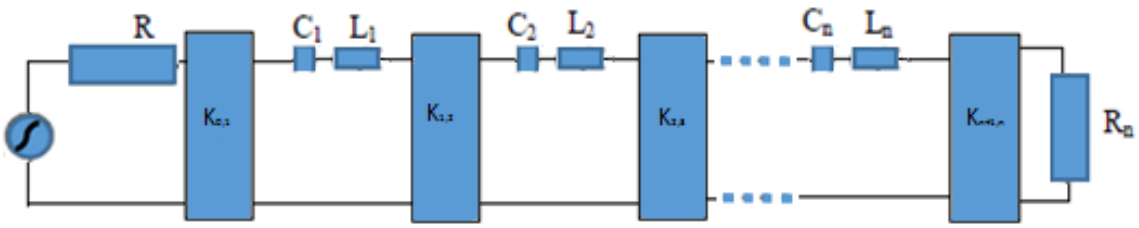

Fig 2.8 Equivalent diagram of a bandpass prototype with impedance inverters

This method of designing bandpass filters is applicable for all types of microwave filters and with different technologies: Planar, Waveguide or SIW "Substrate Integrated Waveguide".

2.1.2 Different types of microwave filters

One of the fundamental challenges in the realization of the filters remains their insertion losses. The resonators used in a microwave filter have a finished vacuum quality factor Q_0 that depends on their physical realization. Insertion losses in a bandpass filter are inversely proportional to the bandwidth of the filter and to the resonance factor *Q* and are proportional to the number of resonators used [12]. Thus, for very narrow band applications, very high-quality factor resonators must be used to achieve a low loss bandpass filter.

In addition, the selectivity of the filter can be improved by increasing the number of resonators, this increase makes the filter longer and the losses become larger [12]. Many technologies have been developed in microwave to overcome these problems.

In the following paragraphs, a number of microwave filters, which can be grouped into three main categories: Planar technology, bulk technology and SIW technology, are briefly described. Knowing the advantages and disadvantages of each technology will help to choose the most suitable for our application.

2.4.1.a.iv **Planar microwave filters**

Since high power transmission is not an essential parameter of the device to be implemented, the use of planar technology is a solution to overcome the congestion problems of these devices. Their perfect integration with the electronic environment and their high reproducibility, associated with relatively low production costs, allow the complete realization of a microwave system in hybrid technology and MMIC [13]. The weak point of planar filters is the present of important losses. Indeed, their low Q_0 quality factor at zero Q_0 reduces the selectivity and does not allow the realization of narrow bandwidths (less than

1%). Among these technologies, we can distinguish two families of planar bandpass filters, broadband and medium band filters and narrowband filters. Broadband filters are characterized by bandwidths between 20% and 80%. Among the topologies that meet these criteria is the stub that uses stub lengths of $\lambda_g / 2$ or $\lambda_g / 4$ (Fig. 2.9).

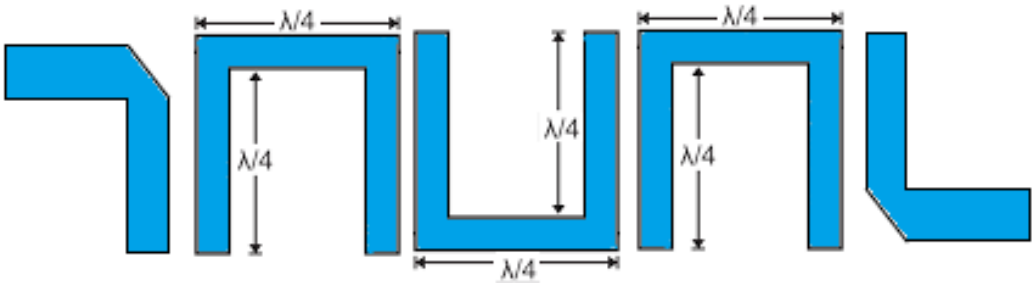

Fig 2.9 Quarter-wave stubs filter

The quarter-wave coupled filters are among the narrow-band filters, based on in-line resonators of $\lambda_g / 2$ or $\lambda_g / 4$ and loaded at their ends by short circuits or open circuits. It has a closely related level of selectivity to the coupling levels. These topologies are particularly well suited to producing devices having a bandwidth of 20%. These filters can be made using microstrip or coplanar technology (Fig. 2.10).

Fig 2.10 Band-pass filter with coupled lines

With the increasing of the number of the resonators in the coupled lines bandpass filter, the size of the filter becomes significant. In order to solve this problem, some alternative topologies have been proposed, such as the combline

and interdigitated topologies [9]. The combline filter consists of coupled parallel resonators network resonators operating in a quasi-TEM mode, charged on one hand by a short-circuit and on the other hand by a capacitance. The transmission of the signal is made by coupling between the short-circuit termination lines (0, n + 1) and the resonators (1, n). This filter is illustrated in Fig. 2.11.

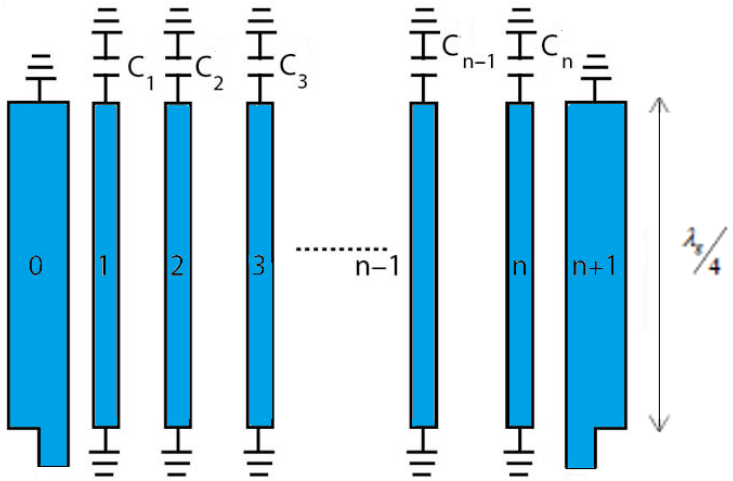

Fig 2.11 Combline filter in transmission lines

The interdigital filter has a similar structure of the combline filter. It consists also of resonators operating in a quasi-TEM mode. The intermediate lines are short-circuited at one end and open circuit at the other, in a way that each line is design to be alternately inverted to the other. The main structure is connected to two input output lines which are open circuit at both ends. Fig. 2.12 shows the general structure of an interdigital filter.

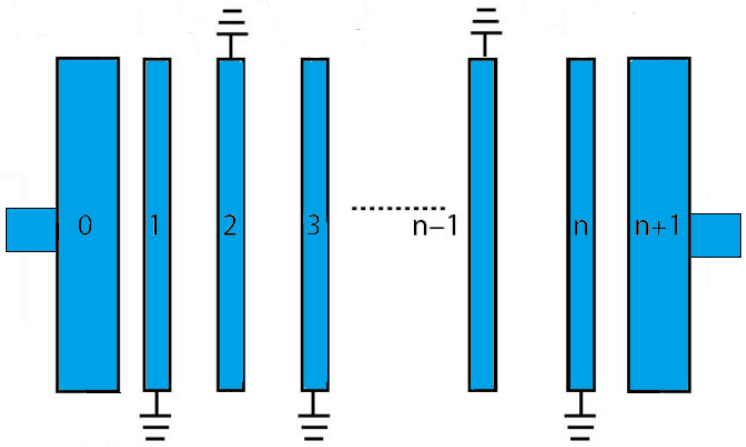

Fig 2.12 Interdigital filter

Narrow band filters have a very small footprint. However, they have very important levels of insertion losses, with very low Q_0 vacuum quality factors and some limitation in power.

2.4.1.a.iv **Passive volume filters**

The main use of the volume filters is the narrow filtering applications. They are mainly used for their good electrical performance. They have very high vacuum quality factors, which benefit directly their response, in addition to being very selective in the band and with strong rejections outside, and have very little insertion loss. Volume filters are classified into three categories: waveguide filters, dielectric resonators and metal cavities.

2.4.1.a.iv **Waveguide filters**

Waveguide resonators are useful for filter design because they provide very high vacuum quality factors which allow these filters to obtain highly selective responses with low losses levels. They have a very large out-of-band rejection. They use as dielectric air, whose insulating properties are remarkable [14]. In addition, they can support high power which makes them attractive for applications in space communications. Fig. 2.13 shows a repeater reception filter which is made using this technology.

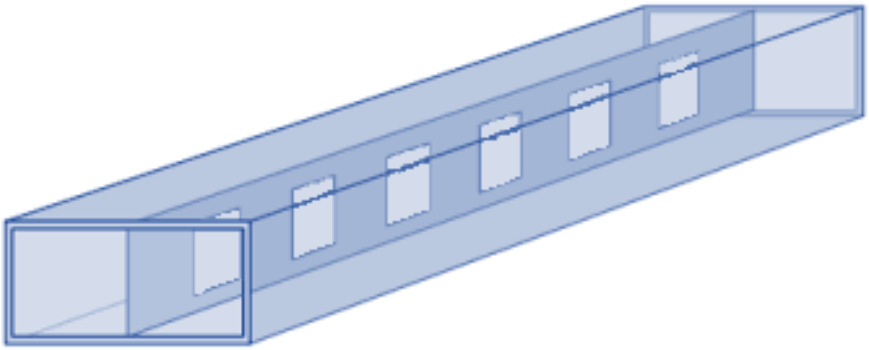

Fig 2.13 Waveguide reception filter

The metal inserts placed in the direction parallel to the electric field of the fundamental mode provide the filtering function. At the slits of the metal strip, reflections will occur, thus allowing the selection of a frequency band. The absence of dielectric, as well as the use of good conductors, can limit losses. The selectivity of these filters can be improved by increasing the number of resonators used which makes it possible to increase the insertion losses. The main disadvantage of bulk technology lies in the significant weight it generates [15]. In addition, the waveguide filters are complex to implement and require a special mechanical treatment contribute the increase in production costs.

In the transmission operation in telecommunication satellites there is an essential need of broadband filters with significant performance. The ridged waveguide technology [16], [17] (Fig. 2.14) meets all the requirements since it has a discontinuity in the guide that destroys the uniformity of the guide, and therefore widens the bandwidth [17], [18].

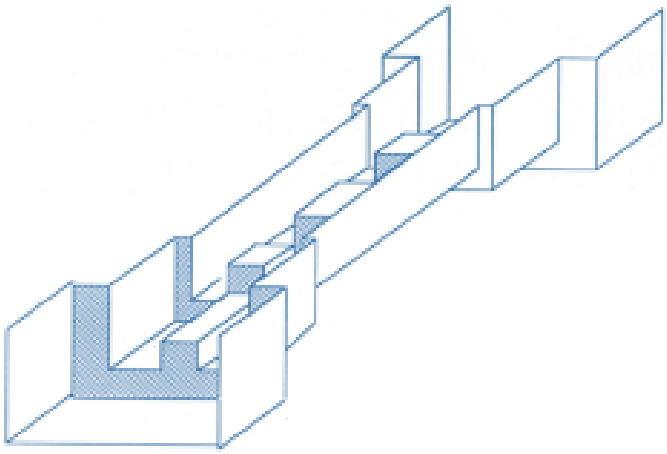

Fig 2.14 Ridged waveguide bandpass filter

2.4.1.a.iv **Dielectric resonator filters**

The dielectric resonator term was firstly mentioned in 1939 by R. D. Richtmyer [20] of Stanford University. He showed that it is a possibility of using the dielectric objects as microwave resonators. However, it was not before the 60's, that several pioneering works were published on the behaviour of dielectrics at microwave frequencies, including the first reports on microwave dielectric resonator filters by Cohn in 1965 [20] and by Harrison in 1968 [20].

Those dielectric resonator filters are generally produced by cavities charged by dielectric resonators [20]. With the use of dielectric resonators made of titanium oxide (TiO2) with very high-quality factors (Q_0 = 10,000). In addition, the loss tangent presented was very low (tgδ = 10^{-4}). However, such filters were not implemented in practical applications because of the poor thermal stability of the dielectric resonator materials available at that time. The dielectric constant of these materials exhibited a significant change in their values with temperature Variation. This in turn caused the temperature drift of the filter center frequency to be as large as 500 ppm/°C.

Nowadays, thanks to technological advances in materials, quality coefficients close to 200,000 can be reached at room temperature. Resonators with a high dielectric constant make it possible to generate compact filters in low

loss waveguides. They are based on the use of dielectric resonators of cylindrical and parallelepiped shapes [19]. The cavities used are often made of aluminium whose inner walls are silvered to reduce any losses (Fig. 2.15).

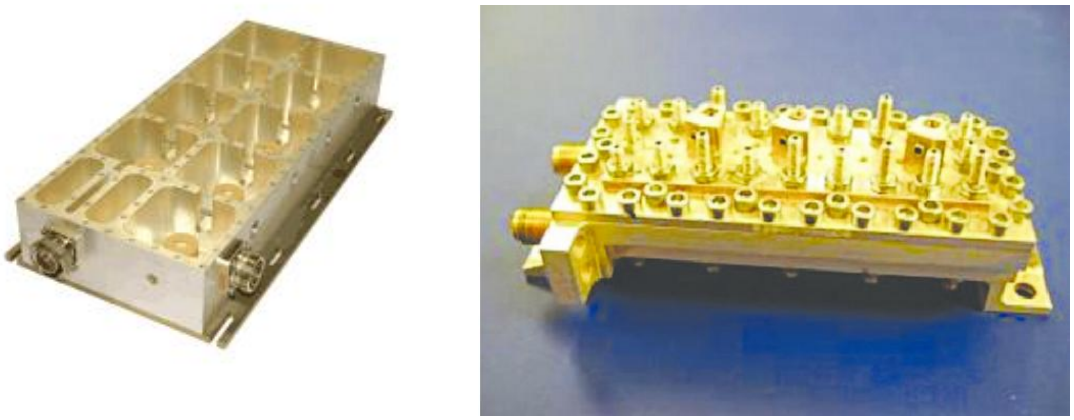

Fig 2.15 Dielectric resonator filter [19]

Fig. 2.16 shows another dielectric resonator filter. Its resonators are coupled together by adjustment irises. In order to achieve the requirements of those filters, a metal cavity is used to cover the resonators to ensure shielding and avoid radiation losses.

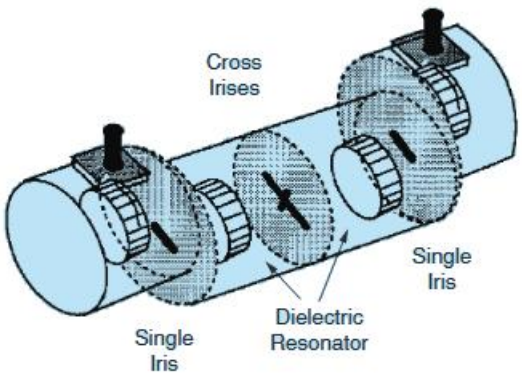

Fig 2.16 Dielectric resonator filter coupled by adjusting iris [20]

This type of filter can be a good option in terms of thermal stability and fabrication. It has a small size and weight which affects directly the

manufacturing cost. It can operate in the monomodal mode or in the multimodal mode. There are other structures have been proposed based on the dielectric resonators. Such as three cylindrical dielectric resonators excited by Teflon waveguides (Fig. 2.17).

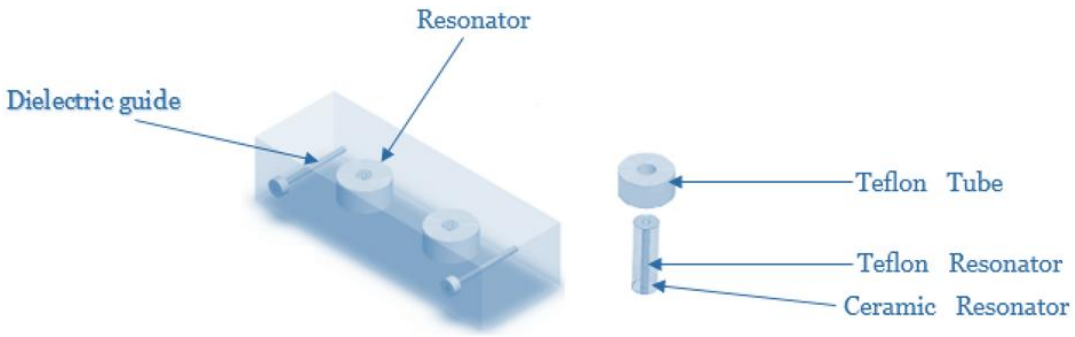

Fig 2.17 Dielectric resonator filter

There exist several issues to develop in the dielectric resonators filters field research. The important one will stay always the excitation of the systems. It has a big influence on the insertion losses, by affecting the vacuum quality factor of the structure and the oversize of the conventional dielectric resonators for millimetre wave applications. However, the positioning of the dielectric resonators with respect to the excitation lines remains difficult to achieve [21].

2.4.1.a.iv **Metal cavity filters**

The metallic cavity filters appeared in the early 1940s. In order to reduce their weight, their size and improve their electrical performance, they are generally used in dual modes, thanks to the implementation of cylindrical microwave or parallelepiped bi-mode cavities. These dual modes have the distinction of presenting two orthogonal polarizations at the same frequency. We can create filters with 2N poles with N resonators [14]. For the adjustment purposes, it is necessary to add screws in order to mechanically modify the coupling coefficients and to tune the resonance frequency of the filter (Fig. 2.18).

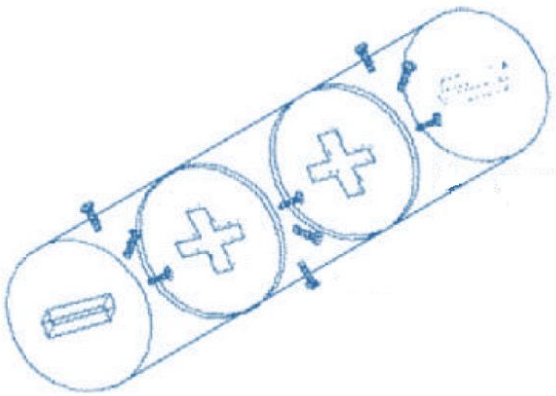

Fig 2.18 Cylindrical metal cavity filter [20]

The second type of structures is based on the use of dual mode rectangular metal cavities (Fig 2.19). Each cavity is excited on two orthogonal modes of a single TE mode family. The electromagnetic energy of all the resonant modes is then coupled into each cavity by inductive asymmetric irises.

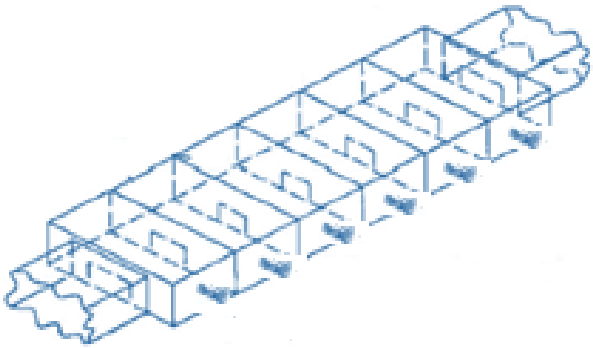

Fig 2.19 Filter with rectangular metal cavities [14]

With a similar performance to the one of the cylindrical metallic cavities the realization of rectangular metal cavities still simple in manufacturing than the realization of cylindrical cavities. Despite their structural differentials, those filters are dedicated to space applications with very low band frequency, which requires a very high selectivity [14]. These filters are always equipped with adjusting screws which leads to low reproducibility and high production cost.

2.4.1.a.iv **SIW filter (Substrate integrated waveguide)**

In microwave and millimeter wave applications, waveguide technologies have better transmission characteristics than planar circuits, such as the CPW coplanar waveguides, due to the inexistence of electromagnetic radiation and the low insertion loss levels. However, they are impractical for PCBs (Printed Circuit Boards) for two main reasons. First, the big size of the transmission line which make it difficult to be inserted into the PCBs. For instance, the size of the waveguide filter designed in the last part of the third chapter, working in the W-band with WR-10 waveguide (a = 2.54 mm, b = 1.27 mm) [24]. Secondly, the waveguides must be surrounded by metal walls. Vertical metal walls cannot be manufactured by standard PCB manufacturing techniques. Advances in technology have made it possible to integrate waveguides and miniature cavities into substrates with the new Substrate Integrated Waveguide "SIW" technology. The resonant cavity of a SIW filter is integrated in the substrate, this cavity is defined by means of cylindrical (vias) and periodic metallized holes defining lateral walls (Fig. 2.20). The main feature of the SIW cavity is the quality factor that exceeds 10.000 easily.

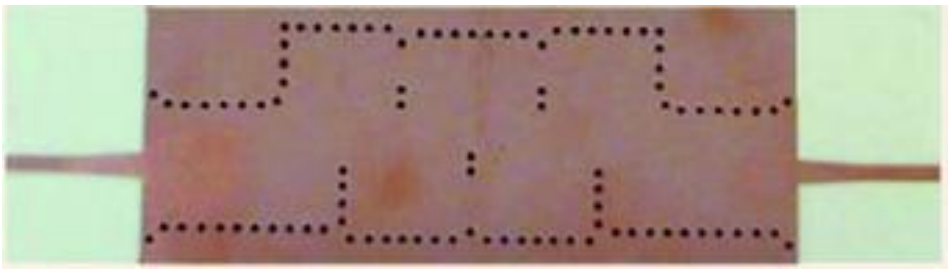

Fig 2.20 SIW filter [24]

The SIW circuits have a narrow band, low losses, and the electrical response is fixed in terms of bandwidth and center frequency. These circuits can be considered as low cost because they are compatible with the standard PCB manufacturing [25], [26]. Microwave filters can be used in combination with

other elements or other passive devices, as is the case in multiplexers or duplexers often used in telecommunications.

2.1.3 Tunable filters

Tunable filters are decisive determinants of modern millimeter and microwave systems and are found mainly in military systems, measurement equipment and communication systems. The mobile telephone chain (2G to 5G) needs some fixed numbers of filters or duplexers. This number is justified by the amount of applications and features offered by a mobile telephone device. By using tunable filters, the overall performance is improved to meet the standards in force (reduction in size, weight, cost, complexity of these multichannel systems ....). With the integration of tunable elements we can reduce the area occupied by the passive elements (filters, duplexers, antennas, etc) [27]. Frequency tuning for filters is achieved through a specific internal or external command. It can be realized using a variation, the permittivity of the host substrate or capacitive or inductive loads that are added to each resonator constituting the filtering device. The choice of tuning elements is very important for the overall quality of the system in which they will be inserted as they will directly affect performance. Most of the tunable bandpass filters presented in the literature are classified into four main categories according to the tuning mechanism: mechanical, magnetic, electrical and MEMS-based [27].

The mechanically tunable filters are often made in volume technology because the mechanical control has significant power handling and low insertion losses. However, they have a slow adjustment speed and are often quite large (screw-nut system, micromotor, piezoelectric transducer ...) [27], [28].

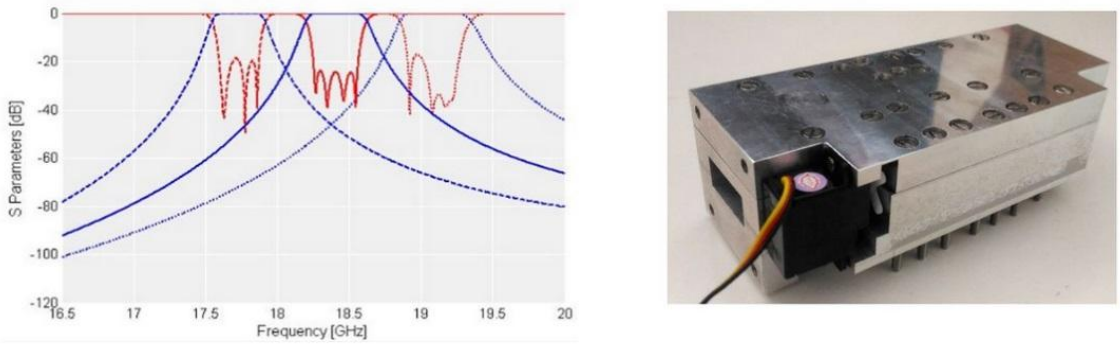

Fig 2.21 Mechanical tunable waveguide bandpass filter, with its simulation results in K-Band [27]

Magnetically tunable filters have been widely used in microwave communication systems. They use ferromagnetic materials whose magnetic properties (permeability μ) change according to the applied static magnetic field μ = f (H). In microwave, ferrites are mainly used. Among these magnetic controls is the YIG resonator (Yttrium-Iron-Garnit), consisting of a resonant frequency-variable ball as a function of the bias current (magnetic field variation). These commands allow to have very wide tuning ranges, low insertion losses, and a good quality factor. Disadvantages include size, current consumption (0.3-3 A), thermal sensitivity, low tuning speed, and incompatibility with embedded systems [27].

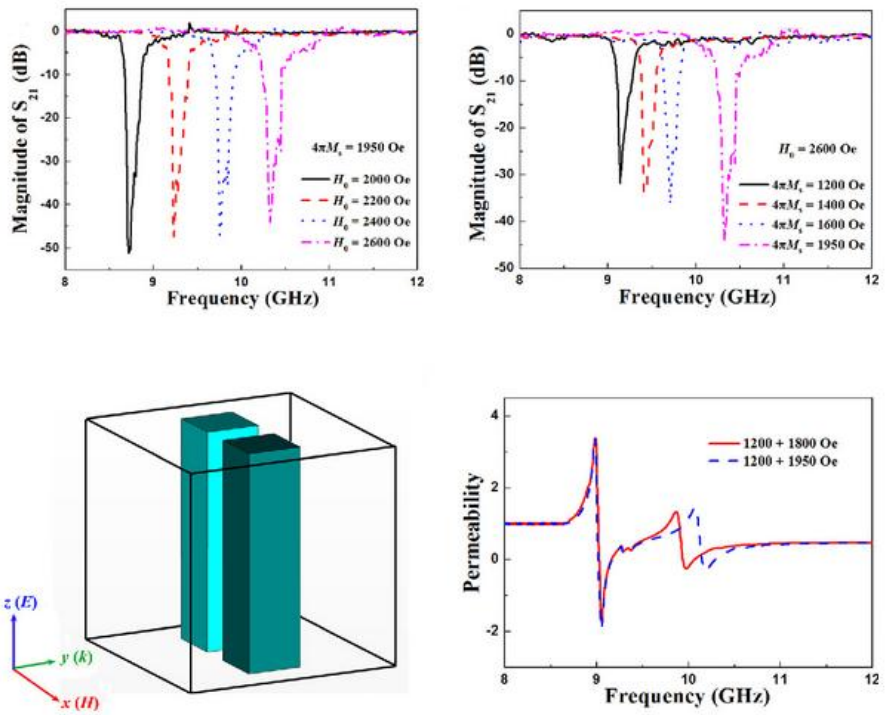

Fig 2.22 Magnetically tunable wideband bandpass filter using ferrite material, with its simulation results in X-Band [27]

Electronically tunable filters typically use variable capacitors, semiconductor diodes, or ferroelectric materials that are controlled by the application of a control voltage (bias). This makes it possible to obtain a variable capacitive or inductive load necessary to modify the central frequency of a resonator. The advantages are numerous: wide adjustment range, compact size, quick adjustment, and compatibility with other miniature systems. However, their performance is lower than magnetic or mechanical filters.

Fig 2.23 Magnetically tunable bandpass filter, with its simulation results in Ka-Band [27]

Tunable filters can also use MEMS ("Micro Electro Mechanical Systems") components. MEMS-based tunable devices are considered a fourth category because their tuning mechanism is multidisciplinary. MEMS have developed with the evolution of micro-machining techniques over the last twenty years. Currently they are widely used in filtering applications or in tunable electronic systems. For our work, we focus on Electronically tunable filter specifically we use a new carbonic material named Graphene has the record of thermal conductivity: up to 5,300 W $m^{-1}k^{-1}$. That material is controlled by the application of a control voltage.

2.2 Electronically tunable phase shifters

2.2.1 Antenna networks

Space launchers are currently equipped with unidirectional telemetry systems. In order to improve the transmission budget by reducing the number of antennas, it is necessary to install electronic pointing antennas. To achieve this project, there are three main possible methods for modifying the radiation pattern:

- A first method is to use reflector antennas and actively modify the characteristic of the different elements of the reflector.
- A second technique involves parasitizing the main antenna with elements placed in its near field. It then consists of varying the radio characteristics of these parasites to modify the radiation.
- The last technique is the use of an antenna array in which a phase shift is generated between each of the patches. It has the advantage of being able to perform an electronic scanning of the radiation beam. The antenna can be electronically controlled and successively pointed in several directions. Thanks to this device, it is possible to save on

power amplifiers thanks to the low consumption of MEMS-RF and to reduce the number of antennas placed on the launcher.

2.2.2 Antenna network based on hybrid couplers

The antenna network proposed by DE Flaviis et al. considered one of the earliest. It is based on 4 antennas powered by a Butler matrix consisted of 4 quarter-wave hybrid couplers with an isolation level greater than 20 dB over 15% of the band (Fig. 2.24). Addressed for WLAN applications, centered at 5.2 GHz [29].

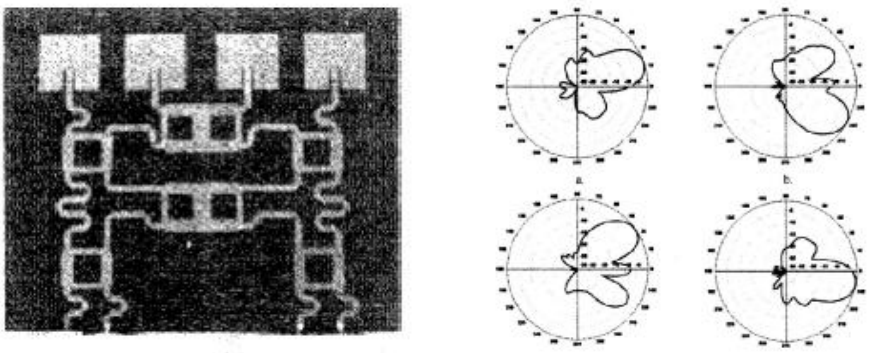

(a) **(b)**

Fig 2.24 (a) Array Antennas Network Photography (b) Radiation Diagram for the 4 Modes [29]

In the following years a team in Uppsala University in 2006 proposed a second device with a network of 5.8 GHz patch antennas [30]. This model is powered by a progressive wave that propagates through the different patches from the left side or the right one (Fig. 2.25.a). The insertion of the phase shifters based on miniature hybrid couplers (to fit between the radiating elements) between the patches was introduced by the team to make the change of the power law possible (Fig. 2.25.b). PIN diodes are used to add an open circuit stub.

Measurements show that the network can detach its beam over an angular range of +/-32° with a gain greater than 11 dBi (Fig.2.25.c).

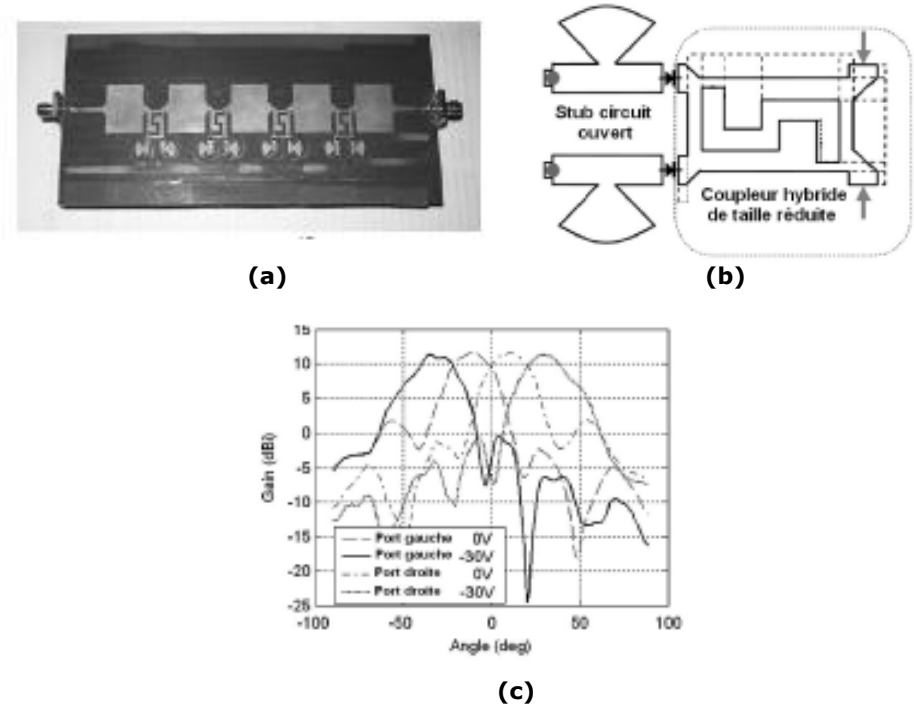

Fig 2.25 (a) Array photograph (b) Principle of the phase shift cell (c)Radiation diagram for different configurations [30]

In the year 2013, Chih-Hsiang Ko and Gabriel Reibez with the help of the University of San Diego, manufactured an electronic pointing antenna works in the frequency band between 1.8GHz and 2.1GHz [31]. It consists of phase shifters based on hybrid couplers with MEMS technology from a company named Omron. To split the input signal from 1 way to 4 ways signals the use of Wilkinson splitters was necessary (Fig. 2.26.a). This device has very low insertion losses <1dB and good isolation <-10dB at 2GHz. Its phase difference at 2GHz is 5 ° and a measured gain of 8.6-8.3dBi at 2GHz. That seems a very promising prototype but the total area including phase shifters and the Wilkinson divider ~ 59400mm² (~ 330 * 180) is very cumbersome, which is making it a very interesting inspiration for further researcher if we take in consideration the reduction of its surface and retaining good RF performance.

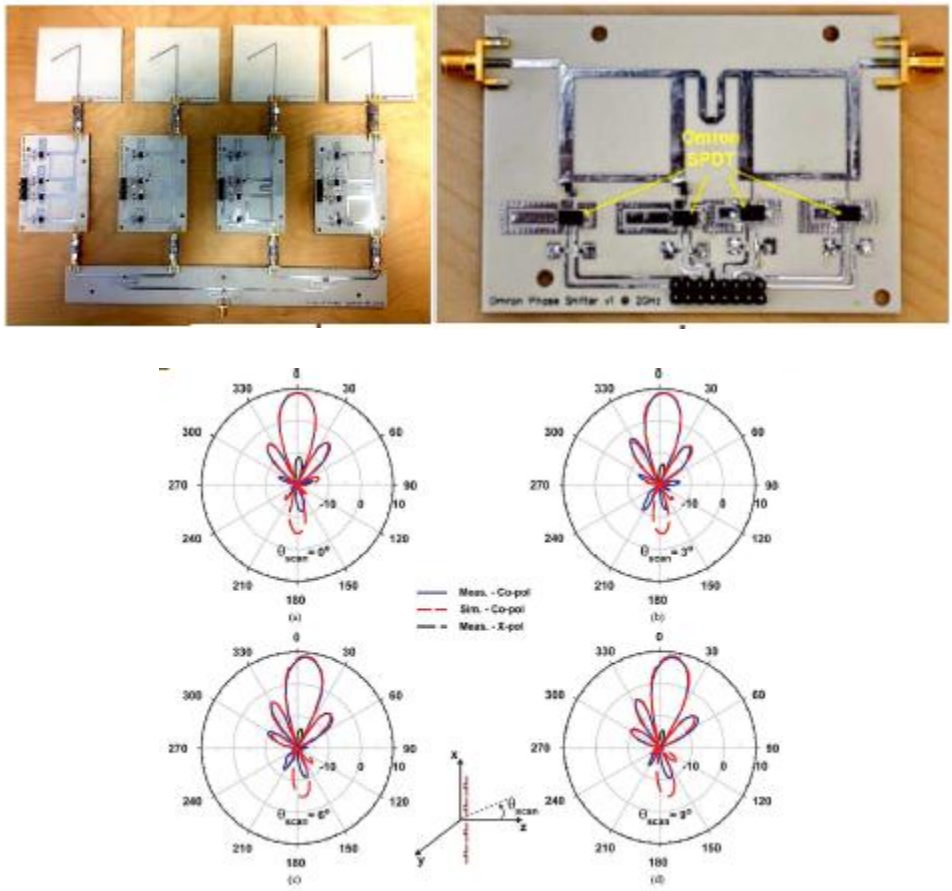

Fig 2.26 (a) Network photography (b) Phase shift cell (c) Radiation diagram for different configurations [31]

2.3 Built-in microwave phase shifters

A phase shifter is a circuit that can change the phase of a microwave signal. It must have low insertion losses as well as stable transmission amplitude. There are two types of phase shifters: Analog and Digital phase shifters. The so-called "Analog" phase shifters make it possible to obtain all the degrees of phase shift, since they make it possible to vary the phase continuously as a function of an applied command. As for "Digital" phase shifters, they have only a limited number of phase states but they have higher noise immunity, better linearity, because they are made with all-or-nothing switches. In addition, it must have a

high linearity, that is to say it must not distort the *RF* signal to be transmitted. This feature is difficult to achieve with semiconductor components and that is why the attention is focused on MEMS-RF phase shifters. On what follows it is presented the different architectures that exist. At first, the phase shifters known as TTD (True Time Delay) as the delay lines and the DMTLs and then the non-TTDs as the phase shifters based on hybrid coupler 90 °.

2.3.1 Phase shifter based on switched lines

The switched-line implementation is by far the simplest of all phase shifters in terms of approach and design criteria. The basic principle involves switching between two transmission line sections of unequal lengths to introduce the desired amount of phase shift. It introduces also the SPNT switches term short abbreviation of Single Pole N Throw switches for the selectivity of the electrical path of the signal [32]. So, it is necessary to use at least to 2 SPNT to obtain N phase shifters. As an example, the university of Michigan manufactured the SP4T (Fig. 2.27.a) [33].

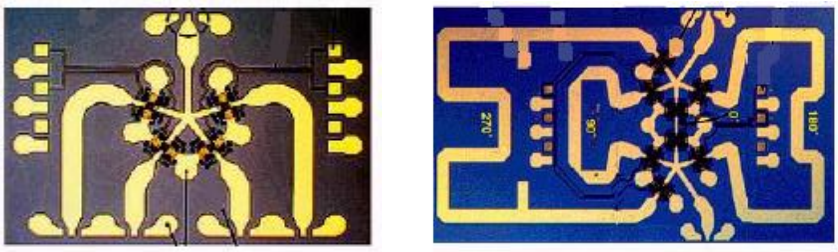

(a)

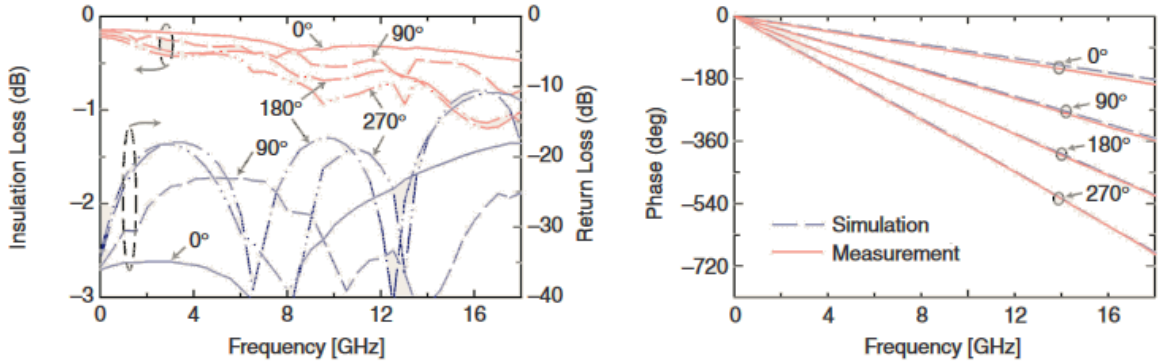

(b)

Fig 2.27 Phase shifter based on switched lines [33], [34]

This phase shifter works in the frequency band between 8-12 GHz, and has 4 phase shift states as we can see in the figure (0°, 90°, 180°, 270°), with the very good levels of Insertion losses getting between 0.3 dB and 1 dB in the worst case (270 °) (Fig 2.27.b) [34], make the increase of the phase states possible if we just cascade several phase shifters.

2.3.2 Phase shifter based on lines loaded with MEMS-RF

This type of phase shifter used periodical transmission lines loaded by capacities. The main role of these capacities is the modification of the time delay of the propagation on the lines, and thus at the output of the circuit. In order to realize this circuit in planar and coplanar technologies, radial stubs connected to MEM-RF switches are placed periodically along the transmission line. Depending on the state of the switches, it is possible to choose the phase shift.

Fig 2. 28 Raytheon's phase shifter, XLIM's phase shifter [35]

In Fig. 2.28, the cells are CPW lines periodically loaded by capacitive RF MEMS. To make the control of each cell independent, the space between them are connected to connection capacities to block the direct current. Reflectance losses at 30GHz are below -11dB over the entire band (27-33 GHz) and insertion losses are between 2dB and 4dB which remain relatively correct [35]. For the DMTL phase shifter made at XLIM, it is designed at 20GHz, its reflection losses are less than -11 dB, and its insertions losses between 0.8dB and 1.8dB for the two-phase states 90° and 180°. This is a very interesting technology. But the switch between operating frequencies will introduce an important change to the size of the circuit. In order to correct it, it would be conceivable to do localized elements to reduce the area occupied but the circuit will have too many losses and it will not be optimal.

2.3.3 Phase shifter based on hybrid couplers at 90°

This type of circuit is completely different from the previous ones. The phase shifter based on the hybrid couplers are not TTDs (True-Time-Delay) circuits like the previous ones. The topology of such a circuit is shown in Fig. 2.29 [36]. The hybrid coupler has four microwave ports, ports 1 (input port) and 2 (direct port) of the coupler are adapted if the ports 3 (isolated port) and 4 (port coupled) are loaded by identical impedances. The phase of the output signal can be controlled by varying an identical reactance on ports 3 and 4, because the incident energy is entirely reflected with a phase change when the termination of the transmission line is a pure reactance. So, by sending a wave through the input port (port 1), it will be fully transmitted to the isolated port (port 3) with a phase shift corresponding to the reactance placed on ports 2 and 4. A RTPS [36] was realized by the University of Nice using hybrid couplers with diodes varactors technology. The merit factor is very low 8°/dB and it does not hold power.

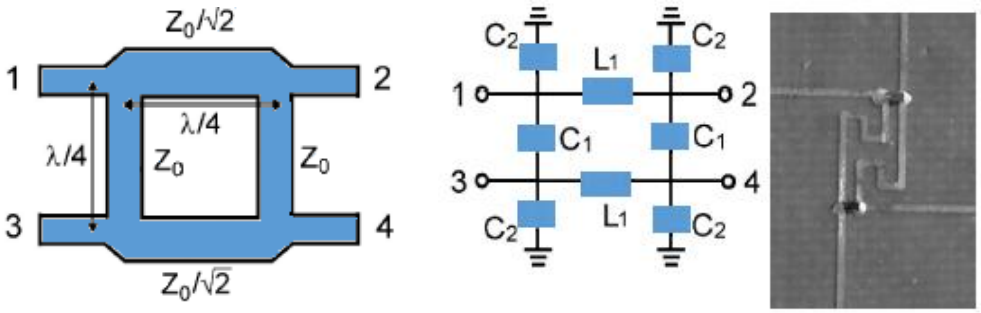

(a) (b)

Fig 2. 29: Equivalent diagram of a hybrid coupler in distributed elements. (a) A hybrid coupler using varactor diodes of the University of Nice (b) in localized elements [36]

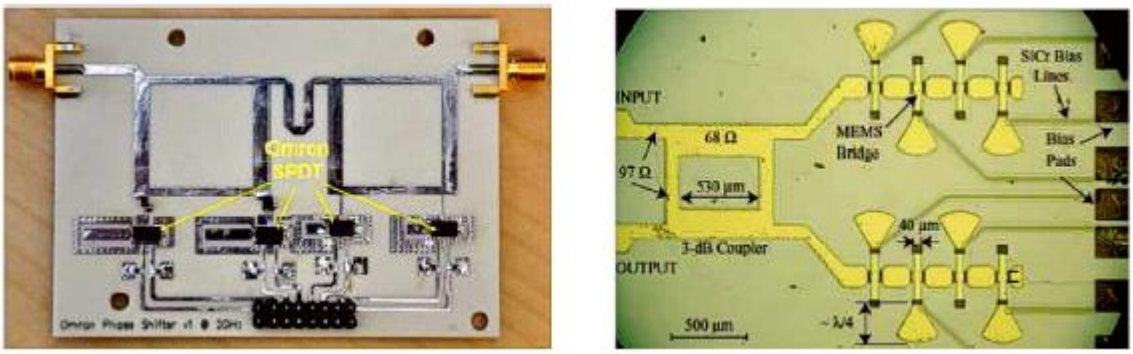

Fig 2.30 Hybrid coupler phase shifter [37]

Then two-phase shifter cells, are proposed by UC San Diego. The first one is composed of reflective lines that can be connected by means of SPDT (Single Pole Double Throw) switches from OMRON, Fig. 2.30 [31], [37]. Depending on the phase shift state that one wishes to achieve, it suffices to choose the switches that one wishes to operate. Insertion losses are less than 0.7 dB between 1.9 and 2.1 GHz for all phases of phase shift. The second is adapted for a band of 80-85GHz, for each phase state, it presents equivalent losses of 1.5dB / bit.

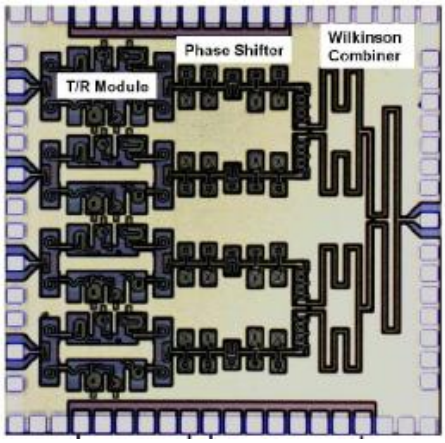

Fig 2.31 2x2 mm phase shifter chip, 1 way to 4 [38]

As shown in Fig. 2.31, this chip is composed of a Wilkinson divider system, 4 phase shifters and 4T/R Modules. This chip is very small 2x2mm was manufactured by the UCSD team [38].

2.4 Electronic circulator

We can define a wireless telecommunication system which only has one antenna that is used for transmission and reception, such as a monostatic system. A monostatic system generally uses an electronic device which is equivalent to a switch. Systems of this type are called duplexers (Fig. 2.32). However, the use of the switches such as, electronic one or mechanical one is excluded for high frequency. They would have to switch constantly at every moment. Thus, the ferrite circulator has been proposed as a general solution. Circulators are indeed devices that provide the function of "switching" signals according to their source, thus allowing to receive and transmit signals using a single antenna.

Passive ferrite devices, such as circulators, isolators, phase shifters, have developed considerably in recent years. Y-junction circulators are used the most in microwave because of their simplicity, rather small size and moderate cost.

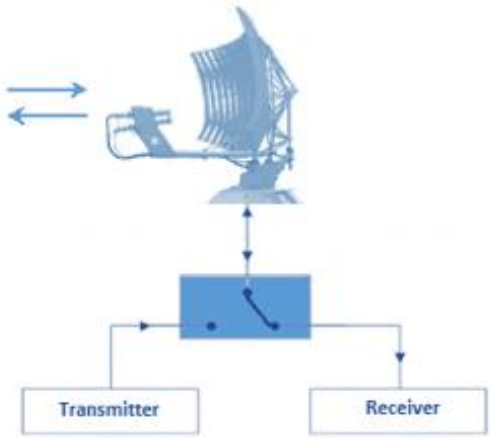

Fig 2.32 Simplified diagram of operation of a duplexer in a radar circuit

2.4.1 Insulator

The insulator is a nonreciprocal passive device which uses the magnetic properties of ferrites. Their operating principle is the prevention of the reflected wave from interfering with the operation of another device in the microwave systems. A great example of this would be generators, which are also used for isolation between amplifier stages. In addition, the circulators can be configured to act as isolators.

2.4.1.1.i Operating principle of an insulator

The Fig. 2.33 shows the operating principle of a microwave isolator. As represented, the electromagnetic wave can propagate in just one direction and it is blocked in the other way. In the telecommunication systems, this type of components is widely used for the elimination of the echoes in transmission by avoiding its appearances to protect the sensitive elements of a reflection transmission chain that could damage them.

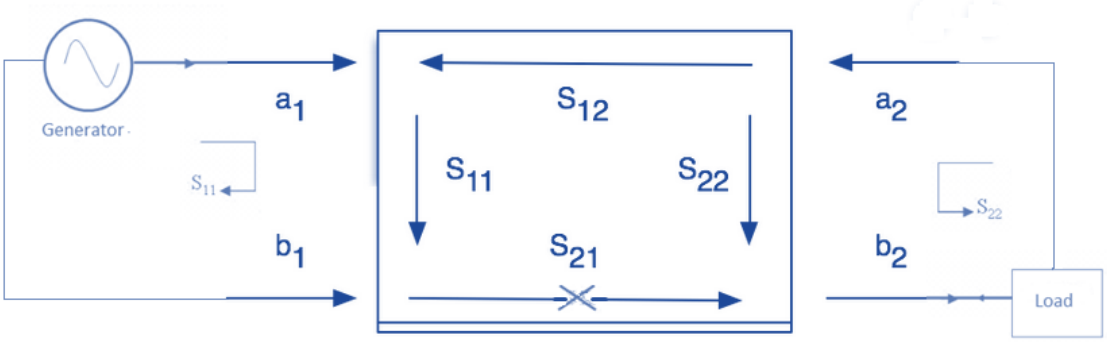

Fig 2.33 Schematic diagram of an insulator

The ideal isolator is a suitable device that allows the energy to pass in one direction and not in the other. Therefore, its S-parameters matrix is the following one:

$$S_{ij} = \begin{bmatrix} 0 & 0 \\ e^{j\varphi} & 0 \end{bmatrix}$$

The phase shift is represented by φ, and it is associated with the transmission of a port to the next one.

The technology of the fabrication can be chosen, whether waveguide of planar, depending on the application and the power levels that it supports. In addition, there are different types of isolators that operate on different principles: Faraday rotation isolators, resonance, field displacement and electromagnetic surface wave.

2.4.1.1.ii Field displacement isolators

Anisotropy and non-reciprocal propagation effects allow ferrites to be used in guided structures to provide insulator-type devices. One of the interesting effects of this is the field shift. A rectangular guide that is partially filled with dielectric (Fig. 2. 34) might be an appropriate example to illustrate the principle. The structure is symmetrical with respect to the center if the magnetic blade is made of an isotropic material and is placed in the center of the guide. Thus, the fields inside the guide will act according to this symmetry. Since the ferrite

placed in the center is polarized, it becomes anisotropic and the movement of the energy is, therefore, non-reciprocal. The field moves in the right or the left part of the guide depending on the fact that whether the propagation is carried out according to the positive or negative axis z (Fig. 2.34).

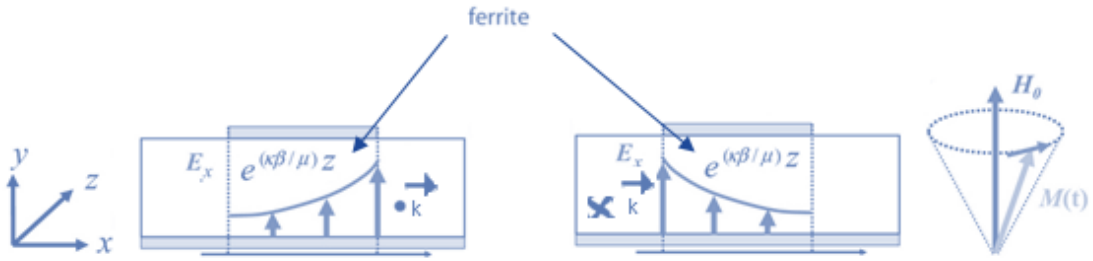

Fig 2.34 Non-reciprocal propagation and field displacement. (a) propagation according to z> 0. (b) propagation according to z <0

2.4.1.1.iii Field displacement isolator in rectangular waveguide

The phenomenon described above is used in the field displacement isolator. The ferrite wafer is covered with a resistive film which acts as an absorbent. Ferrite is no longer positioned in the center of the structure, but positioned in the lateral one. The geometry and the material together ensure the asymmetry of the device. In a propagation direction (Fig. 2.35.a) there might be a strong interaction with the ferrite that attracts the electromagnetic field, which dissipates in the resistive film. In this case, the wave is absorbed and the propagation is blocked. In the other direction (Fig. 2.35.b), the interaction is weak since the absorber is placed in an area where the fields are weak, which cause the attenuation to be negligible. This creates a device where propagation is only possible in one direction, which is the function of an insulator. It is significant to note that the device is supposed to work far from the gyroresonance in order to minimize the magnetic losses in the forward direction.

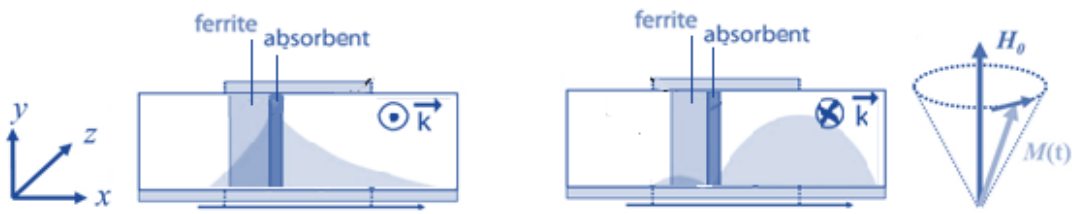

Fig 2.35 Field displacement isolator in rectangular waveguide. (a) Direction blocked for propagation in z> 0. (b) forward direction for propagation according to z <0

2.4.1.1.iv Field displacement isolator made on microstrip line

The phenomenon of field displacement can also be achieved in planar technology. Using a microstrip line on a ferrite type substrate is adequate to accomplish it. If the device is vertically magnetized (Fig. 2.36), the anisotropic ferrite substrate makes the structure unsymmetrical, which leads to a field displacement in line [39]. The inversion of the direction of propagation is equivalent to the inversion of the magnetization, which results in the change of side of the field displacement (Fig 2.36.a and b). We can, therefore, place an absorbent material on one side of the line which will dissipate the propagated wave whose field lines pass through this resistive film (Fig 2.36.d). In this process, it is mandatory that the shape of the conductor ribbon works (Fig 2.36.d) to minimize mismatch between 50 Ω access lines and the "isolator" part, with the central part requiring a large ribbon to achieve effective insulation.

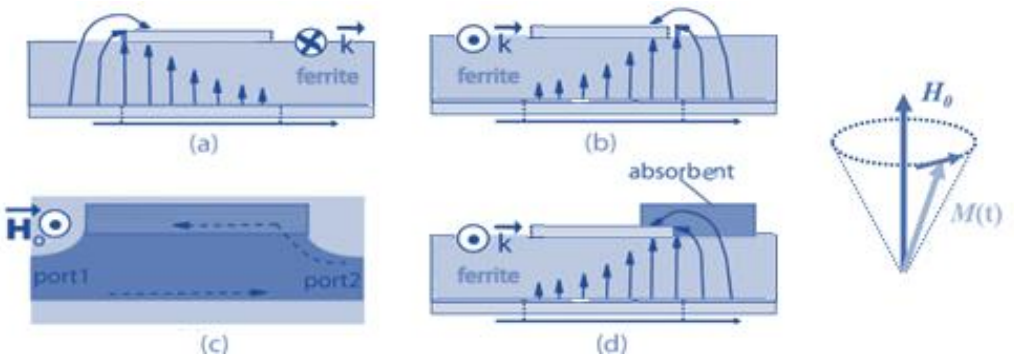

Fig 2.36 Field displacement isolator in microstrip technology. The field lines shown correspond to the vertical electric field. (a) Propagation according to z> 0 for a microstrip line on a polarized ferrite substrate. (b) Propagation according to z <0 for a microstrip line

on a polarized ferrite substrate. (c) Insulator in top view. (d) Positioning the Absorbent to Block the Retrograde Propagation

2.4.1.1.v The coplanar resonance isolator

This component has the particularity of using a dielectric substrate on which a coplanar line is placed. Therefore, only a small volume of magnetic material is needed (Fig. 2.37). This device is relatively simple to implement, and feasibility studies has been carried out by Wen [40] in which insertion losses and insulation are respectively less than 2 dB and equal to 37 dB at 6 GHz.

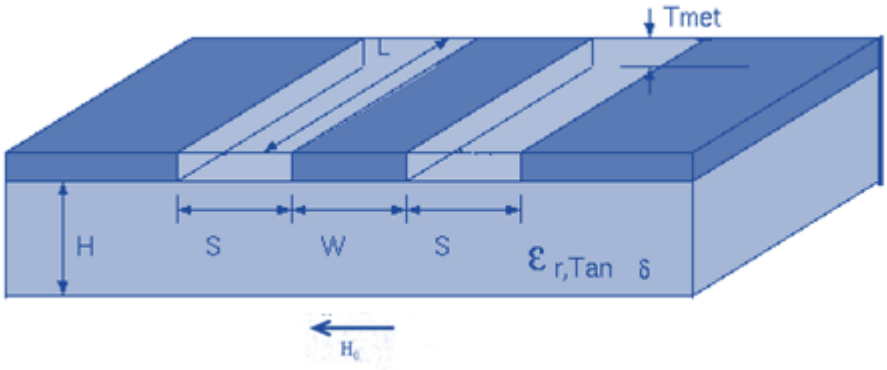

Fig 2.37 Coplanar isolator with resonance

The principle of the resonance coplanar isolator has been adopted by Bayard [41]. For a perfect isolator all the energy is transmitted from port 1 to port 2, while in the opposite direction (port 2 to port 1), the signal is very attenuated. The parameters S corresponding to this function are expressed according to the following matrix:

$$\begin{pmatrix} S_{11} & S_{12} \\ S_{21} & S_{22} \end{pmatrix} = \begin{pmatrix} 0 & 0 \\ e^{j\varphi} & 0 \end{pmatrix}$$

At resonance, the non-reciprocal effect is maximal. The isolator is characterized by different parameters such as insertion losses, isolation, and bandwidth. For this structure, two choices have been made. The first one is a

thin layer of ferrite covering the entire substrate, in which the coplanar line is placed on the ferrite (Fig. 2.38.a). The second one is the placement of ferrite only in the slots of the coplanar line (Fig. 2.38.b).

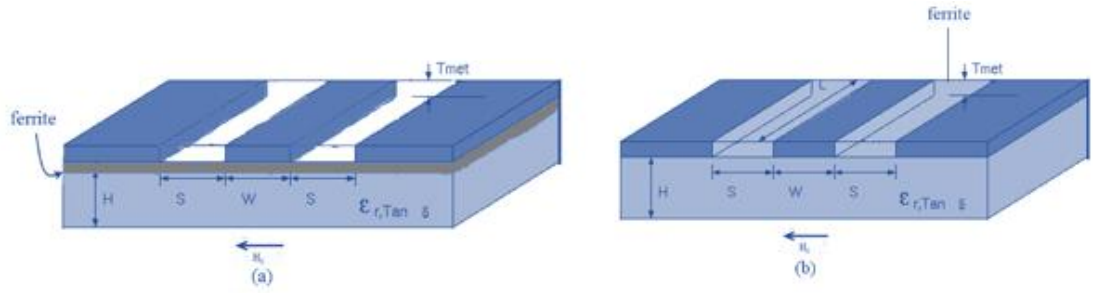

Fig 2.38 Coplanar lines (transverse view)

The studies on the insulators use either BaM or YIG. However, coplanar structures do not allow obtaining sufficient performance for industrial exploitation due to their magnetic material operating limits at resonance. In conclusion, according to the desired application, the insulator has advantages over the circulator, especially in terms of cost and size. In applications that do not require the total capacity of the circulator, insulators are preferable to circulators that are converted to isolators because of the fact that they are rather simple to be implemented.

2.5 Circulators

Non-reciprocal components have an important role in the field of radar and telecommunications. Magnetic materials of the ferrite type make it possible to provide a non-reciprocal function in these components. I will describe the several types of circulators and after explaining how they work, I will analyse their applications and the different technologies with which they are associated, such as triplate, microstrip and coplanar.

2.5.1 Principle and different uses

Fig. 2.39 shows the representation of a three-way circulator (in Y) [42]. A circulator is a hexapole, which has three lanes at 120° from each other around a central body where the elements that give the circulator its non-reciprocity are. These circulators perform cyclic substitution wave transmission. Additionally, when a transverse magnetic field is applied to it, an internal field is created in the central part that resembles a wave entering via channels 1, 2 or 3 that can only come out respectively via channels 2, 3 or 1.

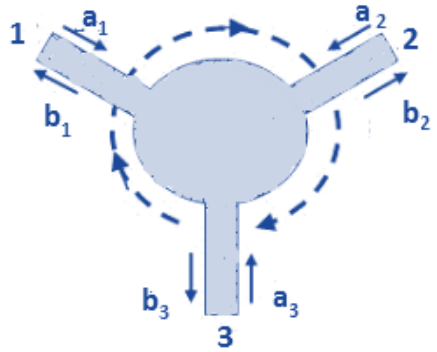

Fig 2.39 Schematic diagram of a 3-port circulator

It is important to notice that a1, a2 and a3 are the amplitudes of the incident waves in the three-way Y circulator while b1, b2 and b3 are the amplitudes of the waves reflected at the three ports. Such device is used for two essential functions within telecommunications systems. Firstly, it makes it possible to provide a radiofrequency signal switching function in all systems where the separation of transmission and reception channels are useful, such as radars, satellite transmissions and mobile telephony. Secondly, the inter-stage isolation functions as a tool to hide a mismatch between two successive elements in a transmission chain. To perform this function, it is sufficient to isolate one of the ports by connecting it to a suitable load. Two of the most important features for a circulator are the insertion losses which must be as small as possible (<-1 dB) and an insulation in a sufficient level (-20 dB). The circulator (Fig 2.39) is characterized by its parameter matrix S or dispersion matrix. It is written as

following:

$$S = \begin{bmatrix} s_{11} & s_{12} & s_{13} \\ s_{21} & s_{22} & s_{23} \\ s_{31} & s_{32} & s_{33} \end{bmatrix}$$

It is significant to note that the parameters S21, S32 and S13 are the transmission coefficients. They are the ones who inform about insertion losses and illustrate the proper functioning of the device. The parameters S12, S23 and S31 are insulation coefficients; they account for power switching faults in the circulator. The other parameters, S11, S22 and S33, are reflection coefficients at ports 1, 2 and 3; they make it possible to evaluate the problems of misadaptation of the structure. Therefore, the ideal circulator is a suitable hexapole that would be able to direct all the energy to the next access, as the third parameters are being isolated. Its matrix S would be the following:

$$S = \begin{bmatrix} 0 & 0 & e^{j\varphi} \\ e^{j\varphi} & 0 & 0 \\ 0 & e^{j\varphi} & 0 \end{bmatrix}$$

The phase shift is represented by φ, and it is associated with the transmission of a port to the next port. The fact that this matrix is non-symmetrical clearly reflects the non-reciprocity of the component. It is this non-reciprocity that makes the whole point of the device and which explains why this function works in many applications in telecommunications. The first example, which is the most general, is the transmission in an antenna circuit (duplexer) (Fig. 2.40). The circulator directs the signals from the transmitter to the antenna without any interference with the receiver (isolated channel). The signal received by the antenna is output to the receiver without interacting with the transmitter. The direction of propagation of the microwave wave inside the circulator is defined by the orientation of the static magnetic field applied to the device.

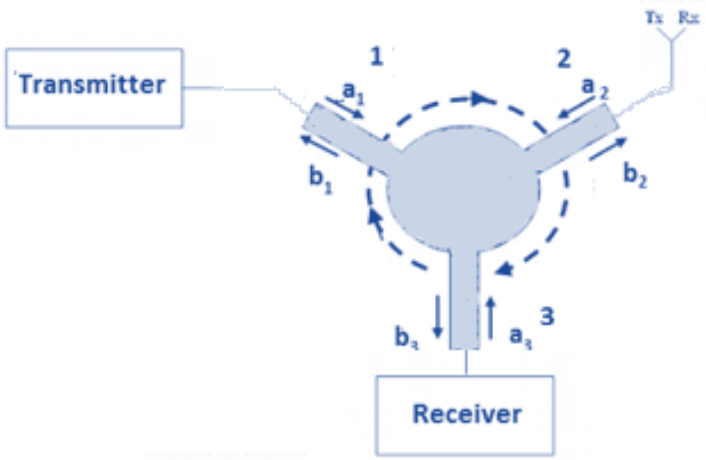

Fig 2.40 Diagram of operation of a circulator in an antenna circuit

The second example is the other applications of the microwave field, in which it is necessary to protect the energy source against the reflected energy. In this case, the circulator is used as an isolator which plays a protective role. The circulator is inserted between the source and the load, the third port being connected to a suitable load which absorbs the energy transmitted to it (Fig. 2.41). Thus, the source emits its signal on port 1 of the circulator, which transmits it to the load connected to port 2. If there is any mismatch at the load, the signal is reflected by the load since this mismatch is transmitted by the circulator to track 3, where it is absorbed by the appropriate load. Through this process, no signal has the possibility to return to the source and damage it.

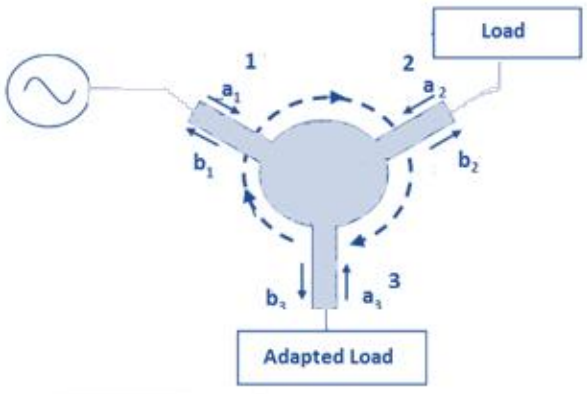

Fig 2.41 Diagram of a circulator mounted in isolator

In this manner, the circulator occupies an important place in monostatic radar circuits which involve only one antenna (Fig. 2.42). Their role is to separate the transmission and reception signals transiting through this single antenna. In this case, the insulation is a paramount parameter due to the very large differences in power between the transmission and reception circuits.

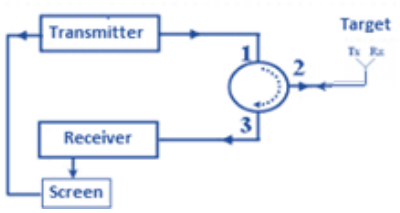

Fig 2.42 Diagram of a circulator in a radar circuit

Besides, the non-reciprocity function of the circulator allows it to occupy a function of choice in orientation of the signals on microwave carriers in multiplexer configurations: (Fig 2.43.a), phase shifter (Fig. 2.43 .b), or negative resistance amplifier (Fig 2.43.c).

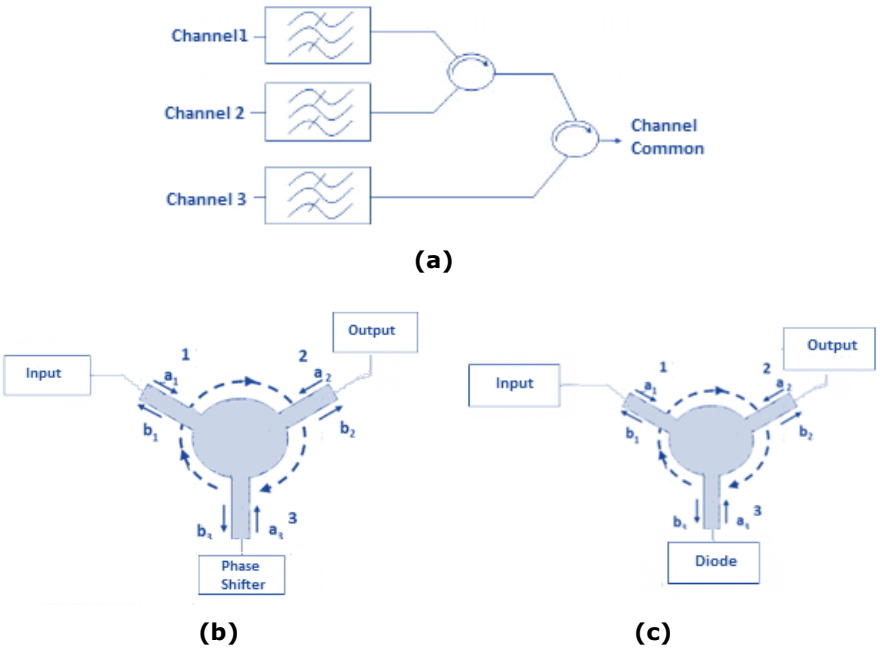

Fig 2.43 Some typical uses of circulators: a) demultiplexer, b) phase shifter, c) resistance amplifier (negative)

Of course, there are different types of circulators that are distinguished by the power level and the transmission frequency band. The majority of the telecommunications systems are manufactured using active or passive circulators. The configuration and the design of active circulators are well detailed by Bayard [41]. Since the specifications of the functional objectives will not be achieved by this type of components, we will only focus on the passive circulators.

We identified two types of passive circulators: circulators with distributed elements and those with element localized. The non-reciprocal properties are provided by ferromagnetic materials and have good performance.

2.5.1.a Circulators with distributed elements

The end of the 50's represented the beginning of the development of the circulator with distributed elements. Due to the key role played it in radar systems and RF circuits, the development of this type of elements has grown too fast. The simplicity in the manufacturing process and the low-cost production of the Y-junction circulators with distributed elements has favourite their use in the industry. Originally, H. Bosma [42] is one of the creators of these type of components, he is the first scientist to publish a complete theory describing the operation function of this type of device in triplet technology. Y-junction circulators can be made according to different technologies, such as the waveguides with field displacement, with Faraday effect, in triplaque guides, microstrip, and coplanar.

2.5.1.a.i Waveguide circulators

The waveguide Y-junction circulator has three channels at 120° from each other around a central body where the ferrite element is located which gives the circulator its non-reciprocity (Fig. 2.44). The dimensions of both the ferrite element and the guide in addition with the value of the external polarizing magnetic field are the responsible of the orientation of the wave through the different elements of the circuits. Making the wave that enters on the channel 1 receives on the channel 2, the wave that presents on the channel 2 is

transmitted to the channel 3 and the wave that enters on channel 3 transmits to channel 1.

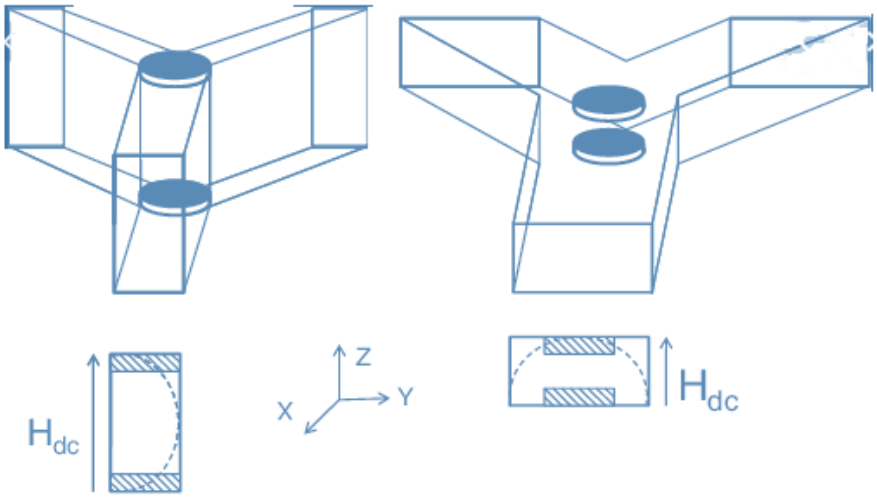

Fig 2.44 Waveguide circulator

Several configurations have been realized, such as the configuration presented by E. Yung [43] which is considerate one of the simplest configurations, due to the equality between both the thickness of ferrite material and the height of the waveguide (Fig. 2.45.a). There are other structures that add plates conductor to improve the impedance matching (Fig. 2.45.b),or other versions that have chosen to reduce the thickness of ferrite and to replace the areas liberated by dielectrics in order to minimize the losses due to the materials and thus to have better performances (Fig. 2.45.c). The waveguides must respect very specific dimensions according to the frequency. Thus, this type of circulator faces a lot of difficulties at millimeter wavelengths. Indeed, it becomes difficult to accurately manufacture the ferrite elements since its dimensions must be small.

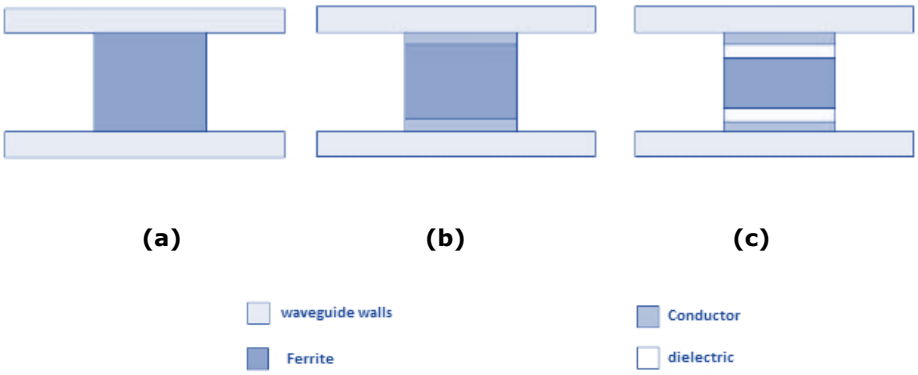

Fig 2.45 Different configuration of Waveguide Circulator

2.5.1.a.ii Field displacement circulator

This type of waveguide Y-junction circulators (Fig. 2.46) also has three channels situated at 120° from each other. The non-reciprocity propriety comes from the elements of the central body. The structure of the central body is so simple and consists of a triangular ferrite prism to which a vertical continuous magnetic field is applied and resistive plates which are affixed on each side of the prism to absorb the electromagnetic field that passes through them [44].

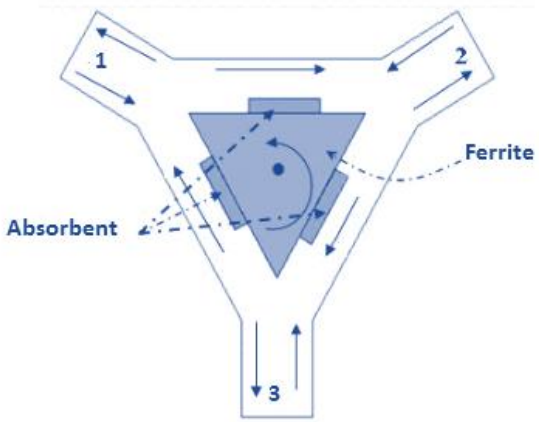

Fig 2.46 Y-circulator using the field displacement phenomenon

The operation function of this type of circulator is based on the phenomenon of field displacement in each of the junctions corresponding to the three faces of the prism. In a propagation direction for instance from port 1 to port 2, the electromagnetic field flows in the free zone of the guide. In the opposite direction (from port 2 to port 1) the propagation is displaced towards the central core and the wave will pass through the lossy material where it will be absorbed, thus not being able to exit through port 1. This phenomenon exists between the different channels and depends on the dimensions of the elements and the applied magnetic field. Finally, a wave entering the channel 1, 2 or 3 can only exit respectively via the channel 2, 3 or 1.

2.5.1.a.iii Faraday effect circulator

As the name indicates, this type of circulator uses the Faraday effect to operate. The Faraday rotation circulator (Fig. 2.47) consists of circular and rectangular waveguide passages [44]. A ferrite cylinder is positioned within the central circular waveguide. The ferrite is polarized along the axis of the cylinder. The length of the ferrite cylinder and the polarizing magnetic field are dimensioned so that the wave undergoes (by Faraday effect) a rotation of 45°. An incoming wave on port 1 is transmitted to port 2, an incoming wave at port 2 comes out on port 3, and so on. It is then a four-way circulator. This circulator makes it possible to obtain insertions losses lower than 0.5 dB and a low bandwidth. These circulators are used in the areas of very high frequencies, when one approaches the optical domain.

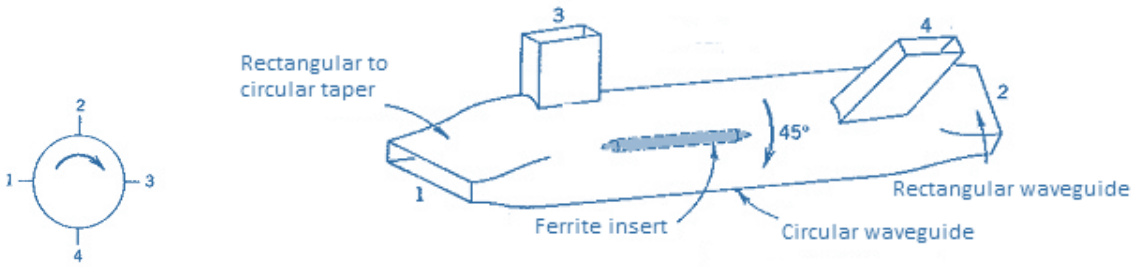

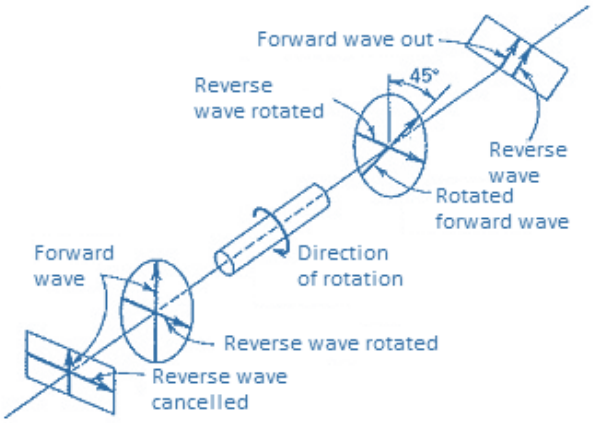

Fig 2.47 configuration of a Faraday rotation circulator

2.5.1.a.iv Triplate circulators

For the signal-type applications, which means applications where the levels of power are modest. The Y-junction triplate circulator is the most widely used one. Its structure consists of three in-outline ports oriented at 120° from each other and connected to a metal central disc (see Fig. 2.48.b). This conductor has an identical shape of the central disk and it is placed between two ferrite pellets. The rest of the structure is similar to a normal stripline structure with Two ground planes located on either side of the structure and a dielectric material set between the two ground planes (see Fig 2.48.a). In order to create the static magnetic field H_0 to polarise the central disk in the perpendicular direction, two magnets are located on either side of the structure.

Bosma in 1962, described the operation functionality of a ferrite Y junction circulator. It is supported on the resonance of two eigenmodes of ferrite disks, which are considered to have electrical walls at the top and bottom faces. Thus, the ferrite disk is supposed to create a magnetic wall except at the channel ports. Since, they are supposed only to carry only TEM modes (Fig. 2.48). Thanks to the work of Bosma's [42], the road was drawn to most of the publications in this field.

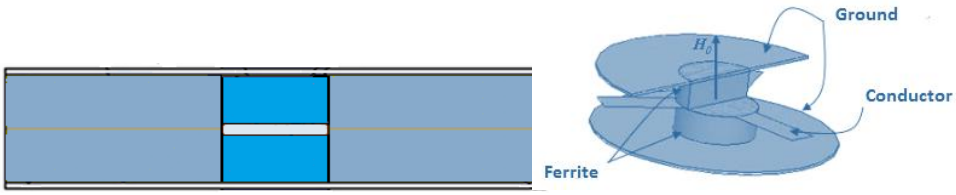

(a) **(b)**

Fig 2.48 Configuration of the Y-plate circulator: (a) sectional view, (b) 3D view

There are also other approaches proposed by many scientists to describe the principle function of the triplate circulator. Such as, the approach proposed by C. E. Fay & R. L. Comstock [45] in 1964. They have shown that in the state of the absence of polarization the ferrite discs act the same as a resonant cavity with just one single resonance mode, accompanied by standing wave regime within the structure.

There exist many geometric shapes of the center conductor and ferrite elements of the Y-junction circulator (see Fig 2.49). For instance, the one has been proposed by J. Helszajn [46]. It has a triangular shape which has been demonstrated some performance advantages over the circular structure. In his study, Helszajn compared two different shape circulators operating in the same central frequency, around 9 GHz [46]. The first one has been manufactured with a circular conductor, while the second one has been manufactured with a triangular conductor. The results show a slight difference in the insertion losses with 0.6 dB for the first one against only 0.5 dB for the second circuit. However, the big influence of the change in the shape of the conductor affects the bandwidth, with a difference up to the double between the two structures. The first one has only 4.4% to 20 dB with 8.8% to the same return loss level for the second one.

Fig 2.49 Geometries used to define the central conductor

These studies were confirmed also by E. Benevent [47] with numerical modelling carried out under Ansoft HFSS for a coplanar circulator circulating around 40 GHz with barium hexaferrite (BaM). The modelling results show that the expected performance of a circulator with a triangular design seems superior to that of a circular circulator.

2.5.1.a.v Microstrip circulator

A Y-junction circulator in microstrip technology consists of a metallized substrate on which is deposited a central conductor connected to three port lines (see Fig. 2.50). The ferrite disk is placed under the central conductor in a way must be dropped into the substrate.

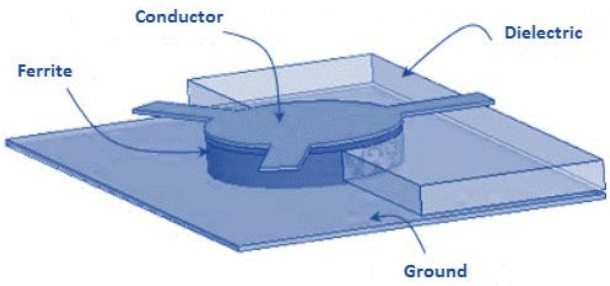

Fig 2.50 Configuration of Y-junction microstrip circulator

The first Y-junction circulator with microstrip technology was proposed by How, Oliver et al. in 1998, operating in the X band (8.2-12.4 GHz) [48]. It uses a ferrite cylinder of Yttrium Iron Garnet (YIG monocrystalline) of thickness equal to

100 μm which is dropped indirectly in a silicon substrate (see Fig. 2.51). The results obtained for this type of structures shown some satisfying level of losses, the insertion losses are less than 1 dB for bandwidth of 10% centered on 9.5 GHz.

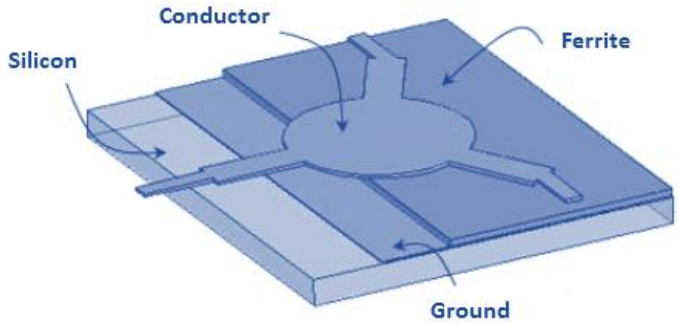

Fig 2.51 Microstrip circulator proposed by How

In addition, for high frequency bands, such as, the U band (40-60 GHz), R.S. Chen [49] proposed a solution to evade the difficulties in manufacturing provided from using a very thin ferrite disks, Chen replaced the old ferrite cylinder by a new sphere one (Fig. 2.52).

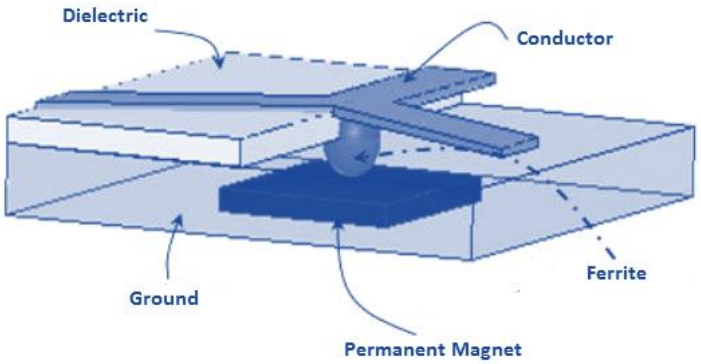

Fig 2.52 Configuring a circulator with a sphere

In 2007, A. Guennou [50] has made a work to demonstrate the possibility of miniature circulators in the X band. The Novelty of this work was the change of the normal substrate materials by a Ferrite substrate of YIG 918. All the other

parts, the ground plane, the conductor and the junction are made with gold layers of 8 μm thick. Thus, the junction is deposited on the ferrite substrate and connected to 50 Ω lines (Fig. 2.53).

The ferrite material was magnetized by an N48 type magnet, and the measured S parameters show some acceptable differences between the theoretical results and the experimental results mainly due to the strong non-uniformity of the internal field in the magnetic material.

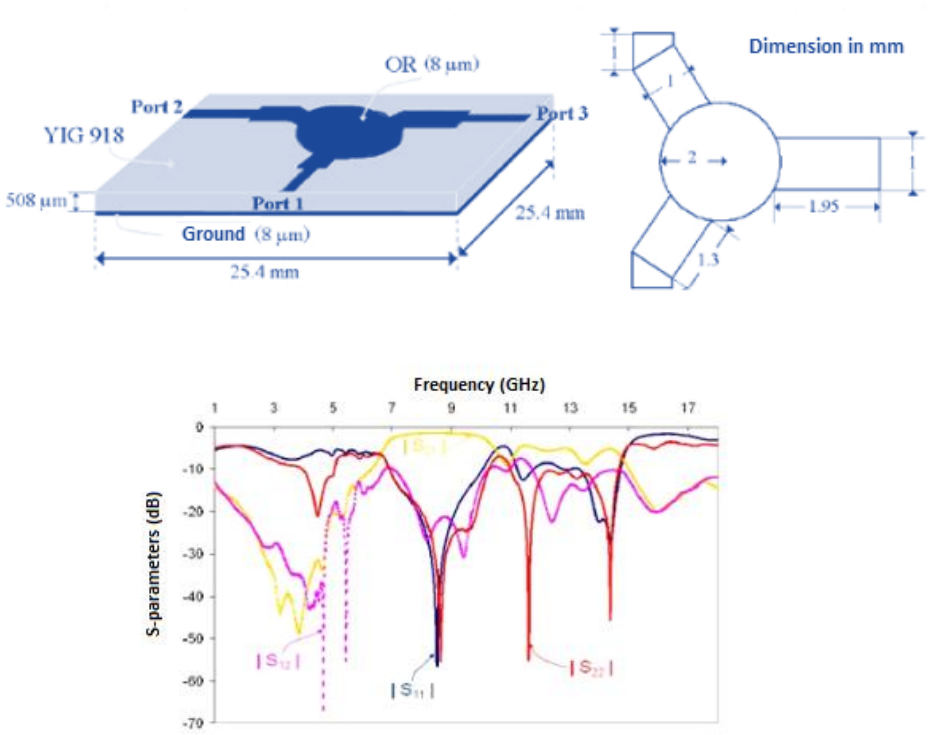

Fig 2.53 Configuration of the circulator proposed by Guennou and the performances obtained [50]

Some recent work published by A. Yalaoui [51], involved of developing planar circulators in microstrip technology operating at cryogenic temperature. The "drop-in" type circuit, consists of a ceramic substrate of 635 µm thick which a 6 mm radius ferrite disk is inserted (Fig. 2.54). The aim of the electromagnetic simulations was to study the effect of the number of sections of quarter-wave transformers in the extension of the operating frequency band. In addition,

several prototypes were made and measured and the results obtained show a good performance in terms of insertions losses which are of the order of 1.8 dB, and the insulation which is of the order of 20 dB in the C band (4-8 GHz) (Fig. 2.54).

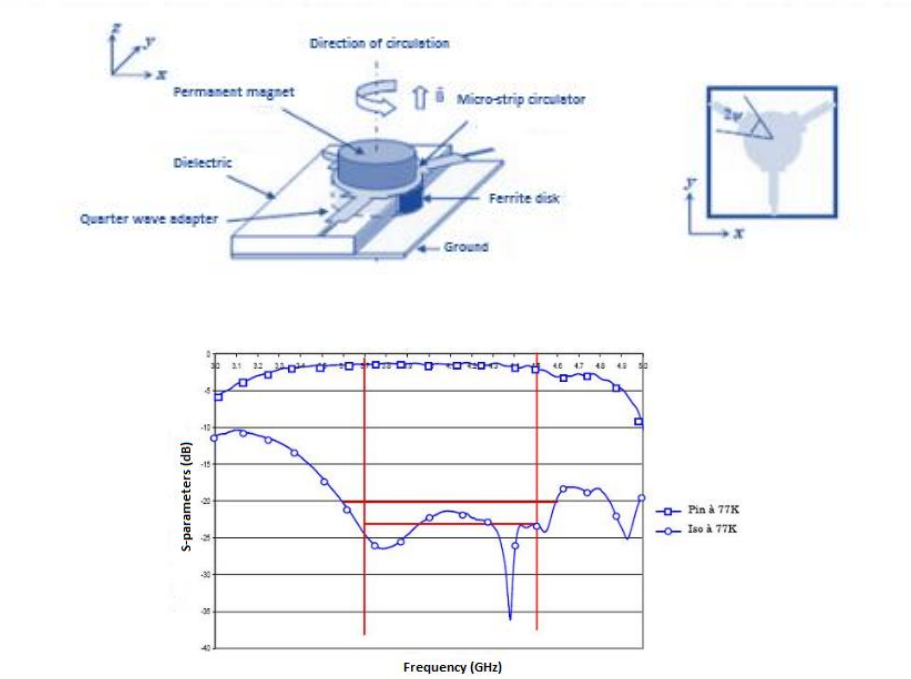

Fig 2.54 Configuration of the circulator proposed by Yalaoui [51] and the results obtained

2.5.1.a.viCoplanar circulators

The number of the studies of Y-junction circulators with ferrite materials in the microstrip or the triplate technology encouraged the scientists to investigate more the feasibility of the fabrication in new technologies, such as the coplanar technology. These new family of circulators has a lot of advantages compared to the old ones, such as their simplicity in manufacturing process which makes the optimization of the fabrication costs possible. The operating frequencies ranges from a few Megahertz to several Gigahertz, and their characteristics are more compatible with those of the field displacement isolators. Their insertion losses are low, strictly less than 0.5 dB, and their insulation is generally between 20 and 30 dB.

In order to integrate this electronic component in the microwave modules, the use of small thickness magnetic materials was highly recommended. The circulators are currently made from massive ferrite materials, generally with a thickness of about one millimeter [52].

A large part of the work on coplanar circulators concerns the X-band. The structures studied are very diverse and most of them optimize the dimension of the height of the ferrite material. In 1971, N. Ogasawara and M. Kaji [53] experimentally realized and tested different coplanar structures. The ferrite element is polarized perpendicular to its surface (see Fig. 2.55.b and 2.55.c). Among these structures, the circulator circuit where probably A. Guennou [50] takes his idea of using a ferrite substrate, unfortunately does not work (see Fig. 2.55.a), although for others, good performance results are achieved.

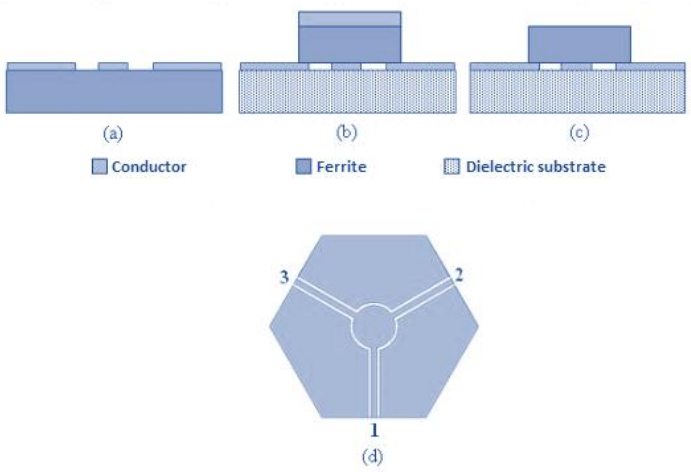

Fig 2.55 Physical configuration of the different structures proposed by Ogasawara [53]: (a, b, c) sectional views of three different configurations (d) top view of the coplanar structure

The investigation on this type of circulators continues with new structure was presented by K. Koshiji and E. Shu [54] in 1986. The idea is always the same with a configuration composed of three in-out ports oriented at 120° which constitute the central conductor and are surrounded by three lateral ground planes. K. Koshiji and E. Shu proposed two different topologies: the first

structure has a ferrite disk placed on the central conductor and the second structure has two magnetic disks, one installed on the central conductor and the other one situated in the same position as the first disk and the central conductor but under the dielectric layer (see Fig. 2.56). The results obtained show good performances (see Fig. 2.57): central frequency of 9.56 GHz, applied DC magnetic field of 7000 Oe, bandwidth at 10 dB of 4.8%, insertion losses of less than 0.8 dB and maximum insulation of 19.1dB.

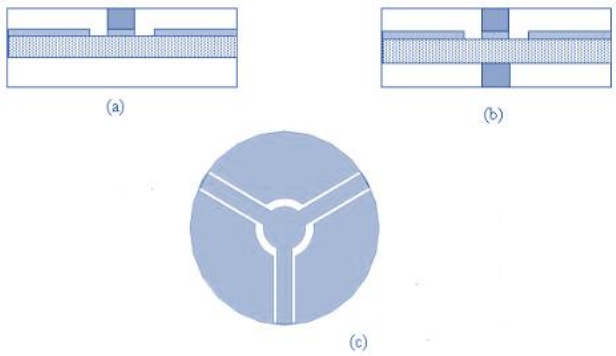

Fig 2.56 Physical configuration of the various structures proposed by Koshiji [54]: (a, b) sectional views, (c) top view

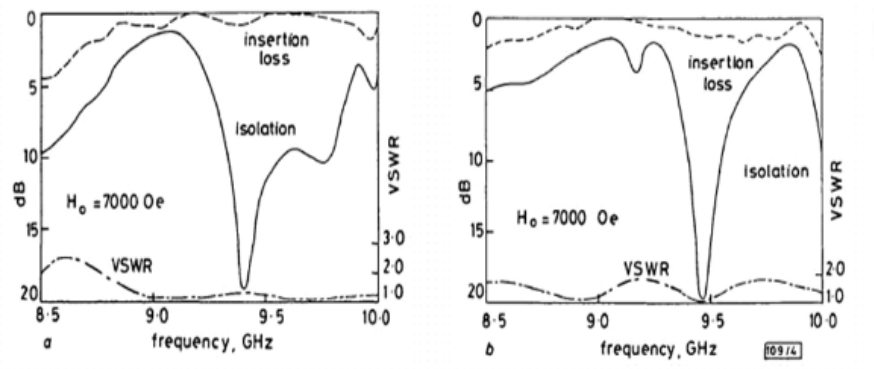

Fig 2.57 Measurement results in terms of insertion loss and insulation for the different versions [54]

In the years 2004, 2005, K. Oshiro et al. have manufactured a new coplanar circulator model using the finite element method [55]. The circulator of

dimensions 10 × 10 × 2 mm^3 operating in C band with two YIG ferrite substrate of thickness equal to 500 µm (Fig. 2.58). The central conductor and the ground planes are made of copper (10 µm thick).

There is a big agreement between simulation and measurement results (Fig. 2.59). Insertion losses levels are of 4.9 dB and the isolation of 28 dB and the working frequency band centered at 8 GHz.

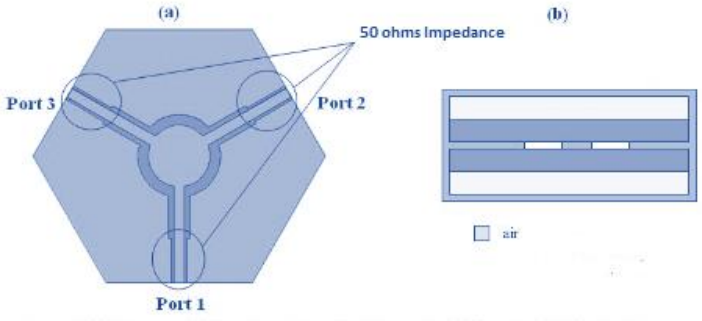

Fig 2.58 Structure of a coplanar circulator proposed by Oshiro [55]: (a) top view, (b) sectional view

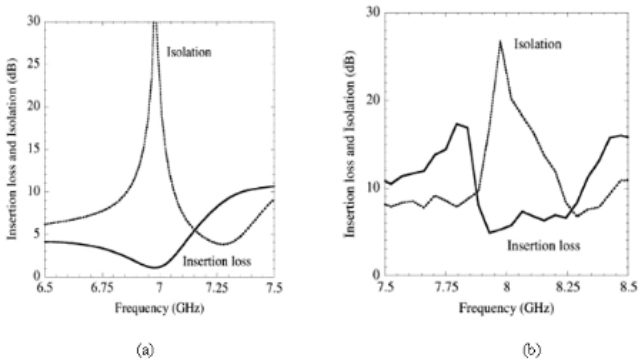

Fig 2.59 Oshiro Device Performance: (a) HFSS, (b) measurement [55]

In 2006, E. Bénevent [47] proposed a new coplanar circulator structure. The structure was modelled and simulated under HFSS software to have a circulating band between 40 and 50 GHz, it shows a miniature structure by using a thin layer of BaM (10 µm thick). In this work, several structures were tested (Fig. 2.60).

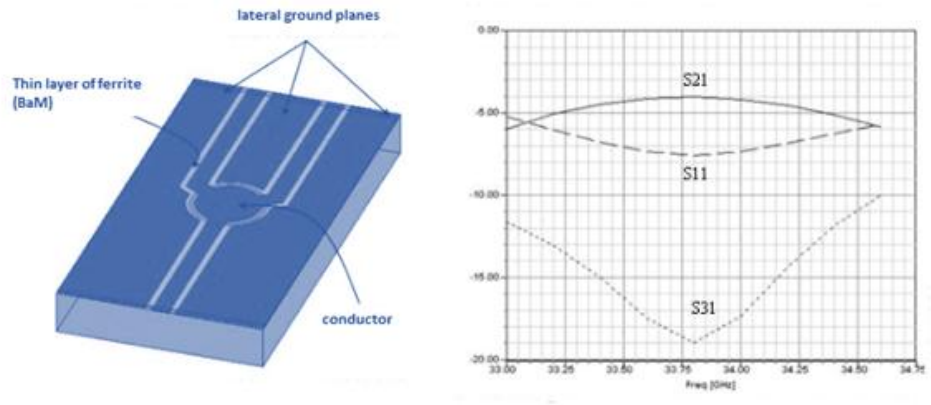

Fig 2.60 Circulator configuration proposed by E. Benevento and performances obtained under HFSS [47]

The recent studies on the coplanar structure proposed solutions for some challenges have been facing the other technologies, such as the complexity of the manufacturing process, reduction of the fabrication cost and solutions for the obstacles that face the measurement process. With the same performance requirements for every circulator, such as the low level of losses, high level of insulation and the variance in the bandwidth recording to the application needs. For instance, the circulators operating in X-band used normally in military applications, for that reason the bandwidth should be as wide as possible while maintaining low magnetic losses.

2.5.1.b Circulator with localized elements

As its name indicates, the localized circulator consists in implanting inductances and capacitances on a ferrite substrate (Fig 2.61). The conductors must be oriented at an angle of 120°, to maintain electrical symmetry and ensure the isolation of the device. When the ferrite material is magnetized a phenomenon of circulation appears. Therefore, the localized circulator acts with the non-reciprocal coupling of one port to the other via the inductive elements. With greater structure size for VHF or UHF applications the main applications of this type of structures are found in GSM mobile phone systems. This type of circulators can be made with only planar type technologies.

Several studies have been carried out on this type of circulator, for example Konishi [56], [57] in 1965 and 1972 dealt with the expansion of the bandwidth of this device into microstrip technology. In 1996, Miura [58] used the theoretical study developed by Konishi to design a new triplate circulator. The performances obtained are acceptable. With just 0.35 dB in the insertion losses and the bandwidth at -20 dB is about 5.8% for an operating frequency of 860 MHz.

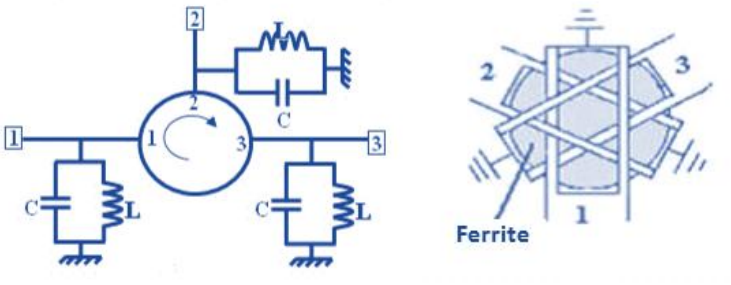

(a) **(b)**

Fig 2.61 Circulator with localized elements: (a) equivalent circuit, (b) the heart of the circulator

The design of localized element circulators using ferrite materials is a very interesting solution for mobile telephony applications, due to their easy miniaturization in low frequency bands. However, these components have significant insertion losses when used at high frequencies. We presented the different planar technologies (triplate, microstrip and coplanar) used for the realization of low power circulators.

Chapter 3:

Coupled Resonator Filters

3.1 Introduction

Today, the field of modern communications is evolving very rapidly. Wireless applications have multiplied: mobile telephony, broadband wireless Internet access and multimedia content in 4G and 5G [59]. 4G technology cannot meet some of today's challenges, such as reduced power consumption or spectral congestion. 5G technology represents the ultimate evolution of network communications reaching download speeds of up to 20 gigabits per second [59]. Its characteristics are called to satisfy, as shown schematically in Fig. 3.1, the needs for:

- The smart-city whose infrastructure can be effectively managed, thanks to sensor networks to optimize energy consumption and resource exploitation.
- Connected transport, with the particular appearance of autonomous cars, which will optimize and secure the road network.
- The connected house which can also be managed efficiently in the form of a resource or can be controlled and secured remotely.

Fig 3.1 Different applications for 5G

The integration of these services has become an important driver for the development of modern communication systems that require larger frequency bands and the exploration of solutions at higher frequencies [60].

A satellite system must perform specific functions in a space environment. Its architecture results from the objectives defined by the mission and the particular constraints related to its evolution in space [60]. The fields of use of telecommunications satellites are numerous, the most important are:

- International telephony: it is the most important application although it is competing with terrestrial or submarine optical cables.
- TV and radio,
- The GPS and GLONASS satellite positioning system, and soon Galileo.
- High speed data transmission (internet, multimedia applications, telemedicine ...).
- Military telecommunications.

For each application, a frequency band is allocated by the ITU (International Telecommunications Union). Fig. 3.2 shows the different frequency bands allocated and their applications.

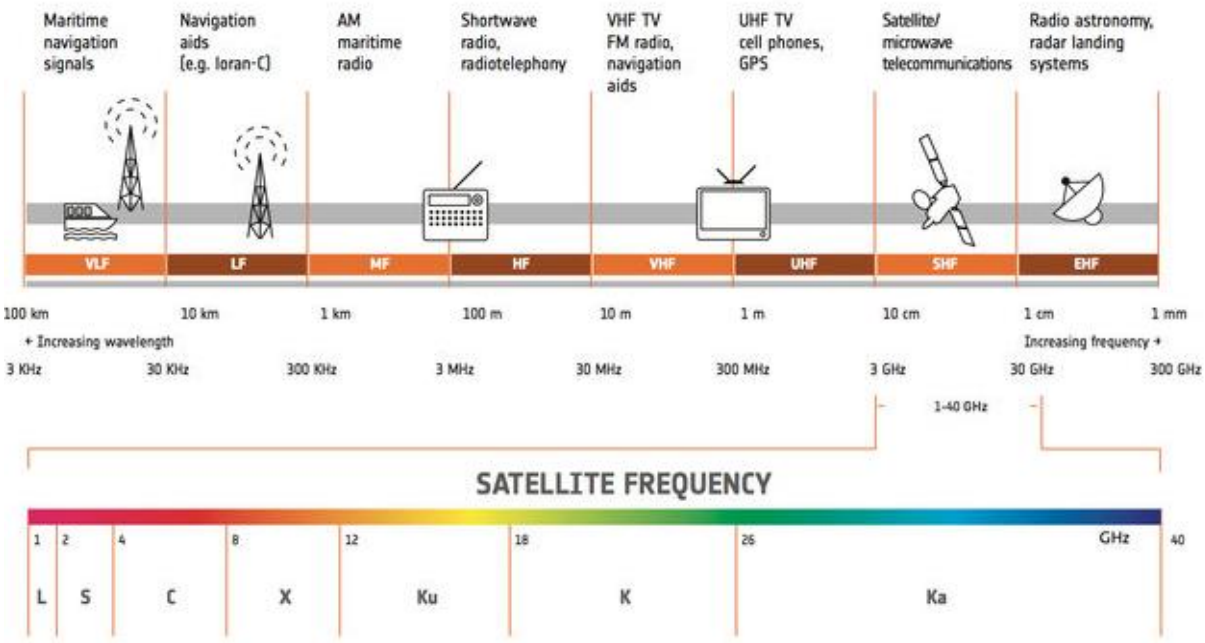

Fig 3.2 Frequency bands allocated by the ITU

3.2 Problematic

Microwave filtering devices (filters, multiplexers) are key elements in many communication systems. Depending on the system under consideration and the position of the filter in the system, their design must meet specific electrical specifications and cost, weight and space constraints. For example, in satellite transponders, cavity-based filters Quality (Q) high quality dielectric resonators are required for output multiplexers, which face severe specifications in terms of insertion loss and power loss. On the other hand, for receiver filters, performance in terms of loss of insertion and power handling is less critical, which allows the use of more compact, lower Q technologies, and makes it easier to integrate them with the active circuits of the receiver.

3.3 Introduction to Coupled Resonator Filters methods

The general coupling matrix method makes it possible to represent a wide range of topologies of filters with coupled resonators [1]. This technique can be formulated either from a set of mesh equations, or from a set of node equations. This leads to a very useful formulation for the analysis and synthesis of coupled resonator filter circuits in terms of coupling coefficients and external quality factors. The goal of coupling theory is the relationship between coupling coefficients and the physical characteristics of synchronous or asynchronous coupled resonators [1].

3.3.1 Coupling matrix representation

The basis of the determination of coupling matrix coefficients has been mentioned in many references [1]. Fig. 3.5 and Fig. 3.6 show the equivalent circuits of n-coupled resonators for two different types. L, C and R respectively denote inductance, capacitance and resistance, while *i* and *v* represents the loop current and the loop voltage. In order to define a general solution for both type of the coupling, it has been observed separately both electric and magnetic coupling behaviour.

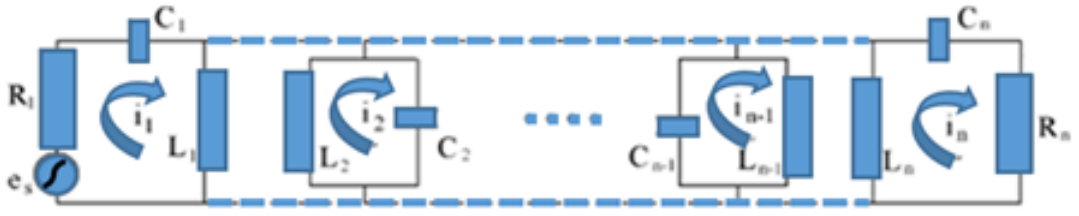

Fig 3.3 Equivalent circuit of n-coupled resonators for the formulation of the equations of the meshes for a magnetic type coupling

The application of one of the two laws of Kirchhoff (for instance the law of meshes for the magnetic coupling circuit, which indicates that the algebraic sum of the voltage drops in a closed mesh in a network is zero) allows us to determine the mesh equations for the circuit.

As shown in Fig. 3.5, the currents of all the loops are assumed to have the same direction, so that the voltage drop due to mutual inductance is of negative sign. The set of the mesh equations can be represented in the following matrix form:

$$\begin{bmatrix} R_1 + j\omega L_1 + \frac{1}{j\omega C_1} & -j\omega L_{12} \ldots. & -j\omega L_{1n} \\ -j\omega L_{12} & j\omega L_1 + \frac{1}{j\omega C_1} \ldots.. & -j\omega L_{2n} \\ -j\omega L_{n1} & -j\omega L_{n2} \ldots. & R_n + j\omega L_n + \frac{1}{j\omega C_n} \end{bmatrix} \begin{bmatrix} i_1 \\ \ldots. \\ i_n \end{bmatrix} = \begin{bmatrix} e_s \\ \ldots. \\ 0 \end{bmatrix} \tag{3.1}$$

Or in the following compact form:

$$[Z][i] = [e] \tag{3.2}$$

Where *[Z]* is an impedance matrix of order n.

Fig 3.4 Equivalent circuit of n-coupled resonators for electric type coupling

With the application of Kirchhoff's current law for the electrically coupled resonators and the use of the equivalent circuit in Fig. 3.6, the node equations can be defined and the set of the equations can be represented in the following matrix form.

$$\begin{bmatrix} G_1 + j\omega C_1 + \frac{1}{j\omega L_1} & -j\omega C_{12} \ldots. & -j\omega C_{1n} \\ -j\omega C_{12} & j\omega C_1 + \frac{1}{j\omega L_1} \ldots.. & -j\omega C_{2n} \\ -j\omega C_{n1} & -j\omega C_{n2} \ldots. & G_n + j\omega C_n + \frac{1}{j\omega L_n} \end{bmatrix} \begin{bmatrix} \vartheta_1 \\ \ldots. \\ \vartheta_n \end{bmatrix} = \begin{bmatrix} i_s \\ \ldots. \\ 0 \end{bmatrix} \tag{3.3}$$

Or in the following compact form:

$$[Y][\vartheta] = [i] \tag{3.4}$$

where *[Y]* is an admittance matrix of order n.

In the case of a synchronous filter, all inductances and capacities are equal. Consequently, all the resonators resonate at the same frequency, namely, the central frequency of the filter ω_0.

$$\omega_0 = \frac{1}{\sqrt{LC}} \tag{3.5}$$

The impedance matrix and the admittance matrix can be expressed by:

$$[Y] = \omega_0 CFBW[\bar{Y}][Z] = \omega_0 LFBW[\bar{Z}] \tag{3.6}$$

where $[\bar{Z}], [\bar{Y}]$ are the normalized impedance and admittance matrices.

And the fractional bandwidth *FBW* is:

$$FBW = \frac{\Delta\omega}{\omega_0} = \frac{\omega_2 - \omega_1}{\omega_0} \tag{3.7}$$

In the previous formulations, we used the normalized impedance and admittance matrices to characterize the coupling between two resonators. These formulations can be generalized in one general matrix for any type filters with n-coupled resonators, by reason of the matching between the two normalized matrices [1]. As a result, the admittance and impedance matrices can be put in a general form:

$$[\mathrm{A}] = \begin{bmatrix} \frac{1}{q_{e1}} & \cdots & 0 \\ \cdots & \cdots & \cdots \\ 0 & \ldots. & \frac{1}{q_{en}} \end{bmatrix} + \mathrm{p}\begin{bmatrix} 1 & \cdots & 0 \\ \cdots & 1 & \cdots \\ 0 & \ldots. & 1 \end{bmatrix} - \mathrm{j}\begin{bmatrix} m_{11} & \cdots & m_{1n} \\ \cdots & \cdots & \cdots \\ m_{1n} & \ldots. & m_{nn} \end{bmatrix} \tag{3.8}$$

Or in the following compact form:

$$[A] = [q] + p[U] - j[m] \tag{3.9}$$

where *[U]* is the identity matrix of order n, *[q]* is a matrix of order *n*, all the elements are zero except for the diagonal elements $q_{ei} = Q_{ei}.FBW$, and the matrix $[m]$, the so-called general coupling matrix, it is a reciprocal matrix of order n ($m_{ij} = m_{ji}$) and with non-zero diagonal elements m_{ii} for an asynchronous filter.

For a given filtering characteristic S_{21} *(p)* and S_{11} *(p)*, the coupling matrix and the external quality factors can be obtained using the synthesis procedure developed by Atia et al. [62] and Cameron [63], [64]. The following equations show the transmission and the reflection matrices expressed using the impedance matrix:

$$S_{21} = \frac{2}{\sqrt{q_{e1}q_{en}}}[\bar{Z}]_{n1}^{-1} \tag{3.10}$$

$$S_{11} = \left(1 - \frac{2}{q_{e1}}[\bar{Z}]_{11}^{-1}\right) \tag{3.11}$$

and the admittance one:

$$S_{21} = \frac{2}{\sqrt{q_{e1}q_{en}}}[\bar{Y}]_{n1}^{-1} \tag{3.12}$$

$$S_{11} = \left(\frac{2}{q_{e1}}[\bar{Y}]_{11}^{-1} - 1\right) \tag{3.13}$$

which can be also built in a general one:

$$S_{21} = \frac{2}{\sqrt{q_{e1}q_{en}}}[A]_{n1}^{-1} \tag{3.14}$$

$$S_{11} = \mp\left(1 - \frac{2}{q_{e1}}[A]_{11}^{-1}\right) \tag{3.15}$$

Non-zero values appear in the diagonal elements of the coupling matrix *[m]* as a result of an asynchronous tuning filter. The existence of the rest of the non-zero elements in the normalized coupling matrix *[m]* needs couplings between each resonator and all the others. As it is practically impracticable, it is generally necessary to carry out a similar transformation which results in a more practical and achievable form of filters. The transformation methods will be discussed in the next sections.

The coupling coefficients and external quality factors, as mentioned in the general coupling structures in Fig. 3.5 and Fig. 3.6, can be determined by the following formulas [1]:

$$M_{i,i+1} = \frac{FBW}{\sqrt{g_i g_{i+1}}}, \text{ for } i=1, \dots, N-1 \tag{3.16}$$

$$Q_{e_1} = \frac{g_0 g_1}{FBW}, \quad Q_{e_N} = \frac{g_N g_{N+1}}{FBW} \tag{3.17}$$

where the fractional bandwidth and the low-pass prototype g-values can be found as:

$$FBW = \frac{\omega_2 - \omega_1}{\omega_0}$$

$$g_0 = 1, g_1 = \frac{1}{\gamma}\sin\left(\frac{\pi}{2N}\right)$$

$$g_i = \frac{1}{g_{i-1}} \frac{\sin\left(\frac{(2i-1)\pi}{2N}\right).\sin\left(\frac{(2i-3)\pi}{2N}\right)}{\gamma^2 + \sin^2\left(\frac{(i-1)\pi}{N}\right)} \tag{3.18}$$

$$for\ i = 2,3, \dots N$$

$$g_{N+1} = \begin{Bmatrix} 1 & for\ N\ odd \\ coth^2\left(\frac{\beta}{4}\right) & for\ N\ even \end{Bmatrix}$$

where:

$$\beta = \ln\left[\coth\left(\frac{L_{Ar}}{17.37}\right)\right] \tag{3.19}$$

$$\gamma = \sinh\left(\frac{\beta}{2N}\right) \tag{3.20}$$

and L_{Ar} is the pass band ripple.

3.3.2 Example of usage: Synthesis of chebyshev low pass prototype method

3.3.2.1 Numerical example

In this section, a six-degree pass-band filter has been taken as an example to evaluate the previous approach synthesis method. This example is chosen randomly just to see if the program proposed is working correctly, so well than in the results that are shown in [1], [65].

The results keep changing with the change of the prototype of the filter or the type of the topology, such as, adding cross-coupled resonators in the general prototype of the filter. Therefore, those changes may change completely the desired filter structure.

In this example, a mathematical approach for the design of a sixth order bandpass filter using the g-values of Nth order Chebyshev low pass prototype filter method. This type of filter or well known as the inline topology filters are the simplest one to treat, with the non-existence of any transmission zeros in the out-side band which leads to a simple geometry, easy design rule, and compact size. A 20 dB return-loss level and two prescribed zeros at +j3.82 and +j4.24 have been taking in consideration.

First of all, the pass-band ripple needs to be calculated using equation (3.21) to generate the g-values presented in Table 1. The g-values are used after to calculate the coupling matrix coefficients in Table 2.

$$LAr = -10log\ (1 - 10^{\frac{-RL}{10}}) \tag{3.21}$$

The pass-band ripple found is: *LAr=0.043648 dB*

The generated g-values coefficients using the equations (3.18) and the coupling matrix elements calculated using the equations (3.17) are illustrated in the Table 1 and Table 2, respectively:

Table 1. The g-values coefficients

n	g_n
1	0.99582
2	1.4131
3	1.895
4	1.5505
5	1.7272
6	0.81475
7	1.2222

Table 2. The coupling matrix coefficients

M	1	2	3	4	5	6
1	0	0.84298	0	0	0	0
2	0.84298	0	0.61108	0	0	0
3	0	0.61108	0	0.5834	0	0
4	0	0	0.5834	0	0.61108	0
5	0	0	0	0.61108	0	0.84298
6	0	0	0	0	0.84298	0

The coupling matrix *[M]* is used to calculate the general matrix *[A]* in order to express the magnitude of transmission function S_{21} and the reflection function S_{11} illustrated respectively in Fig. 3.7 and Fig. 3.8. All the figures are taking using Matlab as computing Software and also a drawer to the results obtained.

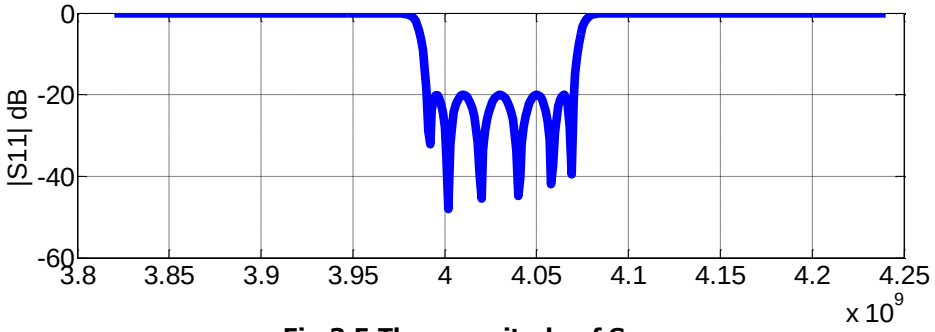

Fig 3.5 The magnitude of S_{11}

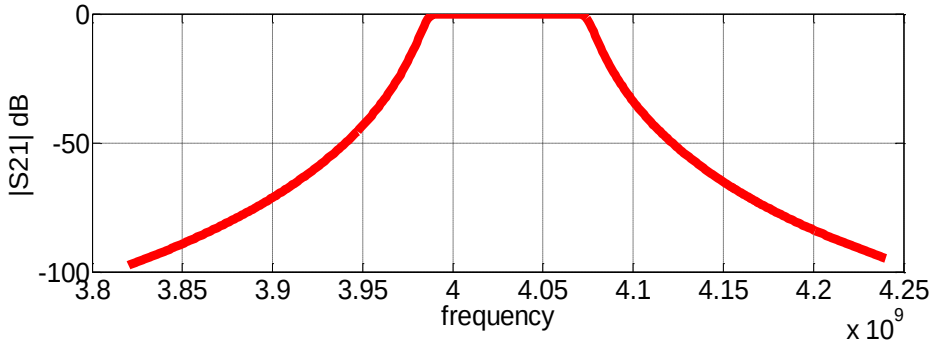

Fig 3.6 The magnitude of S_{21}

The results illustrated in Fig. 3.7 and Fig. 3.8 are kind of just a transformation of the resonators coupling matrix into a Scattering parameters graphs. That is shown clearly in the good quality of the results since they are not taking in consideration any fabrication constraints. Such as, the self-loss levels of the resonators, the transmission loss levels between the resonators, the loss levels of the material used for the fabrication or even the most important one the excitation of the systems. It has a big influence on the insertion losses, by affecting the vacuum quality factor of the structure. However, those results can play a major role in other designing methods, such as the methods based on optimization programs. That kind of results can be a very good starting point to decrease the time calculation of the process.

3.3.2.2 Physical implementation using CST MWS

For the validation of the influences of the design constraints on the simulation results, an 8^{th} order inline band-pass filter was designed using the same mathematical method explained above. The filter has a center frequency at 4 GHz and –20 dB return loss levels over a bandwidth of 100 MHz.

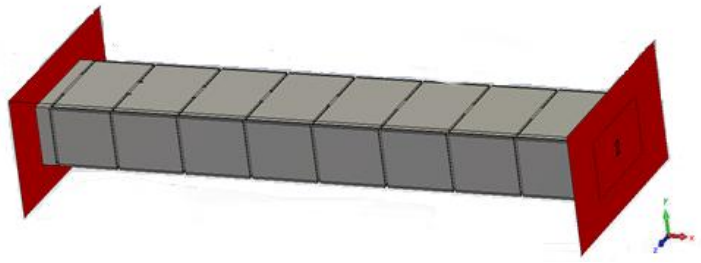

Fig 3.7 The complete design of 8 th order pass-band filter

The complete design illustrated in Fig. 3.9 does not include any novelty since it is a classic structure based on literature [66]. It can be seen clearly from the results the influence of the losses on the performance of the filter, 20% of the bandpass of the filter is basically just electromagnetic perturbation due probably to the excitations of the system and the adaptation of the ports.

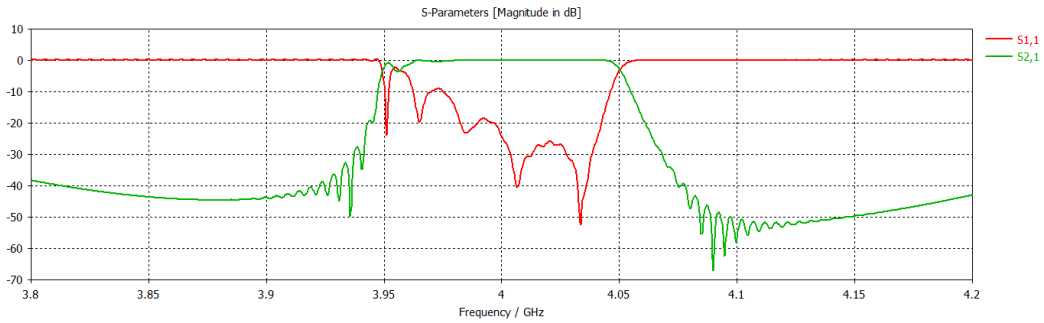

Fig 3.8 The S-parameters of the 8th order waveguide filter

The results obtained are preliminary results so they are not so satisfying, so the next step has to be correcting those results by exploring new method of transforming the resonators coupling matrix elements to a desire structure or just using genetic algorithm to simplify the correction computationally.

3.4 Synthesis of pass-band filters using the Polynomial methods

3.4.1 Cameron's recursive method

The term recursive function designates a class of computable functions, in other words functions whose values can be calculated from their parameters by a finite mechanical process. The recursive mathematical method proposed by R. J. Cameron, is one of these mathematical methods, and has been used to define the filtering function of a lossless n-coupled resonators filter.

The filtering function is a rational function has the same degree as the order of the filter, and it is a ration of polynomial functions to values to values in a field K. In practice, this field is generally R (set of reals) or C (set of complexes). The filtering function $C_N(\omega)$ is defined for all ω such that the N-degree denominator polynomial is not zero as [63], [64], [67]:

$$C_N(\omega) = \frac{F_N(\omega)}{P_N(\omega)} \tag{3.22}$$

The main rule of Cameron's technique is to define the nominator polynomial $F(\omega)$, since the obtention of the coefficients of the denominator $P(\omega)$ is easier, and can be constructed from the chosen transmission zeros. Specify the two polynomials defines also the position of both the reflection zeros and the transmission zeros in the complex frequency domain, as the roots of the nominator polynomial $F(\omega)$ are the reflection zeros and the roots of the denominator polynomial $P(\omega)$ are the chosen transmission zeros.

The N-degree filtering function $C_N(\omega)$ has different forms depends on the approximation function chosen, if it is a function of the Butterworth type, Chebyshev type or Elliptical type. The Cameron's method has been applied on a function of Chebyshev type. And the latter has a general from of:

$$C_N(\omega) = cosh[\sum_{n=1}^{N} cosh^{-1}(x_n)] \tag{3.23}$$

where

$$x_n = \frac{\omega - 1/\omega_n}{1 - \omega/\omega_n}$$

In the case where all the transmission zeros tend towards the infinity, the expression of the N-degree filtering function in equation (3.23), can be convert to the pure chebyshev function [63], [64], [67].

$$C_N(\omega)|\omega \to \infty = cosh(Ncosh^{-1}(x_n)) \tag{3.24}$$

In order to define the two polynomials $F_N(\omega)$ and $P_N(\omega)$, the filtering function in equation (3.23) has to be expressed in a rational function form, so by identity the roots of the numerator will be equal to the reflection zeros in equation (3.22), the same way as the roots of the denominator will be equal to the transmission zeros in equation (3.22) [63], [64], [67].

The procedure continues by setting the Hyperbolic Trigonometric Identity of the term of $\cosh^{-1}$ in equation (3.23), $cosh^{-1}(x) = ln(x + \sqrt{x^2 - 1})$, which leads to:

$$C_N(\omega) = cosh\left[\sum_{n=1}^{N} ln(x_k + \sqrt{{x_k}^2 - 1})\right] \tag{3.25}$$

For a further simplification of equation (3.25), the two terms x_k and $\sqrt{{x_k}^2-1}$ can be matched respectively to a_k and b_k, the equation (3.25) can be re-written as follows:

$$C_N(\omega) = cosh\left[\sum_{k=1}^{N} ln(a_k + b_k)\right] \tag{3.26}$$

Using the exponential identity form of cosh, the N-degree filtering function may be re-expressed as:

$$C_N(\omega) = \frac{1}{2}\left[exp(\sum_{k=1}^{N} ln(a_k + b_k)) + exp(-\sum_{k=1}^{N} ln(a_k + b_k)\right] \tag{3.27}$$

As it generally known that $exp(\sum_{k=1}^{N} ln(x)) = \prod_{k=1}^{N}(a_k + b_k)$ the equation (3.27) may be re-written as follows:

$$C_N(\omega) = \frac{1}{2}\left[\prod_{k=1}^{N}(a_k + b_k) + \frac{1}{\prod_{k=1}^{N}(a_k+b_k)}\right] \tag{3.28}$$

The multiplication of the expression of the filtering function $C_N(\omega)$ in equation (3.28) by $\frac{\prod_{k=1}^{N}(a_k-b_k)}{\prod_{k=1}^{N}(a_k-b_k)}$ leads to:

$$C_N(\omega) = \frac{1}{2}\left[\prod_{k=1}^{N}(a_k + b_k) + \prod_{k=1}^{N}(a_k - b_k)\right] \tag{3.29}$$

The N-degree filtering function Can be built-in a general form, by setting the frequency transformation $\omega' = \sqrt{\omega^2 - 1}$, and identifying respectively the two terms $\omega - 1/\omega_k$ and $\omega'(1 - \frac{1}{\omega_k^2})^{1/2}$ by c_k and d_k:

$$C_N(\omega) = \frac{1}{2}\left[\frac{\prod_{k=1}^{N}(c_k+d_k)+\prod_{k=1}^{N}(c_k-d_k)}{\prod_{k=1}^{N}\left(1-\frac{\omega}{\omega_k}\right)}\right] \tag{3.30}$$

The comparison between the general form and the rational function form of N-degree filtering function leads to that the roots of the nominator of the general form of the filtering function $C_N(\omega)$ are the reflection zeros, and its denominator roots are the prescribed transmission zeros.

$$num[C_N(\omega)] = \frac{1}{2}[G_N(\omega) + G'_N(\omega)] = F_N(\omega) \tag{3.31}$$

where:

$$G_N(\omega) = \prod_{k=1}^{N}(c_k + d_k) = \prod_{k=1}^{N}\left(\omega - \frac{1}{\omega_k} + \omega'\left(1 - \frac{1}{\omega_k^2}\right)^{\frac{1}{2}}\right)$$

$$\mathrm{G'_N}(\omega) = \prod_{\mathrm{k=1}}^{\mathrm{N}}(\mathrm{c_k} - \mathrm{d_k}) = \prod_{\mathrm{k=1}}^{\mathrm{N}}\left(\omega - \frac{1}{\omega_\mathrm{k}} - \omega'(1 - \frac{1}{\omega_\mathrm{k}^2})^{1/2}\right) \quad (3.32)$$

The two polynomials $G_N(\omega)$ and $\mathrm{G'_N}(\omega)$ can be readjusted as summation of two polynomials $U_N(\omega)$ and $V_N(\omega)$, where the polynomial $U_N(\omega)$ is expressed in term of the frequency variable ω, and the coefficient of the polynomial $V_N(\omega)$ are multiplied by the transformed frequency variable ω',

$$G_N(\omega) = U_N(\omega) + V_N(\omega) \quad (3.33)$$

where:

$$U_N(\omega) = u_0 + u_1\omega + u_2\omega^2 + \cdots$$
$$V_N(\omega) = \omega'(v_0 + v_1\omega + v_2\omega^2 + \cdots)$$

Cameron's recursive method has its role in finding the coefficients of the two polynomials $U_N(\omega)$ and $V_N(\omega)$, by putting first k=1, which accords to the first chosen transmission zero ω1, so that:

$$G_1(\omega) = \left(\omega - \tfrac{1}{\omega_1}\right) + \omega'\left(1 - \tfrac{1}{\omega_1^2}\right)^{\frac{1}{2}} = U_1(\omega) + V_1(\omega) \quad (3.34)$$

The procedure continues by setting k=2, and multiplying the term of the first iteration $G_1(\omega)$ by $[c_2 + d_2]$,

$$\mathrm{G_2}(\omega) = \mathrm{G_1}(\omega).[\mathrm{c_2} + \mathrm{d_2}]$$
$$= \left(\omega - \tfrac{1}{\omega_2}\right) + \omega'\left(1 - \tfrac{1}{\omega_2^2}\right)^{\frac{1}{2}}.[\mathrm{U_1}(\omega) + \mathrm{V_1}(\omega)]$$
$$= \omega\mathrm{U_1}(\omega) - \left(\frac{1}{\omega_2}\right).\mathrm{U_1}(\omega) + \left(1 - \frac{1}{\omega_2^2}\right)^{\frac{1}{2}}.\omega'.\mathrm{U_1}(\omega) + \omega\mathrm{V_1}(\omega) - \left(\frac{1}{\omega_2}\right).\mathrm{V_1}(\omega) + \left(1 - \frac{1}{\omega_2^2}\right)^{\frac{1}{2}}.\omega'.\mathrm{V_1}(\omega)$$

$$= [\mathrm{U}_2(\omega) + \mathrm{V}_2(\omega)] \tag{3.35}$$

where:

$$\mathrm{U}_2(\omega) = \omega \mathrm{U}_1(\omega) - \left(\frac{1}{\omega_2}\right).\mathrm{U}_1(\omega) + \left(1 - \frac{1}{\omega_2^2}\right)^{\frac{1}{2}}.\omega'.\mathrm{V}_1(\omega)$$

$$\mathrm{V}_2(\omega) = \omega \mathrm{V}_1(\omega) - \left(\frac{1}{\omega_2}\right).\mathrm{V}_1(\omega) + \left(1 - \frac{1}{\omega_2^2}\right)^{\frac{1}{2}}.\omega'.\mathrm{U}_1(\omega) \tag{3.36}$$

To build-in the general form of the two polynomials $\mathrm{U_k}(\omega)$ and $V_k(\omega)$, the procedure continues in the same way as the second iteration of the process. Setting *k=3,…,N* and multiplying the previous iteration $G_{k-1}(\omega)$ by the next term $[c_k + d_k]$ [63], [64], [67]:

$$U_k(\omega) = \omega U_{k-1}(\omega) - \left(\frac{1}{\omega_k}\right).U_{k-1}(\omega) + \left(1 - \frac{1}{\omega_k^2}\right)^{\frac{1}{2}}.\omega'.V_{k-1}(\omega)$$

$$U_k(\omega) = \omega V_{k-1}(\omega) - \left(\frac{1}{\omega_k}\right).V_{k-1}(\omega) + \left(1 - \frac{1}{\omega_k^2}\right)^{\frac{1}{2}}.\omega'.U_{k-1}(\omega) \tag{3.37}$$

As a conclusion, Cameron found that the numerator of the N-degree filtering function $\mathrm{C_N}(\omega)$ is equal to the polynomial $\mathrm{U_N}(\omega)$, since after repeating the procedure for $\mathrm{G'_k}(\omega)$, it turned out that $\mathrm{U'_N}(\omega) = \mathrm{U_N}$, and $\mathrm{V'_N}(\omega) = -\mathrm{V_N}$. Accordingly, the roots of the two polynomials $\mathrm{U_N}(\omega)$ and $\mathrm{V_N}(\omega)$ are corresponding, respectively, to the reflection zeros and the N-1 in-band reflection maxima [63], [64], [67].

3.4.2 Rhodes and Alseyab Alternating method used to determine the denominator polynomial E(s)

To describe the behaviour of a two port lossless filter using the polynomial synthesis method, it is necessary to define its transfer functions [63], [64]. In other words, the transmission function $S_{21}(s)$ and the reflection function $S_{11}(s)$.

$$S_{21}(s) = \frac{P(s)}{\varepsilon E(s)} \tag{3.38}$$

$$S_{11}(s) = \frac{F(s)}{\varepsilon_r E(s)} \tag{3.39}$$

where $s = \mathrm{j}\omega$ is the frequency variable in the complex frequency domain.

For both functions, the polynomial *E(s)* represents their denominator, as the polynomials *P(s)* and *F(s)* represent respectively their nominators. The filtering systems are isolated systems, thus, the law of conservation of energy may be applied to find the denominator polynomial *E(s)*. Since the two nominator *P(s)* and *F(s)* are found before. The complex roots of the polynomial *E(s)* corresponds to the poles of the filter.

$$S_{11}(s)S_{11}(s)^* + S_{21}(s)S_{21}(s)^* = 1 \tag{3.40}$$

or

$$F(s)F(s)^* + \frac{P(s)P(s)^*}{\varepsilon^2} = E(s)E(s)^* \tag{3.41}$$

As it is been explained before, one of the characteristics of the chebyshev filters is can tolerate a slight ripple constant ε in the pass band, and can be calculated using the prescribed return loss RL. It has a role of normalizing the transmission parameter *S21(s)* to a specific IL levels at *ω=-1* and *ω=1*.

$$\varepsilon = \frac{1}{\sqrt{10^{\frac{RL}{10}}-1}} \left|\frac{P(\omega)}{F(\omega)}\right|_{\omega=\pm 1} \text{(dB)} \tag{3.42}$$

From equation (3.41), the polynomial *E(s)E(s)** is found from the multiplication of the expressions of the two nominator polynomials $P(s)$ and $F(s)$, means that the polynomial is a scalar quantity of *2N* order [68], since the polynomial $F(s)$ is a *N* order one. Therefore, the roots of polynomial E*(s)E(s)** form a symmetric motif in the complex plan as shown in Fig. 3.11.

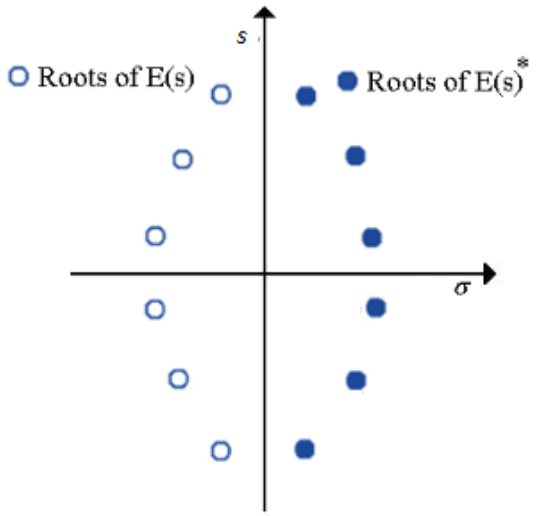

Fig 3.9 The position of the roots of polynomial E(s)E(s)* in the complex plan

The positions of the roots of the polynomials *E(s)* are in the imaginary axis of the complex plan, accordingly to the nature of the polynomial, since it is a Hurwitz polynomial [68]. The inaccuracy problems that face this method specially for higher degree functions, when the *2N* roots of the polynomial *E(s)E(s)** gathered around *s*=±*j*. Leads Rhodes and Alseyab [69] to present an alternative method to find the roots of the polynomial *E(s)* without the need of defining the roots of the polynomial *E(s)E(s)** [69].

The equation (3.41) can be expanded in two different equation depends on the quantity of the substitution of the number of transmission zeros from the number of resonators.

In the first case where the rest subtraction (N-nfz) is odd, the expression of the equation (3.41) may be re-written as follows:

$$\varepsilon^2\varepsilon_r{}^2\mathrm{E}(s)\mathrm{E}(s)^* = (\varepsilon_r\mathrm{P}(s) + \varepsilon\mathrm{F}(s))(\varepsilon_r\mathrm{P}(s)^* + \varepsilon\mathrm{F}(s)^*) - \varepsilon\varepsilon_r(P(s)^*F(s) + P(s)F^*(s)) \tag{3.43}$$

In order to eliminate the term $\varepsilon\varepsilon_r(P(s)^*F(s) + P(s)F^*(s))$ in equation (3.43) the condition $P(s)^*F(s) = -P(s)F(s)^*$ must be satisfied.

For the second case when the rest of the subtraction (N-nfz) is even, the expression of the equation (3.41) may be re-written as follows:

$$\varepsilon^2{\varepsilon_r}^2E(s)E(s)^* = (\varepsilon_r(jP(s)) + \varepsilon F(s))\left(\varepsilon_r\left(jP(s)\right)^* + \varepsilon F(s)^*\right) - \varepsilon\varepsilon_r((jP(s)^*)F(s) + (jP(s))F^*(s))$$

(3.44)

In order to eliminate the term $\varepsilon_r((jP(s)^*)F(s) + (jP(s))F^*(s))$ in equation (3.44) the condition $P(s)^*F(s) = P(s)F(s)^*$ must be satisfied. The two conditions that have been proposed cannot be satisfied, if only if, the system is considerate passive, lossless and reciprocal. Moreover, the reflection zeros of the two ports of the system must to be positioned in the imaginary axis and coincident.

If the conditions are satisfied the equations (3.43) and (3.44) may be reduced as follows:

$$\varepsilon^2{\varepsilon_r}^2E(s)E(s)^* = (\varepsilon_rP(s) + \varepsilon F(s))(\varepsilon_rP(s)^* + \varepsilon F(s)^*) = (\varepsilon_rP(s) + \varepsilon F(s))(\varepsilon_rP(s) + \varepsilon F(s))^*)$$

(3.45)

The equation (3.45) is correct in the case where (N-nfz) is odd, and the following equation is correct in the case where (N-nfz) is even.

$$\varepsilon^2{\varepsilon_r}^2E(s)E(s)^* = (\varepsilon_r(jP(s)) + \varepsilon F(s))(\varepsilon_r(jP(s))^* + \varepsilon F(s)^*) = (\varepsilon_r(jP(s)) + \varepsilon F(s))(\varepsilon_r(jP(s)) + \varepsilon FS)*$$

(3.46)

In the frequency plane, since the polynomial *E(ω)* is Hurwitz, the two nominators *P(ω)* and *F(ω)* will have obviously real coefficients. The modification of the last equation (3.46) can give birth to a general equation to find the frequency plane particularities for both cases, where (N-nfz) is even or odd:

$$\varepsilon^2{\varepsilon_r}^2E(\omega)E(\omega)^* = (\varepsilon_r\left(P(\omega)\right) - j\varepsilon F(\omega))\left(\varepsilon_r\left(P(\omega)\right) - j\varepsilon F(\omega))^*\right) \quad (3.47)$$

By rooting one of the equal expressions to the polynomial $E(s)E(s)^*$ in equation (3.46), it outcomes a motif of particularities alternating between the positive side of the imaginary axis and the negative one, as it is shown in Fig. 3.12.

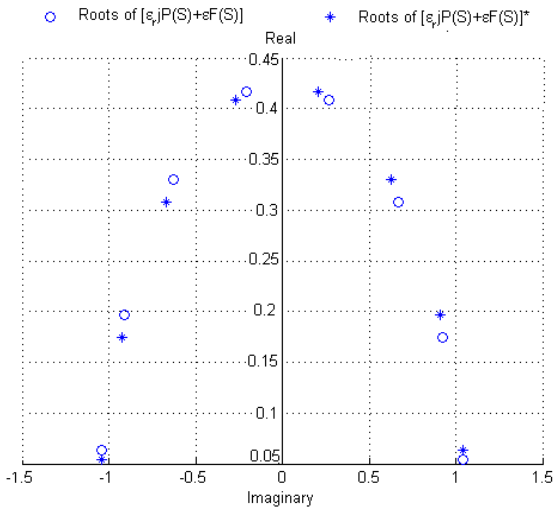

Fig 3.10 Obtained singularities of polynomials for eighth degree filter, (N-nfz) even

The rooting of the other expression will affect a complementary set of particularities, completing the coherence of the pattern around the imaginary axis and ensuring that the two right side expressions of equation (3.46) are scalar as the polynomial $E(s)E(s)^*$ requests [68]. Consequently, forming just one of the two expressions of equation (3.46) is sufficient. Since the polynomial $E(s)$ is Hurwitz, any particularities found in the positive side of the imaginary axis can be just reflected symmetrically to the negative side of the imaginary axis, in order to form the polynomial $E(s)$ [69].

3.4.3 Examples of usage: Synthesis of passband filters using the Polynomial methods

The next section is dedicated to determine the characteristic polynomials of different filter prototypes, to show how the complexity of the prototype influences the characteristic polynomials, and who in turn affects the response of the filter.

Some of these examples have the same results as the examples illustrated in [70].

Example I: N=4, RL=20, no TZ.

The first filter prototype is an inline four degree filter with 20 dB return-loss level without transmission zeros. Initializing it by using equation (3.37) with $\omega_1 = inf$, which is going to be the only ω's value that will be remained till the end of the procedure. Then, after finding the coefficients of the two nominator the polynomials *P(S)* and *F(S)*, the rest is to find the coefficients of the denominator polynomial *E(s)* using the alternative method proposed by Rhodes and Alseyab [69]. Table 3 shows the results obtain by MATLAB as a calculator software of the normalized coefficients of the two nominator polynomials *P(s), F(s)* and the denominator polynomial *E(s)*.

Table 3. Polynomial coefficients of the fourth order filter without TZs

$S^n, n =$	P(S)	F(S)	E(s)
0	1.0000	0.1250	1.2500
1		0.0000	2.8269
2		1.0000	3.2965
3		0.000	2.1431
4		1.0000	1.0000

with *ε=0.8040*, calculated by using equation (3,42).

Since, the polynomial *E(s)E(s)** is forming by multiplying the two nominator polynomials *P(S)* and *F(S)* in equation (3.41). The latter expression of the polynomial *E(s)E(s)** has to be of 2N degree with real coefficients. And its roots are forming a symmetric motif about the imaginary axis in the complex plane. The nature of the denominator polynomial *E(s)* forces the positioning of its roots in the negative side of the complex plan, while, the roots of the denominator E(s)* situated in the positive half of complex plane.

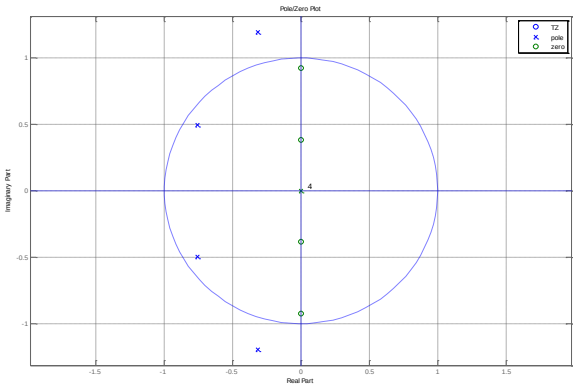

Fig 3.11 Pole-zero diagram of the filtering

The Fig 3.14 shows the scattering parameters of the inline filter built by applying the equations (3.38) and (3.39)

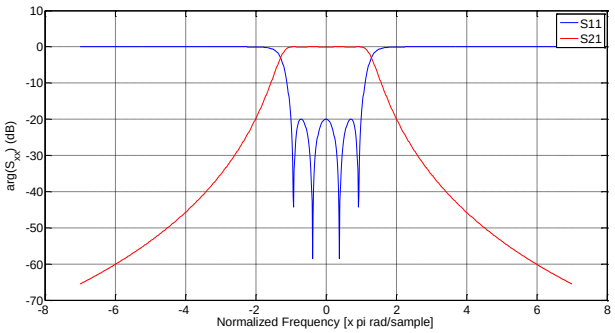

Fig 3.12 Classical Chebyshev response without transmission zeros

The perfect characterisations overwhelm all the mathematical approach results, as it is been mentioned before because of the absence of the losses influences of the physical implementation.

Example II: N=4, RL=20, TZ= [±4]

The second filter is a 20 dB four degree cross coupled filter with just two finite transmission zeros situated at ±4j Hz. Since, the nominator Polynomial P(ω) can be constructed easily from the defined transmission zeros. The second

step is constructing the polynomial *F(ω)*. The procedure starts by setting ω1=4 into equation (3.34) to find the first two polynomials U1 and V1, then, it continues by setting *ω2*=-4 into equation (3.36) to find the second two polynomials. and setting *ωk*=∞ for k= [3, 4] into equations (3.37) to determine the highest degree polynomials U4 and V4. The polynomial can be constructed by normalizing the polynomial U4 and its roots leads to the N-reflection zeros. After finding the two nominator polynomials *P(s)* and *F(s)*, the denominator *E(s)* can be constructed easily by using the alternative method proposed by Rhodes and Alseyab [69].

The ripple constant ε found is ε=12.4591.

The Table 4 shows the coefficients of the nominator and denominator polynomials. The positions of their roots are illustrated in Fig. 3.15.

Table 4. Polynomial coefficients of the filter with two TZs

$S^n, n =$	P(S)	F(S)	E(s)
0	16.0000	0.1291	1.2907
1	0.0000	0.0000	2.8284
2	1.0000	1.0081	3.2799
3		0.0000	2.1316
4		1.0000	1.0000

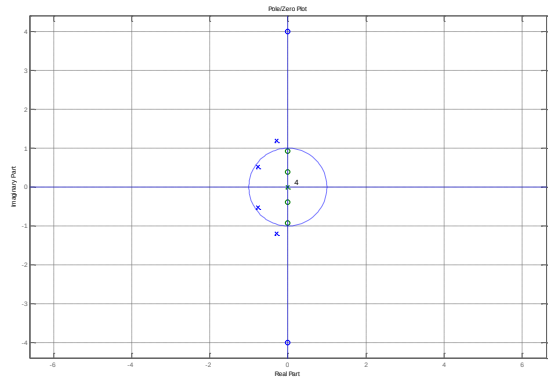

Fig 3.13 Pole-zero diagram of the filtering

The Fig. 3.16 shows the scattering parameters of the cross coupled filter desired.

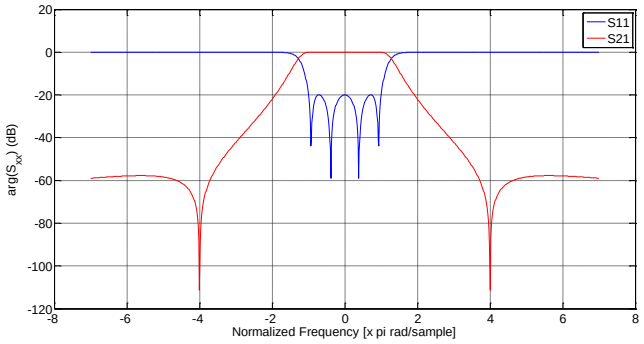

Fig 3.14 Chebyshev response with finite transmission zeros at ±4 rad

It is clearly appeared in the S-graph the two transmission zeros positioned at ±4j on the normalized frequency axis to give two rejection lobes level of 58 dB on the both sides of the pass band.

Example III: N=4, RL=20, TZ= [±4, ±5]

The last example is an example of cross coupled four degree filter with four transmission zeros placed at ±4j, ±5j in the imaginary axes, known as the fully canonical filter topology.

Table 5. Polynomial coefficients of the filter with 4TZs

$S^n, n =$	P(S)	F(S)	E(s)
0	400.0000	0.1317	1.3167
1	0.0000	0.0000	2.8274
2	41.0000	1.0132	3.2708
3	0.0000	0.0000	2.1247
4	1.0000	1.0000	1.0000.

With *ε=305.3279*

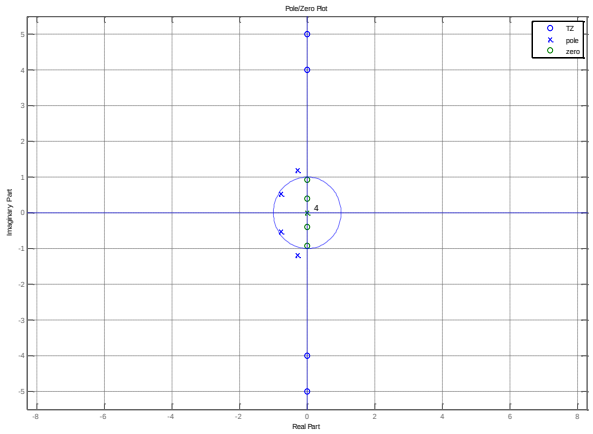

Fig 3.15 Pole-zero diagram of the filtering

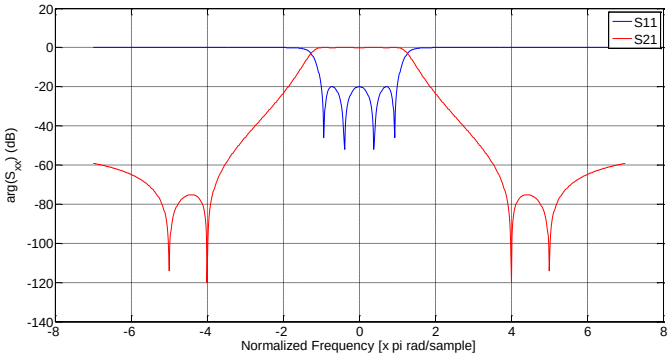

Fig 3.16 Fully canonical filtering function

It is clearly shown in the S-graph illustrated in Fig 3.18, the existence of the four transmission zeros placed at ± 4j and ± 5j on the imaginary axis to give a rejection lobes level of 75 dB on the both sides of the pass-band. The polynomial *P(s)*, *F(s)* and *E(s)* have the same degree, this example called also the fully canonical filtering response in other words, the number of the resonators N is the same as the number of transmission zeros (N-nfz=0).

3.5 Rotation method

3.5.1 The rational forms of the transfer function $S_{21}(s)$ and the reflection $S_{11}(s)$ function for lossless two-port network.

The synthesis of coupled resonators circuits is one of the most important steps to design a radio frequency and microwave filter. Thus, the development of a general mathematical method, easy to applied on any type of filters without taking in consideration its physical structure technology, has been needed for long time [64].

The synthesis of microwave bandpass filters is generally based on an equivalent electrical diagram of the device with resonators coupled into localized elements. This synthesis makes it possible, from the theory of circuits, to determine the values of the localized elements of the equivalent electrical diagram according to the chosen filtering function [1].

In general, a filter can be represented by a passive quadrupole described in the Fig. 3.19.

Fig 3.17 Two port network

where a_i and b_i are the power waves propagation transmitted and reflected from ports 1 and 2, V_i are the in-put and output voltages of the quadrupole and I_i are Input and output current of the quadrupole.

In the microwave domain, a quadrupole is generally defined by its Scattering Parameters, which make it possible to completely define the characteristics of a linear multi-pole system. A quadripole may be linear when it consists only of dipoles and linear elements [1].

The power waves propagation is linked each other by:

$$\begin{bmatrix} b_1 \\ b_2 \end{bmatrix} = \begin{bmatrix} S_{11} & S_{12} \\ S_{21} & S_{22} \end{bmatrix} \begin{bmatrix} a_1 \\ a_2 \end{bmatrix} \tag{3.48}$$

In order to introduce some expressions will use later, especially for defining the admittance parameters matrix $[y]$, the chain matrix ABCD represents the initial step in the next procedure.

The ABCD matrix for a two-port quadrupole system can be expressed as follows [71]:

$$[ABCD] = \frac{1}{P(s)/\varepsilon} \begin{bmatrix} A(s) & B(s) \\ C(s) & D(s) \end{bmatrix} \tag{3.49}$$

where

$$\mathrm{S_{12}(s) = S_{21}(s) = \frac{P(s)/\varepsilon}{E(s)} = \frac{2P(s)/\varepsilon}{A(s)+B(s)+C(s)+D(s)}} \tag{3.50}$$

$$\mathrm{S_{11}(s) = \frac{F(s)/\varepsilon R}{E(s)} = \frac{A(s)+B(s)-C(s)-D(s)}{A(s)+B(s)+C(s)+D(s)}} \tag{3.51}$$

$$\mathrm{S_{22}(s) = \frac{(-1)^N F(s)^*/\varepsilon R}{E(s)} = \frac{D(s)+B(s)-C(s)-A(s)}{A(s)+B(s)+C(s)+D(s)}} \tag{3.52}$$

The expression of the chain matrix in (3.49) shows that all the elements of the matrix have the same denominator, the polynomial $P(s)/\varepsilon$. These elements are extracted from the real model of the filter. Hence, the microwave filters circuits are generally formed by a cascade of simple elements, and the chain matrix ABCD, has a main advantage of cascading elements.

The ability to express the transmission $S_{12}(s)$ and the reflection $S_{11}(s)$, $S_{22}(s)$ parameters with the polynomial $P(s)$, $F(s)$ and $E(s)$ makes relating them to the

Chain matrix elements easier, as it is shown in equations (3.50), (3.51) and (3.52).

The circuit synthesis of any type of filters starts always from the low pass prototype as it is illustrated in Fig. 3.20, to form the prototype desired. A series of changing based mainly on Richard's transformation and Kuroda's identities used to define the appropriate resonating elements to add and the suitable scales for the center frequency and the bandwidth. There exist a lot of physical technologies for the realization of these resonators, for instance, the planar technology such as the U-shape planar resonators or the volume technology, such as the structure illustrated in Fig. 3.20, the coaxial technology.

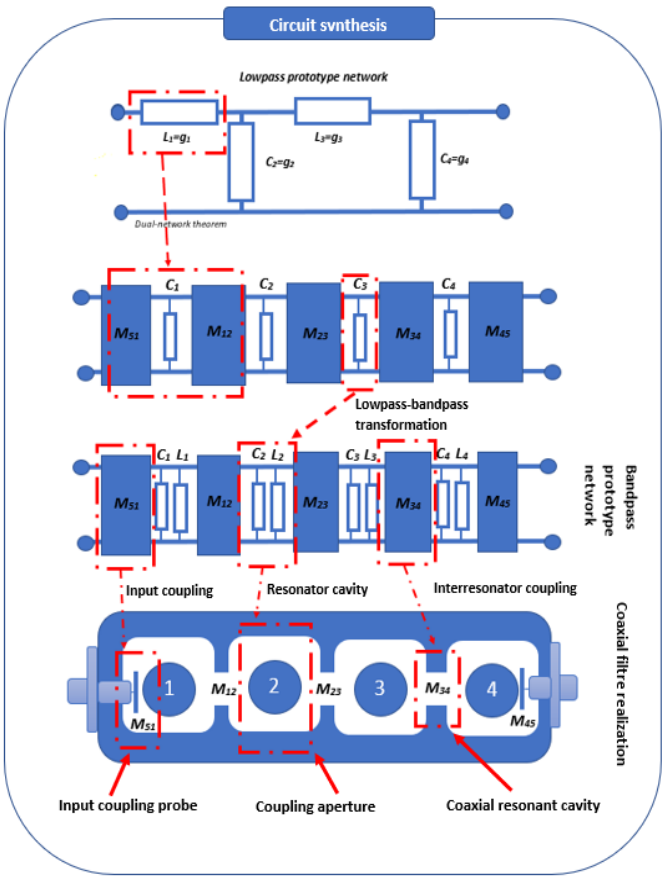

Fig 3.18 Steps in the synthesis process for a fourth-order coaxial resonator band pass filter

The system illustrated in Fig. 3.19 shows the network of a lossless filter with a voltage source with internal impedance *Z01* and load impedance *Z02*. These two source and load impedances connected to the two ports of the circuit, can be normalized to 1 by the insertion of input and output transformers whose transformation ratios are known [1], [68], [72], [73]. The equivalent circuit of such a prototype is detailed in Fig. 3.21.

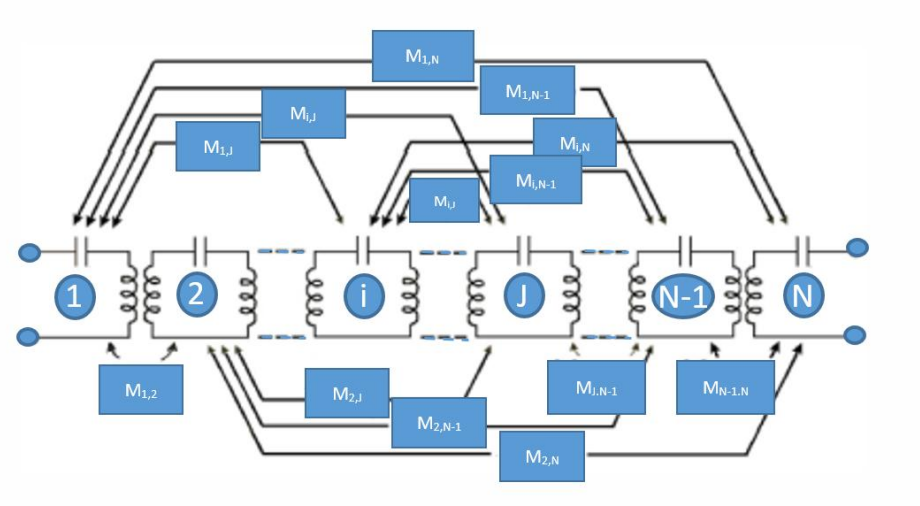

Fig 3.19 N coupled resonators

In the early 1970s, Atia and Williams [62] introduced the concept of coupling matrix applied to waveguide filters. They describe the coupling between the adjacent cavities, but also the coupling of each cavity with all the other cavities of the filter in waveguides. It is synthesized from the transfer function of the filter. Once obtained, the coupling matrix will be the key element of the synthesis of the filter, because from this, we can deduce all the characteristics of the filter, such as the filter order, the number and the position of the transmission zeros, filter topology, etc. then give its equivalent circuit in Fig. 3.21.

The circuit proposed by Atia and Williams [62] is a cascade of several resonators inter-coupled by a coupling factor M_{ij}, either by direct coupling for the

adjacent resonators, or by indirect coupling for the other resonators. Each resonator consists of a capacitor with a value of 1 Faraday in series with an inductance of 1 Henry.

Cameron [63], [64], [68] proposed a new N-order filter configuration called the N+2 transversal Matrix, this configuration introduces also the influence of the self-coupling of the source and load. The general view of the circuit proposed by Cameron is presented in Fig. 3.22. The lossless resonator is modelled by a capacitor C_k, a reactance B_k, and two admittance inverters at input M_{sk} and at output M_{Lk}.

A further explanation of the determination of the coupling matrix of this new configuration with its relation with the chain matrix is held in the next section.

3.5.2 Synthesis of the N+2 transversal Matrix

Since all the elements forming the general circuits proposed by Cameron are cascading, the inverters, the capacitor and the reactance, the chain matrix $[ABCD]$ of the system may be obtained by multiplying the chain matrices of the cascaded elements forming the system.

$$[ABCD]_k = [ABCD]_{Msk}[ABCD]_{Ck}[ABCD]_{Bk}[ABCD]_{Mlk} \tag{3.53}$$

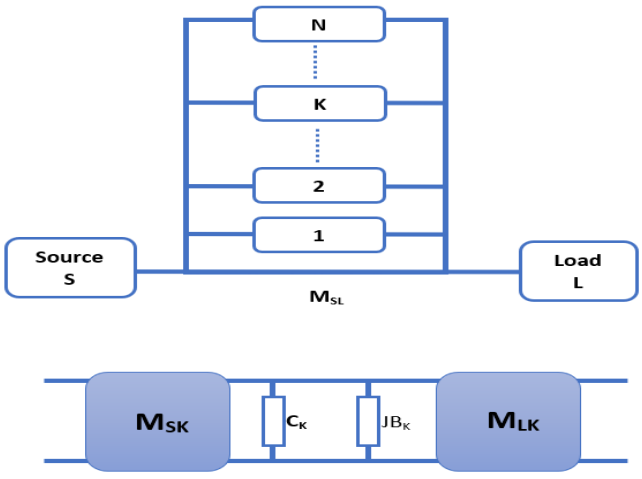

Fig 3.20 the N+2 canoniacal transversal array and its equivalent kth lowpass resonator circuit

The general expression of the chain matrix of the system shows some important characteristics of its elements due to the cascading operation. As it known, in order to synthesis the coupling matrix of any type of filter network using the chain matrix, the introduction of the short circuit admittance matrix is mandatory. Thus, the re-expression of the polynomials *A(s)*, *B(s)*, *C(s)*, and *D(s)* with linked with the y-matrix elements is important and it shows as follow:

$$[ABCD]_k = -\begin{bmatrix} \frac{Mlk}{Msk} & \frac{(s\,Ck+jBk)}{MskMlk} \\ 0 & \frac{Msk}{Mlk} \end{bmatrix} \tag{3.54}$$

Using the expression of the $[ABCD]_k$ matrix elements with the short circuit admittance matrix elements reveals in [64]:

$$\begin{aligned} y_d(s) &= B(s) \\ y_{11n}(s) &= D(s) \\ y_{22n}(s) &= A(s) \\ y_{21n}(s) &= y_{12n}(s) = -P(s)/\varepsilon \end{aligned} \tag{3.55}$$

The k-order chain matrix $[ABCD]$ may be converted now into the k-order admittance parameter matrix $[yk]$:

$$\begin{aligned} [yk] &= \begin{bmatrix} y11k(s) & y12k(s) \\ y21k(s) & y22k(s) \end{bmatrix} \\ &= 1/y_d(s) \begin{bmatrix} y11n(s) & y12n(s) \\ y21n(s) & y22n(s) \end{bmatrix} \\ &= \frac{MskMlk}{(sCk+jBk)} \cdot \begin{bmatrix} \frac{Msk}{Mlk} & 1 \\ 1 & \frac{Mlk}{Msk} \end{bmatrix} \\ &= \frac{1}{(sCk+jBk)} \cdot \begin{bmatrix} Msk^2 & MskMlk \\ MskMlk & Mlk^2 \end{bmatrix} \end{aligned} \tag{3.56}$$

The general form of the short-circuit admittance matrix $[Y_N]$ for the transversal configuration is the summation of the short-circuit admittance

matrices of the pre-elements forming the circuits. In other words, the sum of the short-circuit admittance matrix of the *N* individual sections, with the short-circuit admittance matrix of the directly source-load coupling inverter $[y_{SL}]$, as it is been explained in Fig. 3.22.

$$\begin{aligned}
[\mathrm{YN}] &= \begin{bmatrix} \mathrm{y11(s)} & \mathrm{y12(s)} \\ \mathrm{y21(s)} & \mathrm{y22(s)} \end{bmatrix} \\
&= [\mathrm{ysL}] + \sum_{\mathrm{k=1}}^{\mathrm{N}} \begin{bmatrix} \mathrm{y11k(s)} & \mathrm{y12k(s)} \\ \mathrm{y21k(s)} & \mathrm{y22k(s)} \end{bmatrix} \\
&= \mathrm{j}\begin{bmatrix} 0 & \mathrm{MsL} \\ \mathrm{MsL} & 0 \end{bmatrix} + \sum_{\mathrm{k=1}}^{\mathrm{N}} \frac{1}{(\mathrm{sCk+jBk})} \cdot \begin{bmatrix} \mathrm{Msk}^2 & \mathrm{MskMlk} \\ \mathrm{MskMlk} & \mathrm{Mlk}^2 \end{bmatrix} \\
&= \mathrm{j}\begin{bmatrix} 0 & K_0 \\ K_0 & 0 \end{bmatrix} + \sum_{\mathrm{k=1}}^{\mathrm{N}} \frac{1}{(\mathrm{s-j\lambda_k})} \cdot \begin{bmatrix} \mathrm{r_{11k}} & \mathrm{r_{12k}} \\ \mathrm{r_{21k}} & \mathrm{r_{22k}} \end{bmatrix}
\end{aligned} \tag{3.57}$$

Form equations (3.57), and after equating the two terms of the court-circuit admittance matrix. The elements of the general court-circuit admittance matrix $[YN]$ may be revealed as follows:

$$\begin{aligned}
MsL &= K_0 \\
\frac{r_{21k}}{(s-j\lambda_k)} &= \frac{MskMlk}{(sCk+jBk)} \\
\frac{r_{22k}}{(s-j\lambda_k)} &= \frac{Mlk^2}{(sCk+jBk)}
\end{aligned} \tag{3.58}$$

The rest of the elements also can be revealed from the equations (3.57), and may be related directly to the circuit parameters, by just taking in account their complex form.

The residues r_{21k} and r_{22k} and the eigenvalues λ_k have already been derived from the S_{21} and S_{22} polynomials of the desired filtering function and, thus, by equating the real and imaginary parts of equation (3.56) and equation (3.57), it becomes possible to relate them directly to the circuit parameters.

$$CkMsk = 1 \; and \; Bk(\equiv Mkk) = -\lambda_k$$
$$Mlk^2 = r_{22k} \; and \; MSkMLk = r_{21k}$$

$$Mlk = \sqrt{r_{22k}} = T_{Nk} \tag{3.59}$$

$$Msk = r_{22k}/\sqrt{r_{22k}} = T_{1k} \text{ k=1, 2,…. N}$$

The parameters y_{22} and y_{21} being known as a function of the characteristic polynomials P/ε, F and E, the terms λ_i of the diagonal matrix *[Λ]*, the resistances r and the terms T_{ik} of the first and last line of the matrix *[T]* can then be identified.

The other lines can be chosen arbitrarily provided that *[T]* is orthogonal. An orthogonalization method such as that of Gramm Schmidt can be used. Finally, the coupling matrix can be calculated by applying the relation [63], [64], [68]:

$$[M] = [T].[\Lambda].[T]^{-1} \tag{3.60}$$

3.5.3 The Reduction of the N+2 transversal Matrix to the folded canonical form

In an equivalent circuit, if every resonator is coupled to all the other resonators of the filter, the coupling matrix will contain only non-zero values. This is practically difficult to achieve or even impractical to realize for most cases special for a high order waveguide filter. Therefore, the objective is to use mathematical techniques to reduce the number of non-zero elements, and to achieve *M* matrices similar to the initial matrix and which are practically transformable into a filter.

In its final form, the matrix *M* proposed by Atia and Williams [62] had elements, positioned symmetrically in several diagonals. This form is called "canonical form» Fig. 3.23 [62]. It was the basic element of several researchers; whose aim was to propose other forms of coupling matrices starting from the canonical form. Several matrices have been obtained and successfully tested. They are called "topologies" [64].

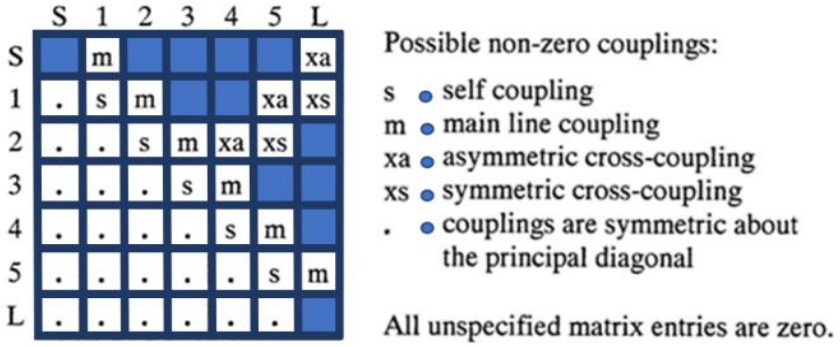

(a)

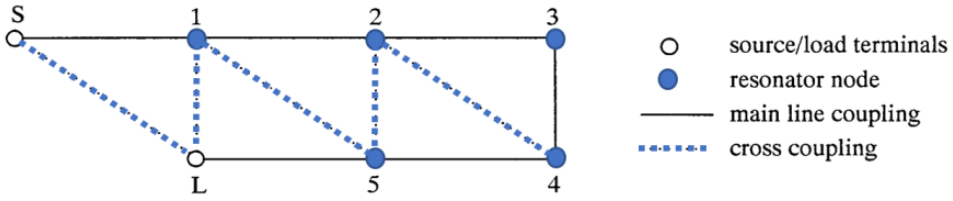

(b)

Fig 3.21 Folded canonical network coupling matrix. (a) Folded coupling matrix. (b) coupling and routing schematic

The first design step consists in synthesizing the network lossless coupling matrix. This coupling matrix can be synthesized the N+2 transversal matrix. The topology of the filter obtained is impractical in practice. Indeed, the coupling matrix needs a reduction or transformation to a practical form, by applying a rotation sequences in order to cancel the couplings which are not physically achievable. The transformation process eliminates alternatively the matrix coefficients from the right to the left along rows and top to bottom down columns. Considering the synthesis studied here a classical lossless synthesis, a trigonometric rotation matrix R is used to transform the original coupling matrix M_0 related to the N+2 transversal matrix to a new coupling matrix M_1 related to the canonical network desired. The new matrix after rotation is given by:

$$M_1 = R_1 M_0 R^t \tag{3.61}$$

where R^t transpose of the trigonometric rotation matrix R,

$$[R] = \begin{bmatrix} C_r & 0 & -S_r \\ 0 & 1 & 0 \\ S_r & 0 & C_r \end{bmatrix} \tag{3.62}$$

where

$$C_r = R_{ii} = R_{jj} = cos(\theta_r)\ \ S_r = R_{ij} = -R_{ij} = sin(\theta_r)$$

Although the rotations are abstract, unrelated to a physical phenomenon, they nevertheless make it possible to cancel M_0 terms while retaining the associated response.

This makes it possible to reveal configurations of coupling matrices which could be linked to a physical reality. In the context of this study, the particular configurations, for which certain precise terms are non-zero, are called topologies.

In general, it is possible to switch from one topology to another using a well-defined series of rotations, due to the fact, that the eigenvalues of the two matrices M_1 and M_0 remain the same even after a series of transformations. The pivots are predefined but the angles are calculated for each rotation according to the values that the matrix takes after the rotation and in order to cancel a precise term in the matrix.

The formulas are presented in equations (3.63) are applied to change the values of k_{th} element in the row or column i or j of the N+2 transversal matrix M_0 to the canonical folder matrix M_1.

$$\begin{aligned} M_{ik}^1 &= C_r M_{ik}^0 - S_r M_{jk}^0 \text{ for an element in row i} \\ M_{jk}^1 &= C_r M_{ik}^0 + S_r M_{jk}^0 \text{ for an element in row j} \\ M_{ki}^1 &= C_r M_{ki}^0 - S_r M_{kj}^0 \text{ for an element in column i} \\ M_{kj}^1 &= C_r M_{ki}^0 + S_r M_{kj}^0 \text{ for an element in column j} \end{aligned} \tag{3.63}$$

where k $(\neq \mathrm{i,j}) = 1,2,3,\ldots \mathrm{N}$.

It is important to remind that the process of the transformation of the coupling matrix is executed in a certain way that guarantees the degeneration of any element once is annihilated by a subsequent transform in the process.

As it is been explained in [64], the reduction method of the N+2 transversal matrix to a folded matrix form uses a series of transformation that involve rotation angles applied on the initial matrix M_0, in order to eliminate the unrealizable elements. The order and the way that these transformation formulas are applied, forces the degeneration of any element has been eliminated by a further transformation in the process. Thus, to achieve the coupling prototype of a filter resonators in folded structure, the unwanted coupling elements will be annihilated one by one, from the right to the left along the rows, and from the top to the bottom down the columns, toward the center of the matrix [64], [68].

The angles formulas are presented in equation (3.64) summarize the elimination process of the k_{th} element in the row or column i or j.

$$\begin{aligned}
&\theta_r = tan^{-1}(M_{ik}/M_{jk}) \text{ for } k_{th} \text{ element in row i } (M_{ik}) \\
&\theta_r = -tan^{-1}(M_{jk}/M_{Ik}) \text{ for } k_{th} \text{ element in row j } (M_{jk}) \\
&\theta_r = tan^{-1}\left(\frac{M_{ki}}{M_{kj}}\right) \text{ for } k_{th} \text{ element in column i } (M_{ki}) \\
&\theta_r = tan^{-1}(M_{kj}/M_{ki}) \text{ for } k_{th} \text{ element in column j } (M_{kj})
\end{aligned} \tag{3.64}$$

3.5.4 Examples of usage: Calculation of the resonators coupling matrix of a folded filter using the method of the rotation

In this unit, a similar four order bandpass filter to the one produced by AMTI, the C0423501 [74] Will be designed. The resonators coupling matrix elements are determined by using the rotation method. The filter has specific characteristics of: working band between 2.4 GHz and 2.5 GHz, insertion loss level and return loss level respectively of at least 1.5 dB and 15 dB, respectively, producing a ripple constant and flatness level smaller than 0.8 dB in the

passband, and with a voltage wave ratio of 2.0:1. Other additional specifications are not taking into account such as the temperature of the filter. With the interval given above, the mid band frequency becomes $f_0 = \sqrt{2.4545 \, . \, 2.5554}$ *GHz = 2.5044GHz*, and the fractional bandwidth *FBW = BW / f_0 = 0.0402*. The small number of resonators (4 resonators) keeps the design of the filter simple and miniature. The VSWR yields to a reflection factor of -9.54 dB, which generally can be achieved by any filter configuration. An introduction of a pair of transmission zeros at about 2.404 GHz and 2.5873 GHz, so that we have Ω_a= (2.404/2.5044 - 2.5044/2.404) /0.0402 = 2.03, will fulfil the requirement of the out-band rejection at both 2.4 GHz and 2.6 GHz.

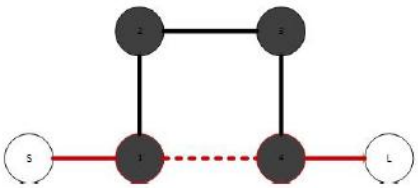

Fig 3.22 The folded quartet configuration of the design filter

The proposed work follows the procedure described before. The coefficients of transfer and reflection polynomials for such a filter with two normalized transmission zeros at $\Omega_a = [\pm 2]$ and a constant ripple of $\varepsilon = 5.0337$ are presented in the table 6:

Table 6. The Transmission and the Reflection polynomials coefficients

$S^n, n =$	P(S)	F(S)	E(S)
0	4	0.1436	0.8075
1	0	0	1.8031
2	1	0.359	2.3928
3		0	1.6474
4		1	1

The realization of the microwave filter comes directly from the folded coupling matrix, its nonzero elements define the topology and strengths of its inter-resonator couplings. Yet, sometimes the complexity of the matrix imposes a

further series of rotation to transform it to realizable matrix. Which one of the objectives of this section. The elements of the transversal coupling matrix extracted from the coefficients of the nominator and denominator polynomials are shown in the table 7.

Table 7. The N+2 coupling matrix M for the transversal array network of the filter of design

	S	1	2	3	4	L
S	0	0.3316	0.3316	0.5495	0.5495	0
1	0.3316	-1.1689	0	0	0	0.3315
2	0.3316	0	1.1689	0	0	-0.3315
3	0.5495	0	0	-0.5900	0	-0.5495
4	0.5495	0	0	0	0.5900	0.5495
L	0	0.3315	-0.3315	-0.5495	0.5495	0

After the reduction method synthesis, we can transform the N+2 coupling matrix M of the transversal array network to the folded coupling matrix desired. The elements of the quartet configuration coupling matrix are shown the Table 8:

Table 8. The folded matrix M of the quartet configuration

	S	1	2	3	4	L
S	0	0.9076	0	0	0	0
1	0.9076	0	0.7780	0	-0.1206	0
2	0	0.7780	0	0.6995	0	0
3	0	0	0.6995	0	0.7779	0
4	0	-0.1206	0	0.7779	0	0.9075
L	0	0	0	0	0.9075	0

3.6 Realization the coupling matrix in the microstrip resonators

3.6.1 Formulation for Coupling Coefficients

This study makes it possible to link physical quantities, which are the spacing and the dimensions of the gap between the two resonant elements, with

an electrical quantity, the value of the resonator coupling matrix determined theoretically.

In the design of a planar band pass filter. A lot of resonators shapes are used extracted from the open loop resonators shape. The particular shape of the $\frac{\lambda}{2}$ resonator allows several configurations of inter-resonator coupling. There is the electric, magnetic and the mixed coupling as illustrated in Fig. 3.25.

The electrical type coupling exists when the ends of a resonant line in $\frac{\lambda}{2}$ are opposite each other with the ends of another resonant line.

The magnetic type coupling exists when the middle or the back of a resonant line in $\frac{\lambda}{2}$ are opposite each other with the middle or the back of another resonant line. The Mixed type coupling, combination of electrical type and type coupling magnetic is also a function of the distance between the resonators.

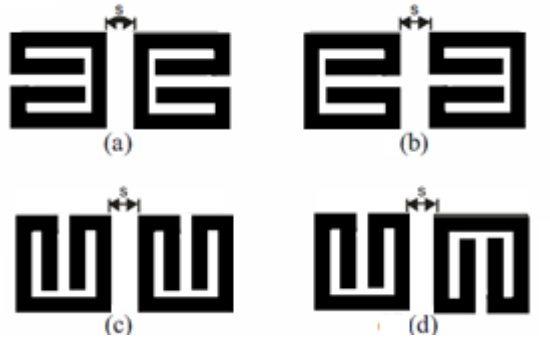

Fig 3.23 Typical coupling structures of coupled resonators with (a) Magnetic coupling (b) Electric coupling, (c) and (d) Mixed coupling

If two resonators excited and situated near to each other, they will automatically interact. The closer they are the stronger the coupling get. It is known that for the case of a very narrow pass band filter (0.26%) the coupling between the resonators require to be very weak [1], [75]. The coupling coefficient between two resonators is expressed from the resonance frequencies f_1 and f_2 as follows:

$$m_{ij} = \frac{f_2^2 - f_1^2}{f_2^2 + f_1^2} \tag{3.65}$$

For a convenient physical implementation of a band pass filter, Jia-Sheng Hong and Michael J. Lancaster [75] developed some closed formulas, which can estimate the spacing between two coupled open-loop resonators. These formulas take into account the type of the coupling, the characteristics of the substrate used and some dimensions of the resonators [75].

The formulas proposed by Jia-Sheng Hong and Michael J. Lancaster [75] for the electric coupling coefficient are:

$$
\begin{aligned}
k_E &= \frac{\pi}{16}.F_e.exp(-A_e).exp(-B_e).exp(-D_e) \\
A_e &= 0.2259 - 0.01571.\varepsilon_r + 0.1.\sqrt{\varepsilon_r + 1}.\frac{w}{h} \\
B_e &= [1.0678 + 0.266.ln(\tfrac{\varepsilon_r+1}{2})].(\tfrac{w}{h})^{pe} \\
p_e &= 1.0886 - 0.03146.(\tfrac{w}{h})^4 \\
D_e &= [0.1608 - 0.06945.\sqrt{\tfrac{a}{h}}] + (\tfrac{s}{h})^{1.15} \\
F_e &= [-0.9605 + 1.4087.\sqrt{\tfrac{a}{h}} - 0.2443\,\tfrac{a}{h}]
\end{aligned}
\tag{3.66}
$$

For the magnetic coupling coefficient are:

$$
\begin{aligned}
k_M &= \frac{\pi}{16}.F_m.exp(-A_m).exp(-B_m).exp(-D_m) \\
A_m &= [-0.06834 + 0.1417.\frac{w}{h} + 0.08655.(\tfrac{w}{h})^3] \\
B_m &= 1.2.(\tfrac{s}{h})^{pm} \\
p_m &= 0.8885 - .1751.\sqrt{\frac{w}{h}} \\
D_m &= [1.154 - 0.8242.\sqrt{\frac{a}{h}} + 0.1417\,\frac{a}{h}] + (\frac{s}{h}) \\
F_m &= \left[-0.5014 + 1.0051.\sqrt{\frac{a}{h}} - 0.1557\,\frac{a}{h}\right]
\end{aligned}
\tag{3.67}
$$

And for the mixed coupling coefficient are:

$$k_B = k'_M + k'_E$$

$$k'_M = 0.5 \qquad (3.68)$$
$$k'_E = 0.6\, k_E$$

Where ε_r is the relative dielectric constant, *h* is the thickness of the substrate, *w* and *a* are respectively, the width and the quarter length of the resonator [75].

3.6.2 Coupling Coefficients as Function of Separation S

The structure of the filter designed in this section is made on substrate of FR-4 material with a relative permittivity of 4.3. The line width of both the standard wave impedance of *50 Ω* and the standard wave impedance of *80 Ω* resonator is respectively, 3 mm and 1.2 mm. The resonator line width gives an effective relative permittivity of $\varepsilon_{r,eff} = 3.05$. The guided half wavelength inside the microstrip line at the center frequency becomes about 44 mm. We use a new resonator design based on the resonator design in [74], the total physical length of the resonator used is about 44.3 mm with a gap length of 1.3 mm.

According to the sign of the resonators coupling matrix elements obtained, the type of the coupling is determined. Thus, due to the negative coupling value between resonator 1 and 4, the type of the coupling must be electric and can be realized by a cross coupling, these indirect coupling produces one of the transmission zeros. The remain couplings between the resonators are supposed to be direct. The type of the coupling between resonators 2 and 3 is magnetic and finally the type of the coupling between the resonators 1 and 2 and between the resonators 3 and 4 is mixed in other words, is a combination of both electric and magnetic couplings.

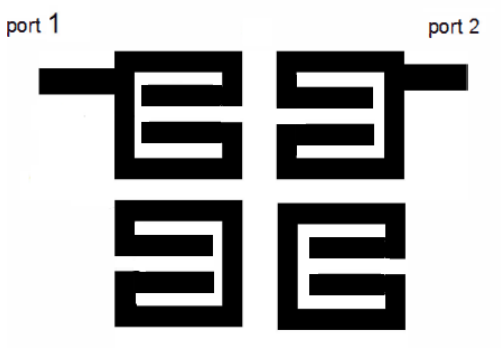

Fig 3.24 Schematic for realizing the couplings

To obtain the coupling coefficients, we build two coupled resonators based on a substrate of type FR-4 with thickness 1.6 mm, has a relativity of 4.3 and tangent loss of 0.0022. According to Michael J. Lancaster [75], the coefficient of electric coupling can be extracted as function of distance s as it is shown in Fig. 3.27.

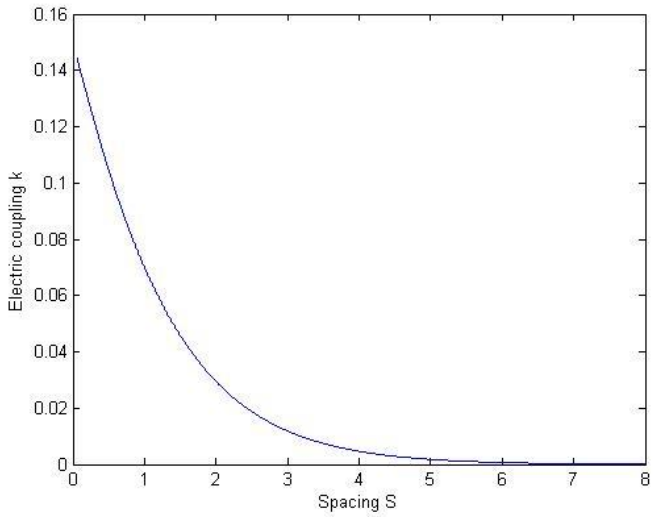

Fig 3.25 Coupling coefficient for electric coupling [75]

From the physical consideration, the small spacing between resonators will cause strong coupling and large spacing lead to weak coupling. the spacing S_{14}, which yields to the coupling coefficient $M_{14} = -0.1206$, namely $S_{14} = 3.098\,mm$.

In a similar way, it can find out the distances $S_{12} = 2.12342\ mm$ and $S_{23} = 2.7619 mm.$

It has to be repeated again that this method is not the only method exist, there is another way to determine the spacing between the resonators, as it is been highlighted before. The method based on the iteration electromagnetic simulations; it is commonly used for the waveguide technology filters. It is generally known that, at the resonance, the transmission parameter S_{21} can be expressed in term of frequencies and will have an optimum value. If it happens that in the same time two resonators are coupled mutually, two resonant frequencies will appear in the response of the system, one of them has to be higher than the other one. From these resonant frequencies the spacing between the resonators can be extracted after calculating the scattering parameter between them.

The external quality factor can be determined by varying the distance between the feed line and the symmetry line of the resonator.

Fig 3.26 Schematic of position of the feed line

After the iterative calculations, the position of the feeding line from the symmetric line of the resonator is t=2.7 mm. The complete schematic of the bandpass filter designed is depicted in Fig. 3.29.

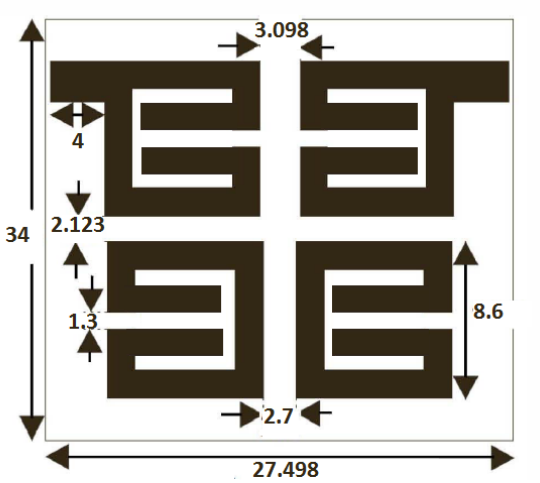

Fig 3.27 Schematic filter (all dimension in mm)

3.6.3 Simulation and Measurement

The schematic of the Fig. 3.29 is the structure under consideration. A full-wave simulation with the software CST MWS gives us a good computation result. Also, in order to verify the simulation with measurements, a prototype is built in Fig. 3.30. The prototype is manufactured on substrate of type FR-4 has the relativity of 4.3 and tangent loss of 0.0022 with thickness 1.6 mm.

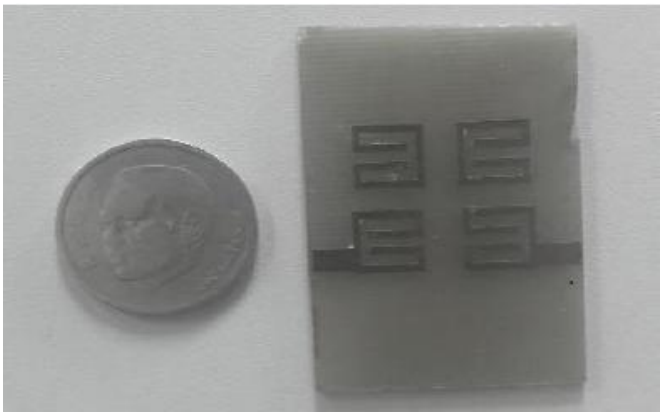

Fig 3.28 Complete filter design

The fabrication process using LPKF protoMat. It is measured by using a Rohde and Schwarz ZVB 20 Vector Network Analyzer. The transmission and the reflection factors are depicted in Fig. 3.31 and Fig. 3.32.

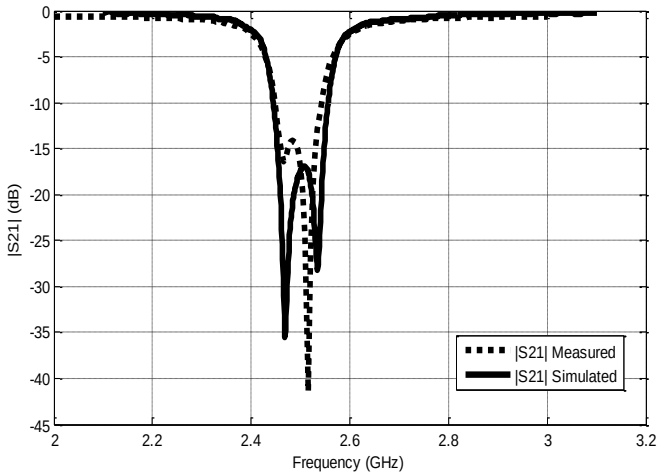

Fig 3.29 Reflection parameters of the realized filter Simulation result (solid line) Measurement result(dashed line)

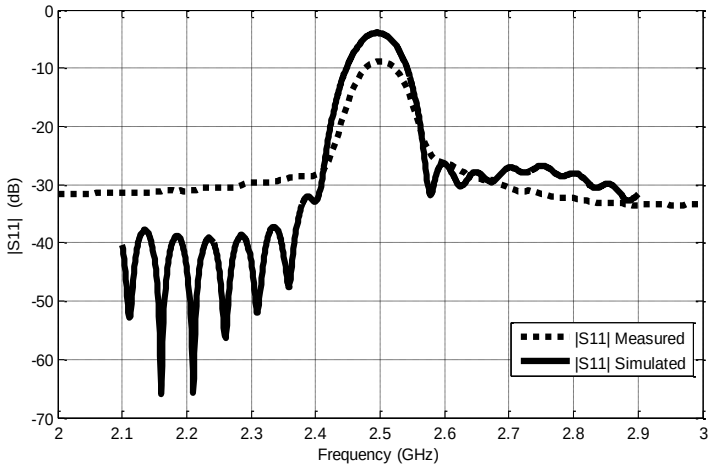

Fig 3.30 Transmission parameters of the realized filter Simulation result (solid line) Measurement result(dashed line)

The resonance frequency is located at about 2.5 GHz with insertion loss of about 5.9 dB for the simulation and for the measured is about 9.3 dB, and return loss is about 15.6 dB for the measurements and this value is near to the simulation about 16.4 dB. All these values are in the region between the frequency 2.45GHz and 2.55 GHz, as the filter has the bandwidth of about 100

MHz for the transmission zeros, that are located around the pass-band in 2.404 GHz and 2.588 GHz. Comparison of the pass region between simulation and measurement data shows that there is a shift of the measurement results to a lower frequency region. We should notice that maybe the reasons of the smaller insertion loss obtained by the measurements are i) in simulation we may have used higher loss tangent, than we have in reality, ii) also the relative permittivity of the FR-4 used in realization has a different value than 4.4, or iii) probably the fabrication tolerance in the photo etching that cause the frequency shift.

3.7 The gradient based optimization method

It this chapter, we went through several mathematical approach to find resonators coupling matrix. Unfortunately, some of those processes face major problems. For instance, the theory of transformations proposed by Atia and Williams does not always converge [62]. Or Cameron's reduction method of a full matrix to a folded form is still unknown [64], [68].

Thus, new optimization method has been introduced to synthesis this type of structure, most of these optimization methods used independent initial inputs for the coupling matrix with very simple cost functions [76].

The optimization method held in this section is based on S. Amari [76] Gradient-based optimization method. The optimization process uses the results of the polynomial transfer functions mentioned before.

The optimization process uses first the results of the polynomial transfer functions to define the scattering parameters of the system [62], [63], [64], [69], then, it can minimize the cost function of the system by minimizing at every each single frequency the difference between the scattering parameters of the surrogate model and the scattering parameters of the desired prototype.

The cost function can be expressed as follows:

$$F = \sum_{freq} \sum_{i=1}^{p} \sum_{j=1}^{p} \left[S_{ij}^{sorrugate} - S_{ij}^{simulated} \right]^2 \quad (3.69)$$

Where both the transmission and reflection functions can be expressed in terms of the polynomials and the general coupling matrix as follows:

$$S_{21}(s) = \frac{P(s)}{\varepsilon E(s)} = -2j\sqrt{R_1 R_2}[A^{-1}]_{N1} \quad (3.70)$$

$$S_{11}(s) = \frac{F(s)}{\varepsilon_r E(s)} = 1 + 2jR_1[A^{-1}]_{11} \quad (3.71)$$

After specifying a desire prototype, the optimization method works in a way that, reproduce the scattering parameters of the filter using the resonators coupling matrix *[M]*, and the terminal resistors R_1 and R_2 extracted from the previous iteration [62], [63], [64], [69].

3.7.1 Gradient calculations

The optimization process inputs are assumed to be independent variables. With the respect of the independence of a variable x the gradient of the cost function will involve the derivatives of the scattering parameters [76], [78].

$$\frac{\partial |S_{11}|}{\partial x} = Re\left[\frac{|S_{11}|}{S_{11}} \frac{\partial |S_{11}|}{\partial x} \right] \quad (3.72)$$

Using the above expression in terms of coupling components to express S_{21} we get [77], [78]:

$$\frac{\partial |S_{11}|}{\partial x} = -2R_1 \frac{\partial I_1}{\partial x} \quad (3.73)$$

$$\frac{\partial |S_{21}|}{\partial x} = 2\sqrt{R_1 R_2} \frac{\partial I_N}{\partial x} \quad (3.74)$$

These above derivatives can be calculated by taking the derivatives of the matrix equation $[I] = -j[A^{-1}][e]$ to get:

$$\frac{\partial [I]}{\partial x} = j[A^{-1}] \frac{\partial [I]}{\partial x} [A^{-1}][e] \quad (3.75)$$

The topology of the filter network $[T]$ is defined in terms of the components in the coupling matrix. If the element of the coupling matrix is zero, the corresponding element of the topology is zero too, otherwise, it would be specified as unity. It is the most valuable advantage for a design engineer that the topology of the filter network can be determined in the first place and it will be enforced at each step in the optimization process [78].

By substituting the variable x by a generic variable of the coupling matrix $M_{p,q} = M_{q,p}$, the equations convert to:

$$\frac{\partial S_{11}}{\partial M_{pq}} = -4jR_1T_{pq}[A^{-1}]_{1p}[A^{-1}]_{q1} \tag{3.76}$$

$$\frac{\partial S_{21}}{\partial M_{pq}} = 2j\sqrt{R_1R_2}T_{pq}([A^{-1}]_{Np}[A^{-1}]_{q1} + [A^{-1}]_{Nq}[A^{-1}]_{p1}) \tag{3.77}$$

where the $M_{p,q}$ are the off-diagonal coefficients of the coupling matrix.

For a symmetric coupling matrix, the off-diagonal coefficients obtain twice not the same as the diagonal coefficients that can be obtained just once [76],[78]. Thus, the adaptation of the above equations with the respect to the diagonal coefficients can be made by just setting *p*=*q* and dividing by 2.

$$\frac{\partial S_{11}}{\partial M_{pp}} = -2jR_1T_{pp}[A^{-1}]_{1p}[A^{-1}]_{p1} \tag{3.78}$$

$$\frac{\partial S_{21}}{\partial M_{pp}} = 2j\sqrt{R_1R_2}T_{pp}([A^{-1}]_{Np}[A^{-1}]_{p1}) \tag{3.79}$$

The values of the termination resistances R_1 and R_2 can be calculated both from theory and optimization [76], [78]. These values are obtained in the same way as the coupling coefficients. The computation of gradients of the reflection and transmission coefficients (S_{11} and S_{21}) with respect to the source resistance R_1 following the aforementioned discussion contributes to the final results as:

$$\frac{\partial S_{11}}{\partial R_1} = 2j[A^{-1}]_{11} + 2R_1([A^{-1}]_{11}[A^{-1}]_{11} + r[A^{-1}]_{N1}[A^{-1}]_{N1}) \tag{3.80}$$

$$\frac{\partial S_{21}}{\partial R_1} = -2j\sqrt{r}[A^{-1}]_{N1} + 2R_1\sqrt{r}([A^{-1}]_{N1}[A^{-1}]_{11} + r[A^{-1}]_{NN}[A^{-1}]_{N1}) \tag{3.81}$$

where $r = \frac{R_2}{R_1}$ is the ration of termination resistors. Note that the derivation demonstrated here is more general and can be even employed in cases where the adjoint network method no longer applicable [78].

3.7.2 Example of usage: trisection bandpass filter with gradient based method

As an application of the method for the determination of the resonators coupling matrix using the gradient based optimization, a trisection bandpass filter structure from the literature [1] is held in this section.

The filter has a center frequency at 905 MHz, bandwidth of pass-band 40 MHz, the return loss in the pass-band < 20 dB and the rejection > 20 dB for frequencies ≥ 950 MHz. The generalized coupling matrix and the scaled external quality factors calculated using the gradient based optimization method are:

$$[m] = \begin{bmatrix} -1.3232 & 1.0746 & -0.0464 \\ 1.0746 & 1.0602 & 1.0746 \\ -0.0464 & 1.0746 & -1.3232 \end{bmatrix}$$

$$qe1 = qe2 = 0.8755$$

To compute the spacing convening for each elements of the coupling matrix we used the iteration method [1].

$$s12 = 0.7,\ s13 = 1.8$$

Fig. 3.33.a shows the layout of the designed microstrip filter with the dimensions on a substrate having a relative dielectric constant of 10.8 and a thickness of 1.27 mm.

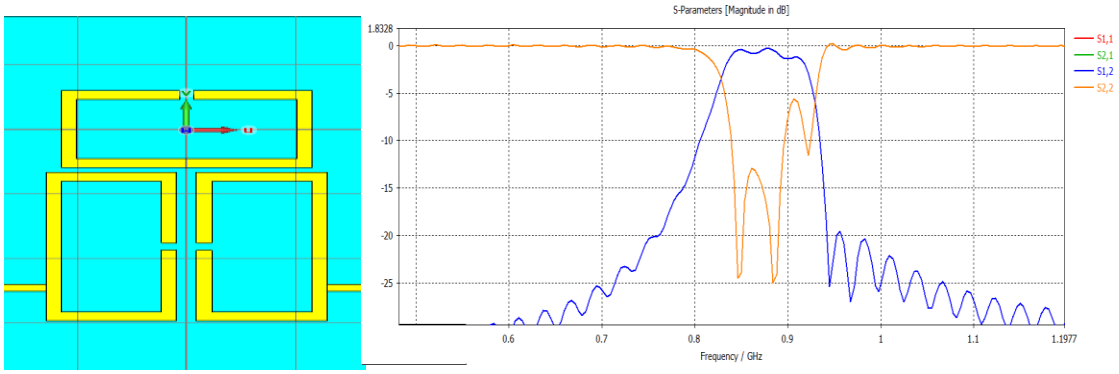

Fig 3.31 Layout of the micros-trip trisection filter designed to have a higher selectivity on high side of the pass-band. (b) Simulated performance of the filter

The Fig. 3.33.b shows the simulated results of the filter using MW CST software. As it shows from the figure, a finite transmission zero appears on the upper side of the passband leads to a higher selectivity on this side of the passband. Due to the losses level of the conductor, the insertion loss level in the transmission band is about -1.15 dB.

3.8 Genetic Algorithm method

As it is been mentioned before, the results of the simulation obtained by the mathematical methods approached our objectives, since they do not take into account a lot of physical implementation constraints. Thus, the use of an optimization technique will allow us to modify the dimensions of the filter so as to correct its frequency response, where the dimensions obtained by the synthesis will be introduced as initial dimensions in the optimization program to reduce the computation time taking by the simulation software CST.

Genetic algorithms are a met heuristic optimization algorithms inspired by Darwinian theory of evolution and the mechanisms of evolution of nature: crossovers, mutations, selections. John Holland's first work on adaptive systems was in 1975 [79]. David Goldberg's work has largely contributed to popularizing them [80].

3.8.1 Fundaments of GA

Genetic algorithms work on a population made up of all different individuals, who are potential solutions to the problem to be solved. The evolutionary process takes place through two mechanisms: natural selection and reproduction. Natural selection means that only the individuals best suited to their environment survive and reproduce. Reproduction allows mixing, recombination of parental genes in their descendants, and elimination of a tiny fraction of those who have been shown to be useless or disastrous. Random mutations occur to a lesser extent during the duplication of a chromosome.

Genetic programming is based on: A chromosomal representation of the solutions of the problem, a method to generate an initial population of solutions, an evaluation function that plays the role of the environment and classifies the solutions according to their aptitudes. The genetic operators define the way in which the characteristics of the parents are transmitted to the descendants (crossing and mutation).

The Fig. 3.34 explains the operation scheme that the algorithm genetics follows for each iteration.

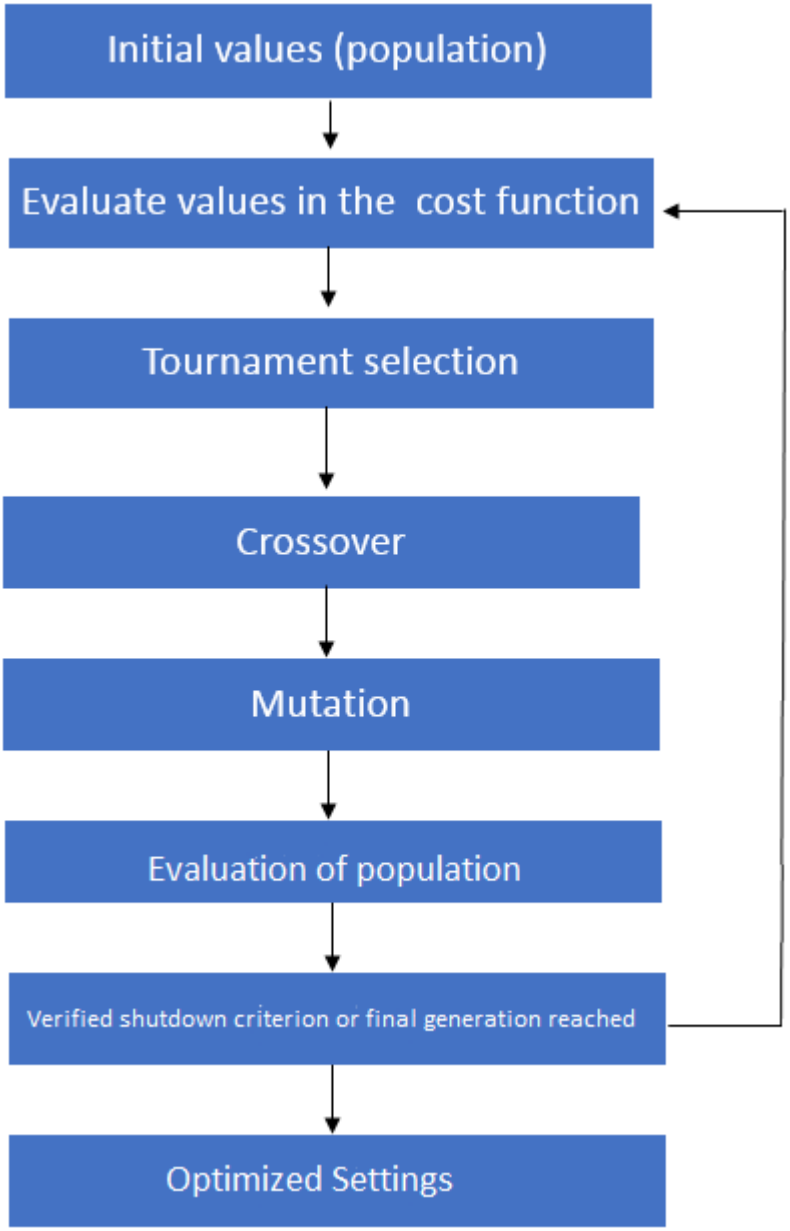

Fig 3.32 Flow chart of the algorithm genetics use

Generation of the initial population: The choice of the initial population of individuals strongly conditions the speed of the algorithm. If the position of the optimum in the state space is completely unknown, it is natural to randomly generate individuals by making uniform draws in each domain associated with the components of state space. If prior information on the problem is available,

individuals are generated in a particular sub-domain in order to accelerate convergence.

Evaluate values for cost function: The genetic operation for the cost function defines the way in which binary chains recombine during the reproductive phase. It allows also the creation of new channels.

Tournament selection: The selection phase specifies the individuals in the population who must survive. The method called the lottery wheel, gives each individual a probability of survival proportional to their adaptation in the population

Crossover: Directly inspired by biological crossing, either two binary chains parents juxtaposed, the crossover is the operation of cutting and exchanging parts from the parents at a randomly point, and give birth to two new binary chains named the descendants [81]. This operation symbolizes in the genetic algorithm reproduction. It should also be noted that only part of the population participates in this operation.

Mutation: Is a random change of one or more bits in the chain encoding the individual. The crossover operator becomes less efficient as the program evolves, as individuals become similar. This is when the phenomenon of mutation becomes important: these mutations generally do not create better solutions to the problem, but they avoid the establishment of uniform populations unable to evolve.

Previously it has briefly shown how the algorithm genetics works. Now we can stop and explain every step of the operation. First the initial population is initialized. This initial population is formed by vectors of n components where each component of the vector is one of the variables to be optimized by the genetic algorithm. Every *n* component is called individuals of the population. Once the genetic algorithm defines the initial population, the algorithm begins to evaluate individual in the cost function defined by the user. An iteration ends when all the individuals in a population are evaluated and therefore, they have been associated with a cost value. Each iteration is also called generation and

therefore, the user can define both the number of individuals that make up a population and the maximum number of generations to be carried out. Now the genetic algorithm passes to the selection phase.

In this step the algorithm chooses the best individuals in the population, usually based on his cost value associated with the objective that these individuals are modified and generate new population of individuals that can achieve better results. In this way, the algorithm replaces in each generation the previous population with a new one. The next phase is the recombination, or the crossover of the individuals chosen in the selection phase, is aimed at generating new population of individuals through the best individuals of the previous generation. Finally, there is the mutation phase. The objective of this phase is to provide a mechanism to prevent the genetic algorithm from being trapped in local solutions of the cost function. For this, a modification or permutation with a probability of predefined mutation by the user of the values of the components that form the individuals of the new generation. The genetic algorithm ends up depending on the stop criteria chosen by the user.

Now to implement the optimization program, we will use MATLAB, which has an intuitive programming language with libraries that implement a wide range of functions related to the genetic algorithms. Specifically, the MATLAB functions GAoptmiset and GA, which have a large number of input parameters to adjust the genetic algorithm to be executed. On the other hand, there is the CST STUDIO SUITE software that will be in charge of simulating the design of the piece that forms the target array and providing the results in the form of scattering parameters with which the algorithm Genetic will evaluate its cost function.

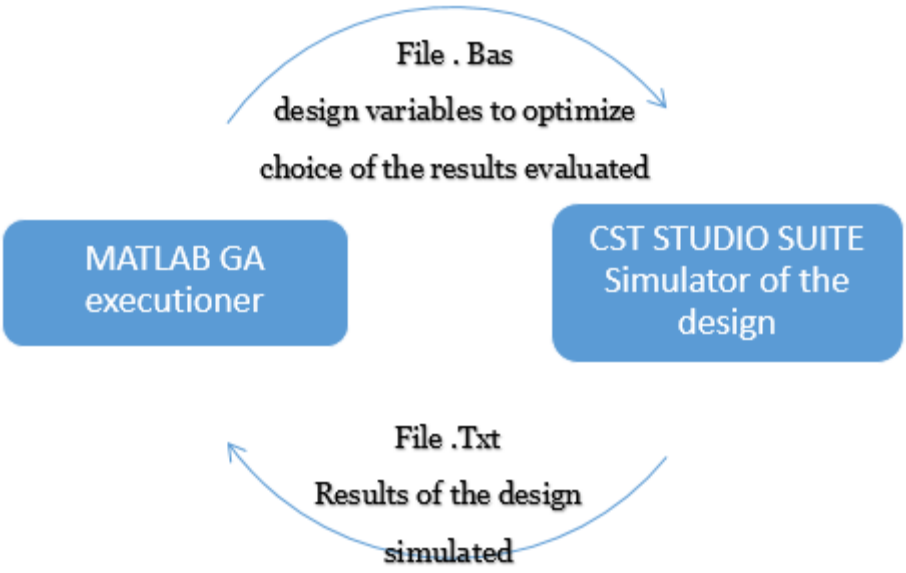

Fig 3.33 The relation between two software used in the optimization process

In Fig 3.35 it can be seen in a simple way what are the files that are generated and read by the two programs. The part that MATLAB is in charge of is directing the optimization process, that is, determining the ranges or search space of the variables to be optimized in each individual, setting the number of individuals per generation, setting the maximum number of generations, stop optimization when the cost function remains constant over a large number of generations, generate the new population in each generation, provide the values of each of the optimization variables and read/evaluate the results provided by CST in each simulation in the cost function.

3.9 Graphene-based structures for filters

The graphene is the thinnest material known, is an extremely diverse two-dimensional material, one-atom-thick layer of carbon in a hexagonal lattice. It is derived from graphite and was isolated by Andre Geim and Konstantin Novoselov [82], [83] in 2004. Since then, Researchers are still constantly investigating

more about new properties and possible applications of the graphene including (batteries, computer chips, water filters, etc.).

It earns the title of the material that could change our world due to its crystal honeycomb structure that gives it unique physical properties, it is incredibly strong that is about 200 times stronger than steel and its very high conductivity of heat and electricity. it has also been announced as one of the potential replacements for silicon although this quality remains to be demonstrated. However, the interest of the scientific community in graphene and by extension in associated two-dimensional materials cannot be denied.

3.9.1 Electronic Structure of the graphene

The carbon atom is the sixth element of the periodic table; therefore, it has 6 protons constitute its nucleus (positive charge). Around the nucleus orbit electrons (negative charges in equal number of positive charges) which are distributed according to electronic orbitals. The configuration of orbitals and their reconfiguration in the presence of other elements play a key role in the chemical and electrical properties of materials. In this section, we will detail the internal structure of carbon and the mechanisms of reorganization of its orbitals which are at the origin of the plane crystal of graphene.

3.9.2 Electronic carbon configuration

The quantum physics defines the elementary particles, such as, the electron haves a wave-particle duality, means the electrons are not punctual and localizable objects. Their movements are governed by Schrödinger's second degree linear differential equation [84]. It is this equation which determines the $\Psi(\vec{\Gamma},t)$ wave function of the electron around the nucleus:

$$i\hbar\frac{\partial}{\partial t}\left(\Psi_{n\mathrm{Im}}(\vec{\Gamma},t)\right)=\left[-\frac{\hbar^2}{2m^*}\nabla^2+V(\vec{\Gamma})\right]\Psi_{n\mathrm{Im}}(\vec{\Gamma},t) \qquad (3.82)$$

where $\Psi_{n\mathrm{lm}}(\vec{\Gamma},t)$ is the wave function, $m^*$is the effective mass that replaces the mass of the electron in a crystal, $V(\vec{\Gamma})$ is the potential confinement energy and $\hbar$ is the reduced Planck constant ($\hbar = \frac{h}{2\Pi}$).

Solving the wave function equation determines the probability of the electron being present in a defined region of space. This region of space where the probability of finding the electron is greater than 95% is called an orbital.

The Fig. 3.36 shows the graphical representations of the different possible orbitals.

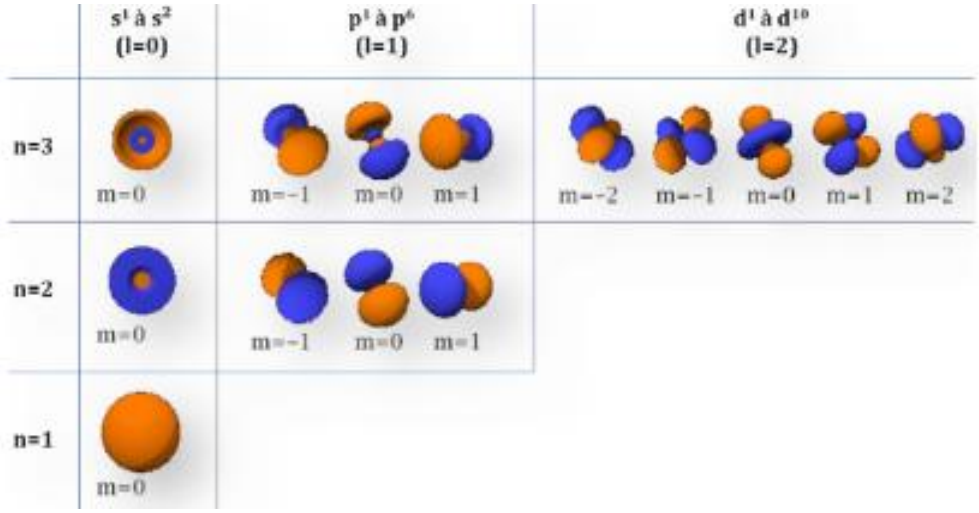

Fig 3.34 different graphic representation of atomic orbitals

where *n, l, m* and *s* are quantic numbers and defined by:

- *n* determines the electron layer and the energy level of the electron around the nucleus.
- *l* defines the symmetry of the orbital.
- *m* describes the spatial orientation of an orbital.
- *s* is the spin parameter.

3.9.3 Crystal structure

The hexagonal honeycomb structure of graphene can be described as the translation of a Bravais network only if we start from two carbon atoms. Indeed,

in the case of graphene, two neighbouring atoms A and B are not fully equivalent as it shows in Fig. 3.37 because they do not see exactly the same environment and the direction of their spin is antiparallel [85], [86]. To obtain such a network in graphene, it is therefore necessary to define the mesh of this honeycomb as consisting of two triangular Bravais sub-networks centered on two different atoms A and B [87]. The translation vectors $\overrightarrow{a_1}$, $\overrightarrow{a_2}$ which link two identical carbon atoms A or B, are given by [86]:

$$\overrightarrow{a_1} = \frac{\delta}{2}\begin{pmatrix} 3 \\ \sqrt{3} \\ 0 \end{pmatrix} \text{ and } \overrightarrow{a_1} = \frac{\delta}{2}\begin{pmatrix} 3 \\ -\sqrt{3} \\ 0 \end{pmatrix} \tag{3.83}$$

where δ the distance between two neighbouring carbon atoms and is equal to $1.42\,\text{Å}$.

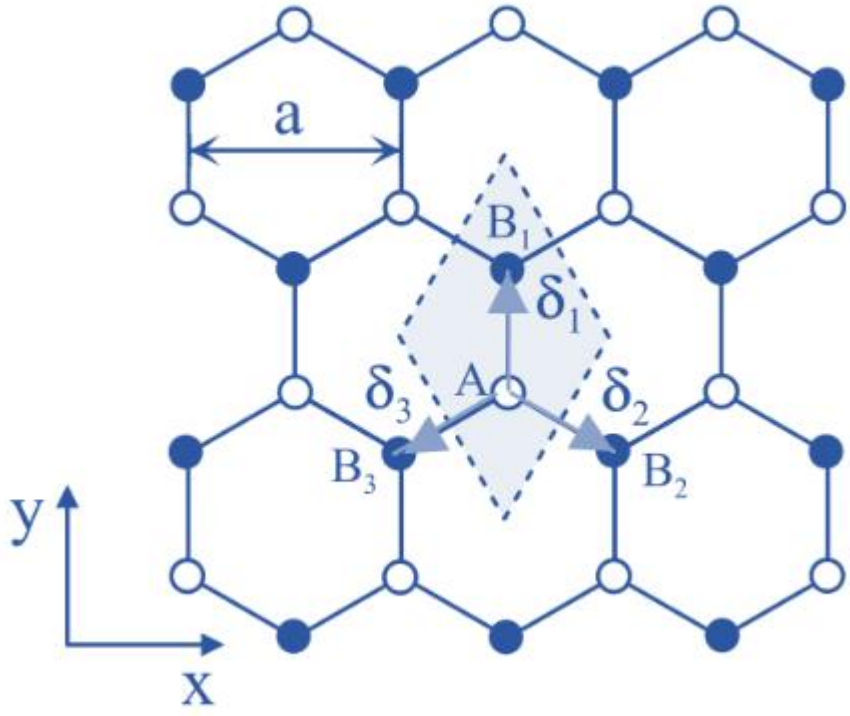

Fig 3.35 Elementary mesh in the real Bravais sub-network of a honeycomb crystal structure 'graphene'

3.9.4 Electrical properties of the graphene

To understand the transport properties in graphene it would be necessary to understand how this 2D electron gas interacts with a crystalline environment made up of an infinity of atoms. In Bloch's theorem, it is possible to describe the standing waves Ψ of the electron of a continuous medium described in equation (3.82), in the form of other waves $\Psi_{\vec{k}}(\vec{\Gamma})$ in vector space $\vec{k}$. These waves called Bloch waves, they are the product of a wave plane function $u_{\vec{k}}(\vec{\Gamma})$ which has the periodicity of the Bravais network, and a phase term $e^{i\vec{k}\vec{\Gamma}}$ [88], [89]:

$$\Psi_{\vec{k}}(\vec{\Gamma}) = e^{i\vec{k}\vec{\Gamma}}.u_{\vec{k}}(\vec{\Gamma}) \tag{3.83}$$

3.9.4.1 Energy band diagram

Just as within an atom several electrons cannot have the same energy, in solid state physics, the electrons of the whole crystal can only take values within very precise energy intervals [89]. Indeed, as the bonds between the atoms, there is a lifting of successive degeneracies of the bond states which create energy bands and forbidden bands as it shows in Fig. 3.38.

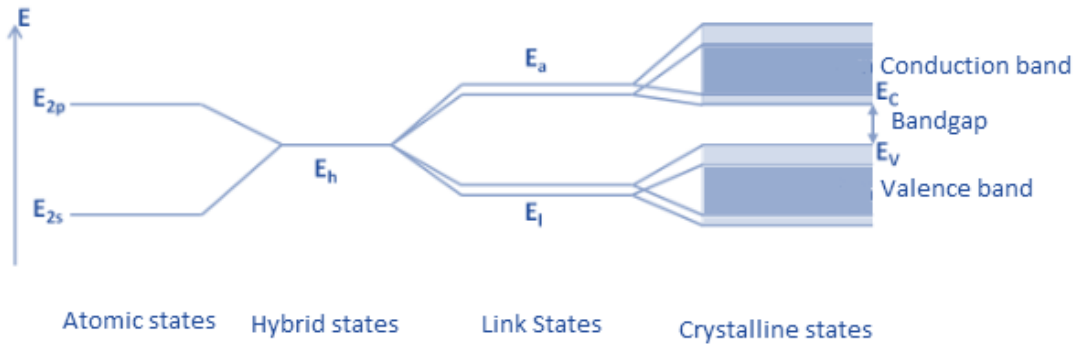

Fig 3.36 Energy band diagram in a crystal structure

It is possible to model these band structures by plotting the limit energy levels allowed by the material in the reciprocal network. The filling of these electrons in the different bands of the material follows the Fermi-Dirac distribution [89]. At the temperature $T = 0\,K$, the highest level of E_F energy

occupied by electrons is called Fermi energy and represents the chemical potential of the electron gas. It is it positioning in relation to the band diagram which explains the diversity of the electrical properties of materials and their conductive nature (E_F in a permitted band), insulator or semiconductor (E_F in a prohibited band). The density of electronic states (DOS) corresponds to the number of electronic states having a given energy of given vector $\vec{k}$. The Fermi surface is therefore the surface delimited by the set of electrons having the energy E_F of vector $\overrightarrow{k_F}$.

3.9.4.2 Dispersion relationship and Tight binding method

Bloch's theorem therefore gives solutions independent of time $H\Psi_{\vec{k}}(\vec{\Gamma}) = E(\vec{k}).\Psi_{\vec{k}}(\vec{\Gamma})$ of Schrödinger's equation (3.82) by replacing the moment $\frac{\vec{p}}{\hbar} = -i\vec{\nabla}$ of the electron in the Hamiltonian *H* with a new noted pseudo-moment $\vec{k}$. This relationship between the energy *E* and the new vector pseudo moment $\vec{k}$, called dispersion, is generally quadratic, means: $E \approx \frac{\hbar k^2}{2m^*}$.

The so-called Tight Binding method assumes that the electron of a π bond can only jump to one of its three closest neighbors [86]. This method, applied for the first time to the case of graphene by P.R. Wallace in 1946 [90], gives an eigenvalue of the Hamiltonian as a function of the wave vector$\vec{k}$:

$$E_+(\vec{k}) = +\sqrt{3 + f(k)} - t'f(k) \text{ and } E_-(\vec{k}) = -\sqrt{3 + f(k)} - t'f(k) \quad (3.84)$$

where $f(k) = 2\,cos(\sqrt{3}k_x a) + 4\,cos(\frac{\sqrt{3}}{2}k_x a)cos(\frac{3}{2}k_y a)$

The term $t \approx$ *2.7 eV* corresponds to the energy required for a π electron to make a jump to a nearest neighbouring site [86] (from A to B or from B to A) and $t' \approx$= *0.1 eV*, often neglected, is the energy to jump to a second neighbour [91]. As for the positive and the negative indexes, the positive index corresponds to the possible solution the boundary bands of conduction band π^* of the graphene structure, are completely empty of electrons, and the negative index represents valence band π of the graphene structure, is full of electrons of the

band structure as it is illustrated in Fig. 3.39.

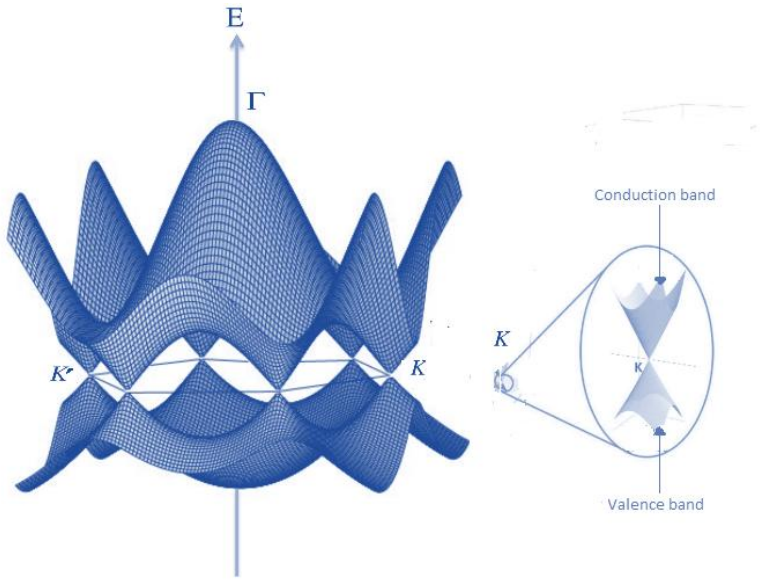

Fig 3.37 Graphical representation of dispersion E as a function of the k_x and k_y wave vectors with its relationship in the vicinity of points K and K' [86]

This solution admits six particular values in the zone where the two dispersion cases are equal to 0, and with differentiation of two series of electronic valleys centered around the points denoted *K* and *K'*. Around these points, the conduction and valence bands form two unequal cones which touch punctually at the Fermi level [86]. Graphene can therefore be likened to a semiconductor without gap and, the Fermi surface being punctual, the electronic state density is also zero [92]. Thus, the graphene material may be classified as a semi-metallic material.

The most interesting in the graphene dispersion relation is that around these points, at Fermi level, the dispersion is no longer quadratic but linear, therefore can be expressed so that *E* it is proportional to the moment $|p| = \hbar|k|$. In reality, the dispersion equation at the level of the cone for vectors k very close

to *K* and *K'*, $|k| << \frac{2\Pi}{a}$ and can be approximated by an expansion to order 1 in the form [90]:

$$E_+(\vec{k}) = +\hbar v_F|k| \text{ and } E_-(\vec{k}) = -\hbar v_F|k| \quad (3.85)$$

Where v_F is Fermi's speed and equal $\frac{\sqrt{3}}{2}\frac{a}{\hbar}t \approx 10^6 m.s^{-1}$.

Such a solution is closer to Dirac's relativistic equation for massless particles than to Schrödinger's equation (3.82) [93] [94] [95]:

$$E_+ = +\sqrt{p^2c^{*2}+m^{*2}c^{*2}} \text{ and } E_- = -\sqrt{p^2c^{*2}+m^{*2}c^{*2}} \quad (3.86)$$

Assuming m^*, the equation (3.86) can be re-written as $E = pc^*$, where $c^* = v_F$ is the speed of effective light analogous to the Fermi speed.

Therefore, there is a very strong analogy between the electrons of graphene and the massless fermions formulated by the 2D relativistic equation of Dirac, so that the charge carriers of graphene can be considered as "pseudo-relativistic" particles [96]. The points K and K', where the Fermi level is exposed, are called Dirac points, and the cone of the dispersion relation is called Dirac cone.

3.9.4.3 Mobility and conductivity

The electrical conductivity σ (expressed in $S.m^{-1}$) of a material (or inverse ρ of the resistivity in Ω.m) characterizes its ability to let an electric current pass. This current results from the displacement of electrons (negative charges) and holes (positive charges) under the action of an electric field so that [88]: $\sigma = ne\mu_n + pe\mu_P$, where n is the density of negative charges, p the density of positive charges (cm^{-2}), $e = 1.602 * 10^{-19}$ C is the elementary charge and μ is the mobility of the different charge carriers.

By varying the position of the Fermi level on either side of the Dirac cone (by the effect of an electric field applied and controlled by a noted potential difference), a current regime is obtained which is dominated by the electrons, or dominated by the holes as it is shown in Fig. 3.40 [97]. This ambipolar effect makes it possible to rapidly increase the conductivity of graphene by modifying the carrier density of one or other of its charges.

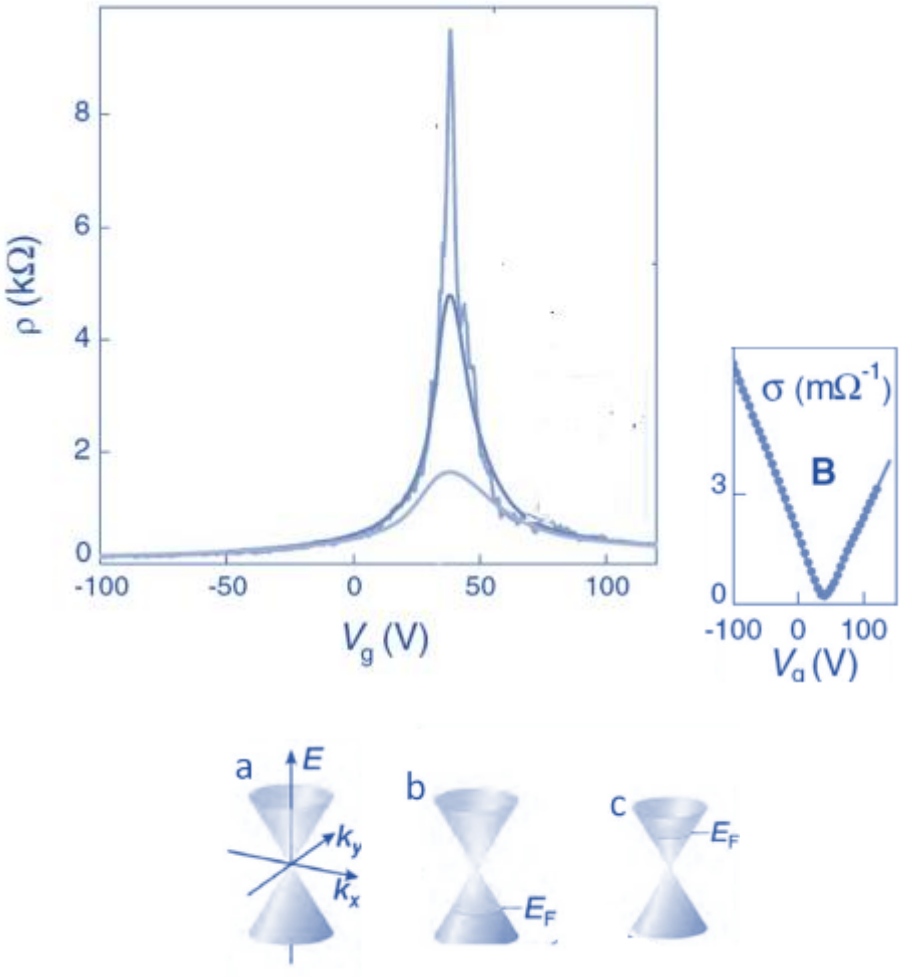

Fig 3.38 Ambipolar effect (resistivity and conductivity as a function of a gate voltage Vg) of a graphene monolayer around the Dirac point at 5K, 70K, 300K. For EF = 0 the carrier density is zero (a). For Vg <0 the graphene is of type p-conduction of holes- (b). For Vg> 0 graphene is said to be of type n-conduction dominated by electrons - (c). Here the mobility measured is μ = 5000 cm². (V.s) -1 [97], [98]

One of the peculiarities of graphene is that despite a zero density of states $V_g = 0V$ around the Fermi level, the conductivity σ remains at all times greater than the minimum quantum of conductivity $\sigma_{min} = \frac{2e^2}{\hbar}$ [99].

The excellent regularity of the crystal structure of graphene, due to the tight covalent bonding between the orbitals, allows the electrons to have a very important mean free path, sometimes bordering the micrometer. Due to this

quasi-ballistic transport in graphene, very high mobilities have been reported. In 2008, a mobility of $\mu = 200000\ cm^2.(V.s)^{-1}$ for a density of $n = 2.10^{11} Cm^{-2}$was obtained on a sheet of exfoliated graphene [100]. This record mobility is much higher than that of InSb, then the best known semiconductor with $\mu = 80000\ cm^2.(V.s)^{-1}$ or other materials conventionally used in the semiconductor industry as, Si or GaAs. In practice, these results are very different according to graphene growth techniques and it often results in much more modest mobilities.

3.9.5 Mechanical and Thermal properties of the graphene

The mechanical properties of a suspended graphene sheet were measured by Lee et al. [101] by nano-indentation using an atomic force microscope. This work evaluates the Young's modulus of graphene at 1.0 TPa, about 5 times that of steel. The tensile strength of graphene is evaluated at 130 GPa.

The thermal properties of suspended graphene were studied using a device using Raman spectroscopy. By varying the power of the laser, the position of the bandgap of graphene is measured. It has been established that the position of the bandgap of graphene varies linearly as a function of temperature [102]. Thus, knowing the evolution of the graphene temperature as a function of the power provided by the laser, we obtain the value of the thermal conductivity. The thermal conductivity of graphene is high. Monolayer exfoliated graphene has a thermal conductivity of 5300 *W/mK* [102]. That of a single-layer graphene obtained by CVD on copper is around 2500 *W/mK* [103]. In comparison, the thermal conductivity of an individual single-walled carbon nanotube is around 3500 *W/mK* [104] and around 400 *W/mK* for a bundle of nanotubes [105].

3.9.6 Some notable applications

In this section, we will not make an exhaustive statement of the various fields of applications. Indeed, graphene has great potential for applications, particularly in the field of electronics, energy storage and composite materials. Below are explained two application areas that are promising to date.

Transistors: The exceptional performance of graphene, in particular with regard to electronic conductivity, makes it, at first sight, a natural competitor to succeed silicon in the field of electronic components. However, to date, the level of technological maturity is still far from being reached. A lot of progress is being made in the design of a high-frequency graphene transistor capable of reaching frequencies of 26 GHz [106], 100GHz [107] and 300 GHz [108]. However, graphene has a zero bandgap, preventing the channel of graphene transistors from being completely closed in the off state. Several approaches are envisaged to open a bandgap in graphene. It is possible to structure graphene into fine bands, called graphene nano-ribbons, which below 100 nm in width have a non-zero forbidden band [109].

In addition, the energy of the band gap created can be controlled as it increases when the width of the nano-ribbon decreases. Another possibility is to use bi-layer graphene which has a bandgap, the energy of which is controllable, when applying an electric field [110], [111]. Finally, applying a uniaxial constraint to graphene also makes it possible to open a forbidden band, the energy of which depends on the stress level [112]. The solutions proposed by these three approaches are complex to implement, especially when considering bandgap energy greater than 350 *meV*. In addition, the production of electronic component using graphene requires a homogeneous graphene and of very good structural quality which is not achieved in the optics of mass production.

Transparent electrodes: In the near future, graphene could compete with ITO (indium tin oxide) in the development of transparent electrodes found in the design of screens and photovoltaic cells. ITO, the current standard, is an expensive and relatively fragile material. Concerning the performance of transparent electrodes, the minimum desired transmittance value is set at 90% which corresponds to approximately four graphene sheets, each sheet absorbing 2.3% of the light [113]. In addition, the sheet strength decreasing with the number of layers of graphene, the use of graphene from two to four layers is quite satisfactory. Since the realization of electrodes does not require strictly monolayer graphene and perfect structural quality, this application is one of the

most conceivable in the near future. Finally, the flexibility of graphene makes it possible to design flexible transparent electrodes [114], [115].

3.9.7 The chosen substrate for the pin structures

Due to all these fascinating physical and electrical properties that the graphene has it, such as, its higher carrier mobility or even its perfect optical transparency, it was not that strange our desire to use it as a main material for our tuneable waveguide band pass filter. Thus, the idea is to introduce small rectangular pins of P-type doped silicon semiconductor covered with a very thin skin layer of oxide silicon and 2-D layer of Graphene, in other words the graphene layer is on a substrate of $S_iO_2 \,/\, S_i$.

The choice of an insulator such as $S_iO_2 \,/\, S_i$ as substrate material comes after a profound research process has been made by several researchers, since, a lot of approaches for graphene production have been reported, such as, the chemical vapor deposit (CVD), mechanical exfoliation from graphite and epitaxial growth on crystalline substrate.

There are many obstacles affect the choice of the substrate material or the preferable method to use, for instance, the production process of the graphene onto a Si substrate using the CVD method, the wet-transfer step of the as-grown graphene onto the pre-defined substrate in the production process, causes a degradation of the graphene due to the incompatibility of the transfer process with the Si-processing technologies. So, as a solution to that the insulator materials such as $S_iO_2 \,/\, S_i$ and Al_2O_3, it start to take a lot of attention from the researchers. The schematic diagrams of the substrate using in this section are illustrated in the Fig. 3.41.

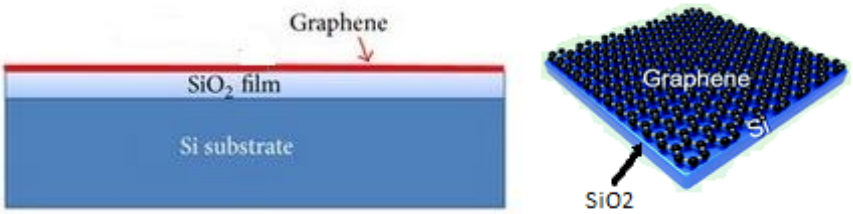

Fig 3.39 The schematic diagrams of a graphene layer grown on S_iO_2 / S_i

3.9.8 Folded graphene-based fourth-order filter

With the change of the electric tension applied on the graphene layer, comes the change of the resistance of the material, which offers the filter a the tuning of the center frequency or a tuning of the bandwidth or even both of them together in the same time, depends on the general pin structures used and the position of the pins into the filter structure. The filter used here is Chebyshev fourth-order waveguide BPFs with the following specifications.

1) a center frequency of 90 GHz
2) 3 dB fractional bandwidth of 8.66 %
3) return loss better 15 dB
4) insertion loss as low as possible
5) high out-of-band rejection with two TZs.

The resonators coupling matrix of the filter deign here is the same got for the microstrip bandpass Filter (Table 8). The difference is in the method used for converting the matrix elements to the dimensions of the waveguide irises used to connect the resonators cavities of the filter.

The elements of the resonators coupling matrix show a negative coupling between resonator 1 and 4, which means, the existence of an electric cross-coupling in this filter. This negative coupling is implemented through a capacitive iris. The rest of coupling are positive and can be made by an inductive iris. The general filter design is composed of four $\boldsymbol{TE_{101}}$ mode waveguide cavities.

The resonators coupling matrix coefficients have been converted using the electromagnetic simulation method. The proximity of the two resonators or in other words the space between two resonators changes their resonant frequency, thus, revealing two peaks in the electromagnetic response. One corresponds to the even or electric resonance mode of frequency f_2 and the other to the odd or magnetic resonance mode of frequency f_1.

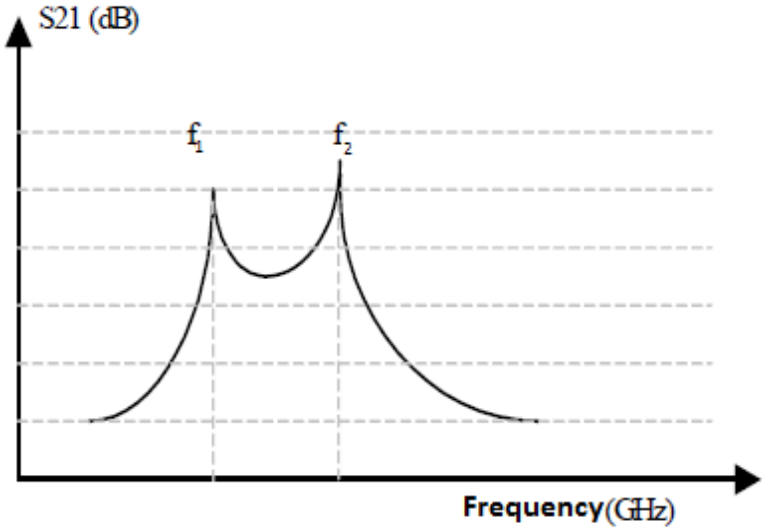

Fig 3.40 Response in transmission of a structure composed of two resonators

The Fig. 3.43 shows the variation of the electrical type coupling coefficient as a function of the length of the iris guide between the resonators 1 and 4, the length of the iris for an electric coupling elements k_{14}=*1,04* can be easily extracted from the graph and it is equal to 0.36 μm.

where

$$k_{ij} = \frac{M_{ij}}{FBW}$$

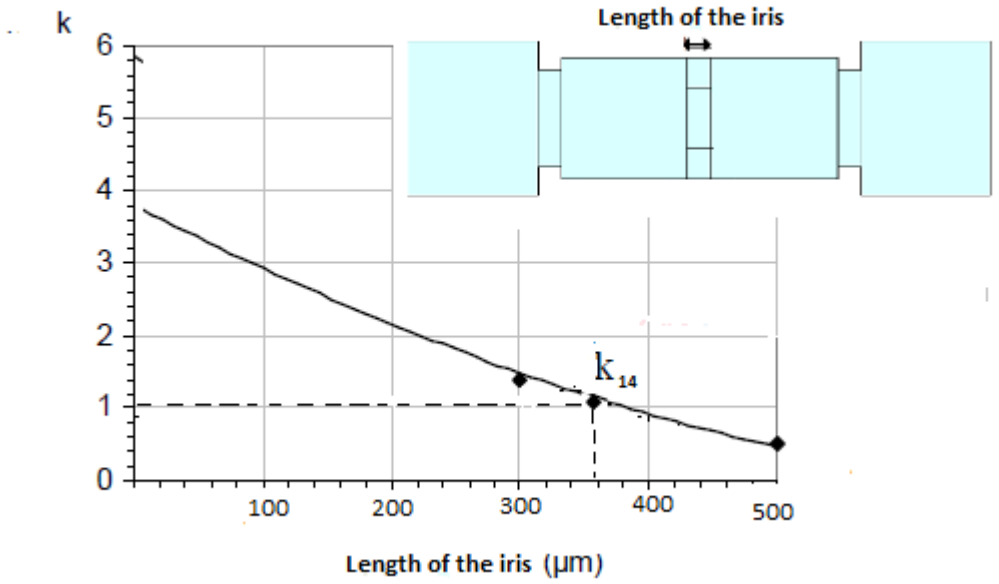

Fig 3.41 the Variation of the electrical coupling coefficient as a function of the length of the iris

The rest of the elements of the coupling matrix have been converted with same method. The general structure of the filter is shown in the fig 3.44.

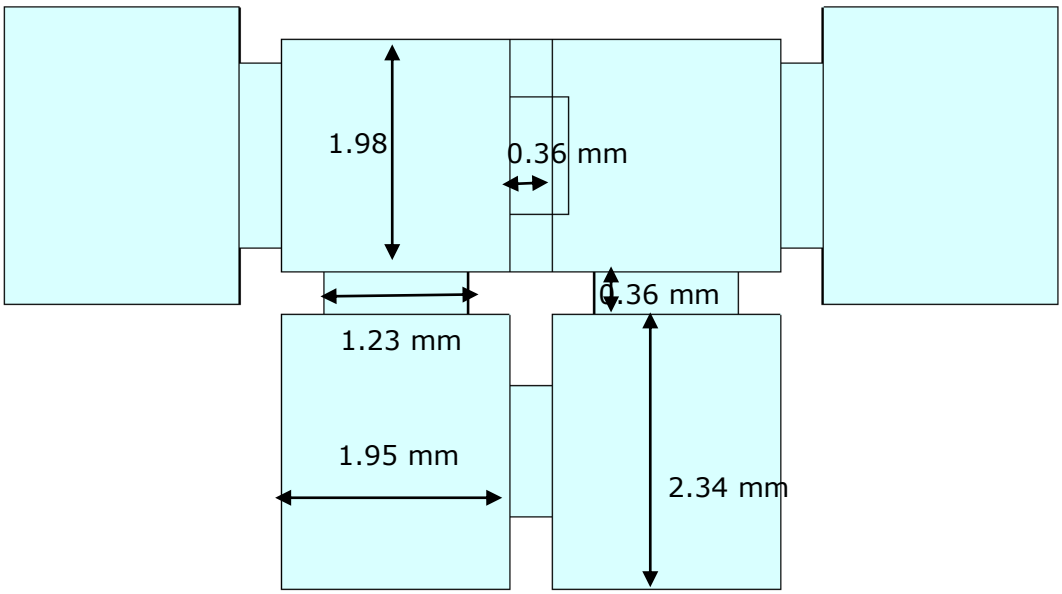

Fig 3.42 Top view of the W-band fourth-order waveguide filter

The simulation of the proposed filter has been through CST MWS. Fig. 3.45 shows the simulated S-parameters of the 90 GHz BPF in wide band between 75-115 GHz. The results show, a 3-dB fractional bandwidth about 8.6% from 86 GHz to 93.78 GHz, a return loss level better than 15 dB in the passband, an insertion loss level lower than 0.15 dB, and also there is a very high rejection due to the two transmission zeros in the stopband, also the simulation shows a peak value at 103 GHz caused by the higher-order modes.

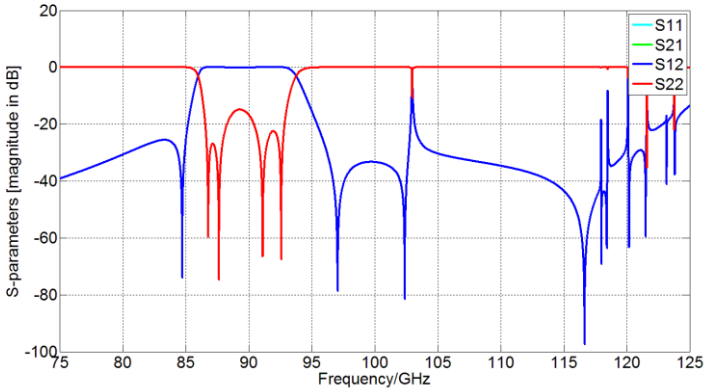

Fig 3.43 The S-parameter results of our proposed W-band waveguide filter.

3.9.9 Tunable band pass filter using graphene material

The main objective here is introducing rectangular pins of P-type doped silicon semiconductor covered with a very thin skin layer of oxide silicon and 2-D layer of Graphene into the structure of the filter, the change of the voltage applied of the graphene material changes the resistance of the graphene material which introduce a tuneable effect to the behaviour of the filter, it shows clearly in the S-parameters simulated.

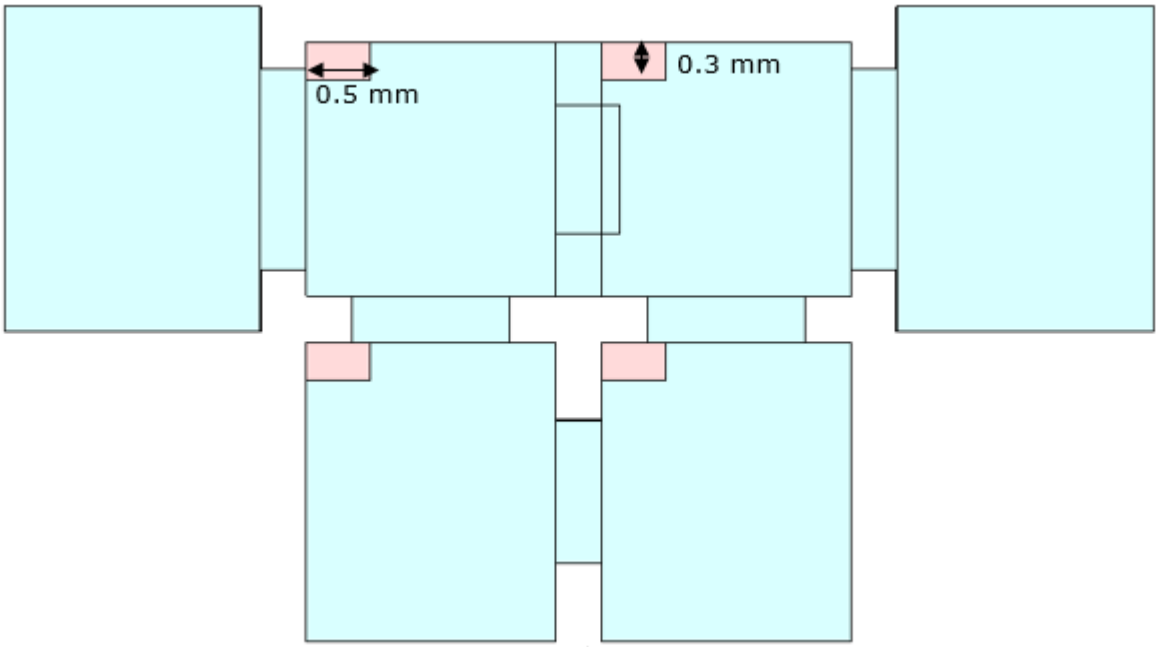

Fig 3.44 The input dimension and position of our proposed filter for optimization process

The initial values of the pins structure have been chosen based on the standard of the graphene structures used on the W-band electronic devices. Fig. 3.47 shows the initial results obtained of the electromagnetic simulation of the proposed filter. The good levels of the transmission and the reflection parameters represent a good starting point for the optimization process. The good choice of the starting point has a key role in the convergence of the cost function of the problem, in addition to the calculation time. The optimization program is based on algorithm genetics methodology with some major changes to make it adapt and fit the complexity of the topology and the technology of the filter proposed, it changes the dimensions and the positions of the pin structures separately and automatically, in order to find out the best results can be achieve, regarding the value of the cost function obtains in every iteration possible.

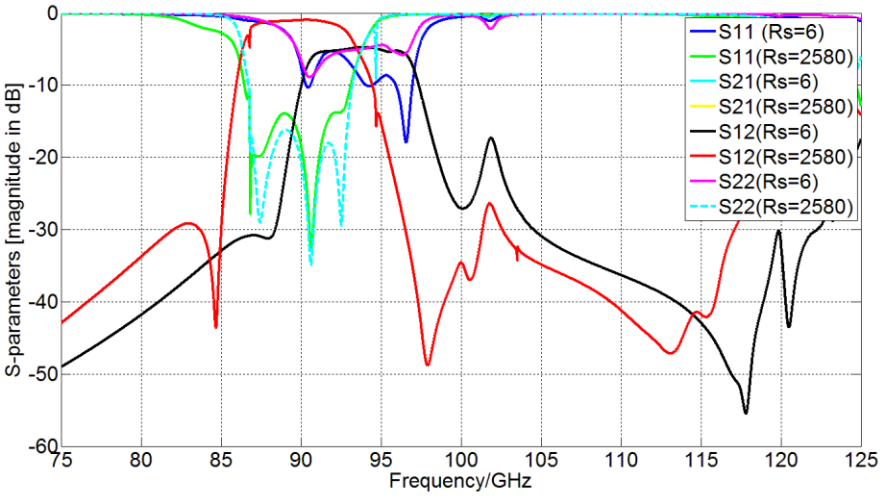

Fig 3.45 The first simulation results obtained of the proposed filter

Moreover, the introduction of the Constraint equations is mandatory. As they are the equations that control the limits of how big or small the dimensions of the pins can be regarding also to the position of the walls of the cavities and the arises. And also, control the fabrication limits, for instance, if the dimensions of the pins are too small, it will be impossible to manufacture. we noticed that the best first tries results come from positioning the pins near to the walls of the cavities structures.

After certain time of calculation, the optimization process found with the best positions and dimension of the pins. Fig. 3.48 shows the dimensions and the positions of the optimized structures.

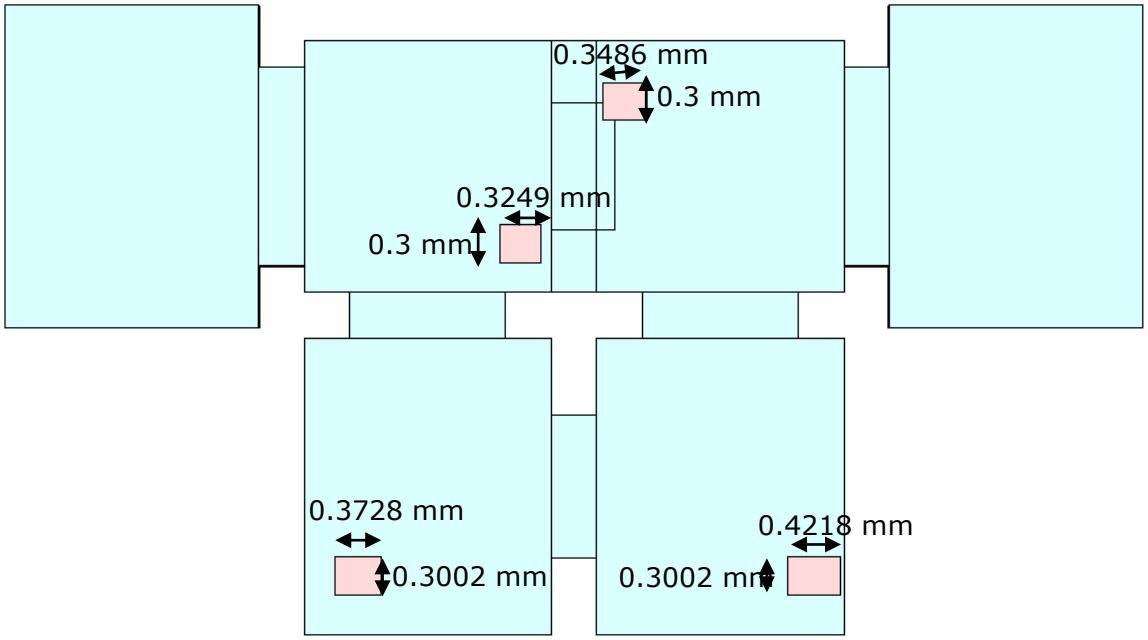

Fig 3.46 Optimized dimension and position of rectangular pins of graphene material

The Fig. 3.49 shows the Scattering parameters results of the structure after the optimization process. The results show the tuning of both the center frequency and the bandwidth in function of the modification of the voltage level, respectively, almost 5 Ghz and 1%.

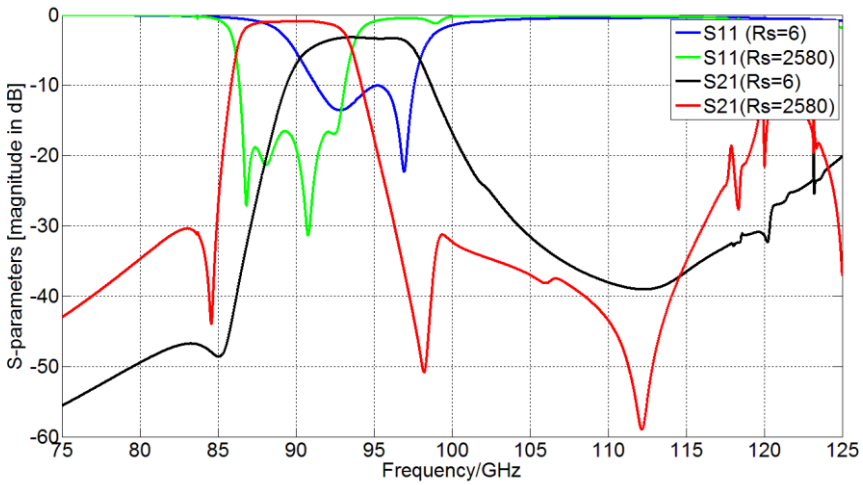

Fig 3.47 Optimized S-parameters results for both resistances of graphene material

The results are remaining acceptable. Both the return loss levels are below -10 dB and both the transmission loss levels are above -3dB. Also, the filter keeps a very high rejection out-band due to the existence of the transmission zeros, which they are creating a rejection loop below -30 dB in both sides of the stopbands.

3.10 Conclusion

The chapter summarizes the design and the fabrication of passband filter for different topologies and technologies. The investigation in Chapter 3 covers the common numerical methods used to calculate the coupling resonators matrix. First method and probably the most common in literature used for the numerical model of the inline passband filters is the Chebyshev low-pass filter method is displayed in detail in this unit. Moreover, the Polynomial method and the Rotation method are investigated to provide a metrology for the design process and then finishing with the famous gradient based optimization method, which it is basically the most general method to find the resonators coupling matrix elements for all the filtering and multiplexing structures.

The chapter highlights also two different methods on how the coupling matrix coefficients can be converted to geometrical values. The first method is more general and does not take into account the technology of the filter, due it, is based on the iteration electromagnetic simulation method. The second method investigated is more specific, it is based on exact mathematical equations for open loop models proposed by Jia-Sheng Hong, and Michael J. Lancaster for the planar technologies.

Chapter 3 begins introducing the methodologies use to determine the resonators coupling matrix elements, the choice of the specific topology was the key enabler of the investigation. Moreover, it helps in finding the appropriate method to calculate the resonators coupling matrix easily. After choosing a

technology adequate then, the calculation of the resonators coupling matrix comes, which leads always to the conversion step of the coupling elements to geometrical spacing values between the resonators if the planar technology. This is the case to the dimensions of the waveguide irises between the cavities if the volume technology.

Finally, the last part of the chapter is devoted to design and the optimization of a tunable bandpass filter. The rectangular pin structures responsible of the tuning behaviour, are made of the famous 2D carbonic material the graphene grown onto a SiO2/Si substrate. The optimization method used here was the genetic algorithm method. The need of a good starting point makes the first results obtained a good candidate to make the computing process efficient, the cost function converges easier and provide a lower processing time for the complex calculation. The MATLAB software is used to implement the optimization program, the reason for this choice is that this software provides high-performance language for technical computing plus is been the most productive computing environment for engineers and scientists makes the results provided by the genetic algorithms in this thesis reproducible. the second process of the genetic algorithm is made by using the CST STUDIO SUITE software, which is used to design and simulate the structures, and to provide the transition coefficient S popularly known also as the scattering parameters in regards to the frequency, those results are used after as input values to the algorithm Genetic in order to evaluate the cost function.

Chapter 4:

Electronically reconfigurable phase shifter

4.1 Introduction

The next part of this doctoral thesis is dedicated to the realization of a Ku band phase shifter to realize electronic phase shifting for radiation pattern configuration. It is necessary to exceed the signal as well in emission as in reception. The idea is to make a command to control the phase of the signal and obtain a misalignment of the main lobe of the radiation pattern of an antenna. This type of system makes it possible to limit the use of mechanical positioners.

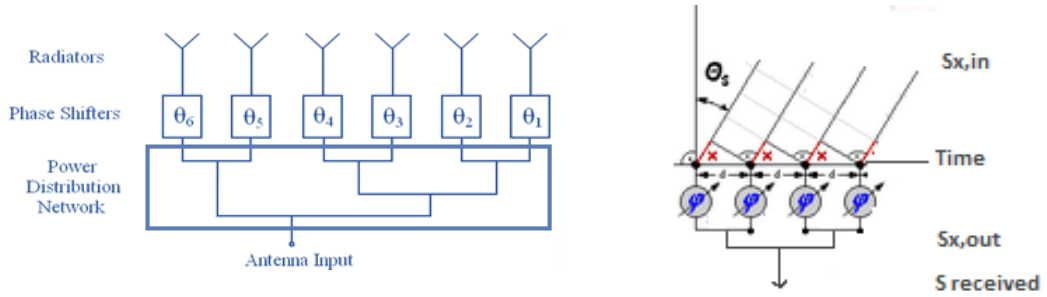

Fig 4.1 Diagram of a receiving electronic network antenna

The Fig. 4.1 shows that the phase shifters are regulated so as to obtain a phase gradient with respect to each other. The received signals $s_{i,in}$ arrive one after the other: $s_{1,in}$ to the last one $s_{4,in}$. The phase shifters make it possible to obtain all the signals at the output of the supply network at the instant t and thus to sum them so as to recover an amplified output signal.

The Electronic misalignment is given by a single formula:

$$\beta = -k \cdot d \cdot \sin\theta_0 \tag{4.1}$$

where β beta is the gradient of phase or the phase shifting between two neighbouring radiating elements, k is the wave number $k = \frac{2\pi}{\lambda}$, d is the distance between the network, expressed according to λ often to simplify calculations and θ_0 is angle of the phase shifting.

The phase shifter to be designed must fulfil the requirements to be used in Ku band: 12-18 GHz. The proposed system does not include frequency transposition and must be placed closer to the antenna to limit losses. It is important to limit the losses when one wishes to design a network antenna with a very strong gain, able to compete with a dish antenna for example (> 30 dBi). Moreover, the price of the network antenna increases when the frequency increases.

The proposed phase variation device consists of a phase shifter with varactor diode, these type of phase shifters is based on the principle of reflection. The input signal passes through a hybrid coupler and reflects on a variable optimized reflection load including a varactor diode. A quarter wave impedance transformer is added to adapt the hybrid coupler with the reflective circuit. The phase shifting is controlled by the polarization variations of the varactor diode.

4.2 Experimental approach

4.2.1 Example of usage: electronically reconfigurable phase shifter at 12 GHz

The phase shifter working strategy for reflect array structures signifies the use of reflective designs with same port acting as input and output port. the generic reflective phase shifter is a base of a 3-dB/90º hybrid coupler connected to two identical LC reflective circuits, act as its loads. The two important functionalities of the hybrid coupler in the phase shifter structure, is division and combination of the input and output signals. Since, the reflection loads are uni-port structures the phase of the reflected signal is extracted from their reflection coefficients [116], [117], [118], [119].

Due to the identic reflection loads, the provided phase shift by the system and by the reflective loads are equal, since, the two reflected signals are combined and cancelled in-phase respectively, at the output and the input ports of the system.

4.2.1.1 Phase Shifter Design and Performance for 12 GHz

The proposed phase shifter consists of a 3dB/90º hybrid coupler with a new prototype design of reflective RF circuit in each adjusting arm. The proposed design of each constituting element, together with the complete device design, must fulfil the matching and insertion losses requirements [116], [117].

4.2.1.1.1 Hybrid coupler (12GHz)

The hybrid coupler is the basic element of the tunable phase shifter. The coupler is printed over the upper side of a Neltec substrate (εr=2.17, h=0.508mm, tanδ=0.0002), where the lower side is a copper ground plane. The structure of the hybrid coupler model is presented in Fig. 4.2.a. The simulation results are provided in Fig. 4.2.b.

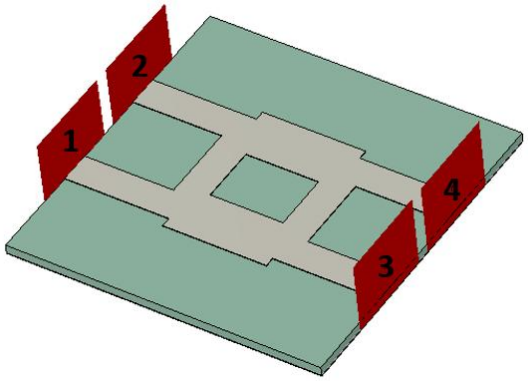

(a)

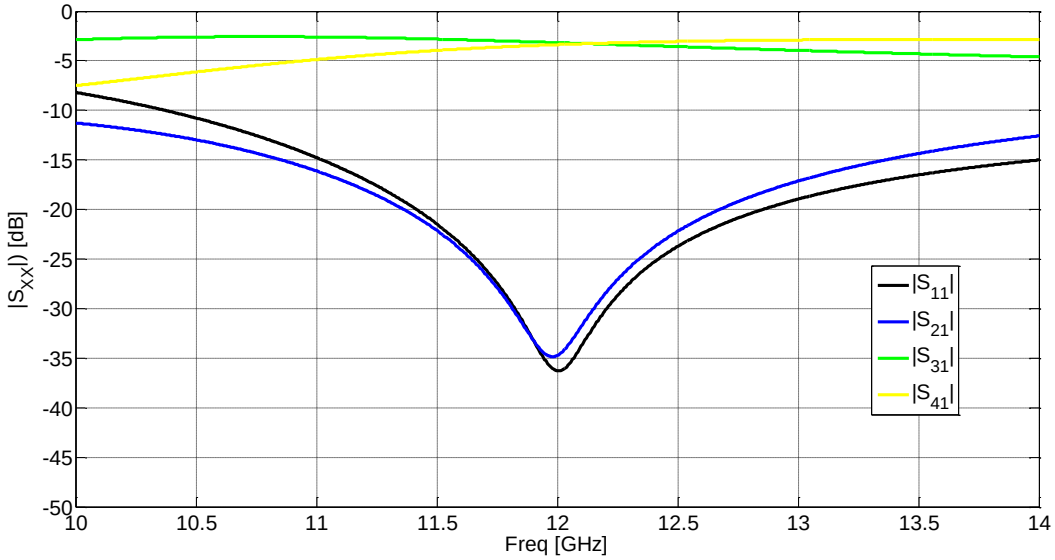

(b)

Fig 4.2 Coupling 3dB/90: (a) Design, (b) simulated S parameters of the design

4.2.1.1.2 Reflective RF circuit

The additional element of phase shifter is a reflective RF circuit formed by an equivalent LC circuit and two cascaded quarter-wave impedance transformers to change the port impedance value.

The LC circuits are varactors (MA46585) with variable capacity value C (0.13 pF to 2.2pF), connected to the ground plane by a metallic via and inductance L, which is designed using an equivalent high impedance micro strip

printed line. Considering the varactor capacity range, the inductance value needed is 0.39 nH, which implies a high impedance line of 300 μm in width and 700 μm in length.

For a given varactor with a variant capacitance range, the increase of the maximum phase shift can be reached by lowering the impedance level Z_0 at the input of the reflection load [119], [120]. Matching the 50 Ω port impedance with 9 Ω one, a 21 Ω quarter-wave impedance transformer is needed to be implemented between the two ports. The impedance characteristic of the line is too low for microstrip line technology. Thus, it is difficult to implement it for prototyping. To overcome this challenge, two cascaded quarter-wave impedance transformers in the proposed phase shifter are realized. The principle of impedance transforming is illustrated in Fig. 4.3. The equation of the input impedance Z_{in} in function of the characteristic impedance Z_1 can be defined as:

$$Z_{in} = \frac{{Z_0}^2}{Z_x} = \frac{{Z_0}^2}{({Z_1}^2/Z_0)} = \frac{{Z_0}^3}{{Z_1}^2} \tag{4.2}$$

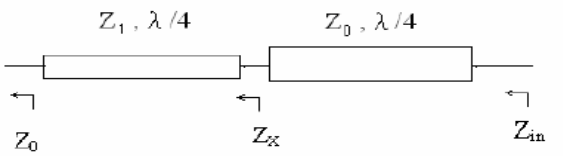

Fig 4.3 Two cascaded quarter-wave impedance transformers

If the input impedance Z_{in} is designed as 9 Ω and port impedance Z_0 of 3dB/90º hybrid coupler is 50 Ω. From the previous equation the characteristic impedance Z_1 is obtained to be 118 Ω. Thus, it can be using the two cascaded quarter-wave impedance transformers with characteristic impedance of 118 Ω and 50 Ω to transform port impedance from 50 Ω to 9 Ω over a moderate bandwidth. Fig. 4.4 provides the new reflective RF circuit mode.

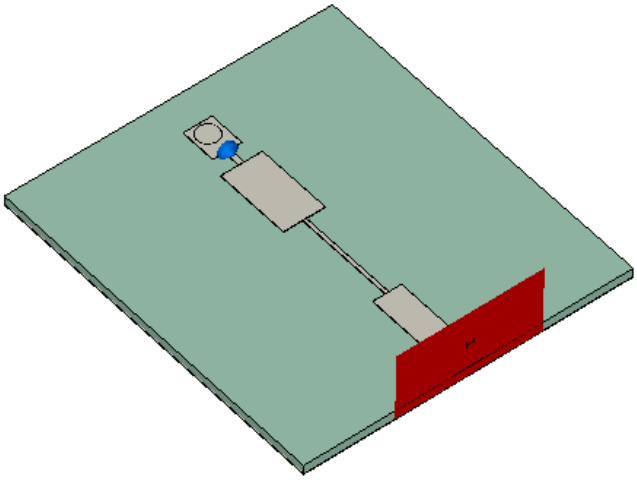

Fig 4.4 Reflective RF circuit design model

The strategy of optimization by genetic algorithms is used in antenna design problems for devices where the method of resolution is not clear [117], [119]. In our case, the design problem that are considered is to obtain the size, width and length of the two stubs in series that provide a good adaptation both in reflection and in transmission, in addition to reaching a maximum in the range of phases that will provide the complete phase shifter. To achieve this fact, an optimization by genetic algorithms is applied to the design of the LC reflective circuit included in the complete phase shifter in such way that the following parameters of the complete phase shifter are optimized reflection coefficient $|S_{11}|$. Transmission coefficient $|S_{21}|$ and phase range of S_{21} for the entire capacitive range provided by the varactor.

The design variables that the genetic algorithm optimizes are the dimensions of the length and width of each stub, that is, a total of 4 optimization variables. The objective function is set in the optimization process is formed by the composition of the three objectives previously mentioned. The obtained the optimal design of the reflective LC circuit, through what is described in the optimization process, is presented in Fig. 4.5.a and Fig. 4.5.b where both, the design of the reflective circuit and the simulation results of the module and the phase of the coefficient of reflection that it provides, are illustrated.

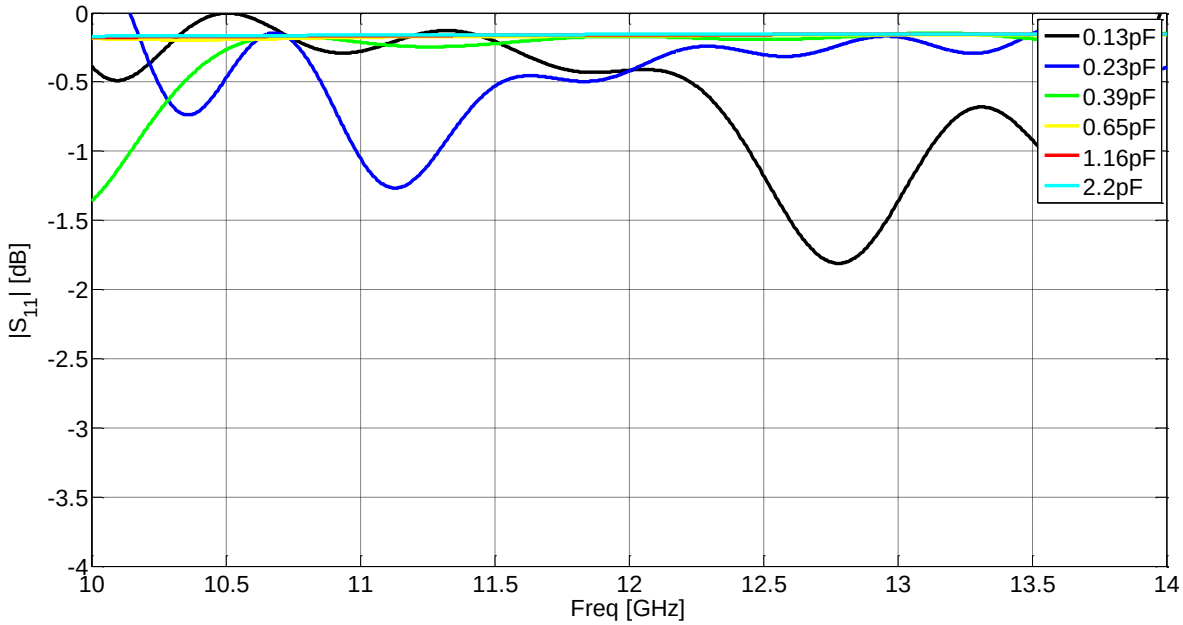

(a)

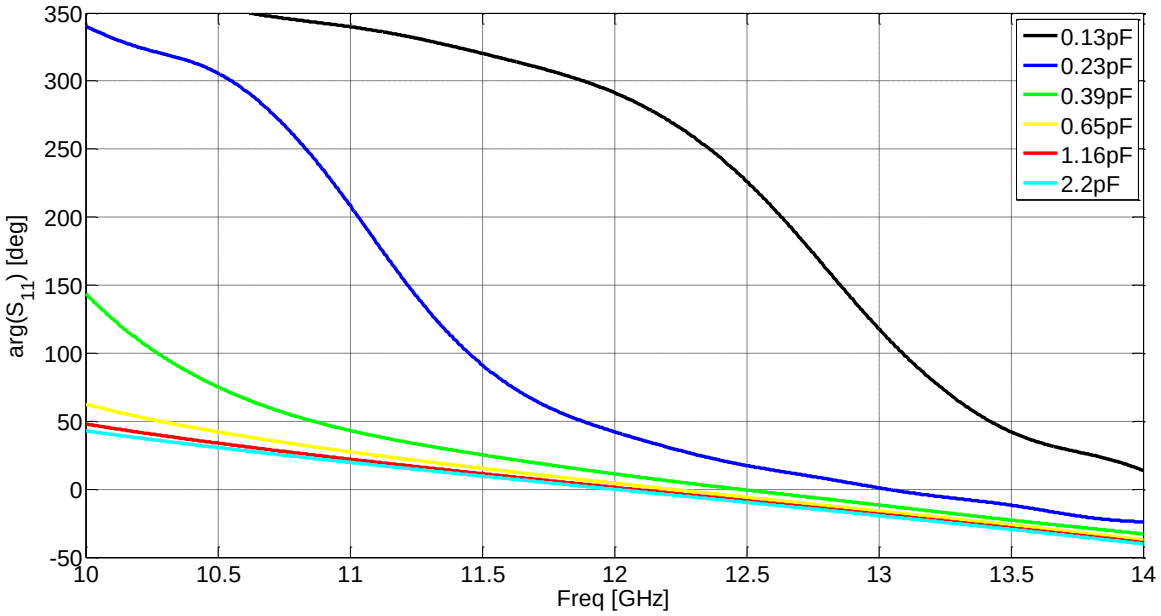

(b)

Fig 4.5 Optimized reflective circuit: (a) $|S_{11}|$, (b) S_{11} phase

As it can be seen, the optimized design using genetic algorithms provides a phase variation of approximately 325 degrees for the entire range of capabilities

provided by the varactor [0.13-2.20pF], with a very low level of reflection losses, which is provided by the new adaptation lines used.

4.2.1.1.3 Complete phase shifter integration (12GHz)

The LC reflective circuit obtained in the optimization process and which provides a large range of variation in phase leads to the design of the complete phase shifter that is presented in Fig. 4.6.

In the proposed design, ports 1 and 2 of the coupler are the input and output ports respectively, and ports 3 and 4 are those to which the optimized LC reflective circuits have been connected [117], [119], [120].

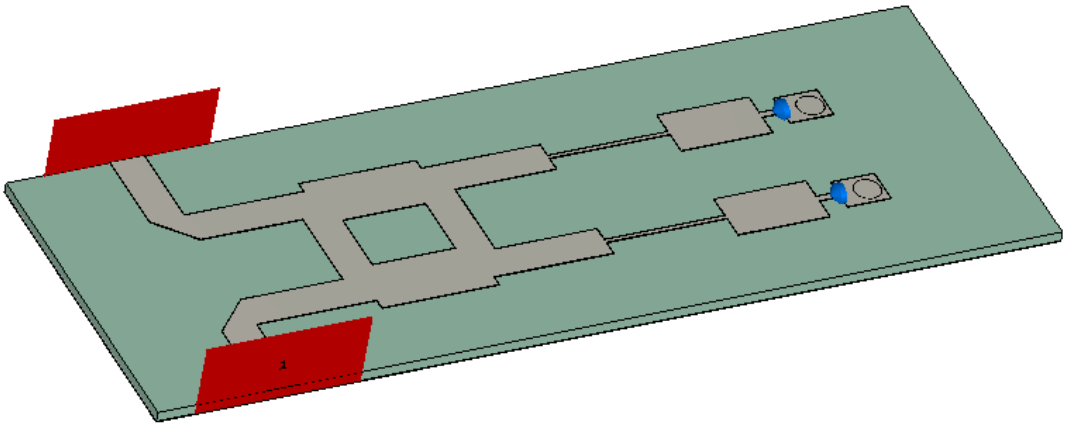

Fig 4.6 Complete design of the phase shifter

The simulation results of the complete shifter are shown in Fig. 4.7. Those results present low levels of losses (2dB in the worst case) and a good adaptation, reflected in it the parameter $|S_{11}|$, in the working band. In addition, the phase shifter produces a lag capability of the input signal of up to 325 degrees, identical to the maximum lag range provided by the LC reflective circuits [121].

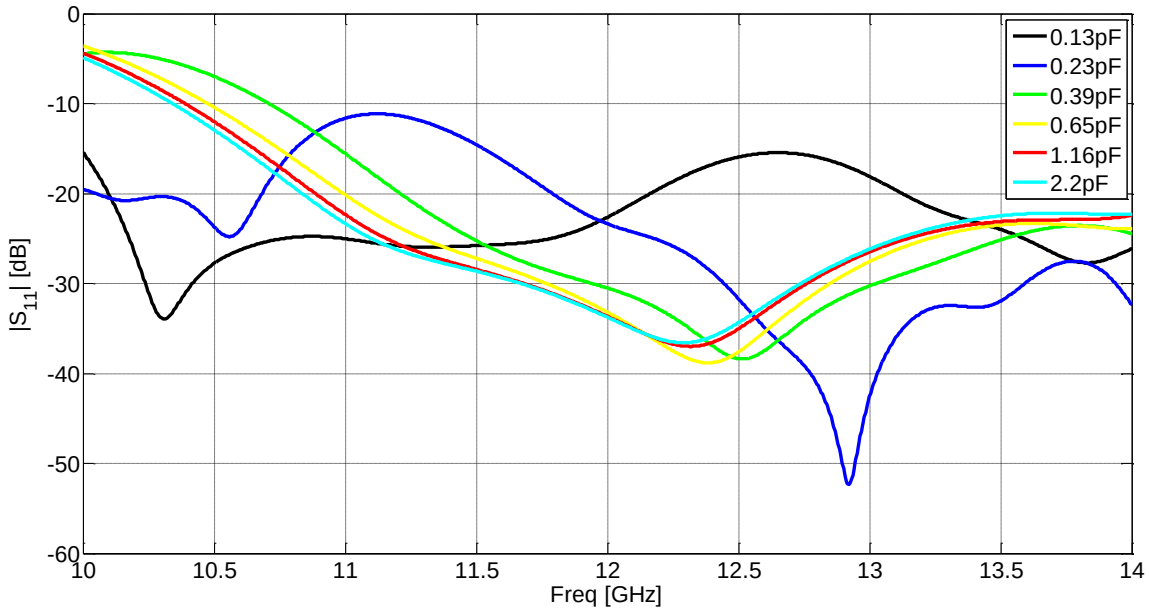
0.13pF
0.23pF
0.39pF
0.65pF
1.16pF
2.2pF
|S11| [dB]
Freq [GHz]
0
-10
-20
-30
-40
-50
-60
10
10.5
11
11.5
12
12.5
13
13.5
14

(a)

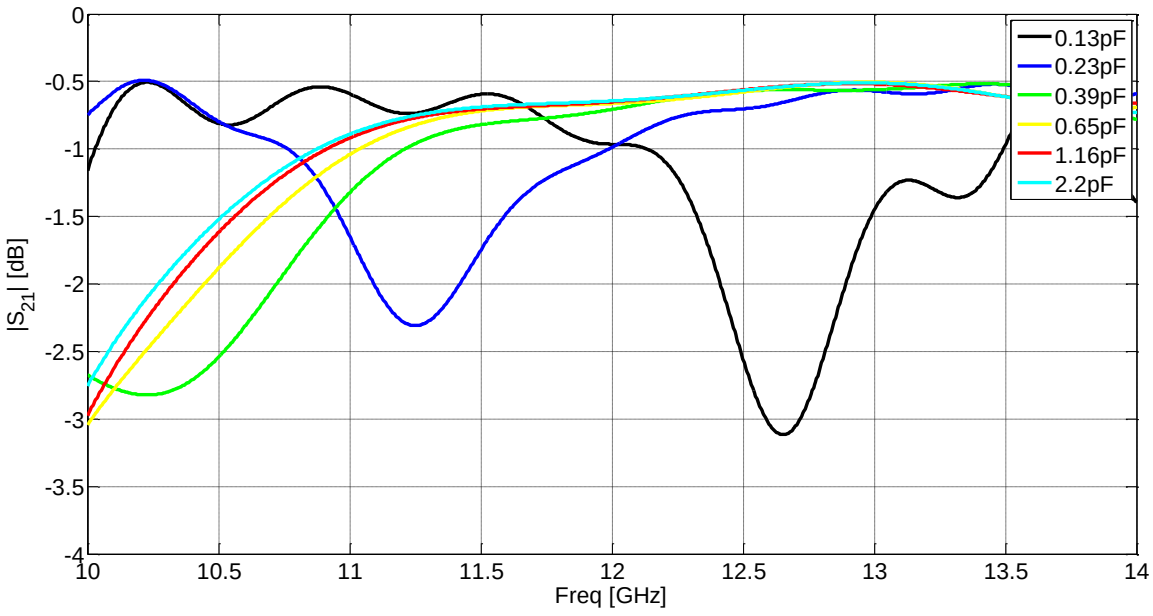
0.13pF
0.23pF
0.39pF
0.65pF
1.16pF
2.2pF
|S21| [dB]
Freq [GHz]
0
-0.5
-1
-1.5
-2
-2.5
-3
-3.5
-4
10
10.5
11
11.5
12
12.5
13
13.5
14

(b)

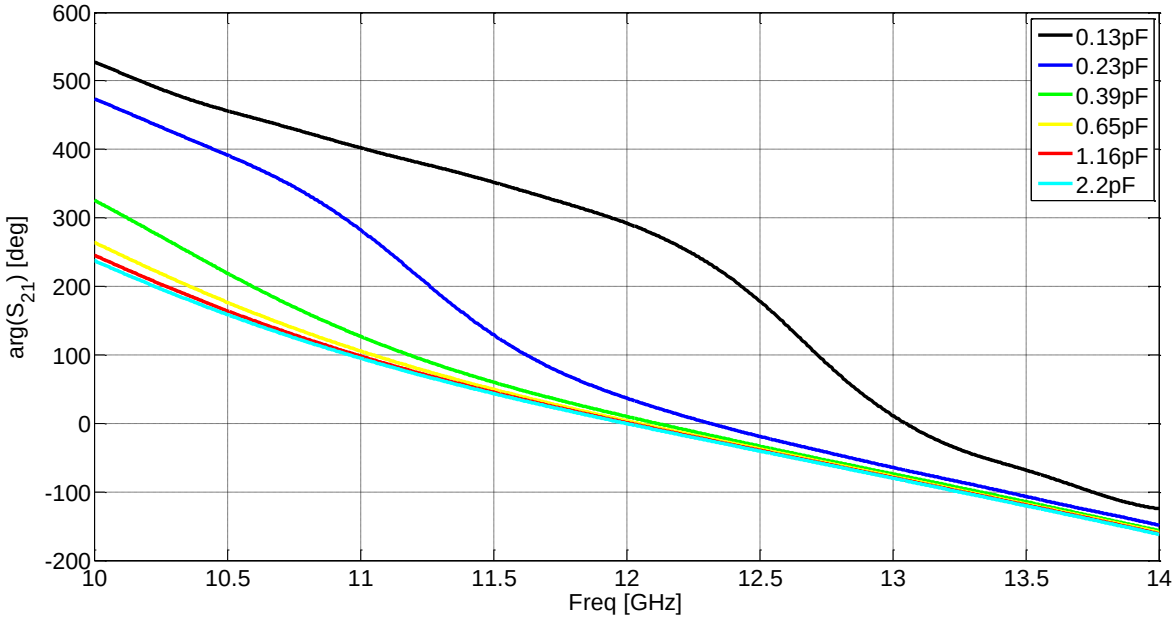

(c)

Fig 4.7 Design results of the complete phase shifter: (a) $|S_{11}|$, (b) $|S_{21}|$, (c) phase of S_{21}

It should be noticed that the proposed design of microwave phase shifter is a compact design, with a small number of elements distributed and with a wide range of phase variation compared to other commercial designs available.

4.2.1.2 Double Phase Shifter Design and Performance at 12 GHz

The phase variation provided by the single-phase shifter is lower than 360 degrees to guarantee the achievement of a phase variation higher than the double phase shifter that was introduced previously. The dimensions of the single-phase shifter received from the optimization process represent good initial input values option for the next optimization process, in order also to optimize the calculating time [117], [119], [120]. The design of the complete double phase shifter is presented in Fig. 4.8.

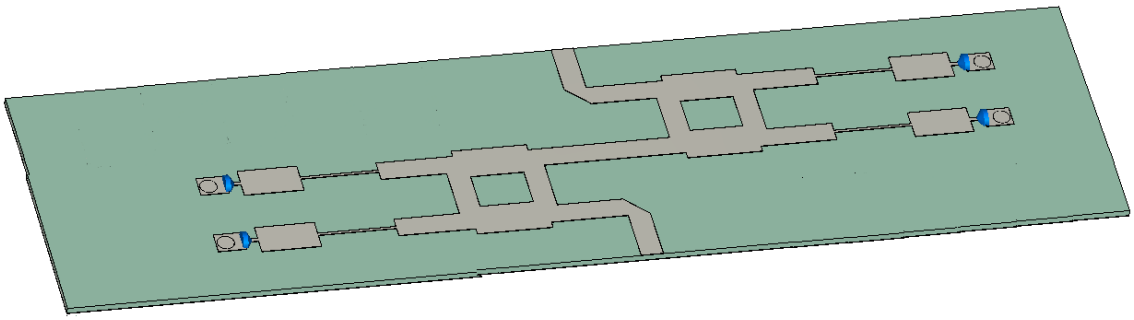

Fig 4.8 Complete double phase shifter design

The Fig. 4.9 shows the results of the reflection and the transmission parameters with also the phase of the transmission parameter.

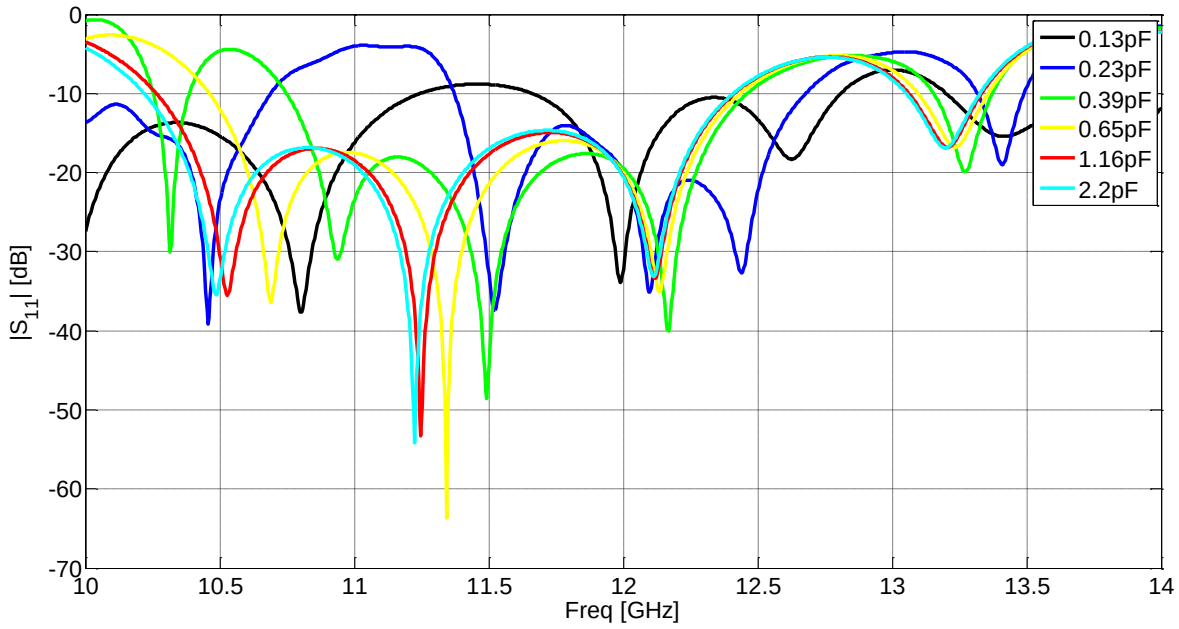

(a)

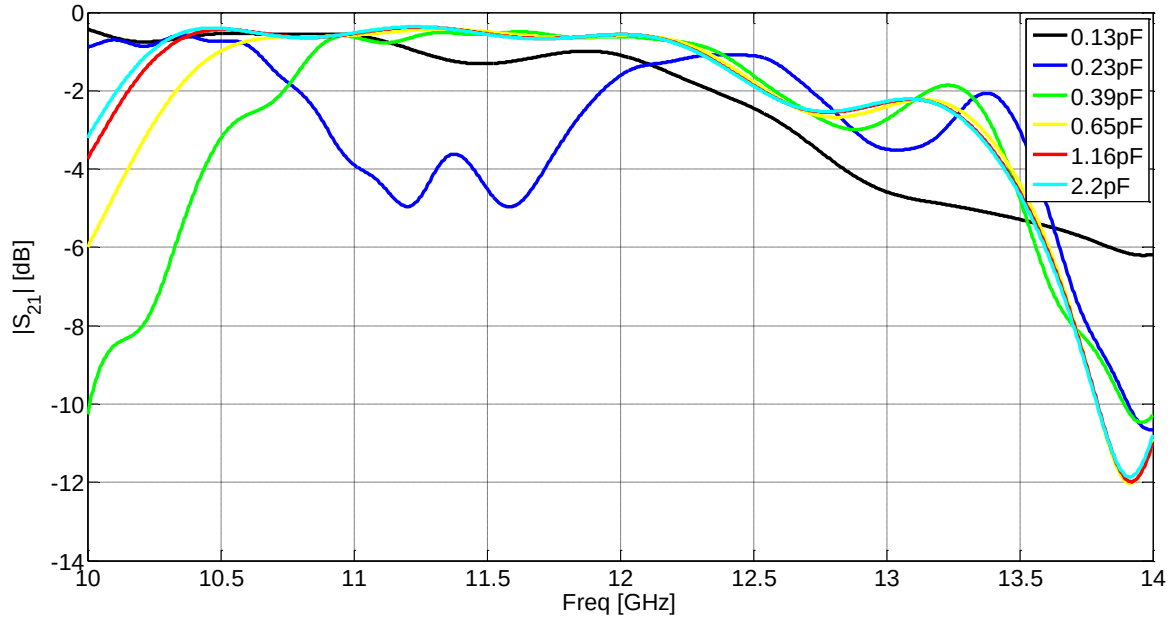

(b)

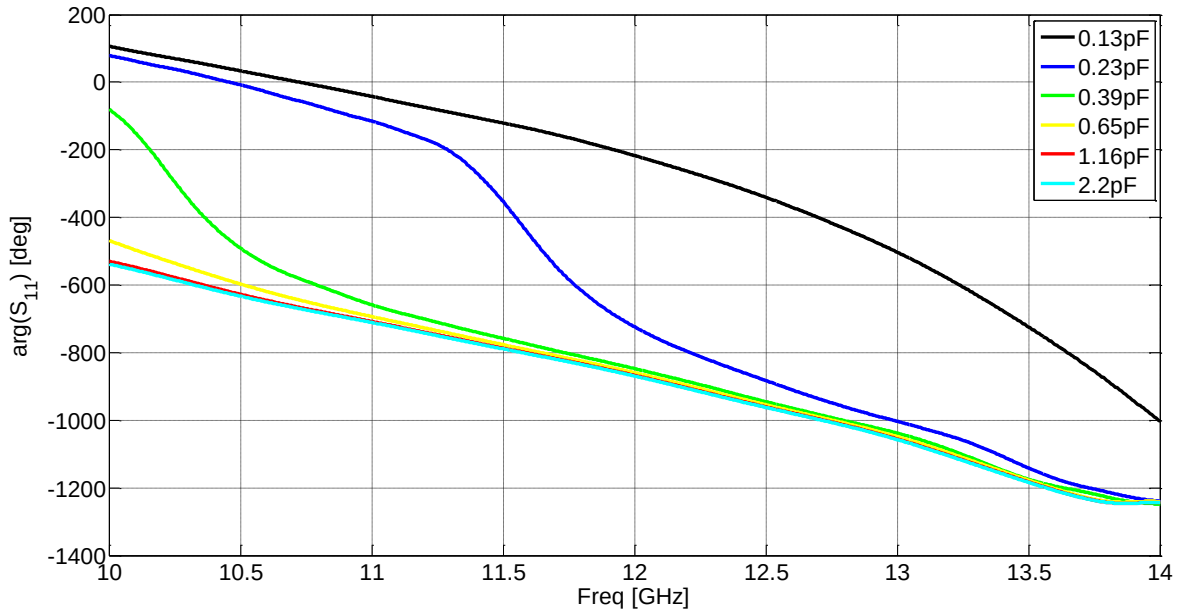

(c)

Fig 4.9 Optimized double phase shifter: (a) $|S_{11}|$, (b) $|S_{21}|$, (c) S_{21} phase

From the results presented in the Fig. 4.9, the shifting level gets to a double point. The shifting variation is up to 680 degrees at 12 GHz, and it varies between 220 degrees presented by the smallest capacitor value to 885 degrees presented by the biggest one. It maintains the good adaptation between the in-output ports and the hybrid coupler, and also the adaptation between the reflective circuits and the hybrid coupler. The good adaptation level shows good effect on both the reflection and the transmission loss levels. The Fig. 4.9.a shows the reflection losses, where all the losses are below -18 dB, and the Fig. 4.9.b shows the transmission loss levels with -5.8 dB for the worse case.

4.2.2 The phase Shifter Design and Performance for 18 GHz

To assure the stability of the optimization method used, maintaining it working on other phase shifters, our research efforts are oriented towards the design of a new phase shifter based on hybrid coupler with two new reflection circuits. All the structures are working in 18 GHz and it results are in satisfaction with the initial suppositions. Thus, the proposed design assures that we cover the Ku band with our two designs (12GHz-18 GHz).

4.2.2.1 The hybrid coupler (18 GHz)

The coupler is printed over the upper side of a Neltec substrate (εr=2.17, h=0.254mm, $\tan\delta$=0.0002). The structure of the hybrid coupler model is presented in Fig. 4.10.a. The simulation results are provided in Fig. 4.10.b.

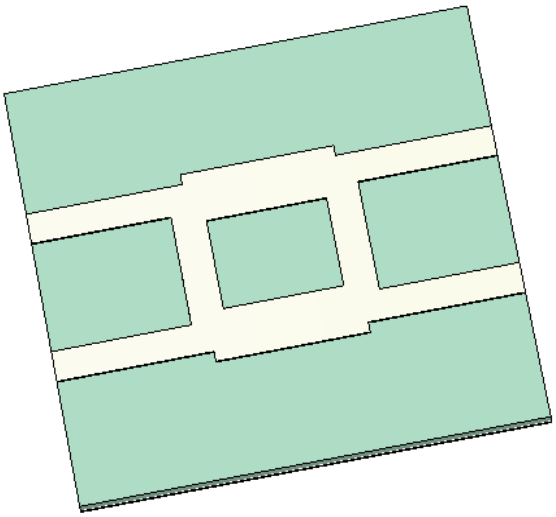

(a)

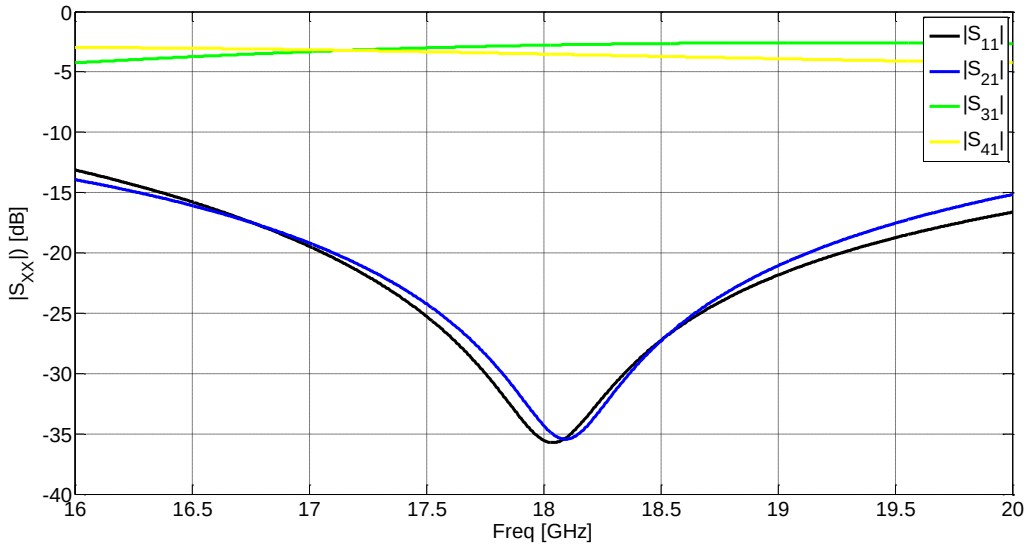

(b)

Fig 4. 10 Hybrid coupler: (a) Design, (b) S-parameters simulated

4.2.2.2 Complete phase shifter integration (18-18.5 GHz)

The complete phase shifter circuit for the range between 18 GHz- 18.5 GHz is presented in Fig. 4.11.a, the simulation results are illustrated also in Fig. 4.11.

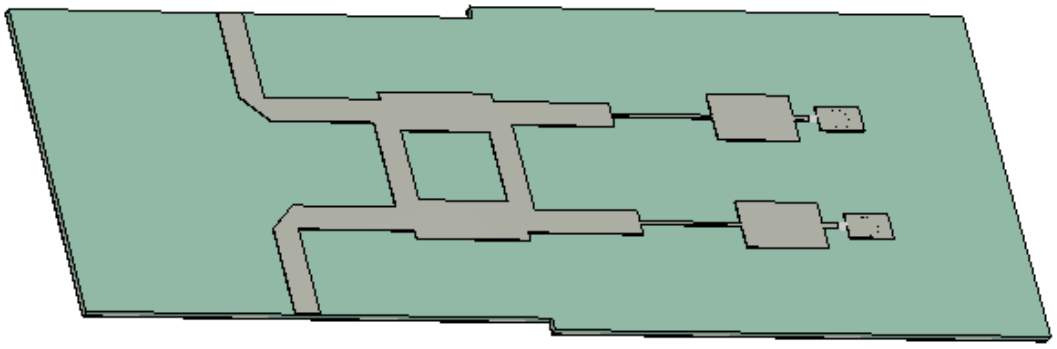

(a)

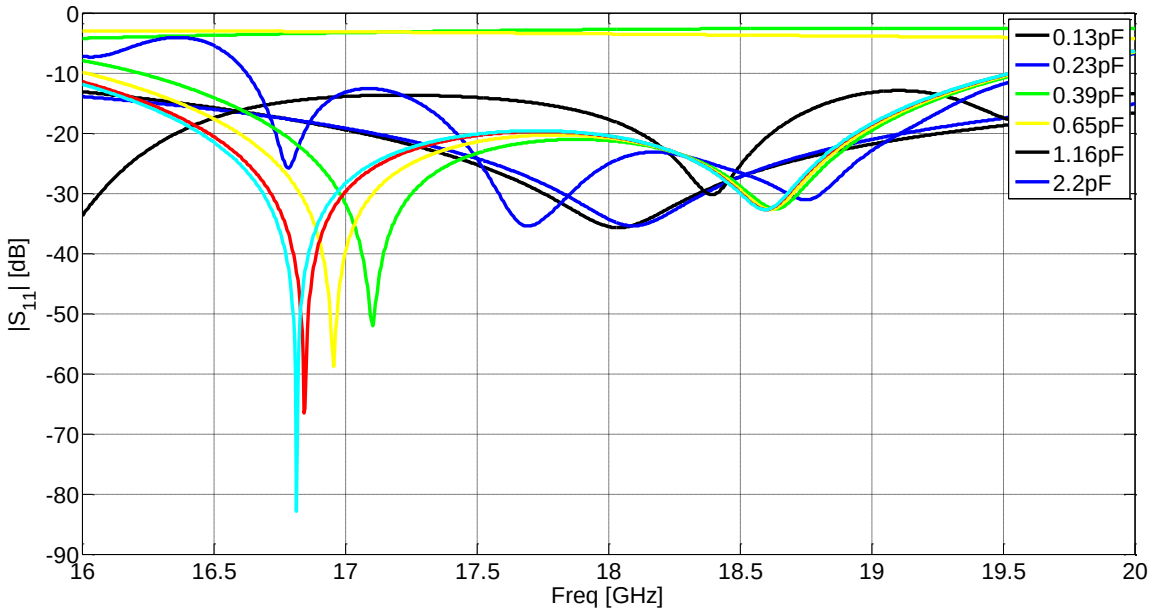
0
-10
-20
-30
-40
-50
-60
-70
-80
-90
16
16.5
17
17.5
18
18.5
19
19.5
20
Freq [GHz]
|S11| [dB]
0.13pF
0.23pF
0.39pF
0.65pF
1.16pF
2.2pF

(b)

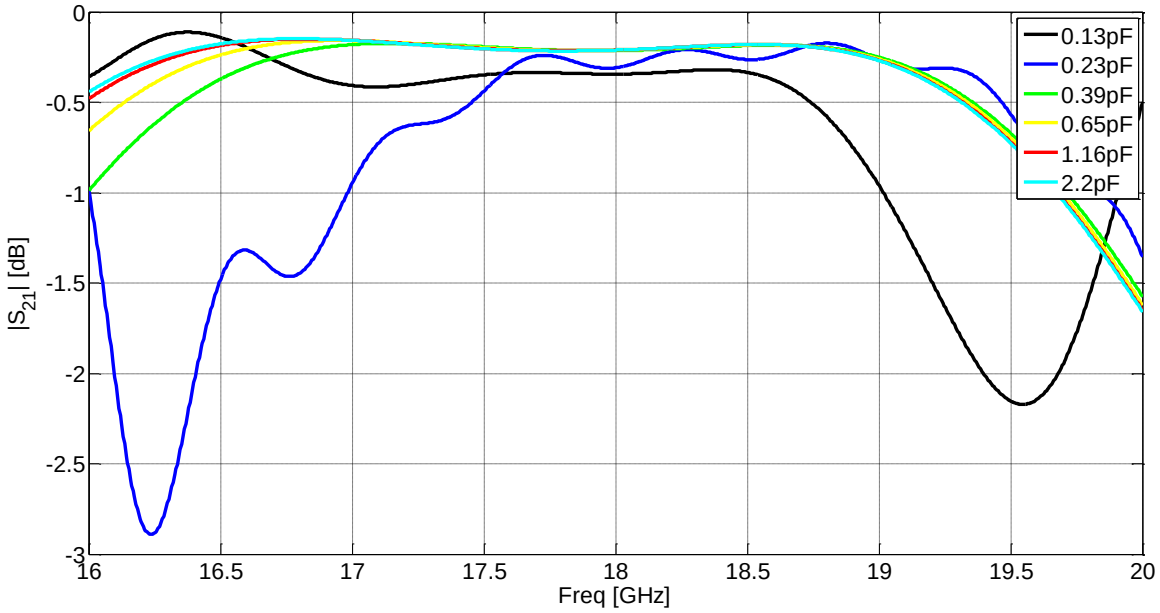

(c)

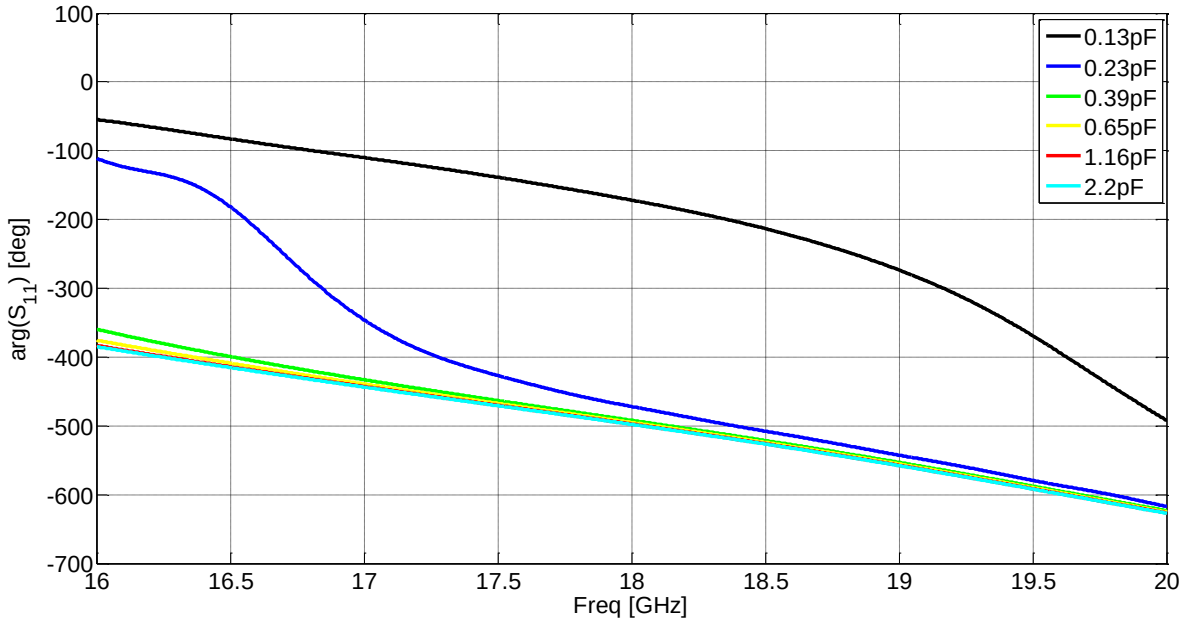

(d)

Fig 4.11 Optimized phase shifter: (a) Design (b) $|S_{11}|$ c) $|S_{21}|$ (d) S_{21} phase

As a conclusion from the results presented, the phase shifting variation level is good as much as the results of the phase shifter of 12 GHz (~328 degrees), also with a very low level of losses which express the good adaptation in the in-output ports.

4.2.2.3 Complete double phase shifter integration (18 GHz)

The following steps are similar to the following design of the complete double phase shifter working 12 GHz. the results illustrated in Fig. 4.12 shows promising results in the level of the phase shifting and the adaptation, which conclude the flexibility and high adaptation of the method used here in several structures even through the difference of the cost function of the structures.

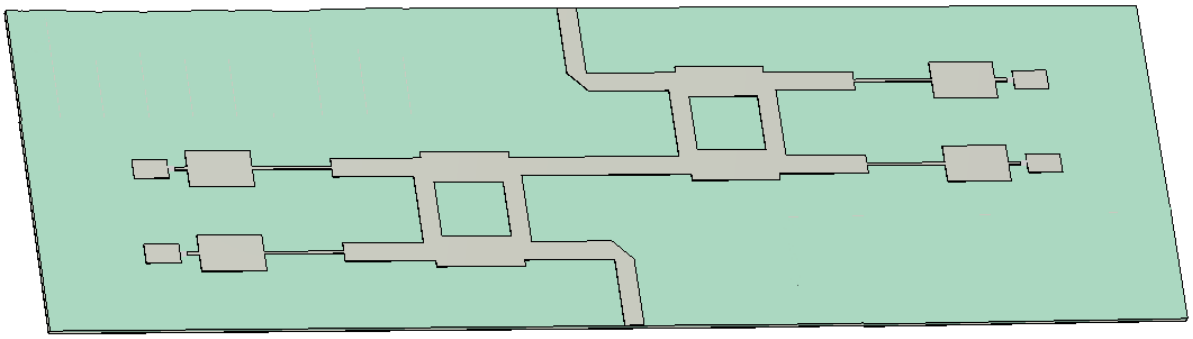

(a)

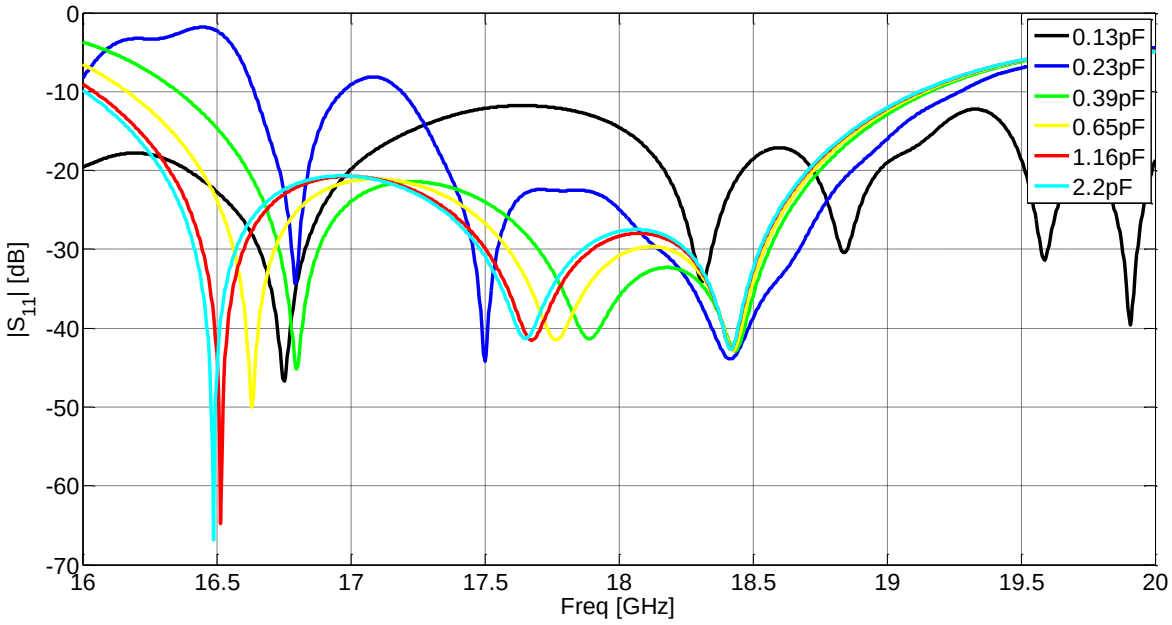
0.13pF
0.23pF
0.39pF
0.65pF
1.16pF
2.2pF
|S11| [dB]
Freq [GHz]

(b)

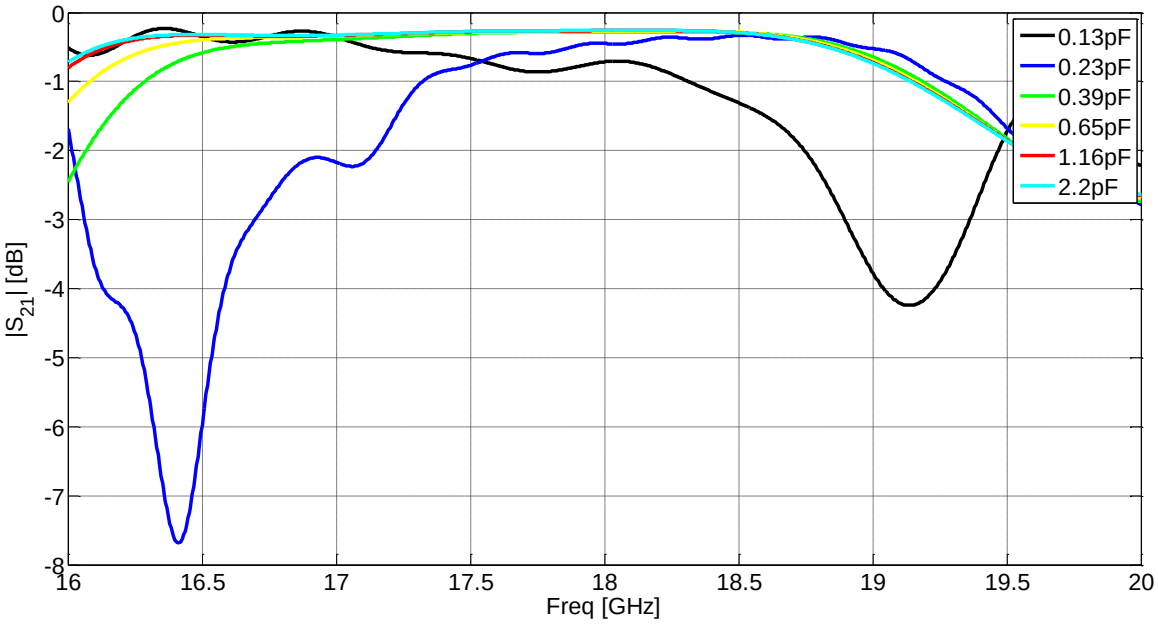
0.13pF
0.23pF
0.39pF
0.65pF
1.16pF
2.2pF
|S21| [dB]
Freq [GHz]

(c)

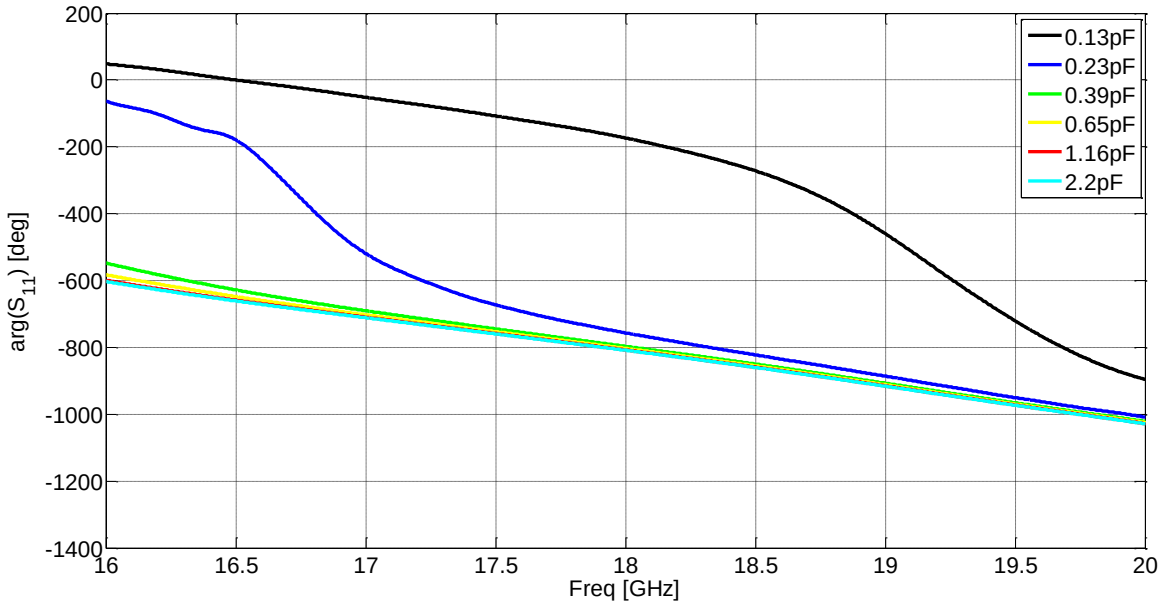

(d)

Fig 4.12 Optimized phase shifter: (a) Design, (b) $|S_{11}|$, c) $|S_{21}|$, and (d) S_{21} phase

The Fig. 4.12 shows the S-parameters results of the double phase shifter. These results show a very good phase shifting variation up to 640 degrees which almost the double of the variation for the single-phase shifter. In addition, of very good level of adaptation and transmission losses, with level lower than -14 dB in 18.50 GHz for the reflection loss and better than -1 dB for the transmission loss. Those values reinforce our expectations when manufacturing the designs, specially the 18 GHz- 19 GHZ phase shifter because we use it for TX/RX antenna system for both Ku band and Ka band.

4.3 Phase Shifter Prototype Performance

The design of the phase shifter proposed in this chapter has been validated through the fabrication of a prototype and its measurement. The results from measurements prove the accuracy of the simulated results. Fig. 4.13 shows the

front and the back side of phase shifter prototype, and the TRL (transmission-reflection-line) kit for the calibration prior to the measuring process. The measured results are shown in fig. 4.13, it displays the arg(S_{21}), Δ(arg(S_{21})) (related to min arg(S_{21}) value), |S_{21}| and |S_{11}|, that reinforce the validity of the simulation results.

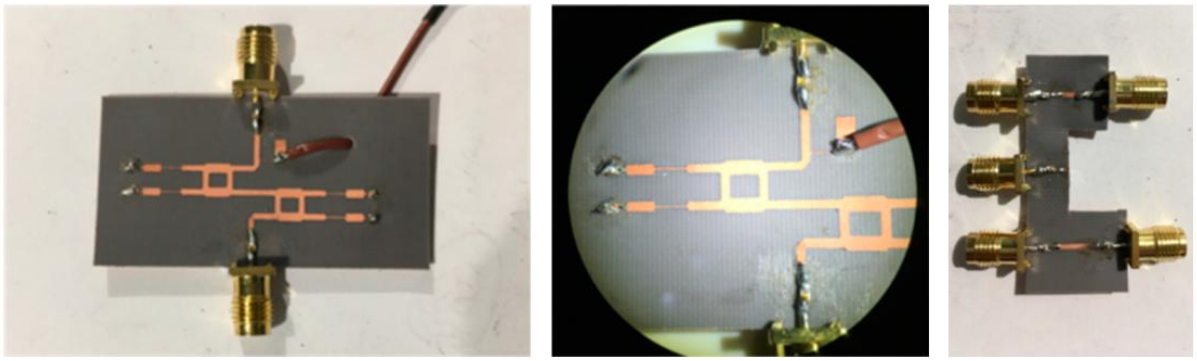

(a)

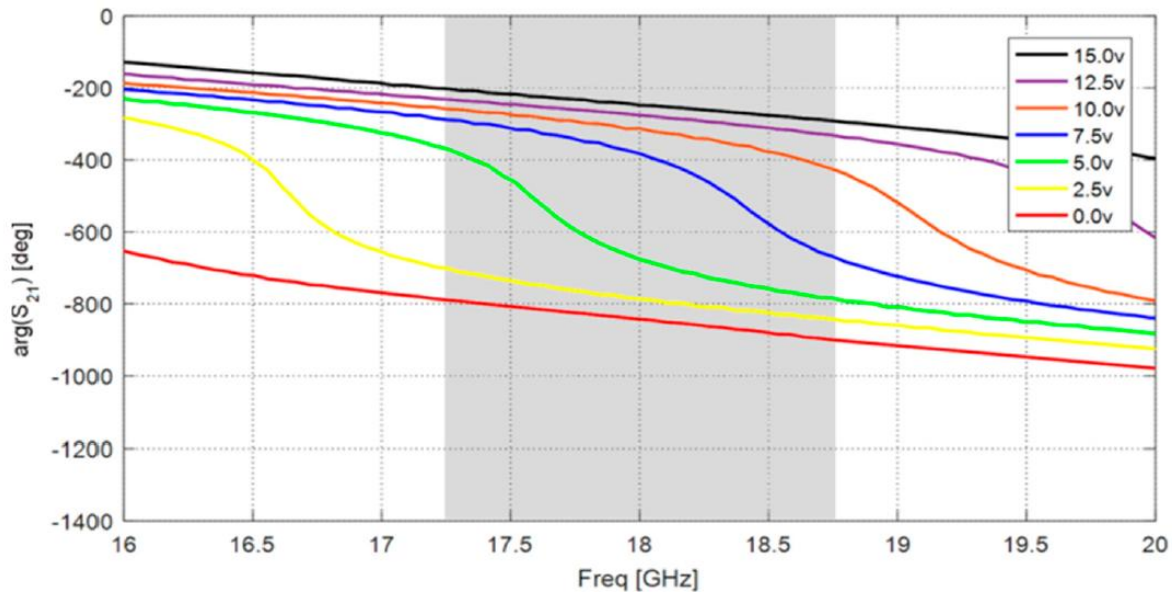

(b)

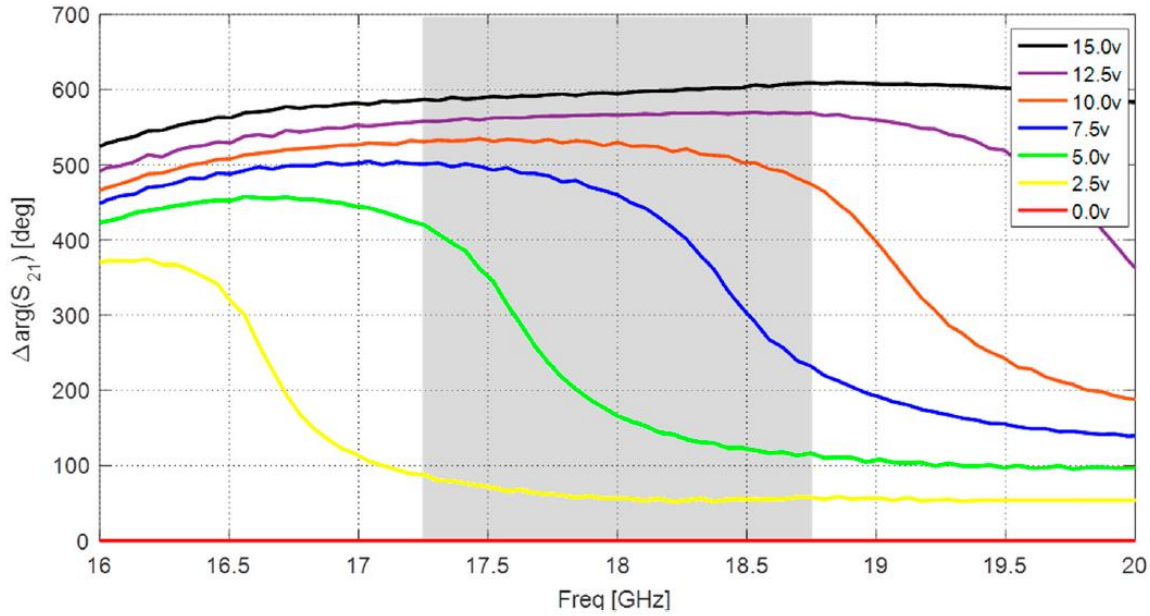
700
600
500
400
300
200
100
0
16
16.5
17
17.5
18
18.5
19
19.5
20
Freq [GHz]
Δarg(S21) [deg]
15.0v
12.5v
10.0v
7.5v
5.0v
2.5v
0.0v

(c)

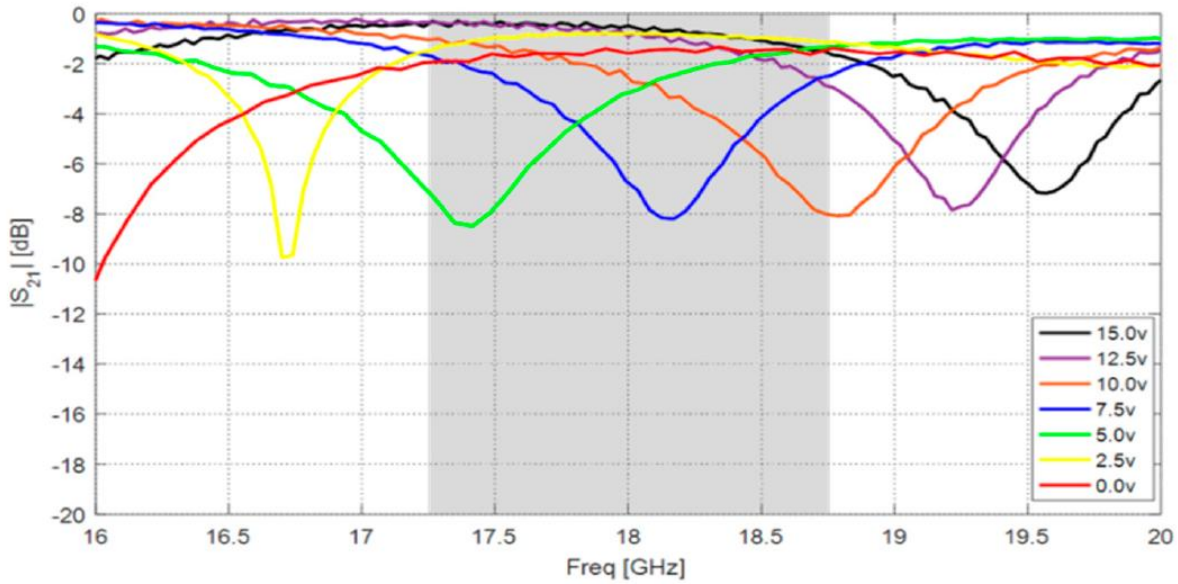
0
-2
-4
-6
-8
-10
-12
-14
-16
-18
-20
16
16.5
17
17.5
18
18.5
19
19.5
20
Freq [GHz]
|S21| [dB]
15.0v
12.5v
10.0v
7.5v
5.0v
2.5v
0.0v

(d)

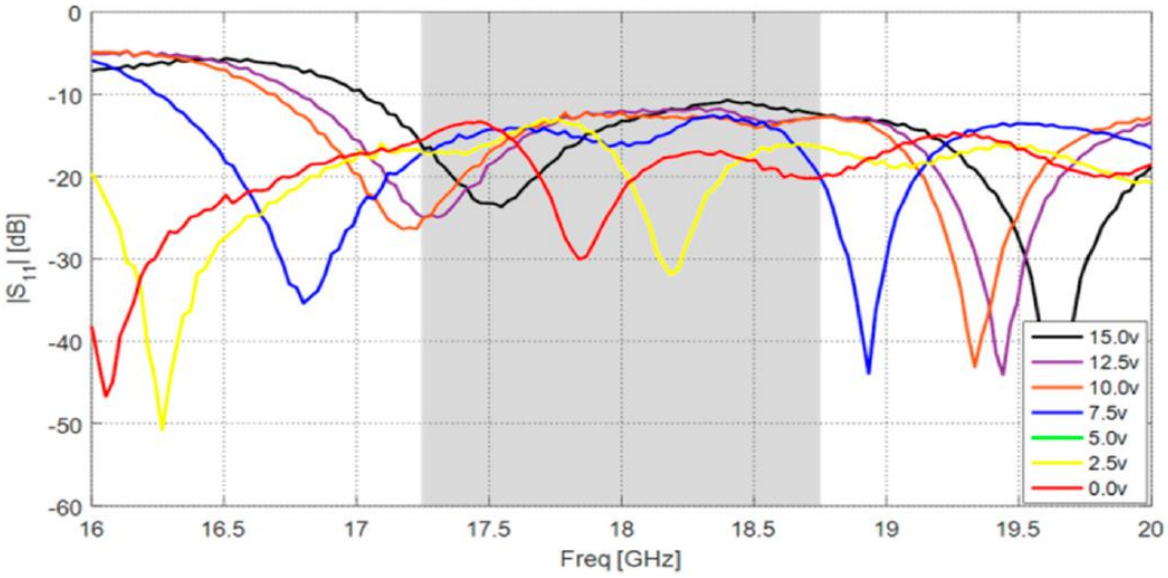

(e)

Fig 4.13 Prototype results of the 18 GHz phase shifter: (a) prototype and TRL kit (central image corresponds to a microscope zoom view), (b) arg(S_{21}), (c) Δ(arg(S_{21})) (related to min arg(S_{21}) value, 0 v), (d) $|S_{21}|$ and (e) $|S_{11}|$

As it can be noticed from the results shown in Fig. 4.13, there is a good agreement between the proposed phase shifter simulated results and the measured results. The insertion loss levels of the prototype are higher than the expected in the simulation results and that was expected due to manufacture errors that can be explained by different reasons. The difference in the intersection loss levels may occur due to the parasitic components of the varactor, conductive epoxy resistance or roughness of the shifter printed line limits to site a few. Fig. 4.14 compares the simulation phase results with the experimental ones (Fig. 4.14.a) and provides an insight of the linearity of the device in terms of phase/voltage relation (Fig. 4.14.b).

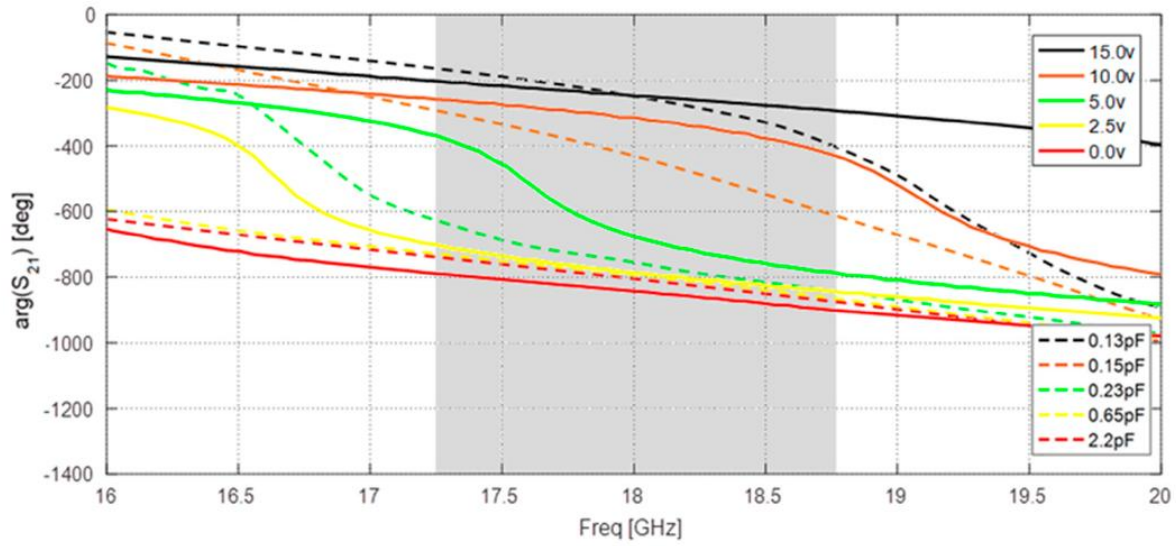

(a)

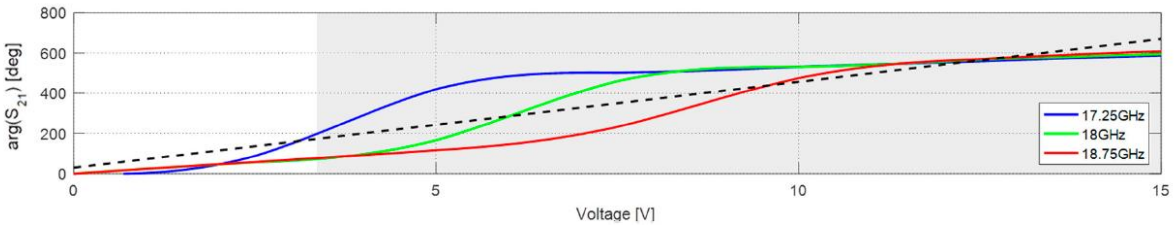

(b)

Fig 4.14 Phase shifting performance: (a) comparison between simulation and measurement phase results of the 18 GHz phase shifter, (b) phase/voltage relation (the dashed line is the linear reference and the grey zone is the one that provides at least 360 degrees variation)

Fig. 4.14.a shows the comparison between the simulation results in regard of the capacitance and the experimental ones in regard of the voltage. There is an insignificant difference between pairs of simulation and experimental curves. This slide difference does not influence the novelty and the importance of the results. The prototype of the phase shifter is fully functional, and the phase variation range is maintained, and only needs a voltage/phase conversion table.

In addition, it must be pointed out that, although the phase/capacitance relation is not linear, it is compensated by additional non-linear behaviour of the capacitance/voltage relation. It is worth mentioning that, although the device provides a quasi linear phase/voltage response at the central frequency, this

linearity is strongly degraded at the band limits, as it can be seen in Fig. 4.14.b. However, since the prototype provides a complete phase shift of around 600 degrees, part of this possible variation can be sacrificed in order to increase the linearity of the device, as detailed in Fig. 4.14.b, where the grey region is the one that provides at least 360 degrees phase variation.

4.4 Conclusion

Chapter 4 presents different designs of microstrip electrically controllable phase shifter for Ku band and Ka band applications. The applications include controlling the relative phase of each element in a phase array antenna in a RADAR or steerable communications link and in cancelation loops used in high linearity amplifiers. All the designs are based on 3dB/90° hybrid couplers with two ports connected to reflective circuit loads. The novelty introduced to improve the adaptation between the LC reflective circuits and the hybrid couplers is using a non-sequential impedance transformer. And the use of an optimization program based on Genetic Algorithm to control the position and the dimension of the impedance lines in order to improve the phase variation and remains the low losses level.

The introduction of Genetic Algorithm as a numerical optimization program gives the full control of the variation of the optimization variables and their influences on the final result provided. The examination at each iteration of the results obtained calculating the cost function, let evaluate its value depending on our criteria area in the end of every iteration possible, taking in consideration also our main goal of the optimization.

The dimensions and the positions of the transformers were the metrics used to qualify the efficiency off the optimization. All the results obtained by the optimization programmes were favourable and validated the methodology through the design of a prototype. The proposed designs are a good novel design aspect for multiple applications. One of the applications can be the reconfigurable

phased arrays such as transmit arrays or reflect arrays. Moreover, the genetic algorithm can be used for the distribution of the electronic pieces since not all the architectures are suitable for miniaturization. Knowing that, the final prototype is being fully embeddable in such designs due to the optimized reduced footprint.

Chapter 5:

Microstrip Wideband Circulator

5.1 Introduction

Circulator is a passive three-four ports electronic device, very important to the telecommunication systems, non-reciprocal and symmetrical device, its ports are arranged in a way that signal is coupled to an adjacent port, and not to the other. Means the signal is transmitted to the next port in rotation only, which explains the name of it. The circulator structure wins it non-reciprocity property from the excited ferromagnetic materials used. They are a ceramic material considered as a subgroup of the magnetic materials, with the behaviour of making the circulator very suitable for low-loss high frequency applications.

5.2 The Wideband Circulator Design in The Literature

By its simple form of a three-port circuit, the junction circulator is one of the members of a large family of non-reciprocal devices. The general properties including the existence and the method of connection for symmetrical junction circulators have been treated first by Milano [122] and Auld [124] by studying

their distribution matrix S. However, Bosma [123], [125], [126], [127] was one of the first to focus on the intrinsic quality of the circulation mechanism in terms of the frequency behaviour of the electromagnetic field.

It is true that several attempts have been made to explain the functioning of circulators. We can cite as an example: the work of Allen [128] and Bownes [129] who used the principle of Faraday's rotation, the work of Feoktistov [130] who was interested in asymmetric diffractions, or still the first works of Bosma on the displacements of the fields [123]. Despite these efforts, this work has just confirmed, more or less, a kind of intuitive thinking of the phenomenon and has not led to a consistent and manageable theory.

Later, Skomal [131] tried to explain the functioning of the circulator by considering two surface waves in counter rotation. Thanks to this concept, he was able to evaluate certain design parameters. However, some of its results, such as, the dependence of the applied field on magnetization, were at odds with the results published by Bosma [125]. Bosma had explained these differences by the fact that some of the assumptions made by Skomal are not realistic. In particular, this happens with the distance between adjacent ports of the circulator which is not always equal to the effective wavelength as shown by Davies and Cohen in [132].

Bosma's research in their first attempts published in [123] ended in semi-failure, since part of the results obtained did not correspond to the experiments. Although according to him, the problem was stated correctly mathematically.

Subsequently, Bosma [125] based on experimental findings, reformulated his problem by making a number of approximations and assumptions including the conditions at the edges. This allowed him to establish traffic conditions and from there, he deduced the physical parameters essential to the design of circulators.

5.3 The definition of the important parameters of Ferrite Materials

For the design of circulator, they are some important parameters of the ferrimagnetic materials that have a big influence on the performance and the operation frequency band of the circuits. Such as, the saturation magnetization ($4\pi M_s$), resonance linewidth (ΔH) and compensation temperature (T_N).

Therefore, the choice of the characteristic values of those parameters is mandatory to reach a high-performance circulation.

5.3.1 Saturation Magnetization ($4\pi M_s$)

Under the effect of an external static magnetic field (H_{ext}) applied on the structure of a ferrite material, the saturation magnetization is the threshold magnetization level that a ferrite material can reach before the magnetic domain inside it will be aligned [133], [134].

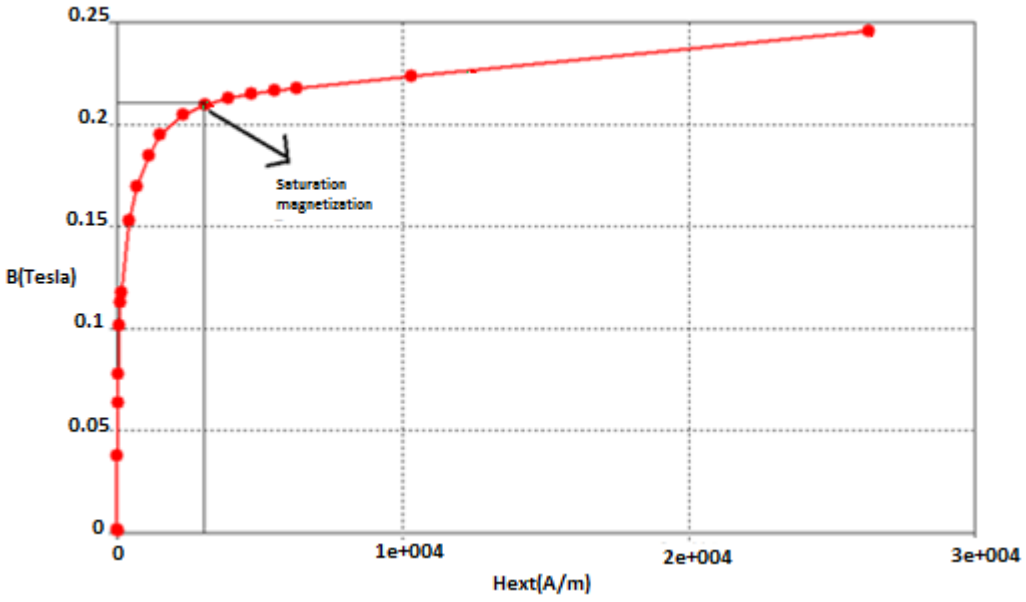

Fig 5.1 the variation of the magnetization level in terms of the external static magnetic field [133], [134]

5.3.2 Resonance Linewidth (ΔH)

The resonance linewidth ($\Delta \boldsymbol{H}$) is one of the three contributors that caused the loss mechanism in the ferrite materials along with the internal static magnetic field and the frequency of microwave signal. It is the resonance intrinsic field that defines the width of the internal static magnetic field [135], [136], [137], [138].

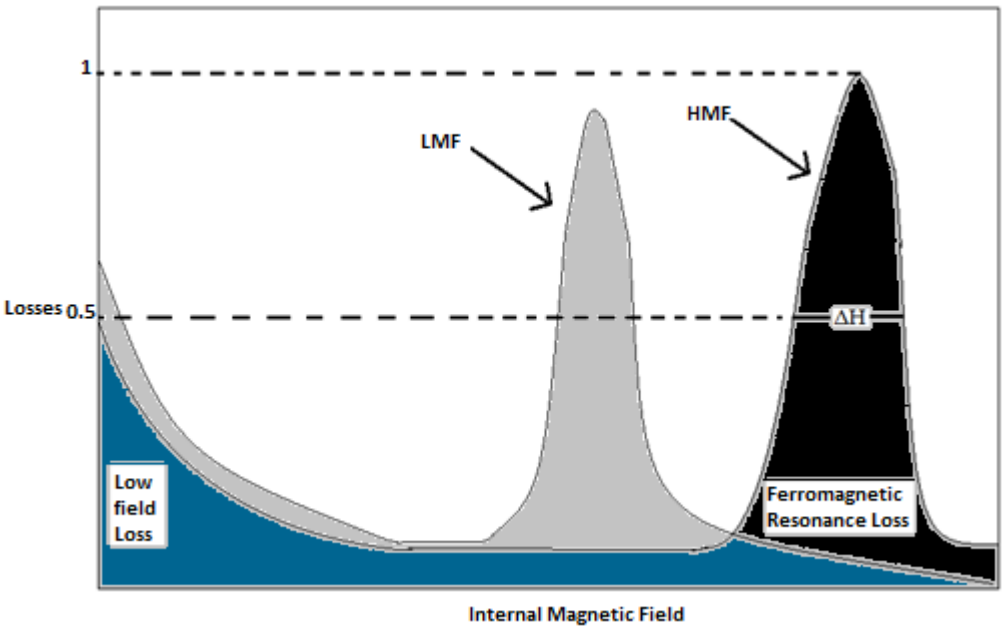

Fig 5.2 The variation of the losses in the ferrite materials in terms of the internal magnetic field

5.3.3 Compensation Temperature (T_N)

Increasing the temperature of a ferromagnetic material above its Curie temperature leads to the reduction of magnetization level of the material until reached zero [139].

The ferromagnetic materials have both the magnitude magnetizations and the opposite direction equal to zero is not the same as the ferrimagnetic materials, where the magnetic domains are aligned in both the directions.

This difference in the alignment of the magnetic domains determines the difference between a ferromagnetic material and a ferrimagnetic material [139].

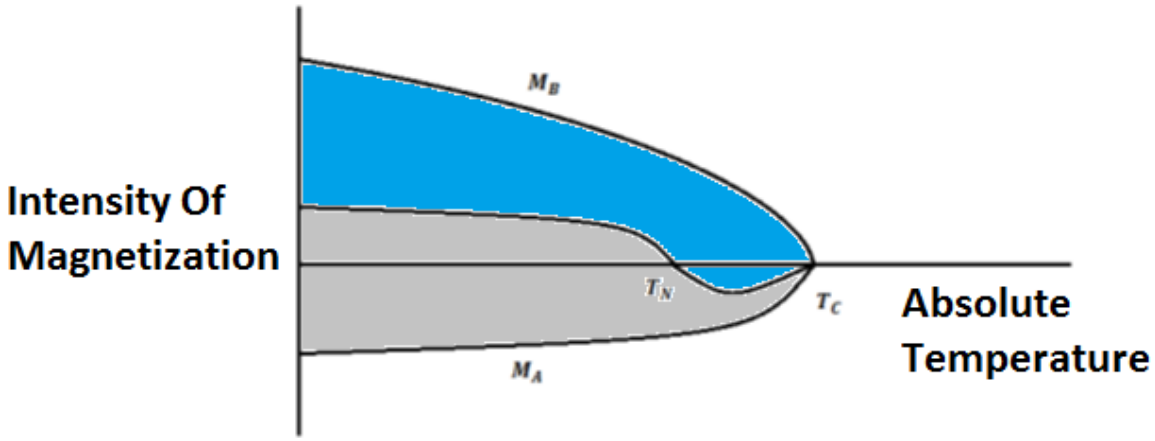

Fig 5.3 The variation of the intensity of magnetization in term of the absolute temperature

5.4 The Wideband Circulator Design

The next section discusses the theoretical design methodology for wide band microstrip circulators.

5.4.1 The Structure of a microstrip Circulator

The structure of three ports microstrip circulator is symmetrical around z=0 plane. The design is divided to four-parts: part number 1 is the ground plane, the ferrite disk (number 2), which is in most cases is covered radially by a dielectric material and the Y-junction conductor (number 3) located on it. The characteristics of the Y-junction as the thickness and the conductivity are of the highest importance for the performance of the circulator, as well as the conductivity that affects the insertion loss of the structure. The parameter $\boldsymbol{H_i}$, which is the internal static field generated in the ferrite, is necessary for the

operation of the circulator, because the ferrite materials gain permeability tensor when an external static magnetic field is applied [140].

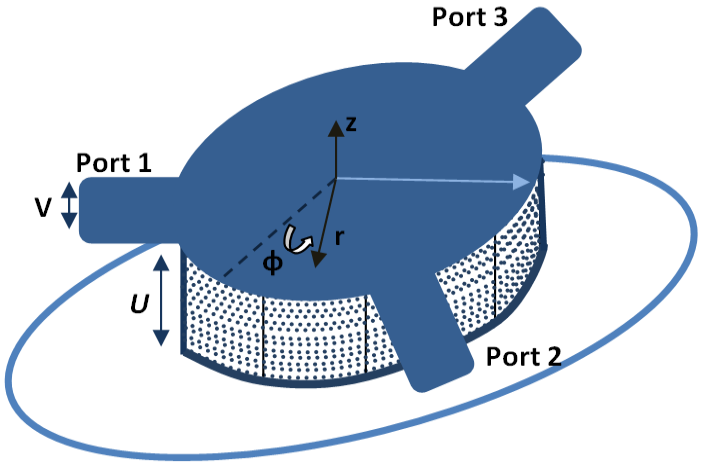

Fig 5.4 The 3-Dimensions structure of a microstrip circulator

5.4.2 The Theoretical Basis of Wideband Circulator Design

The following section dedicated to find high frequency, electric and magnetic field relations in the ferrite disks and provide circulation conditions, which is given by using an approach called Green's function approach [140]. Then, it is applied the continuous tracking technique, to clarify the design of one octave circulator [141].

5.4.2.1 The Green's Function Approach

To design a circulator, it is necessary to define the high frequency HF, electric E and magnetic H fields inside the ferrite disk resonators. The most accurate method used is the Green's function approach. With the use of Bosma method, 2 perfect circulation graphs are derived. With help of them, it is feasible to design analytically any circulator for any desired centre frequency.

The ferrite disks and the centre conductor can have different radius or even different shapes like a triangular or cloves leaves central conductor shape. The only important point is the symmetry of the design. During the process, we choose a circular centre conductor with 120 degrees apart displacement for his line connectors.

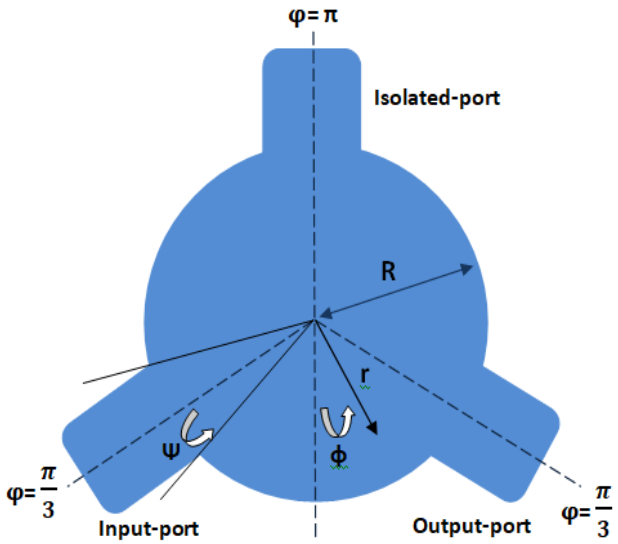

Fig 5.5 Top view of the central conductor studied by Bosma and the placement of 3 ports

Ψ, or the coupling angle, is a very important parameter for the design of the circulator. It is the relation between the width connections W_{int} and the radius of the center conductor.

$$\Psi = sin^{-1}\left(\frac{W_{int}}{2R}\right) \text{ (in radians)} \qquad (5.1)$$

5.4.2.2 The Design of One Octave Frequency Band Circulator

According to Bosma, Wu and Rosenbaum, the use of the perfect circulation graphs, make the design of a circulator working in any specific frequency possible. Also due to the low filed losses, the insertion loss values below the

saturation magnetization frequency become too high. So approximately at these point the circulation of the waves inside the ferrite material.

In continuous tracking circulator approach, we use the frequency band $[\boldsymbol{f_m}, \boldsymbol{2f_m}]$ which is the saturation magnetization frequency given by

$$\omega_m = 2\pi(f_m) = 2\pi(4\pi M_s \gamma') \tag{5.2}$$

The impedance ratio is given by

$$\frac{Z_{eff}}{Z_d} = (\frac{\varepsilon_d}{\varepsilon_f})(1 - (\frac{k}{\mu})^2)^{1/2} \tag{5.3}$$

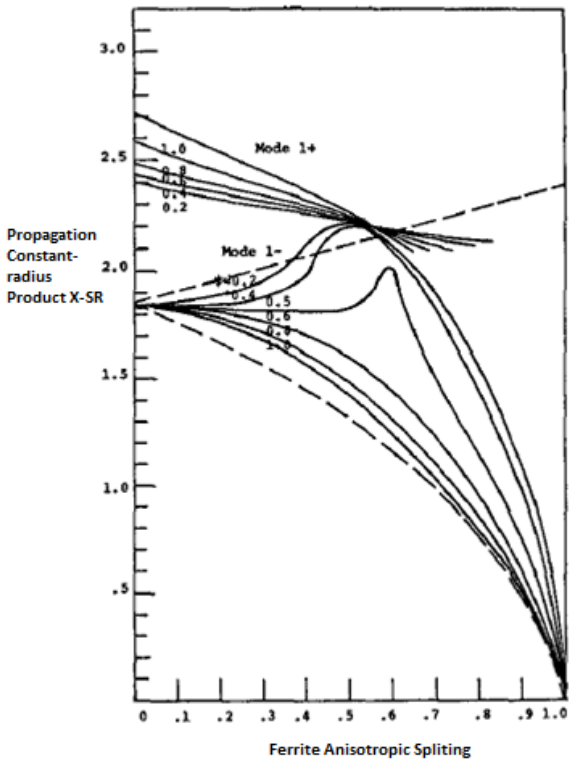

Fig 5.6 Numeric solutions for traffic conditions condition for various coupling angles [141]

For lower frequency band limit:

$$\left|\frac{k}{\mu}\right| \sim 1$$

For upper frequency band limit:

$$\left|\frac{k}{\mu}\right| \sim 0.5$$

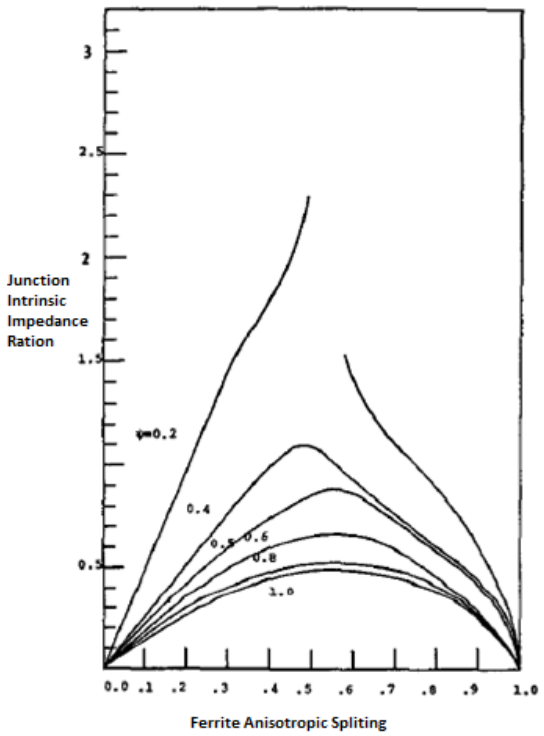

Fig 5.7 Normalized junction impedance ratio as a function of anisotropic splitting factor calculated from the second circulation condition for various coupling angles [141]

The intersection of the second perfect circulator graph has to be between $\left|\frac{k}{\mu}\right| \sim 0.5$ and $\left|\frac{k}{\mu}\right| \sim 1$, for the design of one octave circulator. So, to summarize the procedure, firstly, it is so important to choose the dielectric and ferrite materials properly, then a presentation of the variation of the impedance ratio a function of $\left|\frac{k}{\mu}\right|$ is needed to be on the second perfect circulation graph. The choose of a proper coupling angle Ψ.

It is very important to guarantee the intersection of the ratio of the impedance and the second circulation curve. If both curves intersect for a small region, it means that circulator operation is limited to a very narrowband region. However, if they intersects between $\left|\frac{k}{\mu}\right| \sim 0.5$ and $\left|\frac{k}{\mu}\right| \sim 1$, that means operation

frequency band can be between the $[f_m, 2f_m]$. And finally the remaining parameter is the ferrite disk radius (R) from the first perfect circulation graph.

5.5 The Design, and Simulation of one octave Frequency Band microstrip circulator

The main goal in this section is the realization of Ku-band micro strip circulators. First step the analytical approach to define the circulator parameters, then the optimization of the results using algorithm Genetic.

5.5.1 Analytical Design of One Octave Frequency Band Circulator

First, the continuous tracking technique is used to define the geometry and the materials parameters. Then, the matching between the impedance of the circulator ports and a port of 50 ohms using two-section impedance transformers is needed. This analytical approach possibly does not give the best circulator structure. However, it provides a very satisfying starting point for the optimization process. Therefore, with an optimization process, all the parameters achieve the best performance possible for the structures. The solution that been proposed in the example is $\frac{\varepsilon_d}{\varepsilon_f}$ =1 and Ψ=0.51.

5.5.2 Determination of Ferrite Material

For the determination of the ferrite material appropriate for the design, it is preferable to know the circulator operating band. In this case, the circulator has to be operating between 9-18 GHz. To cover all the Ku-band the value $f_m = 9\,GHz$.

The modification of the equation (5.2) with the consideration of the effect of the Lande factor (g), which is a ferrite materials parameter, turn it into:

$$f_m = 4\pi M_s \gamma (\frac{g}{2}) \quad (5.4)$$

With a constant gyro magnetic ratio equal to 2.8 MHz/Oe, then

$$4\pi M_s = 3214 \left(\frac{g}{2}\right) \quad (5.5)$$

As it is been explained before, the determination of a ferrite material that satisfies the requirements is so important for the high-performance of the circulator. The use of the datasheets of well-known ferrite manufacturers like TCI or TTECH may be useful. The nickel ferrites like TT2-2750 and TT1-102 seem to be proper for this project.

Table 9. Ferrite materials characteristics

	SAT.MAG $4\pi M_s$	Lande Fac.	Reso. Linewidth	Dielectric constant	f_m
TT2-2750	2750G±10%	2.2	≤540 Oe	12.8±5%	8.47
TT1-102	2150G±10%	2.19	≤315 Oe	13±5%	9.24

There exist a lot of dielectric materials with the same dielectric constants as the chosen ferrite TT2-2750. The preferable two are the Roger AD1000L and AD 600L. The properties of the Roger PCBs are presented in Table 10. Each one of them can be used for a different example, the first one for a circulator device has a centre frequency of 12 GHz, and the second one can be a very good option for 18 GHz circulator.

Table 10. The properties of the Rogers PCB

	Dielectric constant	Dielectric Loss TAN.
AD 1000L	10.7±5%	≤0.0023
AD 600L	6.15±5%	≤0.0023

So, in terms of the desired requirements, the AD 1000L, AD 600L and TT2-2750 seem to be proper for the design of 9-18 GHz circulator.

5.5.3 The calculation of the coupling angle

In Fig. 5.8, it clearly appears that if the coupling angle chosen is 0.51 and $\frac{\varepsilon_d}{\varepsilon_f}$ =1, both curves intersect each other in the desired range.

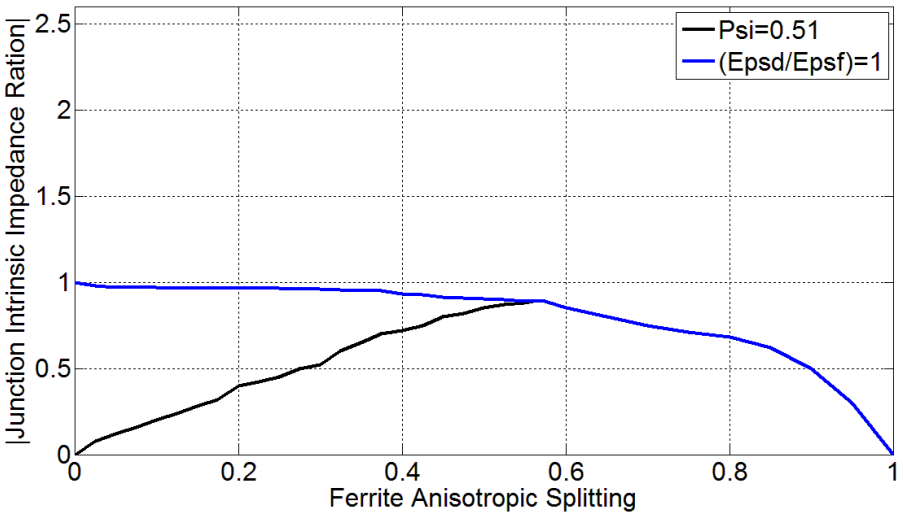

Fig 5.8 The second circulation condition for Ψ=0.51 and impedance ratio equation

5.5.4 The calculation of both the Radius and the Thickness characteristics of Ferrite Disk

As the operation region is below resonance, the anisotropic splitting value $\left|\frac{k}{\mu}\right|$ is directly equal to the ratio $\frac{f_m}{f}$. In Fig. 5.8, each anisotropic value contributes to a different SR value. Which means, for every frequency value in the band, a different radius is obligatory.

$$f_0 = \sqrt{f_m 2 f_m} = f_m\sqrt{2} = 12.72\ GHz \qquad (5.6)$$

So, the anisotropic ratio equal to:

$$\left|\frac{k}{\mu}\right| = \frac{f_m}{f} = 0.67 \tag{5.7}$$

This anisotropic splitting value is corresponding to SR=1.58, where R is the radius of the ferrite disk and S is the propagation constant in ferrite.

$$S = (\frac{\omega}{c})(\mu_{eff}\varepsilon_f)^{1/2} \tag{5.8}$$

For below resonance $\mu = 1, k = \frac{f_m}{f}$:

$$\mu_{eff} = \frac{(\mu^2 - k^2)}{\mu} = \frac{(1^2 - 0.67^2)}{1} = 0.55 \tag{5.9}$$

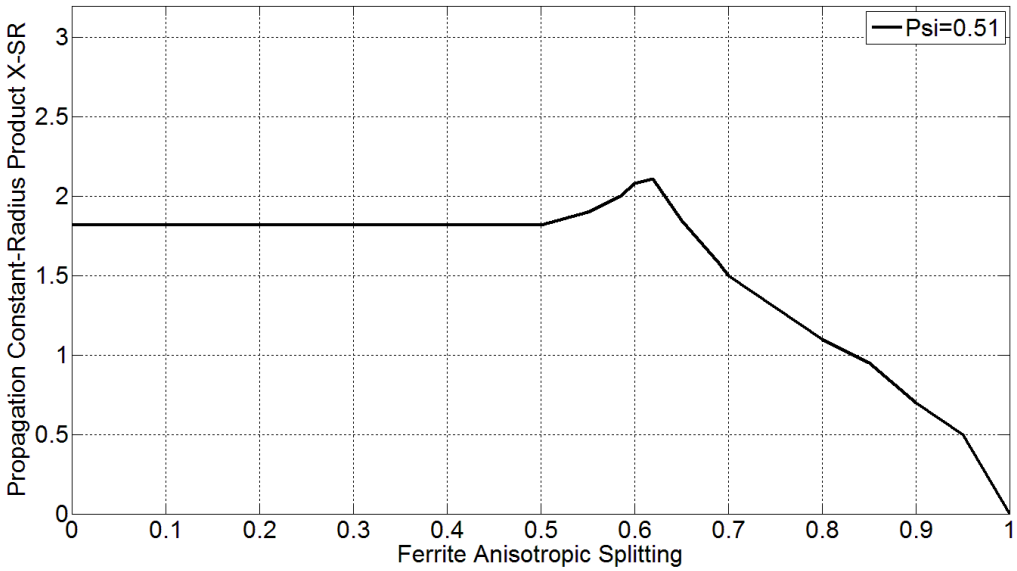

Fig 5.9 The first circulation condition for 0.51

The use of the propagation constant formula at our centre frequency gives,

$$S = \left(\frac{2\pi\ 12.72\ 10^9}{3\ 10^8}\right)(0.55\ 12.8)^{1/2} = 706.85 \qquad (5.10)$$

Thus, the radius of the ferrite material is R=2.23 mm.

Wu and Rosenbaum suggest using a good approximation SR=1.2 that provide a smaller radius to improve the performance in the tightly coupled designs. Hence, the new radius used according to Wu and Rosenbaum is going to be R=1.73 mm.

Finally, the last parameter that has to be calculated is the width of the transmission lines ($\boldsymbol{W_{int}}$), that can be determined easily by using equation (5.1), so by triangular properties.

W_{int}=0.915318 mm

5.5.5 Analytical design of Impedance transformer

Here the use of the same optimization method introduced in previous chapters is imperative to make some changes on the script used, in order to adapt it to the characteristic parameters of the ferrite accompanied by its position and dimension. The use of the equation (4.2) has the same purpose, to adapt the port of the circulator and the 50 ohms in-output ports.

Thus, the two cascaded quarter-wave impedance transformers have characteristic impedance of 68.84 Ω and 50 Ω to transform port impedance from 58.40 Ω to 50 Ω over a moderate bandwidth. Fig. 5.10 shows the design of the ports impedance transformers.

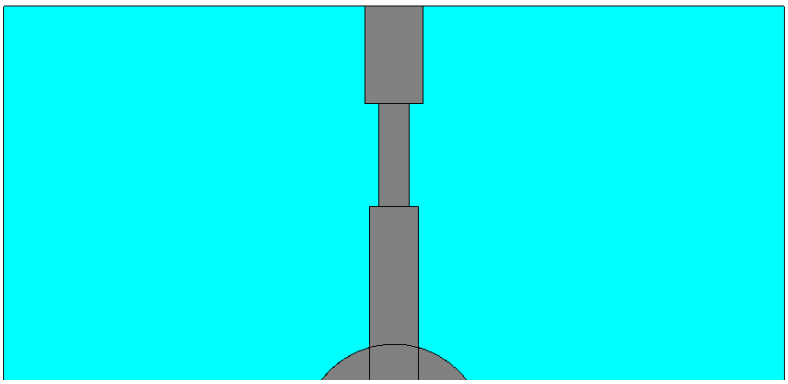

Fig 5.10 Ports impedance transformer

Now the corresponding design characteristics for the impedances found are:

W_int= 0.9153 mm, L_int= 4.3402,
W_match= 0.575720 mm, L_match= 1.950510 mm,
W_50= 1.1 mm, L_50= 1.8395 mm

In Fig. 5.11, the Y-junction circulator with the impedance transformers is shown. The overall structure is matched to 50 Ω, so can be easily connected to connectors.

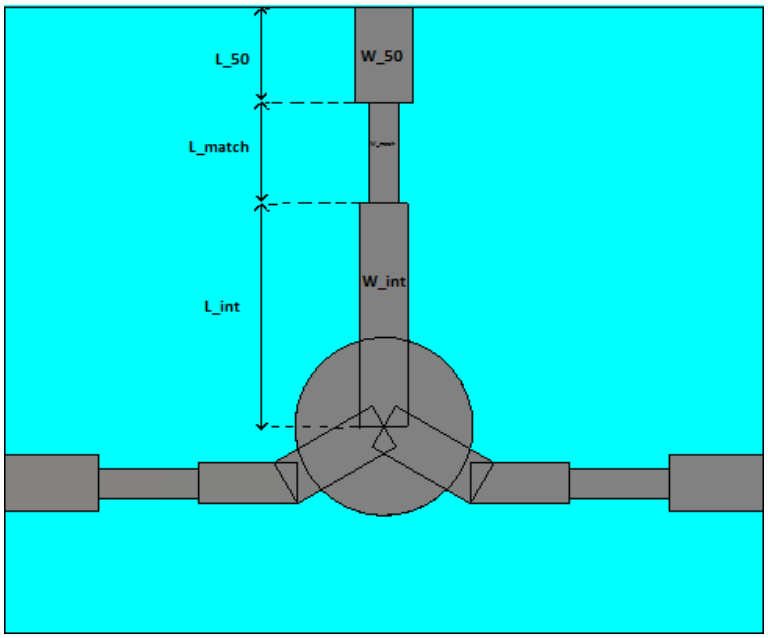

Fig 5.11 Y-junction circulator with impedance transformers

5.5.6 Simulation results of the circulator designed using the analytically Frequency Band method

The next section summarizes the design parameters values of the 12 GHz circulator. The Fig. 5.12 shows the first simulation results obtained by just using the mathematical approach proposed. Those results are promising due to the good levels in terms of adaptation, isolation and transmission parameters. Those results represent a very good starting point to the optimization process, with good levels of the return loss and the isolation parameters, so that both are below -10 dB. All the insertion loss values are acceptable, with 1.15 dB as the maximum insertion loss obtained from the S-parameter (S_{13}) of the third port.

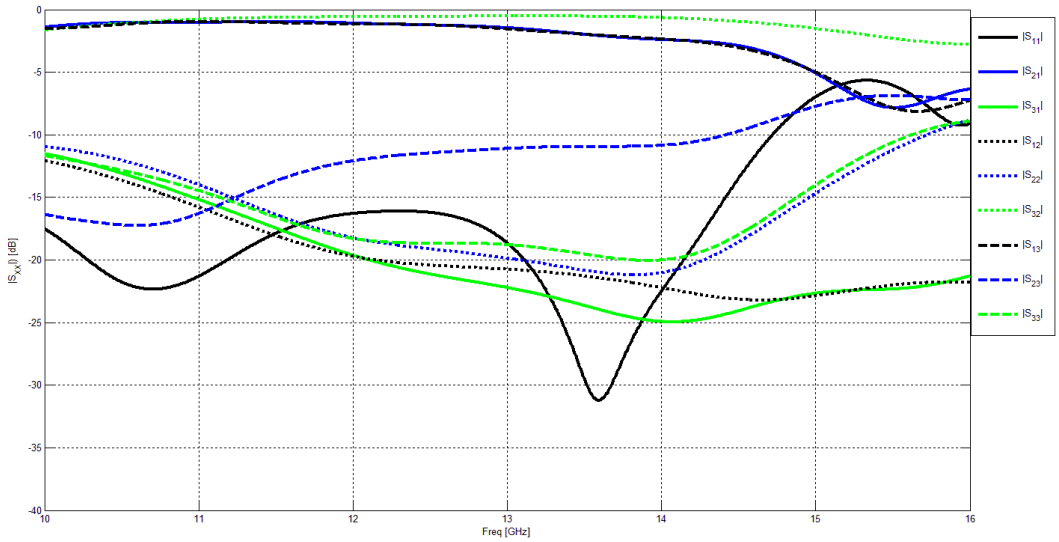

Fig 5.12 Simulation results of first try circulator

5.5.7 Simulation results of optimized Y-junction circulator

As it was mentioned before, the first try results represent the input values for the optimization process. The GA optimization keeps modifying the structure

with taking in consideration the cost function value, till it gets to a point that the cost function remains constant. The Fig. 5.13 shows the optimized structure.

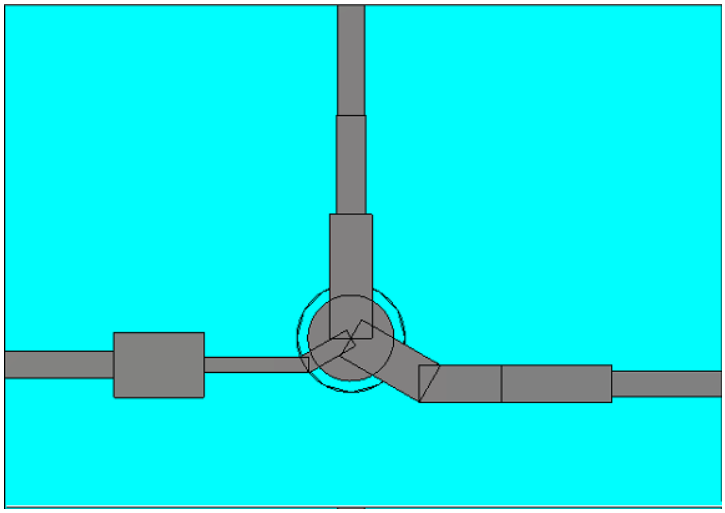

Fig 5.13 Optimized Circulator circuit

The process changed several dimension variables like the impedance lines matching and even the radius of the conductor covered the ferrite disk. It is clearly observed that the ferrite top area is not totally covered with the dielectric. The results obtained show that the surface of the contact area between dielectric and the ferrite materials has a big influence on the performance of the circuit. This is due to the magnetic field created by the ferrite material and the share goes to the dielectric part. The creation of induced electric field also creates another induced magnetic field.

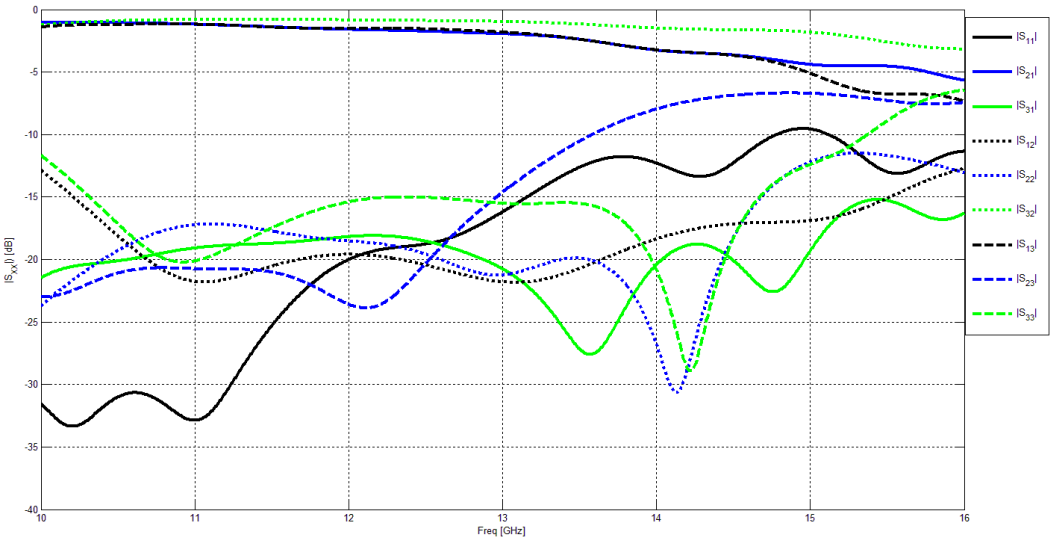

Fig 5.14 The results of the optimization process for 12 GHz Y-circulator

The results show very good adaptation levels, so that the return loss and the isolation are below 15 dB at the centre frequency (12 GHz). It also shows the good levels obtained of the transmission parameters, with values higher than 1.5 dB. The reliable and acceptable results are just another reason for the continuation of the exploitation and the development of the optimization programmes, in order to decrease the calculation time or even the development of a platform for some software, that gives the users an easy access and design of several electronic devices circuits with the possibility of the optimization of one particular parameter of several once.

5.6 Conclusion

Chapter 5 introduces the proposed optimization method for a novel electronic device named wideband microstrip circulators. The proposed circulators are applicable in two different frequency ranges. It is used as duplexer to share common antenna between transmitter and receiver or can be used as Isolator to protect test equipment from undesired reflections. It helps in protecting circuit elements from reverse signal reflections due to mismatch at junctions, cross junctions, at the input and output ports.

First, the method to design the stripline wide band circulators was used to determine the first dimension for the circulators proposed in this chapter. The favourable simulation results displayed in chapter 5 proves that the input for the optimization process is a key point in the efficiency of the genetic program. The optimization process in this unit takes into account more geometrical variables than the one used before such as the shape and the position and even the dimension of surface contact of the ferrite disk. The number of input variables has a direct influence on the processing time and the accuracy of the programme. The increase of input variables increases the calculation leading to a higher processing time but a higher accuracy. Therefore, an error margin was set in the simulation to avoid any inaccuracy. With the error margin, the results obtained by the optimization process displays again an improvement on all the parameters level comparing to the first results obtained from the mathematical method introduced.

To sum up, the proposed work has been able to prove the accuracy of our optimization process in different devices in different technologies, topologies in different frequency band applications.

Chapter 6:

Conclusion and future work

This Thesis raises the methodology and the challenges of **"the design of filtering and multiplexing RF devices and structures for wireless and satellite communication applications"**. The work during this period has been carried out at the Signal Theory, Telematics and Communications Department at the University of Granada (UGR). The main objectives of this thesis were the realization, the analytical, numerical, and experimental studies of different electronic devices. The innovation of this work is the development and the adaptation of different optimization programs to fit and work on generally any electronic device and specifically on ”Filters, phase shifters and circulators”. The various experiments demonstrated the feasibility of fabrication of all the devices mentioned in different technologies also in frequency bands widely used in telecommunications systems, specifically satellites telecommunication (Ku band- K band- W band) and applications in Worldwide Interoperability for Microwave Access and Wireless Local Area Network. The expected performance during the design process of the devices manufactured to provide a good prototype are low level of insertion and reflection losses, small footprint and low cost and ease of integration.

A State of the Art study, **in chapter 2**, made it possible to recall the different technologies and typologies of those devices. The planar technologies were chosen because of the different advantages, such as the low cost and ease

of the manufacturing process and the good interconnection with the microwave components. The waveguide structure was an obvious choice for the tuneable filter because of the simplicity in integrating the carbonic material into the structure with the very high possibility of the achievement of good results. A bibliographic study of magnetic media has made it possible to recall the different forms of magnetism and the different types of ferrites used in microwave applications. The need for miniaturization as well as the high-frequency operation led to the choice of "nickel ferrites" as a magnetic material to be integrated into the circulator.

Chapter 3 to 5 present the outcomes of the designs that matter of research in this work. In all those proposed devices were studied and modelled analytically and numerically using Matlab software and MWS CST electromagnetic simulation software before the manufacturing process. Through these chapters, they are also provided the optimization algorithms used along the Thesis. The optimization program implemented in MATLAB used in this work based on the genetic algorithm. The choice of the MATLAB software is due to its provision a high-performance language for technical computing which makes the results provided by the genetic algorithms in this thesis reproducible. The second part of the process is made by CST STUDIO SUITE software, which is used to simulate the design of the filter and to provide the transition coefficient S in regards to the frequency, which is used as input in the algorithm Genetic to evaluate the cost function. The need of good input values makes our first results a good candidate to make the computing process efficient and provide a lower processing time for a complex calculation. The introduction of Genetic Algorithm as a numerical optimization program gives the full control of the variation of the optimization variables and their influences on the final result. The dimensions and the positions of the transformers were the metrics used to qualify the efficiency off the optimization. Moreover, the examination of the results obtained in every iteration by calculating the cost function, then evaluating it depending on the criteria area defined, without also forgetting to take in account the main goal of the optimization.

Chapter 3 englobes the methodology of the design and the fabrication process of the pass-band filter for different topologies and technologies. The investigation covers first the common numerical methods used to calculate the resonators coupling matrix in the recent literature. We start with the most common method in literature used for the numerical calculation which is Chebyshev low pass topology filter models. We finish with the general method which is the Gradient based method, with passing by the Polynomial method and the Rotation method to provide a metrology for the design process. Thus, after the introduction of the methodologies used for the determination of the resonators coupling coefficients, comes the choice of the topology. This is a very important step for the design of a filter, the key enabler of the investigation. It gives a previous global view to the final structure of the filter. Defines the nature of coupling between the resonators, if it has to be self-coupling, main line coupling and also defines the nature of cross-coupling if they are necessary and need it. The choice of the topology also plays a very important role in the choice of the method to calculate the coupling matrix. The complexity of the topology affects directly the difficulty and complexity of finding the coupling matrix coefficients.

The chapter also highlights two different methods on how the coupling matrix coefficients can be converted to geometrical values. The first method is more general and based on electromagnetic iteration simulation method. So, it does not take in consideration the technology of the filter. But it depends directly on the results of the simulation which leads to a very high calculation time to find the right spacing values. The second method investigated, is more specific. It is based on mathematical equations for open loop models proposed by Jia-Sheng Hong and Michael J. Lancaster for the planar technologies and it takes in consideration the dielectric and some of the structure parameters to find the

exact spacing values for the circuits. So, it is less complicate and it does not take long time because no needs for any simulation process.

Chapter 4 illustrates the different results obtained for reconfigurable microstrip phase shifter devices in two different bands, Ku band and Ka band. It also presents the key points of the functionality and the efficacy of the genetic algorithm. All the designs are based on 3 dB/90° hybrid couplers with two ports connected to reflective circuit loads. The novelty is the use of a non-sequential impedance transformer to improve the adaptation of the LC reflective circuits with the hybrid couplers. These devices have been also validated through measurements and quite promising results have been obtained and published. All the results obtained by the optimization procedure validated the methodology of the design of the prototypes. The proposed designs can be categorised as novel and applicable for multiple applications. One of the applications can be the reconfigurable phased arrays such as transmit arrays or reflect arrays.

Chapter 5 introduces an optimization-based design method for the wideband microstrip circulators. The proposed circulators are applicable in two Ku band frequencies. It can be used as duplexer to share common antenna or as an isolator for the protection of equipment from undesired reflections. Due to the similarity of operation of the stripline and planar circulators, the analytical study was mainly based on the analytical modelling of the stripline circulator. This work makes it possible to have the dimensions of the circulator as well as its performances by calculating the transmission parameters S. The first circuit parameters have been determined using the method for designing Stripline circulators. The method presented the continuous tracking technique by Wu and Rosenbaum, which is based on the Green's function approach and provided for the design of one octave band circulators. The favourable simulation results prove the need of good input values for the efficiency and the convergence of the genetic program to the right solution. Then, the use of Genetic Algorithm makes the optimization of the results possible. It is important to highlight that the optimization process of this circuit takes in consideration more geometrical

parameters than the previous ones, due to the introduction of the magnetic material into the circuits. Some of the new variables are the shape, the position and even the dimension of surface contact of the ferrite disk. The number of input variables has a direct influence on the processing time and the accuracy of the programme. The increase of input variables increases the calculation leading to a higher processing time but also to higher accuracy.

The proposed work on this Thesis has been able to prove the accuracy of our optimization process in different electronic devices, with easy implementation without facing any problems in using different technologies, topologies or even work bands. At the same time, as mentioned before, the analytical studies and the composite materials models combine with the optimization scripts either the Algorithm genetic or the Gradient based have introduced new dimensional into the CST simulator, opens plenty of new doors of possibilities and opportunities to explore new fields of work and even create easy solution for some of the most delicate problems, such as, design complexity, signal speeds or even the electromagnetic (EM) interconnect modelling.

However, there are some challenges we face it all along the way. One of the major challenges in this work has been the ability to represent and digitally simulate (CST) the magnetic and the carbonic materials in its composites form. It was necessary to modify the magnetic properties, the value of the saturation magnetization and to take into account the volume concentration that for the Ferrite materials. Moreover, the dimension of the different layers that form and make the carbonic pins work appropriately. The realization and the implementation of different structures were the important part of the experimental work. Many difficulties were encountered during the various technological stages. The adhesion between the different layers, the etching, etc. are good examples of that challenges. The microwave characterization is the final step to validate all the experimental work. This was not always obvious because of the difficulties of connecting the contacts to the samples, due to the no homogeneously of the surfaces (surfaces are not always homogeneous).

The performance of the prototypes can be always improved. For that we present several ways of working for a resolution of certain difficulties:

Analytical study:

In this work an approximation has been introduced to predict the properties of the composite magnetic and carbonic materials. The new models have been proposed to suitably simulate analytically and electromagnetically those materials. But these models take into account just the dimension side but didn't take any of the materials characteristics into account such as the size of the magnetic particles distributed randomly in the composite, their arrangement and their interactions or even the dimensions of the oxide and semiconductor layers and their impact on the performance of the graphene material. All of these lines can be improved, in particular by taking into account RF demagnetizing fields and dispersion in particle sizes.

Numerical study:

The MWS CST software used for 3D electromagnetic simulations is limited, especially in exploring new materials performance such as graphene material and introducing all the right influenceable parameters. Then model of the graphene material can analytically with our model which seems more appropriate and introduce the values in CST software provide the models of the device as digitally as possible. The ferrite materials if the interest of composite magnetic materials is to be demonstrated, it remains to show the possibility of having oriented composites sufficiently concentrated to ensure better functionality of non-reciprocal microwave devices. Several parameters are decisive: intensity of the applied field during the development of the micro and the nanocomposite, concentration of magnetic material as high as possible and parameters of elaboration and fabrication of the device optimized (adhesion of the different layers, homogeneity and others).

Microwave Characterization:

In the possibility of the realization of the tunable waveguide filter using the carbonic material. The lack of a calibration kit really suitable for this configuration is hard to be solved. Calibration methods should therefore be developed to refine the quality of microwave measurements.

To sum up, the studies conducted during this thesis clearly showed the feasibility of planar and waveguide technologies of different devices with magnetic and carbonic materials. All the improvement routes listed above probably open the way for further studies leading to the production of efficient and industrialize micro-nanocomposites.

Contributions of the scientific work

Scientific JCR journals

- Mohamed T. ElKhorassani, Angel Palomares-Caballero, , Antonio Alex-Amor, Cleofás Segura-Gómez, Pablo Escobedo, Juan F. Valenzuela-Valdés and Pablo Padilla Electronically Controllable Phase Shifter with Progressive Impedance Transformation at K Band, Applied Sciences, Passive Planar Microwave Devices, 2019

International conference communications

- Mohamed Taha El Khorassani, Miguel Angel Vaquero, Ángel Palomares, Juan F. Valenzuela-Valdés, Pablo Padilla y Naima Amar Touhami, "Electronically tunable phase shifter with enhanced phase behaviour at Ku Band", European Conference on Antennas and Propagation, EuCAP 2018, London, UK
- Mohamed Taha El Khorassani, Abdelkrim Farkhsi, Naima Amar Touhami, "General synthesis method for Chebyshev filtering function of pass-band filters", ICCWCS' 16 FST of Settat, University Hassan 1st Morocco, 2016.
- Mohamed Taha El Khorassani, Abdelkrim Farkhsi, Naima Amar Touhami, "An Approach Synthesis Method for Coupling Matrix pass-band Filters", The 5th Mediterranean Congress of Telecommunications, Tetouan, Morocco, 2016.

National conference communications

- Mohamed Taha El Khorassani, Miguel Angel Vaquero, Ángel Palomares, Juan F. Valenzuela-Valdés, Pablo Padilla y Naima Amar Touhami, "Desfasador electrónicamente reconfigurable en banda Ku optimizado con algoritmos genéticos", XXXIII Simposio Nacional de la Unión Científica Internacional de Radio, URSI 2018, Granada, España

- Ángel Palomares-Caballero, Antonio Alex-Amor, Mohamed Taha ElKhorassani, Juan Valenzuela-Valdés, Pablo Padilla." Estudio de tolerancias en un array en banda V fabricado mediante estereolitografía (SLA) y metalizado " URSI 2019, Sevilla, España

Other JCR publications related to the doctoral period:

- M.T. ElKhorassani, A. Palomares-Caballero, A. Alex-Amor, J.C. González-Macías, A. Valenzuela-Valdés and Pablo Padilla "Near field pattern uniformity for high resolution Magnetic Resonance Imaging (MRI) systems based on metaheuristic optimization". the International Journal of RF and Microwave Computer-Aided Engineering, edition 2019.

REFERENCES:

[1] **J.S. Hong and M.J. Lancaster** "Microstrip filters for RF/microwave applications*". New York: Wiley, 2001.*

[2] **C. HUNTER, L. BILLONET, B. JARRY and P. GUILLON** "Microwave. filters – applications and technology," *IEEE Trans. Microwave Theory Tech.*, vol. 50, no. 3, pp. 794–805, 2002.

[3] **G. MATTHAEI, L. YOUNG and E. M. T. JONES** "Microwave filters, impedance-matching networks, and coupling structures*" Boston, Artech House*, 1980.

[4] **R. LEVY, R. V. SNYDER and G. MATTHAEI** "Design of microwave filters" *IEEE Trans. Microwave Theory Tech.*, vol. 50, no. 3, pp. 783–793, 2002.

[5] **T. VUONG** "Contribution à l'étude des discontinuités dans les guides d'ondes métalliques creux Application aux antennes et aux filtres", *Thèse de Docteur de l'Institut National Polytechnique de Toulouse, Décembre 1999.*

[6] **P. COMBES** "Circuits passifs, Propagation, antennes" *Dunod, Paris,* 1996*.*

[7] **S. YIN, T. VASILYEVA and P. PRAMANICK** "Use of three-dimensional in the synthesis of waveguide round rod bandpass filters" *International Journal of RF and Microwave CAE*, vol. 8, pp. 484-497, June 1998.

[8] **M. CHAUBET** "Filtres microondes à résonateurs diélectriques" *Thèse de Docteur de l'Université de Limoges,* Juillet 1987

[9] **E. RAMPNOUX** "Analyse, conception et réalisation de filtres planaires millimétriques appliqués à la radiométrie spatiale" *Thèse de Docteur de l'Université de Limoges,* Mars 2003.

[10] **P. LENOIR,** "Développement de méthodes et d'outils dédiés à la conception des dispositifs de filtrage microonde complexes" *Thèse de Docteur de l'université de Limoges,* Septembre 2005.

[11] **J. UHER, J. BORNEMANN and U. ROSENBERG** "Waveguide components for antenna feed systems" *Theory and CAD. Norwood*, Artech House, 1993.

[12] **E. OFLI** "Analysis and design of microwave and millimeter-wave filters and diplexers" *Thèse de Docteur de l'Institut Technology Zurich,* 2004.

[13] **S. COHN** "Parallel-coupled transmission-line resonator filters" *IRE Trans. Microwave Theory Tech.*, vol. 10, no. 4, pp. 223–231, 1958.

[14] **M. CHATRAS** " Filtres micro-usinés à bande étroite pour les applications spatiales" *Thèse de Docteur de l'Université De Limoges,* 15 Décembre 2003.

[15] **L. THOUREL** "Calcul et conception des dispositifs en ondes centimétriques et millimétriques, Circuits passifs" *Cepadues Editions,* 1988.

[16] **M. GUGLIELMI** "Simple CAD procedure for microwave filters and multiplexers" *IEEE Trans. Microwave Theory Tech*., vol. 42, no.7, pp. 1347-1352, July 1994.

[17] **S. AMARI, J. BORNEMANN, W. MENZEL and F. ALESSANDRI** "Diplexer design using pre-synthesized waveguide filters with strongly dispersive inverters" *IEEE MTT-S Digest*, pp. 1627-11630, 2001.

[18] **Y. KOBAYASHI and M. MINEGISHI** "Precise design of a bandpass filter using high dielectric ring resonators" *IEEE Trans. Microwave Theory Tech.*, vol. 35, pp. 1156–1160, December 1987.

[19] **O. PIQUET, D. CROS and AL** "New design of high Q sapphire resonator with distributed Bragg reflector" *IEEE Symp. Microwave Theory Tech.*, vol. 3, pp.1993-1996, 2002.

[20] **D. KAJFEZ and P. GUILLON** "Dielectric Resonators" *Vector Fields, Oxford, Mississippi,* 1986.

[21] **S. AMARI, R. VAHLDIECK and J. BORNEMANN** "Full-wave design and analysis of bandpass filters using 1/8-cut high-dielectric resonators" *Proc. 28 th European Microwave Conf.*, *Amsterdam, The Netherlands*, pp. 424– 427, October 1998.

[22] **R. LEVY** "Tapered corrugated waveguide low-pass filter" *IEEE Trans. Microwave Theory Tech.,* vol. 21, no 8, August 1973.

[23] **V.A. LABAY and J. BORNEMANN** "A new evanescent mode filter for densely packaged waveguide application" IEEE *Symp. Microwave Theory Tech.,* pp. 901-904, 1992.

[24] **Y. L. ZHANG, K. WU, J. X. CHEN and H. J. TANG** "Novel substrate integrated waveguide cavity filter with defected ground structure" *IEEE Trans. Microwave Theory Tech.,* vol. 53, no. 4, pp. 1280 – 1287, April 2005.

[25] **F. XU** "Guided-wave and leakage characteristics of substrate integrated waveguide" *IEEE Trans. Microwave Theory Tech.,* vol. 53, no. 1, pp. 66 – 73, January 2005.

[26] **Z. C. HAO** "Multilayered substrate integrated waveguide (MSIW) elliptic filter" *IEEE Microwave and Wireless Components Letters,* vol. 15, no. 2, pp. 95 – 97, February 2005.

[27] **Ke Bi, Wenting Zhu, Ming Lei, and Ji Zhou Citation** "Magnetically tunable wideband microwave filter using ferrite-based metamaterials", Applied Physics Letters 106, 173507 (2015).

[28] **J. R. Stanec and N. S. Barker** "Fabrication and integration of micromachined submillimeter-wave circuits," IEEE *Microw. Wireless Compon Lett., vol. 21, no. 8, pp. 409–411, Aug. 2011.*

[29] **Pham N.T., Lee G-A., De Flaviis F.** " Microstrip antenna array with beamforming network for WLAN applications ", *Antennas and Propagation Society International Symposium, 2005 IEEE, Vol. 3a, pp. 267-270, Jul. 2005.*

[30] **Cheng S., Ojefors, E., Hallbjorner, P., Rydberg, A.,** "Compact reflective microstrip phase shifter for traveling wave antenna applications", *IEEE Microwave and Wireless Components Letters, Vol. 16, No. 7, pp. 431- 433, Jul. 2006.*

[31] **Chih-Hsiang Ko; Ho, K.M.J.; Rebeiz, G.M.,** "An Electronically-Scanned 1.8–2.1 GHz Base-Station Antenna Using Packaged High-

Reliability RF MEMS Phase Shifters," *Microwave Theory and Techniques, IEEE Transactions on, vol.61, N°.2, pp. 979-985, Feb. 2013.*

[32] **Guan-Leng Tan, Robert E. Mihailovich, Jonathan B. Hacker, Jeffrey F. DeNatale and Gabriel M. Rebeiz, "**Low-Loss 2- and 4-bit TTD MEMS Phase Shifters Based on SP4T Switches", *IEEE Trans. Microwave Theory Tech., vol. 51, pp. 297–304, Jan. 2003.*

[33] **Rebeiz, G.M.; Tan, Guan-Leng; Hayden, Joseph S.,** "RF MEMS phase shifters: design and applications," *Microwave Magazine, IEEE, vol.3, N°2, pp.72-81, Jun. 2002.*

[34] **Tan G.L., Mikailovitch R.E., Hacker J.B., Denatale J.F., Rebeiz G.M.,** "Low loss 2- and 4-bit TTD MEMS phase shifters based on SP4T switches", *IEEE Transactions on Microwave Theory and Techniques, vol.51, N°1, Jan. 2003.*

[35] **Hacker J.B., Mihailovich E., Kim M., Denatale J.F.,** "A Ka-band 3-bit RF MEMS true time delay network", *IEEE Transactions on Microwave Theory and Techniques, vol.51, N°1, Jan. 2003.*

[36] **Cetinoneri, B.; Atesal, Y.A.; Jeong-Geun Kim; Rebeiz, G.M., «**CMOS 4×4 and 8×8 Butler matrices," *Microwave Symposium Digest (MTT), 2010 IEEE MTT-S International, vol., N°., pp. 69-72, 23-28, May 2010.*

[37] **Jad B. Rizk and Gabriel M. Rebeiz,** "W-Band Microstrip RF-MEMS Switches and Phase Shifters", *Microwave Symposium Digest, IEEE MTTS International, pp.1485-1488, Jun. 2003.*

[38] **Gabriel M. Rebeiz,** RF MEMS: From research to product, "Low-Loss RF MEMSPhase Shifters", *Presented in Limoges, Fev. 2014.*

[39] **M.E. Hines,** "Reciprocal and nonreciprocal modes of propagation in ferrite stripline and microstrip devices", *IEEE Trans. MTT, Vol. 19, pp. 442-451, 1971.*

[40] **C.P. Wen,** "Coplanar waveguide: A surface strip transmission line suitable for nonreciprocal gyromagnetic device applications", *IEEE Trans. MTT, vol. 17, pp. 1087-1090, 1969*

[41] **B. Bayard, «** Contribution au développement de composants passifs magnétiques pour l'électronique hyperfréquence », *PhD thesis, Jean Monnet University, Saint-Etienne, pp. 30-32, octobre 2000.*

[42] **H. Bosma,** "On Stripline Y-circulation et UHF", *IEEE Trans. MTT, Vol.12, pp.61-72, Jan 1964.*

[43] **E.K.N. Yung, D.X. Wang, R.S. Chen,** "Ferrite circulators", *Encyclopedia of RF and Microwave Engineering, vol.2, pp.1462, 2005.*

[44] **P-F. Combes, R. Crampagne,** « circuits passifs hyperfréquence : éléments passifs non réciproques ». *Engineering Technique, Electronic Treaty, E1 404, 2002.*

[45] **C.E. Fay and R.L. Comstock,** "Operation of the Ferrite Junction Circulator", *IEEE Trans.MTT, Vol.13, pp.61-72, January 1995.*

[46] **J. Helszain, "**Fabrication of very weakly and weakly magnetized microstrip circulators", *IEEE Trans. MTT, Vol.46, No5, May 1998.*

[47] **E. Bènevent,** « Contribution à l'étude et à la réalisation d'un circulateur hyperfréquence à couche magnétique dans la bande 40-50 GHz », *PhD thesis, Jean Monnet University, Saint-Etienne, octobre 2006.*

[48] **H. How, S.A. Oliver, S.W. McKnight, P.M. Zavracky, N.E. McGruer, C. Vittoria, R. Schmidt,** "Theory and experiment of thin film junction circulator", *IEEE Trans. Microwave Theory & Tech., Vol. 46, N°11, pp 1645-1653, Nov. 1998.*

[49] **R.S. Chen, E. K.N. Yung,** "Analysis of Microstrip Circulator with a Ferrite Sphere", *IEEE Antennas and Propagation Society International Symposium, Vol. 1, pp 384-387, 2002.*

[50] **A. Guennou,** « Etude magnétostatique et électromagnétique de circulateurs miniatures pour les modules actifs émission/réception des systèmes de télécommunications », *PhD thesis, University of Western Brittany, Brest, 2007.*

[51] **A. Yalaoui, J.W. Tao, M. Maignan, C. Laporte, C. Zanchi,** "Cryogenic Microstrip Ferrite Circulator Development for Superconductive

Multiplexer Use", *International workshop on microwave filters, october 2006.*

[52] **http://www.questmw.com**

[53] **N. Ogasawara, M. Kaji,** "Coplanar-guide and slot-guide junction circulators", *Electronics Letters, Vol. 7, N°9, pp. 220-221, 6th May 1971.*

[54] **K. Koshiji, E. Shu,** "Circulators using coplanar waveguide", *Electronics Letters, Vol. 22, N°19, pp. 1000-1002, 11th Sep. 1986.*

[55] **K. Oshiro, H. Mikami, S. Fujii, T. Tanaka, H. Fujimori, M. Matsuura, S. Yamamoto,** "Fabrication of circulator with coplanar waveguide structure", *IEEE Trans. Magnetics, Vol. 41, N°10, pp. 3550-3552, Oct. 2005.*

[56] **Y. Konishi,** "Lumped element Y circulator", *IEEE Trans. Microwave Theory Tech., MTT-13 (6), pp. 852-864, Nov. 1965.*

[57] **Y. Konishi,** "New Theorical Concept for Wide Band Gyromagnetic Devices", *IEEE Trans. on Magnetics, pp. 505-508, Sept. 1972.*

[58] **T. Miura, M. Kobayashi, Y. Konishi,** "Optimization of a Lumped Circulator Based on Eigenvalues Evaluation and Structural Improvement", *IEEE Trans. Microwave Theory & Tech., vol. 44, pp. 2648-2654, Dec. 1996.*

[59] **M. Ahmad,** *"4G and 5G wireless: how they are alike and how they differ", 2015, June 10.*

[60] **NGMN Alliance and M. Iwamura,** *"NGMN View on 5G Architecture", May 14, 2015.*

[61] **V. Belvitch**, "Recent development in filter theory", *IRE Trans. Circuit Theory, Vol.5, no.4, pp. 236-252, Dec.1958.*

[62] **A.E. Atia and A.E. Williams,** "New type of waveguide band pass filters for satellite transponders", *COMSAT Tech. Rev., Vol. 1, no. 1, pp. 21-43, 1971.*

[63] **Richard J. Cameron,** "General Coupling Matrix Synthesis Methods for Chebyshev Filtering Functions", *IEEE Transactions on Microwave Theory and Techniques*, Vol. 47, No. 4, 1999.

[64] **Richard J. Cameron,** "Advanced Coupling Matrix Synthesis Techniques for Microwave Filters", *IEEE Transactions on Microwave Theory and Techniques*, Vol. 51, No. 1, 2003.

[65] **M. Radmanesh,** "RF & Microwave Design Essentials", Authorhouse, 2007.

[66] **X. Shang Y. Wang G.L. Nicholson M.J. Lancaster,** "Design of multiple-pass-band filters using coupling matrix optimization" IET Microwaves, Antennas & Propagation

[67] **Talal F. Skaik,** "Synthesis of Coupled Resonator Circuits with Multiple Outputs using Coupling Matrix Optimization", PhD Thesis at the University of Birmingham for the degree of Doctor of Philosophy School of Electronic, Electrical and Computer Engineering the University of Birmingham March 2011.

[68] **R. Cameron, C. Kudsia, and R. Mansour,** "Microwave filters for communication systems". Wiley, 2007.

[69] **J.D. Rhodes and S.A. Alseyab.**, "The generalized Chebyshev low-pass prototype filter"*. IEEE Trans. Circuit Theory* 8, 113-125, 1980.

[70] **Eden Corrales Lopez,** "Analysis and Design of Bulk Acoustic wave filters based on Acoustically Coupled Resonators". Cerdanyola del Valles (Barcelona), May 2011

[71] **F.R. Gantmacher.** "The Theory of Matrices", Vol.1. Chelsea Publishing, 1959.

[72] **G.L. Matthei, E.M.T Jones, and L. Young,** Microwave Filters, Impedance-matching Networks and Coupling Structures. Artech House, 1980.

[73] **G.L. Matthaei, L. young, E.M.T. Jones,** Microwave Filters, Impedance Matching Networks and Coupling structures, *New York: McGraw-Hill, 1964.*

[74] **H.C. Bell,** "Canonical asymmetric coupled-resonator filter", *IEEE Trans. Microw. Theory*, 30, (9), pp. 1335–1340, 1982.

[75] **Jia-Sheng Hong and Michael J. Lancaster,** "Couplings of Microstrip Square II Open-Loop Resonators tor Cross-Coupled Planar Microwave Filters", IEEE *Transactions on Microwave Theory and Techniques*, Vol. 44, No. 12, 1996.

[76] **S. Amari,** "Synthesis of cross-coupled resonator filters using an analytical gradient based optimization technique", *IEEE Transactions on Microwave Theory and Techniques*, vol. 48, no. 9, pp. 1559-1564, 2000.

[77] **K.C. Gupta, R. Garge, R. Chadha,** "Computer Aided Design of Microwave Circuits", Norwood, MA: Artech House, 1981.

[78] **S. Amari, P. Harscher, R. Vahldieck, J. Bornemann,** "Novel analytic gradient evaluation technique for optimization of microwave structures", IEEE MTT-S International Microwave Symp. Dig., pp. 31-34, Anaheim, USA, June 1999.

[79] **J. H. Holland,** "Adaptation in Natural and Artificial Systems", First MIT Press edition, 1975.

[80] **D.E. Goldberg**, "Genetic Algorithms in Search, Optimization, and Machine Learning", Addison-Wesley Publishing Company, INC, 1989.

[81] **Erick Cantu-Paz**, "Efficient and Accurate Parallel Genetic Algorithms", Kluwer Academic Publishers, 2001.

[82] **K. S. Novoselov, A. K. Geims, S. V. Morozov, D. Jiang, Y. Zhang, S. V. Dubonos, I. V. Grigorieva, and A. A. Firsov,** "Electric field effect in atomically thin carbon films ", science, vol. 306, n 5696, p. 666-669, 2004.

[83] **S. Novoselov**, "The Nobel Prize in Physics 2010 honours two scientists, who have made the decisive contributions to this development. They are Andre K. Geim and Konstantin S. Novoselov, both at the University of Manchester, UK. They have succeeded in producing, isolating, identifying and characterizing graphene. ", 2010

[84] **E.P. Adams,** "Review: E. Schrödinger, Mémoires sur la Mécanique Ondulatoire", Bull. New Ser. Am. Math. Soc., vol. 39, no11, p. 854-854, nov. 1933

[85] **J. Schneider,** "Propriétés Électroniques du Graphite", Université de Grenoble, 2010

[86] **A. H. Castro Neto, N. M. R. Peres, K. S. Novoselov, et A. K. Geim**, "The electronic properties of graphene", Rev. Mod. Phys., vol. 81, no1, p. 109-162, janv. 2009.

[87] **P. R. Wallace,** "The Band Theory of Graphite", Phys. Rev., vol. 71, no9, p. 622-634, mai 1947.

[88] **Henry Mathieu et H. Fanet,** "Physique des Semiconductors et des Composants Electroniques, 6eéd. Paris: Dunod, 2009.

[89] **C. Kittel,** "Introduction to Solid State Physics". New York: John Wiley and Sons, 1996.

[90] **Y. H. Wu, T. Yu, et Z. X. Shen,** "Two-dimensional carbon nanostructures: Fundamental properties, synthesis, characterization, and potential applications", J. Appl. Phys., vol. 108, no7, p. 071301, 2010.

[91] **S. Das Sarma, S. Adam, E. H. Hwang, et E. Rossi**, "Electronic transport in two-dimensional graphene", Rev. Mod. Phys., vol. 83, no2, p. 407-470, mai 2011**.**

[92] **M. I. Katsnelson**, "Graphene: carbon in two dimensions", Mater. Today, vol. 10, no1, p. 20–27, 2007

[93] **D. P. DiVincenzo et E. J. Mele,** "Self-consistent effective-mass theory for intralayer screening in graphite intercalation compounds", Phys. Rev. B, vol. 29, no4, p. 1685, 1984

[94] **. P. Avouris,** "Graphene: Electronic and Photonic Properties and Devices", Nano Lett., vol. 10, no11, p. 4285-4294, nov. 2010.

[95] **J.-N. Fuchs, M. O. Goerbig, et M. Potemski**, "Des électrons sans masse dans une feuillede carbone", Images Phys. CNRS, p. 50–56, 2007.

[96] **P. Avouris, Z. Chen, et V. Perebeinos**, “Carbon-based electronics“, Nat. Nanotechnol., vol. 2, no10, p. 605–615, 2007.

[97] **A. K. Geim et K. S. Novoselov**, “The rise of graphene“, Nat. Mater., vol. 6, no3, p. 183-191, mars 2007.

[98] **S. Novoselov**, “The Nobel Prize in Physics 2010 honours two scientists, who have made the decisive contributions to this development. They are Andre K. Geim and Konstantin S. Novoselov, both at the University of Manchester, UK. They have succeeded in producing, isolating, identifying and characterizing graphene. “, 2010

[99] **J.-H. Chen, C. Jang, S. Adam, M. S. Fuhrer, E. D. Williams, et M. Ishigami**, “Charged-impurity scattering in graphene“, Nat. Phys., vol. 4, no5, p. 377-381, avr. 2008.

[100] **K. I. Bolotin, K. J. Sikes, Z. Jiang, M. Klima, G. Fudenberg, J. Hone, P. Kim, et H. L. Stormer,** “Ultrahigh electron mobility in suspended graphene“, Solid State Commun., vol. 146, no9-10, p. 351-355, juin 2008.

[101] **C. Lee,X. Wei, J. W. Kysar, and J. Hone,** “Measurement of the Elastic Properties and Intrinsic Strength of Monolayer Graphene,” Sci. , vol. 321 , no. 5887 , pp. 385–388, Jul. 2008.

[102] **A. a Balandin, S. Ghosh, W. Bao, I. Calizo, D. Teweldebrhan, F. Miao, and C. N. Lau**, “Superior Thermal Conductivity of Single-Layer Graphene 2008,” Nano Lett., vol. 8, pp. 902–907, 2008.

[103] **W. Cai, A. L. Moore, Y. Zhu, X. Li, S. Chen, L. Shi, and R. S. Ruoff,** “Thermal transport in suspended and supported monolayer graphene grown by chemical vapor deposition,” Nano Lett., vol. 10, no. 5, pp. 1645–1651, 2010

[104] **E. Pop, D. Mann, Q. Wang, K. Goodson, and H. Dai**, “Thermal Conductance of an Individual Single-Wall Carbon Nanotube above Room Temperature,” Nano Lett., vol. 6, no. 1, pp.96–100, Jan. 2006.

[105] **P. Kim, L. Shi, A. Majumdar, and P. L. McEuen**, “Thermal Transport Measurements of Individual Multiwalled Nanotubes,” Phys. Rev. Lett., vol. 87, no. 21, p. 215502, Oct. 2001.

[106] **Y.-M. Lin, K. a Jenkins, A. Valdes-Garcia, J. P. Small, D. B. Farmer, and P. Avouris**, “Operation of graphene transistors at gigahertz frequencies.,” Nano Lett., vol. 9, no. 1, pp. 422–426, 2009.

[107] **Y. Lin, C. Dimitrakopoulos, K. A. Jenkins, D. B. Farmer, H. Chiu, A. Grill, and P. Avouris**, “100-GHz Transistors from wafer-scale epitaxial graphene,” p. 100.

[108] **L. Liao, J. Bai, R. Cheng, Y. Lin, S. Jiang, Y. Huang, and X. Duan,** “Top-gated Graphene Nanoribbon Transistors with Ultrathin High-k Dielectrics,” pp. 2–6.

[109] **J. Cai, P. Ruffieux, R. Jaafar, M. Bieri, T. Braun, S. Blankenburg, M. Muoth, A. P. Seitsonen, M. Saleh, X. Feng, K. Müllen, and R. Fasel**, “Atomically precise bottom-up fabrication of graphene nanoribbons.,” Nature, vol. 466, no. 7305, pp. 470–473, 2010.

[110] **L. M. Malard, J. Nilsson, D. C. Elias, J. C. Brant, F. Plentz, E. S. Alves, A. H. C. Neto, and M. A. Pimenta**, “Probing the electronic structure of bilayer graphene by Raman scattering,” pp. 1–4, 2007.

[111] **Y. Zhang, T.-T. Tang, C. Girit, Z. Hao, M. C. Martin, A. Zettl, M. F. Crommie, Y. R. Shen, and F. Wang**, “Direct observation of a widely tunable bandgap in bilayer graphene.,” Nature, vol. 459, no. 7248, pp. 820–823, 2009.

[112] **Z. H. Ni, T. Yu, Y. H. Lu, Y.Y. Wang, Y. P. Feng, and Z. X. Shen**, “Uniaxial Strain on Graphene : Raman,” vol. 2, no. 11, pp. 2301–2305, 2008.

[113] **R. R. Nair, P. Blake, a N. Grigorenko, K. S. Novoselov, T. J. Booth, T. Stauber, N. M. R. Peres, and a K. Geim**, “Fine structure constant defines visual transparency of graphene.,” Science, vol. 320, no. 5881, p. 1308, 2008.

[114] W. Cai, Y. Zhu, X. Li, R. D. Piner, and R. S. Ruoff, "Large area few-layer graphene/graphite films as transparent thin conducting electrodes," Appl. Phys. Lett., vol. 95, no. 12, p. 123115, 2009.

[115] S. Bae, H. Kim, Y. Lee, X. Xu, J.-S. Park, Y. Zheng, J. Balakrishnan, T. Lei, H. R. Kim, Y. Il Song, Y.-J. Kim, K. S. Kim, B. Ozyilmaz, J.-H. Ahn, B. H. Hong, and S. Iijima, "Roll-to-roll production of 30-inch graphene films for transparent electrodes.," Nat. Nanotechnol., vol. 5, no. 8, pp. 574–578, 2010

[116] J. L. Padilla, P. Padilla, J. F. Valenzuela-Valdes and J. M. Fernandez-Gonzalez, "High-frequency radiating element and modified 3dB/90ºelectronic shifting circuit with circular polarization for broadband reflect array device cells, ¨, *in Electronics Letters,* vol. 50, no. 15, pp. 1042-1043,2014.

[117] P. Padilla, A. Munoz-Acevedo, M. Sierra-Castaner and M. Sierra-Perez, "Electronically Reconfigurable Transmit array at Ku Band for Microwave Applications," *IEEE Transactions on Antennas and Propagation*, vol.58, no. 8, pp. 2571-2579, 2010.

[118] P. Padilla, J. M. Fernández, J. L. Padilla, J. F. Valenzuela-Valdés and M. Sierra-Castañer, "Circularly polarized broadband planar light weight reflect array with eligible pattern for satellite communications in Ku-band", *IET Microwaves, Antennas & Propagation,* vol. 11, no. 4, pp.513-518, 2017.

[119] P. Padilla, J. F. Valenzuela-Valdés, J. L. Padilla, J. M. Fernández-González and M. Sierra-Castañer, "Electronically Reconfigurable Reflective Phase Shifter for Circularly Polarized Reflect Array Systems", *IEEE Microwave and Wireless Components Letters*, vol. 26, no. 9, pp. 705-707, 2016.

[120] M. T. Elkhorassani, A. P Caballero, A. Alex-Amor, C. Segura-Gomez, P. Escobedo, J. F. Valenzuela-Valdes and P. Padilla, " Electronically Controllable Phase Shifter with Progressive Impedance Transformation at K Band", Appl. Sci., 9, 5229, 2019.

[121] M.T. ElKhorassani, M.A. Vaquero, Á. Palomares, J.F. Valenzuela, P. Padilla, and N.A. Touhami, "Electronically tunable phase shifter with enhanced phase behaviour at Ku Band", European Conference on Antennas and Propagation, EuCAP 2018, London, UK.

[122] U. Milano, J. Saunders and L. Davies, " A Y– junction stripline circulator ", IRE Transactions MTT, vol. 8, pp. 346–351, May. 1960.

[123] H. Bosma, "On the principle of stripline circulator", Proceedings IEE, vol. 109, pt. B, suppl. no.21, pp. 137–146, Jan. 1961.

[124] B. A. Auld, « The synthesis of symmetrical waveguide circulator, », IRE Transactions MTT, vol.7, pp. 238–247, Apr. 1959.

[125] H. Bosma, "On stripline Y–circulation at UHF", IEEE Transactions MTT, vol. 12 ,pp. 61–72, Jan. 1964.

[126] H. Bosma, "Performance of lossy H–plane Y circulators, ", IEEE Transactions MTT, vol. 2 ,pp. 273–277, Sep. 1966.

[127] H. Bosma, "A general model for junction circulators, choice of magnetization and bias field, ", IEEE Transactions MTT, vol. 4 ,pp. 587–596, Sep. 1968**.**

[128] P. J. Allen, "The turnstile circulator ", IRE Transactions MTT, vol. 4, pp. 223–228, Oct. 1958.

[129] C. Bownes, "discussion on microwaves ferrites II, ", Proceedings IEEE, vol.109, pt. B, suppl. no.21, pp. 163, Jan. 1962.

[130] V. G. Feoktistov, " diffraction model of Y-circulator, " Radiotekhnika I Electronika, vol. 7, pp. 1773-1768, Oct. 1962.

[131] E. N. Skomal, " Theory of operation of a 3–port Y–junction ferrite circulator,», IEEE Transactions MTT, vol. 11, pp. 117–123, Mar. 1963.

[132] J. B. Davies and P. Cohen, « Theoretical design of symmetrical junction stripline circulators, », IEEE Transactions MTT, vol. 11 ,pp. 506–512, Nov. 1963.

[133] E. Schloemann and R.E. Blight, "Broad-band stripline circulators based on YIG and Li-Ferrit single crystals," IEEE Trans. Microwave Theory Tech., vol. MTT-34, no.12, December 1986.

[134] E. Schloemann and R.E. Blight, "Low-field loss in ferrites-relevance to broadband circulator design," IEEE Trans. Microwave Theory Tech., vol. MTT-34, no.12, December 1992.

[135] R.A. Waldron, "Ferrites: An Introduction for Microwave Engineers," D. Van Nostrand Co., 1961.

[136] B. Lax K.J. Button, "Microwave Ferrites and Ferrimagnetics," McGraw-Hill, 1962.

[137] D.B. Cruickshank, "Microwave materials for wireless applications," Norwood MA: Artech House, 2011.

[138] J. Helszajn, "Ferrite Phase Shifters and Control Devices," London: McGraw Hill, 1989.

[139] K. Chang, "Encyclopaedia of RF and Microwave Engineering," New York: John Wiley & Sons, 2005.

[140] H. Bosma," On stripline Y-circulation at UHF," IEEE Trans. Microwave Theory Tech., vol. MTT-12, pp. 61-72, January 1962.

[141] Y.S. Wu and F.J. Rosenbaum, "Wideband operation of microstrip circulators," IEEE Trans. Microwave Theory Tech., vol. MTT-22, pp.849-856, October 1974.